A STUDY OF NATURAL CONVECTION ONSET AND MELTING PROCESS OF PHASE CHANGE MATERIALS IN HORIZONTAL CYLINDRICAL ENCLOSURES

by

Mohammad Azad

Submitted in partial fulfilment of the requirements
for the degree of Doctor of Philosophy

at

Dalhousie University
Halifax, Nova Scotia
August 2020

TABLE OF CONTENTS

LIST OF TABLES

LIST OF FIGURES

ABSTRACT

Phase change materials (PCMs) are a promising medium to store thermal energy in latent heat energy storage systems. While these materials offer a large storage density, their thermal conductivities are low and offer challenges for practical applications. It has been reported by researchers that natural convection plays a dominant role in the melting of the PCMs, the energy-storing phase. However, natural convection does not exist at the beginning of the heating process but rather comes into existence after some PCM melts by conduction first. This study was undertaken to explore the conditions for the onset of natural convection.

Melting of *n*-octadecane and dodecanoic acid in horizontal cylindrical enclosures with center-tube diameters of 18, 27, and 36 mm were studied. The PCMs were initially subcooled by 2.5, 7.5, 15, and 22.5 °C. The melting temperature differentials (the difference between the melting temperature of the PCMs and the heating temperature) were 8.44, 16.9, 25.3, 33.8, and 42.2 °C for *n*-octadecane and 8.44, 25.3, and 42.2 °C for dodecanoic acid.

The results indicate that the melt volume at the onset of natural convection increases with the diameter of the center-tube. Also, a lesser amount of liquid PCM is required for the onset of convection when the melting temperature differential is high. It was found that the convection onset occurred faster at higher Stefan numbers. Subcooling of the PCMs delayed the occurrence of convection onset. No such clear trend was observed for the center-tube diameters.

Correlations to predict the moment of onset of convection and the volume of liquid PCM required for the onset of convection were developed. The correlations developed separately for each PCM were comparable. A generic correlation was developed from the combined results of the two PCMs that can be used to predict the convection onset occurrence for different geometric and thermal conditions.

LIST OF ABBREVIATIONS AND SYMBOLS USED

Symbols

c	Specific heat capacity (J kg^{-1} K^{-1})
d	Diameter of the center-tubes (m)
D	Diameter of the outer shell (m)
f	Melt fraction (-)
H	Height (m)
H_{onset}	Projected height of the liquid PCM on the central vertical axis (m)
I_{onset}	Intercept of the straight line in Eq. (7.21)
k	Thermal conductivity (W m^{-1} K^{-1})
L	Latent heat of fusion (J Kg^{-1})
L_c	Characteristic length (m)
M_{onset}	Slope of the straight line in Eq. (7.21)
N	Number of samples
q	Heat transfer rate per unit length of the enclosure (W m^{-1})
r	Radius of the center-tube (m)
R	Radius of the outer shell (m)
R^2	Coefficient of determination (-)
R_θ	Thermal resistance (K W^{-1})
t	Time (s)
u	Uncertainty (%)
T	Temperature (°C or K)
v	Velocity of liquid PCM (m s^{-1})
V_m	Volume of liquid PCM (m^3 m^{-1})
V_{onset}	Melt volume at the onset of natural convection (cm^3 cm^{-1})
X	Product of dimensionless numbers in Eq. (7.21)
X_G	Product of dimensionless numbers for global melting in Eq. (8.3)

Dimensionless numbers

Fo	Fourier number $\left(\frac{\alpha t}{L_c^2}\right)$
Gr	Grashof number $\left(\frac{g\beta\Delta T_f L_c^3}{\nu^2}\right)$
Pr	Prandtl number $\left(\frac{\nu}{\alpha_l}\right)$
Ra	Rayleigh number $\left(\frac{g\beta\Delta T_f L_c^3}{\nu\alpha}\right)$
Ste	Stefan number related to liquid PCM $\left(\frac{c_l(T_w - T_m)}{L}\right)$
Ste_s	Stefan number related to solid PCM or degree of subcooling $\left(\frac{c_s(T_m - T_i)}{L}\right)$

Greek symbols

α	Thermal diffusivity ($m^2\ s^{-1}$)
β	Thermal expansion coefficient (K^{-1})
δ	Melt thickness (m)
μ	Dynamic viscosity (Pa s)
ν	Kinematic viscosity ($m^2\ s^{-1}$)
ρ	Density ($kg\ m^{-3}$)

Subscripts

Corr.	From correlation
eff	Effective
exp.	From experiment
f	Fusion
H	Heat flux
i	Initial
l	Liquid
liquid	Of liquid PCM
m	Melting point
max	Maximum value
onset	At the onset of natural convection
s	Solid
steel	Stainless steel 304
sur	On the surface of the sleeve
t	Tube
thick	Thickness of the sleeve
w	Wall
width	Width of an enclosure

Abbreviations

HTF	Heat Transfer Fluid
LED	Light Emitting Diode
LHESS	Latent Heat Energy Storage System
MAE	Mean Absolute Error
MBE	Mean Bias Error
PCM	Phase Change Material
RGB	Red, Green, Blue
TES	Thermal Energy Storage
XPS	Extruded polystyrene

ACKNOWLEDGEMENTS

I want to thank my supervisor, Prof. Dominic Groulx, for allowing me to work at the LAMTE. Prof. Groulx gave me full freedom in deciding what I wanted to do and how I wanted to do it. Yet, he was always there to pull me on the track whenever it was necessary. Thank you, Prof. Groulx, for your unlimited support!

I would also like to thank my other supervisor Prof. Adam Donaldson. Prof. Donaldson always helped me with ideas and technical know-how. Thank you, Prof. Donaldson.

My sincere thanks to the other committee members, Prof. Stephen Corbin, and Prof. Jan Haelssig. I received numerous valuable comments from them in every committee meeting.

My journey to the completion of this thesis would be much more difficult if Ms Kate Hide were not there as the Administrative Secretary. No matter what I needed help with, she was always there with her smiling face. Thank you, Kate!

Without the help of Mark MacDonald, Albert Murphy, Peter Jones, and Jonathan MacDonald in the Department of Mechanical Engineering, this work would never be the same. Thank you all.

It is hours of discussions with all exceptional minds in the lab that made me rethink and reshape the thesis. Thank you, everyone. Your input was a tremendous help!

I am grateful to the Natural Sciences and Engineering Research Council of Canada, the Government of Nova Scotia, and the Faculty of Graduate Studies at Dalhousie University for supporting this study through different scholarships.

Lastly, thanks to all my family members and friends, who till today continue to inspire me.

CHAPTER 1 INTRODUCTION

Thermal energy storage systems can lessen the problem arising from the unpredictable availability of clean sources of energy for water and space heating purposes. Thermal energy can be stored as sensible and latent heat, and thermochemical energy, a detailed discussion follows in section 1.1. In latent heat energy storage systems (LHESS), phase change materials (PCMs) are used as the storage medium. Phase change materials melt during the storing phase and solidify when the stored energy is released. During the melting of PCMs, heat transfer takes place by conduction in the beginning, and soon natural convection becomes the dominant heat transfer mode. The current work aims to explore the influences of different parameters of a LHESS on the onset of natural convection. The objective is to develop a correlation to identify the onset of natural convection during the melting of PCMs. The PCMs used in this experimental study are *n*-octadecane and dodecanoic acid. These PCMs from *n*-alkane and fatty acid groups are suitable for low-temperature applications such as heating/cooling of residential or commercial spaces, solar thermal energy storage, and storing off-peak energy and temperature management (Agyenim *et al.*, 2010).

1.1 Methods of storing thermal energy

Thermal energy can be stored as sensible heat, latent heat, or thermochemical energy (Mehling and Cabeza, 2008; Sharma *et al.*, 2009). In sensible energy storage systems, energy is stored in a material by increasing its temperature without changing the phase (Aneke and Wang, 2016). The storage materials are usually solid or liquid, such as rock, metal, brick, water, or oil (Mahlia *et al.*, 2014; Kousksou *et al.*, 2014). The amount of energy that can be stored depends on how large the temperature increase of the storage material can be (Fernandez *et al.*, 2010). Storing energy at high temperature is disadvantageous because it causes heat loss from the system and requires increased amount and cost in insulation. Another disadvantage of sensible energy storage systems is the requirement of a large mass/volume of the storage material.

In latent heat energy storage systems, on the other hand, the change of phase of the storage materials, the phase change materials, is utilized to exploit its latent heat capacity (Murray

et al., 2011; Farid *et al.*, 2004). The phase change can be solid-solid, solid-liquid, or liquid-gas (Kousksou *et al.*, 2014; Sharma *et al.*, 2009).

Solid-solid phase change materials store heat between two solid phases, one in crystalline or semi-crystalline phase and the other in amorphous, crystalline or, semi-crystalline phase (Fallahi *et al.*, 2017; Sharma *et al.*, 2009). The transition from one lattice structure to another takes place at a fixed temperature (Su *et al.*, 2015). Since the solid-solid PCMs do not transition to the liquid phase, their container does not need to meet stringent design requirements (Sharma *et al.*, 2009). The solid-solid PCMs, however, exhibit unstable thermal properties and have lower latent heat capacities than solid-liquid PCMs (Sarı *et al.*, 2012).

The liquid-gas phase change materials offer high latent heat capacity but also come with a large change in volume/pressure. The large change in volume/pressure of the liquid-gas PCMs makes them impractical for engineering applications (Abhat, 1983).

Solid-liquid PCMs offer high density, high latent heat of fusion, and high values of specific heat capacity (Su *et al.*, 2015). Moreover, solid-liquid PCMs exhibit a small change in density upon transition from one phase to another (Su *et al.*, 2015). Because of the transition to the liquid phase, extra care must be exercised in designing their containers. The solid-liquid PCMs are broadly classified into inorganic and organic categories. Organic PCMs have high latent heat of fusion and excellent thermal stability; they are inexpensive, non-corrosive, and non-toxic (Sharma *et al.*, 2016; Baetens *et al.*, 2010). Nonetheless, organic PCMs have very low thermal conductivity, which is disadvantageous for practical applications (Baetens *et al.*, 2010).

Lastly, thermochemical thermal energy storage (TES) systems utilize the chemical properties of the working materials instead of their physical properties. These systems utilize reversible chemical reactions, exemplified by Eq. (1.1), to charge or discharge the system (Abedin and Rosen, 2011):

$$C + \text{heat} \leftrightarrow A + B \tag{1.1}$$

The thermochemical material C absorbs energy and converts chemically to two other components. The reverse reaction occurs when A and B combine to form C and release heat.

Thermochemical TES systems have high storage density, and they are suitable for loss-free long term storage (Prieto *et al.*, 2016). However, thermochemical storage is more complex and costlier than the other two methods (Niedermeier *et al.*, 2016), and it is mostly used in high-temperature applications (Wu *et al.*, 2018; Carrillo *et al.*, 2014).

1.2 Latent heat energy storage systems

While thermochemical energy storage technology is still in its infancy, latent heat thermal energy storage systems are preferred to sensible heat storage systems because more energy can be stored in latent form, especially when operating over small ranges of temperature (Murray *et al.*, 2011). This high storage capacity translates to a substantial reduction in the amount of the storage material required. While the high density of energy storage is the most beneficial factor of latent heat storage systems, they also offer the benefit of storing energy almost isothermally (Mahlia *et al.*, 2014). Solid-liquid phase change is favorable over solid-gas or liquid-gas phase change, considering the amount of latent heat, the change in pressure and, the working temperature range of the PCMs. However, in addition to checking the suitability of solid-liquid PCMs for an application in terms of their melting temperature, latent heat, safety, and economic feasibility, it is also imperative to check their thermal stability; the thermophysical properties of the PCMs should not deteriorate after a number of thermal cycles (Rathod and Banerjee, 2013). The most disadvantageous aspect of PCMs, especially the organic ones, is their low thermal conductivities (Kousksou *et al.*, 2014; Kenisarin, 2014). This results in organic PCM-based TES systems having low heat transfer rates in and out of the systems (Medrano *et al.*, 2009; Farid *et al.*, 2007). This problem is termed the 'rate problem' (Groulx *et al.*, 2016). For LHESS to become a viable alternative to sensible energy storage systems, the problem of low heat transfer rates needs to be overcome. Different approaches have been adopted by researchers to improve the heat transfer rates into and out of PCM-based systems, as introduced in Section 1.3.

1.3 Improvements in latent heat storage systems

Different methods have been investigated by researchers to overcome the 'rate problem' of LHESS. Some methods aimed at increasing the conductive heat transfer rates through the addition of metallic matrix/foam (Li *et al.*, 2012; Esapour *et al.*, 2018; Zhou and Zhao, 2011; Cheng *et al.*, 2010; Allen *et al.*, 2015) and fins (Liu *et al.*, 2012; Murray and Groulx, 2014; Shatikian *et al.*, 2005; Shatikian *et al.*, 2008; Stritih, 2004) to the heat exchangers. Other methods of enhancing conductive heat transfer rate involve the addition of conductive nanoparticles to PCMs (Mahdi and Nsofor, 2017; Mettawee and Assassa, 2007; Motahar *et al.*, 2017; Şahan *et al.*, 2015). Addition of fins increases the heat transfer rates in LHESS, however, use of nano-enhancement of PCMs is not perhaps worth it (Groulx, 2015). Also, any improvement in heat transfer rates by the addition of nanoparticles to the PCMs or addition of fins to the heat exchangers comes with a reduction in the system storage density in addition to the initial cost involved in modifying the heat exchanger or enhancing the PCMs.

While the heat transfer rates can be improved through modification of heat exchangers, the beneficial aspect of natural convection is that it increases the heat transfer rates both in the basic and modified heat exchangers. However, the contribution of natural convection slows down in the later stage of the melting process. The contribution period of natural convection can be extended by changing the design of the heat exchangers, for example, by using eccentric annular enclosures in place of concentric (Darzi *et al.*, 2012; Pahamli *et al.*, 2016) or tilted vertical annular enclosures instead of purely vertical enclosures (Sharifi *et al.*, 2013). Fast onset and presence of strong natural convection heat transfer could increase the overall heat transfer rate without any reduction in the storage density and any extra cost involved in modifying the heat exchangers or in enhancing the PCMs.

1.4 The motivation for the present work

During the charging phase (melting of the PCM), the heat transfer rate increases significantly once natural convection in the melted portion of the PCM becomes dominant (Farid *et al.*, 2007; Sun *et al.*, 2016). As has been discussed, natural convection does not exist as soon as the heat source is applied; a certain amount of PCM first needs to be melted

by conduction. Faster initiation of natural convection could directly result in a faster heat transfer rate during melting of PCMs. Yet, there exists no guideline as to when the natural convection starts, or in other words, what influences the onset of natural convection during PCM melting.

It is not rare to see that in numerical simulations of PCM melting, natural convection is ignored on the assumption that the volume of the PCM is so small that natural convection can be neglected (Akhilesh *et al.*, 2005; Seeniraj and Narasimhan, 2008). In many other simulations, natural convection is accounted for through effective thermal conductivity (Adine and El Qarnia, 2009; Pointner *et al.*, 2016; Tao and He, 2011). There exists, whatsoever, no guidelines as to when the natural convection in the phase change melting process can be neglected.

This work was undertaken to fill in this knowledge gap on the onset of natural convection during melting of PCMs.

Furthermore, there is no evidence of any parametric study for global melting in horizontal annular systems where both the geometry and the temperature are varied. Most studies focused on the effects of extended surface area, the orientation of the enclosure (Sharifi *et al.*, 2013), or the heating temperature (Avci and Yazici, 2013). A benchmark data of the melting behavior in horizontal annuli in different geometric and thermal operating conditions would be useful for validation of numerical models. Therefore, a parametric study was done to understand the effects of geometric and thermal conditions, as well as of PCM on global melting in horizontal annuli. The same experimental setup was used and the experiments for the onset of convection were run for a period of 8 hours to obtain the global melting data.

1.5 Objectives

As has been discussed, natural convection plays an important role during melting of PCMs. Despite its significant importance in increasing heat transfer rates in LHESS during the heat storage phase, no attempt has been put forward in understanding what influences the onset of natural convection. The objective of this study is to develop a guideline on how

different parameters influence the onset of natural convection. The overall objective would be achieved by fulfilling several sub-objectives. These are:

1. to investigate the influence of center-tube diameter in horizontal annular enclosures on the onset of natural convection
2. to study the effects of center-tube temperature on the onset of convection
3. to examine if the initial temperature of the PCM (degree of sub-cooling) influences the onset of natural convection
4. to identify any dependence of natural convection onset on the properties of the PCMs, especially the viscosity
5. to obtain a correlation for the onset of natural convection.

The secondary objective of this study is to provide a benchmark dataset for global melting of the PCMs that could be used to validate numerical models.

1.6 Scope of the thesis

Chapter 2 of this thesis presents a literature review that covers works involving different heat exchangers, where natural convection plays a significant role. This chapter also explores the work devoted to studying natural convection onset regardless of the shape of the heat exchanger. Also, this chapter presents numerical works that have accounted for natural convection during melting of PCM and the ones that did not. It will be seen in this chapter that the importance of natural convection during melting of PCM is evident from numerous amounts of work. Yet, no efforts have been devoted to understanding what influences the onset of natural convection. Moreover, it can be seen that natural convection has been neglected in numerical simulations, although there exists a lack of understanding as to when the natural convection can be neglected.

Two PCMs, *n*-octadecane and dodecanoic acid, have been used in this work to investigate the influences of PCMs on the onset of natural convection. The properties of these PCMs are given in Chapter 3. The experimental setup and procedures used for this thesis work are also presented in Chapter 3. This chapter explains how the PCM enclosures were fabricated, the experimental setup was built, and how different instruments were used during the experiments. All the results in this work were obtained through image analysis.

The details of this image analysis techniques and uncertainty calculation methods are presented in Chapter 4 of this thesis.

Chapter 5 summarizes the results obtained from experiments involving *n*-octadecane and Chapter 6 summarizes the results obtained from experiments with dodecanoic acid. These results include the melt profiles of the PCMs at different time intervals, volume requirement of liquid PCM for the onset of natural convection against the diameter of the center-tube, and the Stefan numbers for four different initial temperatures of the PCMs.

Dimensional analysis was carried out to identify different dimensionless groups that are involved in the melting process and play a role in the onset of natural convection. This analysis is presented in Chapter 7. It can be seen in this chapter that one of the obtained dimensionless groups is the Grashof number. Defining the Grashof number poses a challenge in the context of PCM melting. The challenge is discussed in this chapter, and a definition in the context of PCM melting is proposed. Correlations for the onset of natural convection based on the dimensional analysis are developed in this chapter and presented sequentially for different subcooling temperatures used in the present study and finally combined to obtain a single correlation that is functional regardless of the initial temperature of the PCM.

Chapter 8 of this thesis presents the global melting results for both PCMs. In Chapter 9 of this thesis, different numerical models used to analyze the PCM melting process are reviewed. The modified heat capacity-porosity method was adopted in this study to analyze the onset of natural convection. The results from these numerical simulations are compared with those from experiments in this chapter. Chapter 10 concludes the findings of this study and recommends future works.

CHAPTER 2 LITERATURE REVIEW

The generic melting process of PCMs is first briefly discussed in this chapter. Later in the chapter, the melting of PCM in different geometries, in their different orientation and under different thermal conditions is thoroughly reviewed. The research work on the onset of natural convection in a single-phase fluid and in liquid PCMs during melting of solid PCMs is also reviewed. Finally, the numerical models that involved natural convection during melting of PCMs and that did not are reviewed.

2.1 Melting phenomenon of phase change materials

At the beginning of the charging process inside latent heat thermal energy storage systems, the PCM exists in the solid phase, either at the melting temperature of the PCM or at a subcooled temperature. As the charging process starts, the heat source remains in contact with the solid PCM, and the PCM is preheated when it is initially subcooled. Once the PCM reaches the melting temperature, melting of the PCM takes place by conduction (Hosseinizadeh *et al.*, 2013; Hamdan and Al-Hinti, 2004; Liu and Groulx, 2014; Agyenim *et al.*, 2010). When enough liquid PCM is there, natural convection initiates, and shortly after that dominates the melting process (Liu and Groulx, 2014; Agyenim *et al.*, 2010). The whole melting process is often divided into four stages as (i) pure conduction, (ii) mixed conduction and convection, (iii) convection dominant, and (iv) shrinking solid (Jany and Bejan, 1988; Jones *et al.*, 2006). This division gives a general overview of the melting process. The exact melting process depends on the shape of the geometry and orientation of the heat source. For example, a cubical heat exchanger that is heated from the top would not exhibit any natural convection. Similar to this phenomenon is the last phase of melting in an annular heat exchanger where the annular space is filled with the PCM, and the heat source is placed at the center. Once at least half of the PCM is melted, when the solid-liquid interface remains below the heat source, the melting process is dominated by conduction (Azad *et al.*, 2016). Unlike this, during constrained melting in a spherical enclosure where the heat source is applied to the outer surface, the last phase of conduction dominated melting is nonexistent (Tan, 2008). Regardless of the geometry of the heat exchanger or the position of the heat source, it is evident from numerous studies that heat transfer takes place much more rapidly when there is convection in the liquid phase

compared to when there is not (Archibold *et al.*, 2014; Tao and He, 2015; Kamkari and Amlashi, 2017). Although the presence of convection causes faster heat transfer, convection does not start immediately, as has already been discussed; natural convection begins only after a certain amount of PCM melts by conduction.

Use of Rayleigh number to characterize convective heat transfer during melting of PCMs and the heat transfer phenomenon in common shapes of heat exchangers, namely rectangular, spherical, vertical cylindrical, horizontal cylindrical, vertical annular, horizontal annular are reviewed in the following subsections.

2.1.1 Characterization of convective heat transfer using Rayleigh number

The Rayleigh number is commonly used to characterize the significance of convection in a heat transfer process. The Rayleigh number is the product of Grashof and Prandtl numbers, which is defined as:

$$\mathrm{Ra} = \frac{g\beta\Delta T L_c^3}{\nu\alpha} \tag{2.1}$$

where β, ν, and α are the thermal expansion coefficient, kinematic viscosity, and thermal diffusivity of the fluid, respectively; g is the gravitational force, ΔT is the temperature difference between the hot and cold surfaces or fluid layers, and L_c is the length scale.

For heat transfer in a single-phase fluid confined in a small enclosure, the temperature difference in the definition of Rayleigh number is taken as the difference between the hot and cold walls. For a semi-infinite system, the temperature difference is considered as the difference between the temperature of the heated wall and the fluid far from the thermal boundary layer. The thermophysical properties of the fluid are taken at the average of the above-mentioned two temperatures. All the above measures are possible to be taken in a single-phase fluid because the thickness of the fluid layer always remains the same. That is not, however, the case during melting of a PCM. The use of all those parameters poses a challenge in using Rayleigh number in the context of melting of PCMs because the thickness of the liquid PCM layer changes with time. Therefore, the Rayleigh number has been defined differently by researchers in the context of PCM melting. The Rayleigh

number, although not appropriately defined in some cases, has been used by many researchers in the context of natural convection during melting of PCMs (Gong and Mujumdar, 1998; Hlimi *et al.*, 2016; Regin *et al.*, 2006).

2.1.2 Melting of PCMs in rectangular enclosures

The most common PCM enclosures that have been studied are the rectangular ones where heat is applied to one of the vertical sides, and the opposite vertical side is cooled simultaneously or kept insulated. It is seen from experimental studies that a thin layer of PCM parallel to the heat source melts first (see Fig. 2.1a). Once there is enough liquid PCM, more PCM melts at the top of the enclosure than at the bottom (see Figs. 2.1b and 2.1c), driven by natural convection (Pal and Joshi, 2001; Shokouhmand and Kamkari, 2013). Afterward, natural convection becomes stronger until the last phase of the melting process when natural convection fades away.

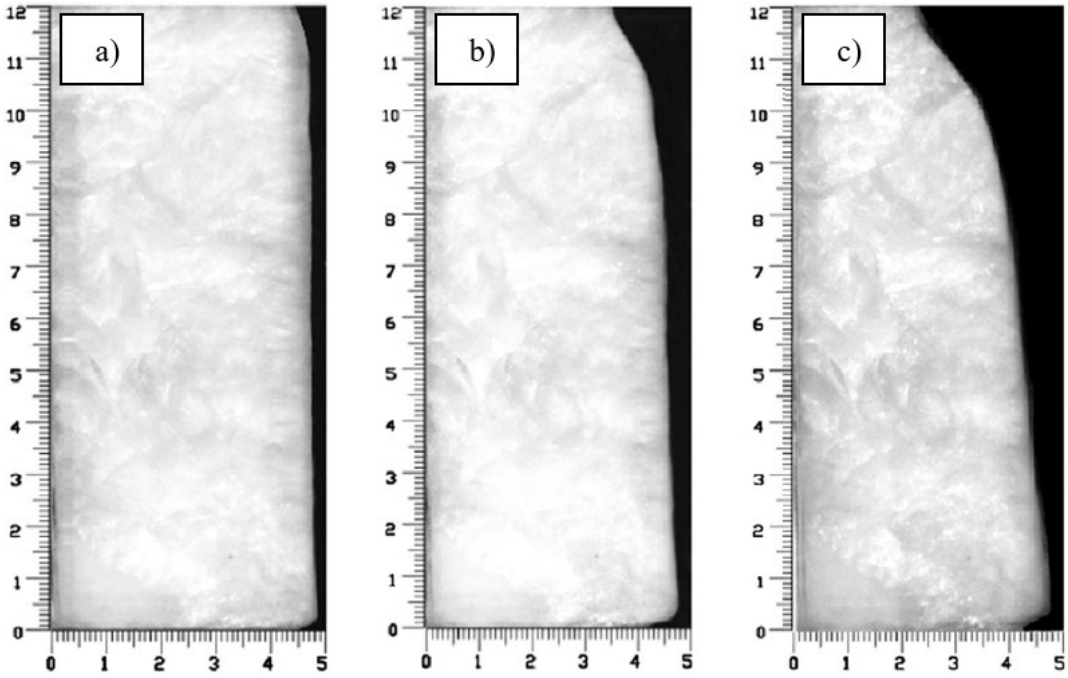

Figure 2.1 Melting of dodecanoic acid in a rectangular enclosure at a) t = 10 min, b) t = 30 min, and c) t = 50 min (Shokouhmand and Kamkari, 2013).

Another configuration of a rectangular enclosure is the one where heat is applied to the bottom side while the other sides are kept insulated. Unlike the case where heat is applied to the vertical side, during bottom heating, the melt height changes with time. If the melt height is used as the length scale in the definition of Rayleigh number, then the Rayleigh

number becomes a transient quantity in such systems. In the numerical study of melting of *n*-octadecane in a rectangular enclosure heated from the bottom side, Gong and Mujumdar (1998) defined the Rayleigh number as given in Eq. (2.1). In their definition, ΔT was the difference between the wall temperature and melting temperature of the PCM. They adopted the height of the enclosure, instead of the melt height, as the length scale. However, it has been noted by the authors that the choice of the length scale was not appropriate. During melting from the bottom side, as the liquid layer grows, convective rotating cells form and augment heat transfer rate. These rotating cells develop faster as the applied temperature on the bottom side grows higher. The number of cells and their interaction depend on the Rayleigh number. As has been reported by Gong and Mujumdar (1998), two convective rotating cells form when the Rayleigh number is in the order of magnitude of 10^4. The number of cells doubles for every order of magnitude increase in the Rayleigh number. Once the Rayleigh number is in the order of magnitude of 10^7, the cells interact and merge as they form. The effects of inclination of rectangular enclosures on the melting of PCM have been studied experimentally by Kamkari *et al.* (2014). The heat was applied to one of the longer sides, and the opposite side was thermally insulated. Similar to the vertical enclosures, a thin layer of PCM first melts by conductive heat transfer along the heated surface, and natural convection takes over once there is enough liquid PCM. A comparative study of the melting from the bottom surface, an inclined bottom surface (at 45°), and from the vertical side shows that PCM melts much faster when it is heated from the bottom surface due to the presence of chaotic multi-cellular structures (Kamkari *et al.*, 2014).

Fins are often added to the vertical sidewalls of rectangular enclosures to increase the heat transfer surface area. Usually, these fins are arranged horizontally with the vertical walls. As the heat transfer area increases through the additions of fins, heat transfer rates in the finned rectangular enclosures increase. It has been observed in an experimental and numerical comparative study that vortex cells form in the liquid PCM above the fins; chaotic motion of the liquid PCM is also observed (Kamkari and Shokouhmand, 2014). Heat transfer rate does not increase proportionally to the number of fins. There appears to be an optimum number of fins that can be added to maximize the heat transfer rate; however, the optimum number has not yet been established. It has been seen

experimentally, when an excessive number of fins is added to the heat exchanger, it reduces the volume of liquid PCM between two adjacent fins and thus inhibits natural convection (Kamkari and Shokouhmand, 2014; Stritih, 2004).

Fins are also used in vertical orientations where they are attached to the heated base surface of the rectangular enclosures. The melting dynamics, in this case as well, depends on the fin density. Numerical studies show that in the cases where the thickness of solid PCM between two fins is large, the initial phase of melting is dominated by conduction. In this phase, the melt interface remains parallel to the hot surface. However, as the thickness of solid PCM between two fins gets narrower, PCM in the top portion of the fin remains in solid-state while at the bottom of the fin, PCM melts. Therefore, the conductive melting all along the heat source is not observed when the solid PCM thickness is too small (Shatikian *et al.*, 2005). Experimental studies show, in vertically oriented finned systems as well, that the addition of too many fins limits the onset of natural convection and reduces the heat transfer rate (Huang *et al.*, 2011).

2.1.3 Melting of PCMs in spherical enclosures

In spherical systems, where the sphere is filled with PCM and heat is applied to the outer surface, the PCM first melts in the regions that are in contact with the surface. A thin layer of liquid PCM forms surrounding the hot surface. Experimental studies show that when the solid PCM is constrained, natural convection starts dominating the melting process once there is enough liquid PCM (Khodadadi and Zhang, 2001). The melt fractions of *n*-octadecane after 20 and 40 minutes of constrained melting in a spherical container studied experimentally by Tan *et al.* (2009) are presented in Fig. 2.2. The thickness between the PCM surface and the enclosure wall is almost the same surrounding the enclosure wall after 10 minutes of melting, and after 20 minutes, more PCM melts in the upper portion of the enclosure. In constrained melting, the solid PCM cannot move to the bottom of the enclosure. As the liquid PCM at the bottom of the container gets hotter, it moves up along the hot surface of the container, and the colder liquid at the top of the container moves down along the edge of the solid PCM. This movement of the hot and cold fluid leads to more melting at the top than at the bottom. When the natural convection is strong, multiple cells of rotating vortices are observed (Khodadadi and Zhang, 2001). The convection exists

until the end of the melting process, although it becomes weak, as in other geometries, in the last phase of the melting process.

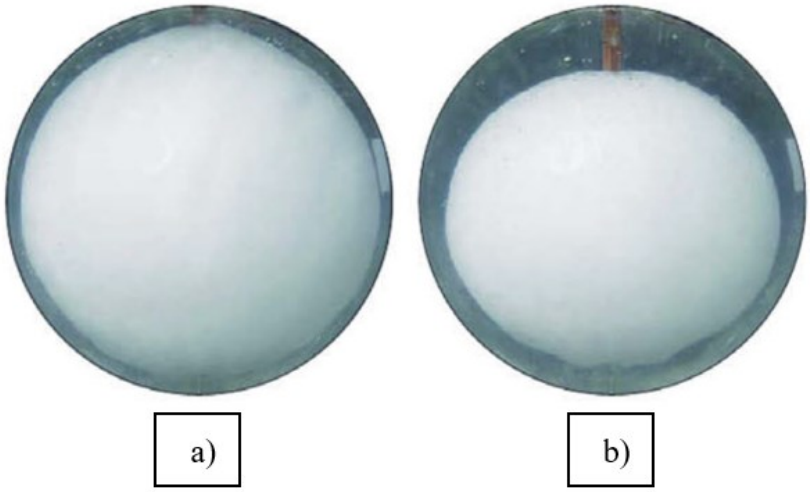

Figure 2.2 Constrained melting of *n*-octadecane in a spherical container of 102 mm diameter and a melting temperature differential of 12 °C at a) *t* = 20 min and b) *t* = 40 min (Tan *et al*., 2009).

During melting of PCM in an unconstrained spherical container, PCM first melts in close contact with the outer surface, just as it does in the case of constrained melting. As the melting progresses, the solid PCM keeps sinking to the bottom of the sphere. The liquid PCM layer between the solid PCM and the bottom surface of the sphere gets pushed by the solid PCM as it sinks to the bottom. This pressure of the solid PCM on the liquid layer at the bottom causes upward movement of the hot fluid and thus augments the natural convection, as has been seen experimentally by Tan (2008) and Hosseinizadeh *et al.* (2013). Thus, the sinking of the solid PCM facilitates melting due to natural convection in addition to close contact melting, as shown by different experimental studies (Rizan *et al.*, 2012; Assis *et al.*, 2007). Unlike most other PCMs, the density of ice increases as it melts to water. Accordingly, experimental studies show that instead of sinking to the bottom, ice floats on water and remains in contact with the top surface during melting in a spherical container heated from the outer surface (Adref and Eames, 2002; Eames and Adref, 2002). Based on the presence of the spherical shape of the ice almost until the end of the melting process, Adref and Eames (2002) concluded that conductive heat transfer dominated the entire melting process.

2.1.4 Melting of PCMs in cylindrical enclosures

Two configurations of cylindrical enclosures have been widely studied. In one configuration, the cylinder is filled with PCM and is heated at the outer surface. Most studies on this configuration were conducted for vertical cylinders. In this configuration, since the PCM is not held in place by an inner tube, the melting is often referred to as unconstrained melting. In the other configuration, which is commonly referred to as annular heat exchangers, the annular space is filled with the PCM and heat is applied either at the inner surface or outer surface. Since the PCM is held in place by the inner tube when heated from the outer tube and vice versa, the melting in this configuration is often referred to as constrained melting. Both horizontal and vertical systems have been studied extensively for these configurations.

Figure 2.3 Melting of RT27 in a vertical cylinder of 3 cm diameter and a melting temperature differential of 10 °C at a) t = 4 min and b) t = 28 min (Shmueli *et al.*, 2010).

When a vertical cylinder filled with PCM is heated from the outer surface, a thin layer of PCM first melts by conduction adjacent to the outer surface, as can be seen in Fig. 2.3a). As this liquid layer grows larger, natural convection initiates in the liquid PCM, which causes faster melting of the PCM in the top portion of the container, presented in Fig. 2.3b). These experimental results also show that in small aspect-ratio (the ratio of diameter to height) vertical cylinders, the solid PCM takes a conical shape (Shmueli *et al.*, 2010). In

large aspect-ratio vertical cylinders, the experimental results show that the solid PCM takes the form of a dome (Jones *et al.*, 2006).

During unconstrained melting in a horizontal cylinder heated from the outer surface, PCM first melts by conduction as indicated by the solid-liquid interfaces that are concentric to the cylinder. The experimental work of Ho and Viskanta (1984) shows that the solid PCM floats concentrically to the cylinder. As the liquid layer grows, natural convection dominates the melting process, and the solid PCM sinks to the bottom portion of the cylinder. However, as the solid PCM sinks, there is experimental evidence that it may or may not come to close contact with the bottom surface (Regin *et al.*, 2006; Ho and Viskanta, 1984). Whether the solid PCM completely sinks and meets the bottom surface or not perhaps depends on the change in density of the PCM as it melts. For example, solid PCM sinks completely in the experimental study of Regin *et al.* (2006); the PCM in their study was paraffin wax (with a melting temperature of 59.9 °C), which is 15% heavier when it is solid compared to the liquid phase. The PCM used by Ho and Viskanta (1984) in their study was *n*-octadecane, which is approximately 8% heavier in the solid phase and does not come in close contact with the container. Rather, circulating vortices, three-dimensional in nature, were observed in the bottom layer of the liquid PCM. As the liquid layer of the PCM grows thicker, these vortices merge with the larger vortices in the upper region of the cylinder (Ho and Viskanta, 1984). The shape of the solid-liquid interface in this type of melting depends on the thermal condition at the boundary layer. The Rayleigh number for a horizontal cylindrical system where the PCM was heated from the outer surface was defined by Chung *et al.* (1997) in their numerical study as:

$$\mathrm{Ra} = \frac{g\beta(T_\mathrm{w} - T_\mathrm{m})R^3}{\nu\alpha_\mathrm{l}} \tag{2.2}$$

In Eq. (2.2), β is the thermal expansion coefficient, ν and α_l are the kinematic viscosity and thermal diffusivity of the liquid PCM, R is the radius of the cylinder, T_w and T_m are the wall temperature and melting temperature of the PCM, respectively.

At low Rayleigh number (in the order of 10^4), the flow of liquid PCM in the symmetric half is dominated by a single cell of rotating vortex, and the solid-liquid interface remains

almost concentric to the cylinder (Chung *et al.*, 1997). It is also observed in a numerical study that in the later stage of the melting process, this single cell may break into multiple cells, and a non-concentric shape of the solid-liquid interface emerges (Hlimi *et al.*, 2016). At large Rayleigh numbers (in the order of 10^6 and higher), the flow in the liquid layer between the solid PCM and the bottom surface is dominated by multi-cell vortices; but a single large vortex encompasses most of the liquid PCM volume including the upper portion of the cylinder (Chung *et al.*, 1997; Hlimi *et al.*, 2016). Numerical studies also show that the number of cells at the bottom portion depends on the Rayleigh number; as the Rayleigh number increases, the number of cells increases (Chung *et al.*, 1997; Rieger *et al.*, 1983; Ng *et al.*, 1998). The existence of multi-cells in the bottom portion causes a non-concentric shape of the solid-liquid interface.

In vertical annular systems where the annular space is filled with PCM, and the heat source is applied at the center-tube or the outer surface, PCM first melts in the vicinity of the heat source. As the volume of the liquid PCM increases, more PCM melts at the upper portion of the heat exchanger compared to the bottom portion, as seen in the numerical and experimental study of Longeon *et al.* (2013). Experimental study of melting of dodecanoic acid in a vertical annulus, where longitudinal fins are attached to the center-tube, shows that the melting is significantly affected by natural convection (Murray and Groulx, 2014). Melting and solidification of paraffin wax (with a melting temperature of 52 °C) in a vertical annulus were studied experimentally by Ettouney *et al.* (2004). It was found that natural convection dominated the melting process and conduction dominated the solidification process.

During melting of PCM in horizontal annular systems where the annular space is filled with PCM and heated from the center, the PCM first melts concentrically to the center-tube. Once enough PCM is melted by conduction, natural convection comes into existence, and more PCM melts at the top of the heat source than at the bottom, as seen experimentally by Avci and Yazici (2013). Natural convection dominates the melting process until all the PCM above the heat source is melted. Once all the PCM above the heat source is melted, and the solid-liquid interface of the PCM remains below the heat source, natural convection

fades away, and conduction dominates the rest of the melting process, as seen in the numerical study of Azad *et al.* (2016).

Since most of the PCM in the bottom half of a horizontal concentric annulus remains unaffected by natural convection, the melting rate is not fast once the upper half of the PCM is melted. Therefore, the benefit of natural convection in this stage of the melting process cannot be realized. However, this problem is overcome to some extent by using an eccentric enclosure. In eccentric enclosures, the inner tube is located below the center of the outer tube. The eccentricity leaves more space above the heat source than below it. As the PCM keeps melting, natural convection gets more space compared to the concentric enclosure, and thus a faster heat transfer rate over a longer period is achieved in the eccentric configuration, as has been reported in their numerical study by Darzi *et al.* (2012). An experimental study shows that in an eccentric configuration, the total melting time can be reduced as much as 67% by moving the inner tube down from the center of the outer tube by 30 mm when the diameters of the inner-tube and outer shell are 28.5 and 110 mm, respectively (Yazıcı *et al.*, 2014).

In longitudinally-finned horizontal annular heat exchangers, the presence of natural convection has also been observed experimentally by Liu and Groulx (2014). Four longitudinal fins were welded to the inner tube at 90° apart from each other; in one configuration, the first fin is horizontal, and in the other, the first fin being at 45° with the horizontal. Natural convection played a significant role in melting in both the heat exchangers.

A photographic investigation of melting in a horizontal annulus was done by Rozenfeld *et al.* (2015). They added three longitudinal fins in a 'Y' orientation to the inner tube that carried the heat transfer fluid. It is interesting to note that the fins served not only as extended surfaces for heat transfer purposes but also as the source of close contact melting. The close-contact melting was facilitated by submerging the PCM enclosure in a transparent hot water tank. The contribution of the hot water tank to the melting of the PCM was small, but it allowed the PCM to slide as it melted. As soon as solid PCM in contact with the hot surfaces melted, the solid PCM above the 'Y' shape slid vertically and

rested in contact with the two inclined sides of the 'Y' shape and the solid PCM on two sides moved to the bottom of the enclosure and remained in contact with the vertical fin. As reported by the authors, close contact melting reduced the melting time by 2.5 times compared to the case where fins are absent. Nonetheless, it can be observed that the PCM confined in the upper portion of the equally spaced 'Y' shape fin becomes completely liquid while the PCM in contact with the vertical fin is solid. The faster melting of PCM in the upper portion of the enclosure indicates the presence of natural convection. It can be easily attributed that vortex cells form in the liquid PCM on both sides of the vertical fin, which drives the hot fluid to the upper portion and thus heats the two inclined fins, eventually transferring the heat to the inclined fins. This additional heat in the inclined fins would cause stronger natural convection in the upper portion of the 'Y' shape.

Heat transfer is also enhanced in differently oriented finned enclosures. A comparative study of melting in three horizontal annular enclosures was done experimentally by Agyenim *et al.* (2009). One enclosure had no fins, one had eight radial fins along the length, and the other had eight longitudinal fins. The study suggests that for the same duration of melting, the highest amount of energy was charged in the enclosure with the longitudinal fins followed by the one with radial fins and the one without fins, respectively. The total heated surface area in contact with the PCM was 0.78, 0.36, and 0.17 m^2, respectively, for the longitudinally finned, radially finned, and un-finned enclosures. This study shows that PCM melts faster at the upper portion of the enclosure, regardless of the configuration of the enclosure, suggesting the influence of natural convection.

A numerical study shows that in horizontal annular heat exchangers, thermal stratification of the liquid PCM occurs in the top portion of the heat exchangers. However, the thermal stratification can be minimized by heating the PCM from both the inner and outer surfaces (Khillarkar *et al.*, 2000). Another numerical study that compared melting in horizontal and vertical annular heat exchangers shows that for the first half of the melt volume, the horizontal heat exchanger has a faster melting rate than the vertical heat exchanger (Seddegh *et al.*, 2016), signifying that natural convection affects the melting differently in horizontal and vertical systems.

Irrespective of the shape of the heat exchangers and their orientation, it is seen that PCM first melts by conduction, and once there is enough liquid PCM, natural convection starts to play a dominant role in the melting process.

2.2 Onset of natural convection

It is evident from the above discussion that natural convection significantly dominates the melting process of PCMs, regardless of the shape of the geometry. It also should be noted that heat exchangers are often modified to achieve increased heat transfer rates through the addition of extra heat transfer surfaces, facilitation of close contact melting, and having the heat exchanger in different orientations. Regardless of the modification, natural convection plays a vital role in every configuration. Before discussing the onset of convection during melting of PCMs, it would be beneficial to review the onset of natural convection in single-phase fluids. In subsections 2.2.1 and 2.2.2, the onset of natural convection in single-phase fluids and PCM is reviewed, respectively.

2.2.1 Natural convection onset in single-phase fluids

When an initially stagnant fluid layer is heated at the critical Rayleigh number, buoyancy-driven natural convection occurs in the liquid as long as there exist unstable thermal layers under the gravitational force (Incropera *et al.*, 2007). The Rayleigh number for a heat exchanger with a specific geometry and working fluid solely depends on the heating temperature or the heat flux at the heating surface. Since the height of the fluid layer in a specific geometry does not change, the Rayleigh number can be increased only by increasing the heat flux or temperature at the hot surface. A significant amount of effort has been put forward in studying the onset of natural convection in a single-phase fluid. Most work has focused on the onset of convection during heating of a horizontal fluid layer from the bottom. In the theoretical study of a horizontal layer of fluid heated from the bottom surface, the onset of convection occurs at a Rayleigh number of 1296 (Kim and Kim, 2001), where the Rayleigh number is defined based on the heat flux as given in Eq. (2.3). In this equation, q_{w} is the heat flux at the hot wall, and d is the depth of the fluid, and k is the thermal conductivity. It should be noted here that the contribution of the geometric scale to the Rayleigh number is an order of magnitude higher in Eq. (2.3) compared to Eq. (2.2).

$$\mathrm{Ra} = \frac{g\beta q_w d^4}{k\nu\alpha} \tag{2.3}$$

Experimental studies show that the Rayleigh number at the onset of natural convection in a very long and wide rectangular enclosure filled with air is given by Eq. (2.4) (Hollands *et al.*, 1976):

$$\mathrm{Ra}_{\mathrm{onset}} = \frac{1708}{cos\phi} \tag{2.4}$$

where ϕ is the inclination angle with the horizontal axis. A horizontal air layer, for which ϕ = 0°, has a critical Rayleigh number of 1708, shown experimentally by Hollands and Konicek (1973). It is well known that when a fluid in a horizontal rectangular enclosure of height H, a very large length ($L/H >> 1$) and width ($w/H >> 1$) is heated from the bottom, natural convection onset occurs at the critical Rayleigh number of 1708. The flow of the fluid remains laminar, and regularly spaced roll-cells are observed as long as the Rayleigh number is less than 5×10^4, after which the flow becomes turbulent (Incropera *et al.*, 2007).

The Rayleigh number, however, depends on both the thermal and geometric conditions. The Rayleigh number can be altered by changing the height of the fluid layer while keeping all other parameters the same. It is, therefore, important to establish the relationship of critical Rayleigh number with the aspect ratio of a finite system. It is found from numerical studies in single-phase fluid (air) in rectangular enclosures that are heated from the bottom side and cooled from the top side, that the transition to natural convection depends on the aspect ratio (D'Orazio *et al.*, 2004). The critical Rayleigh number for the transition to convection varies as given in Eq. (2.5).

$$\mathrm{Ra}_{\mathrm{onset}} = 900\, A^{3.7} \tag{2.5}$$

where A is the height-to-width aspect ratio.

2.2.2 Natural convection onset in phase change materials

Although many studies have been done on the onset of natural convection during heating of a single-phase fluid, studies on the onset of natural convection during melting of PCM are rare if not completely absent. Some studies are present for rectangular enclosures;

however, these studies do not extend over all possible parameters that may influence the onset or strength of natural convection. Before reviewing the studies on the onset of natural convection during melting of PCMs, it is worthwhile to note that a critical Rayleigh number is being associated with the onset of natural convection in single-phase fluid, as seen in the preceding subsection. Some researchers have associated the Rayleigh number with the onset of natural convection during melting of PCMs as well.

2.2.2.1 Natural convection onset in PCMs – experimental studies

An experimental study of melting of Polyethylene glycol (with a melting temperature of 34 °C) in a rectangular enclosure heated from one of the vertical sides reveals that the time required for the onset of convection decreases as the heat flux applied to the side increases (Wang *et al.*, 1999). The Rayleigh number was defined by Wang *et al.* (1999) as:

$$\mathrm{Ra} = \frac{g\beta(T_\mathrm{w} - T_\mathrm{m})H^3}{\nu\alpha} \tag{2.6}$$

In Eq. (2.6), H is the height of the enclosure.

They found that the critical Rayleigh number at which the onset of convection occurs varies over about an order of magnitude (10^6 and 10^7) when the applied heat flux changes from 2307 to 9012 W/m^2. It should be noted that since the heat is applied to one of the vertical sides, the height of the liquid layer remains the same at all times (103 mm), and thus the Rayleigh number varies only based on the heating condition.

At the beginning of the melting process in a horizontal annular heat exchanger, concentric melting of *n*-octadecane around the inner cylinder was observed by Bathelt and Viskanta (1980). In their experimental study, a cylinder was installed through the center of the front, and back faces (glass) of a rectangular enclosure and a constant heat flux was applied to the cylinder. The instantaneous shapes of the solid-liquid interfaces were obtained photographically. The concentric solid-liquid interfaces indicated that the heat transfer in the early stage of melting was purely by conduction. The deviation from concentricity of the solid-liquid interfaces started at the condition given by Eq. (2.7).

$$\mathrm{Ste_H}.\mathrm{Fo} = 1.2 \tag{2.7}$$

In Eq. (2.7), $\mathrm{Ste_H}$ is the Stefan number based on the constant heat flux, which is defined as:

$$\mathrm{Ste_H} = \frac{c_\mathrm{l} q_\mathrm{w} r}{k\, L} \tag{2.8}$$

and Fo is the Fourier number defined as:

$$\mathrm{Fo} = \frac{\alpha_\mathrm{l} t}{r^2} \tag{2.9}$$

In Eqs. (2.8) and (2.9), c_l and α_l are the specific heat and thermal diffusivity of the liquid PCM, k and L are the thermal conductivity and the latent heat of fusion of the PCM, q_w is the applied constant heat flux, and r is the radius of the inner cylinder.

Following the condition in Eq. (2.7), a deviation of the solid-liquid interfaces from concentricity indicated the onset of natural convection. This study extended to the melting of subcooled PCM, where the degree of subcooling was defined as:

$$\mathrm{Ste_s} = \frac{c_\mathrm{s}(T_\mathrm{m} - T_\mathrm{i})}{L} \tag{2.10}$$

In Eq. (2.10), c_s, T_m, and T_i are the specific heat of the solid PCM, and melting and initial temperatures of the PCM, respectively.

The subcooling parameter given by Eq. (2.10) had a maximum value of 0.03. They reported that even for this small degree of subcooling, the thickness of the melt portion of the PCM, at the onset of convection or thereafter, was narrower compared to the non-subcooled cases.

While Eq. (2.7) gives the condition for the onset of natural convection for constant heat flux boundary conditions during melting of *n*-octadecane, Bathelt and Viskanta (1980) reported that this dimensionless number is 0.0255 for constant temperature boundary conditions during melting of *n*-heptadecane. The greater details of this study can be found in the PhD thesis of one of the authors (Bathelt, 1979).

2.2.2.2 Natural convection onset in PCMs – numerical studies

Whereas Wang *et al.* (1999) identified the discrete times for the onset of convection in their experimental study, an equation to calculate the convection onset time during melting of PCM in a rectangular enclosure heated from one of the vertical sides has been given by Benard *et al.* (1985) in their numerical study as in Eq. (2.11).

$$t_{\text{onset}} = 4.59 \frac{\text{Pr}}{\text{Ste}} \frac{\rho_{\text{s}}}{\rho_{\text{l}}} \text{Ra}^{-1/2} \tag{2.11}$$

The Prandtl number in Eq. (2.11) was defined with the thermal diffusivity of the liquid PCM. The Rayleigh number in Eq. (2.11) was defined as:

$$\text{Ra} = \frac{g\beta(T_{\text{w}} - T_{\text{m}})H^3}{\nu\alpha_{\text{l}}} \tag{2.12}$$

It should be noted that the solid PCM was assumed to be isothermal at a temperature of 0.4 °C below the melting temperature of the PCM. The Stefan number in Eq. (2.11) was defined as:

$$\text{Ste} = \frac{c_{\text{l}}(T_{\text{w}} - T_{\text{m}})}{L} \tag{2.13}$$

where c_{l} is the specific heat capacity of the liquid PCM.

Vogel *et al.* (2016) reported a correlation for the onset of natural convection during melting of PCM in a rectangular enclosure heated from the two opposite vertical sidewalls. In their numerical study, they used the enthalpy-porosity method with the Boussinesq approximation to simulate the melting process in ANSYS Fluent. Since the heat was applied to the two opposite vertical sidewalls, only half the domain about the vertical symmetry line at half-width was simulated. The PCM height and width in the domain were 930 and 38 mm, respectively. The numerical model was validated against the temperatures measured at two locations. Both these locations were at a height of 500 mm. One location was 8 mm away from the hot wall, and the other location was at the half-width of the enclosure.

The heating temperature was fixed at one value, and the height and width of the enclosures were changed. Correlations for the convective enhancement factor and the onset of natural convection involved the Rayleigh number and the aspect ratio of the enclosures. In determining the convective enhancement factor, results from simulations were obtained, including natural convection and without; the convective enhancement factor was defined as the ratio of liquid fractions with convection to that without. A ratio larger than one would mean convection was present in the melting process. The criterion for the convective enhancement of heat transfer was determined as:

$$\mathrm{Ra}_{\mathrm{width}}^{1/6}\mathrm{A}^{-1/4} \geq 2.73 \tag{2.14}$$

In Eq. (2.14), A is the height-to-width aspect ratio and, the Rayleigh number was defined as:

$$\mathrm{Ra}_{\mathrm{width}} = \frac{g\beta(T_{\mathrm{w}} - T_{\mathrm{m}})W^3}{\nu\alpha} \tag{2.15}$$

In Eq. (2.15), W is the width of the enclosure.

The width of the liquid layer was taken as the length scale to calculate the Rayleigh number at the onset of convection. Since the vertical side of the enclosure was used as the heat source, melting would approach in the horizontal direction leaving the liquid PCM height the same all the time. On the assumption that the solid-liquid interface is vertical at the onset of convection, melt fraction was considered the ratio of the liquid layer thickness to the width of the enclosure. This consideration yielded a relationship between the Rayleigh number calculated using the width of the enclosure as the length scale and the melt fraction of the PCM. In their study, the critical melt fraction for the onset of natural convection was given by Eq. (2.16).

$$\mathrm{f}_{\mathrm{onset}} = \left(\frac{150\mathrm{A}}{\mathrm{Ra}_{\mathrm{width}}}\right)^{\frac{1}{4}} \tag{2.16}$$

It should be noted that the choice of the length scale in the definition of Rayleigh number in this study differs from that of the research done by Wang *et al.* (1999) and Benard *et al.* (1985).

It is evident that studies on the onset of convection during melting of PCM are scarce in the literature. All the studies reviewed above focused on a single parameter that could influence the onset of convection. Wang *et al.* (1999) varied the heat flux applied to one of the vertical sides without changing anything else. On the other hand, Vogel *et al.* (2016) varied the aspect ratio of the enclosure from 0.5 to 40 but limited the Stefan number to a single value of 0.17. Bathelt and Viskanta (1980) varied the wall temperature while keeping the geometry the same. No study used more than one PCM to investigate the effects of PCM on the onset of convection. Also, no study thoroughly investigated the effects of initial subcooling of the PCM. Effects of different heating temperatures on different geometry have not been explored. It is clearly seen that a comprehensive experimental study on the onset of natural convection during melting of PCM is well warranted to know what influences the onset of convection. Is it a minimum volume of liquid PCM, a minimum thickness of the liquid layer, a minimum temperature gradient, a minimum size of the heat transfer area, the properties of the PCM?

2.3 Natural convection in numerical models

Modelling natural convection during melting of PCM involves additional complexity to simple conduction models. Not only the presence of natural convection in the liquid PCM but also the moving solid-liquid interface during melting of PCMs makes the simulation process very challenging (Chen *et al.*, 2011). Knowing that at the beginning of the melting process, heat transfer takes place by conduction, natural convection is sometimes neglected in simulation models. Natural convection is neglected, especially when the system is small or the PCM is confined in a small space. However, in most cases, natural convection is neglected on the assumption, without any justification that it does not exist in a small amount of PCM. Simulation works that neglected and that considered natural convection during melting of PCMs are reviewed in subsections 2.3.1 and 2.3.2.

2.3.1 Simulations neglecting natural convection

Numerous studies on the melting of PCMs have neglected convective heat transfer without justifying the reason for it (Esen and Ayhan, 1996; Fan *et al.*, 2014; Li *et al.*, 2013; Pirasaci and Goswami, 2016; Tay *et al.*, 2012; Tao and Carey, 2016; Ogoh and Groulx, 2012b; Ogoh and Groulx, 2012a).

Studies show that increased density of fins limits the influence of natural convection (Huang *et al.*, 2011; Abdulateef *et al.*, 2019; Biwole *et al.*, 2018). It has also been reported that during solidification of PCM, natural convection in the liquid portion is inhibited when fins are placed in the heat exchanger (Ismail *et al.*, 2001). In numerical studies of melting of PCMs enclosed between two closely placed fins, natural convection is often neglected on the assumption that the thickness of PCM between two fins is small enough to neglect it (Akhilesh *et al.*, 2005; Seeniraj and Narasimhan, 2008; Jaworski, 2012).

Some authors neglected natural convection for flat thin containers, on the assumption that there is not enough space for the existence of natural convection (Zivkovic and Fujii, 2001; Liu and Ma, 2002). Natural convection is also neglected in close contact melting on the assumption that the liquid layer between the heat source and the solid PCM is too thin to have natural convection (Lacroix, 2001). However, it was shown by Groulx and Lacroix (2007) that during the melting of an ice block resting on a hot flat surface, convection (although would be considered forced) played a dominant role in the melting process when $\mathrm{Ste}_{\mathrm{eff}} \gg 0.1$. The effective Stefan number was defined as:

$$\mathrm{Ste}_{\mathrm{eff}} = \frac{\mathrm{Ste}}{1 + \mathrm{Ste}_{\mathrm{s}}} \tag{2.17}$$

In Eq. (2.17), Ste accounts for the heat transfer in the liquid phase and $\mathrm{Ste}_{\mathrm{s}}$ accounts for the heat transfer in the solid phase.

2.3.2 Simulations including natural convection

The relative importance of natural convection during melting compared to solidification can be inferred from the study of Stritih (2004). It was concluded that natural convection is an order of magnitude stronger during melting of PCM than during solidification. These studies show that although natural convection can be conveniently neglected in

solidification models, neglecting natural convection during melting would produce erroneous results.

For simulations of melting and solidification of PCMs with high melting temperatures ($325 - 525$ °C), errors originating from not considering the natural convection have been quantified by Tehrani *et al.* (2018). Melting and solidification in vertical annular enclosures were simulated using the enthalpy-porosity method in ANSYS Fluent 15.0 without and with natural convection in the phase-change heat transfer process. The amount of error in the results depends on many factors, such as the geometry of the heat exchanger, properties of the PCMs, the thermal condition, and the heat transfer process. The extent of error depends on the effectiveness of the charging/discharging process, which is defined as the ratio of energy stored or released to the full capacity of the heat exchanger. It should be noted that the amount of energy stored or released is a transient quantity while the full capacity of a heat exchanger is a constant. For both the charging and discharging process, the amount of error from neglecting natural convection increases as the effectiveness increases. This is because convection affects the meting dynamics differently at different times during the melting process. The error in the solidification process is always less than that of the melting process when natural convection is neglected. It is noteworthy that for the effectiveness of almost 1, the error from neglecting natural convection can be as much as 100% during charging and 30% during discharging.

Tehrani *et al.* (2018) defined a geometric parameter as given in Eq. (2.18).

$$S = \frac{R^2 - r^2}{2rH} \tag{2.18}$$

where R, r, and H are the radius of the outer tube, the radius of the inner tube, and the height of the vertical annular enclosure.

They concluded that natural convection could be neglected when $S < 0.005$. Also, Tehrani *et al.* (2018) defined the Rayleigh number based on the thickness of the vertical annulus, as given in Eq. (2.19).

$$\mathrm{Ra} = \frac{g\beta(T_\mathrm{w} - T_\mathrm{m})(R - r)^3}{\nu\alpha} \tag{2.19}$$

They identified a critical Rayleigh number of 8×10^5 below which natural convection could be neglected with an error of less than 1% in the results. However, it should be noted that the most appropriate geometric scale in their study would be the height of the annulus since the thickness of liquid PCM is not always the same as the thickness of the annulus. No such studies exist for PCMs with low melting temperature (<100 °C) or other geometries or other orientation of the geometry.

There are a few studies that accounted for natural convection not directly but rather through the effective thermal conductivity of the general form of:

$$\frac{k_\mathrm{eff}}{k} = C\ \mathrm{Ra}^n \tag{2.20}$$

In Eq. (2.20), C and n are constants.

These studies include one-dimensional melting of PCM (Farid *et al.*, 1998) and melting in a finned annulus with multiple PCM (Seeniraj and Narasimhan, 2008).

Many other studies have considered natural convection during melting of PCMs in their simulations in different geometries and operating conditions. In all those studies, the melting process was simulated using the popular enthalpy-porosity method. The natural convection in the melted PCM was directly accounted for in these studies.

Melting of PCM in spherical containers of diameter ranging from 50 to 100 mm and heated at melting temperature differentials ranging from 12 to 50 °C were simulated including natural convection by many researchers (Sattari *et al.*, 2017; Khodadadi and Zhang, 2001; Hosseinizadeh *et al.*, 2013; Tan *et al.*, 2009; Assis *et al.*, 2007). Other studies included natural convection in simulating melting of PCM in rectangular enclosures heated from one of the vertical sides (C. Kheirabadi and Groulx, 2015; Kamkari and Amlashi, 2017), in a finned rectangular enclosure heated from one of the vertical sides (Ji *et al.*, 2018), and in inclined and horizontal rectangular enclosures (Kamkari and Amlashi, 2017). Numerical models have also been used to study the melting of PCMs in a vertical annulus with radial

fins (Kozak *et al.*, 2014), horizontal annular enclosures (Darzi *et al.*, 2012; Agrawal and Sarviya, 2015; Azad *et al.*), and a horizontal annular enclosure with longitudinal fins (Cao *et al.*, 2018). The validation of these studies shows that the simulated results are comparable to those of the experimental ones subject to the limitations of the model.

2.4 Conclusions

Research work on melting of PCM in different geometries and thermal conditions were reviewed in this chapter. It was seen that regardless of the geometry and its orientation and, the orientation of the heat source, the melting of the PCM was mainly by conduction at the beginning of the melting process. Shortly after, once there was enough liquid PCM, natural convection assumes the dominating role in the melting process. The review also showed that the dominance of natural convection affects the entire melting process. It was also seen in the review that while many researchers considered natural convection in their simulation models, some accounted for the natural convection through effective thermal conductivity, and some researchers completely neglected natural convection in their simulation models. A literature search shows that there has been almost no attempt to investigate the onset of natural convection. There are a couple of experimental and numerical studies that have reported on the onset of natural convection. These studies, however, are limited to the effects of a single parameter, either geometric or thermal. Extensive research work is well warranted to answer questions such as:

(i) What are the effects of geometry (center-tube diameter in annular systems)?
(ii) What are the effects of heat source temperature on the onset of natural convection?
(iii) What are the effects of the initial temperature of the PCM?
(iv) Does the PCM itself play a role in the onset of convection?
(v) What are the effects of the orientation of the geometry on the onset of convection?
(vi) Is there a threshold melt volume that the onset of natural convection depends on?
(vii) Is there a threshold velocity of the liquid PCM that the natural convection depends on?

This research work is undertaken to look for the answers to the above questions except (v).

CHAPTER 3 EXPERIMENTAL SETUP AND PROCEDURE

The construction of the experimental setup, the experimental procedure, the experimental conditions, repeatability of the experimental results, and the storage materials (the PCMs) used in these experiments are discussed in this chapter.

3.1 Experimental setup

The experimental setup consisted of three PCM enclosures made of cast acrylic sheets, three circulating water baths, three LED lamps to illuminate the area of interest, three web cameras, thermocouples, and one National Instrument data acquisition module with a computer running LabView and MATLAB.

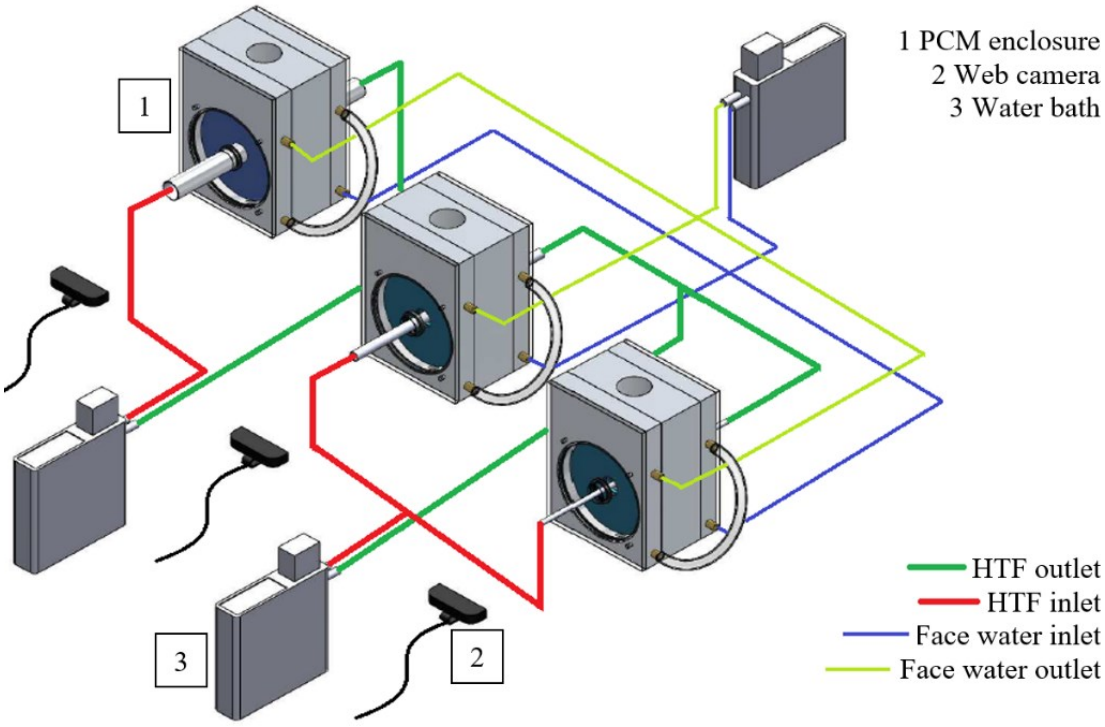

Figure 3.1 Schematic diagram of the experimental setup.

The heat transfer fluid (HTF), which was water at different temperatures, was circulated through the center-tubes of the enclosures by two of the baths. Water at the PCM melting temperature was circulated through the axial faces (front and back faces) of the enclosures by the third bath. Water was circulated through these faces to ensure that no solidification took place on them. This was required so that clear images of the melting process could

be obtained. T-type Thermocouples, one at the HTF inlet, one at the HTF outlet, and another at the outlet of the axial faces of each enclosure were used to monitor the temperatures at the respective locations. The NI Compact DAQ 9178 and temperature input module NI 9213 were used in conjunction with LabVIEW to record the temperatures. Logitech C920 HD Pro web cameras were programmed in MATLAB to acquire images at different time intervals. A schematic diagram of the experimental setup is shown in Fig. 3.1, and a photograph of the experimental setup is shown in Fig. 3.2.

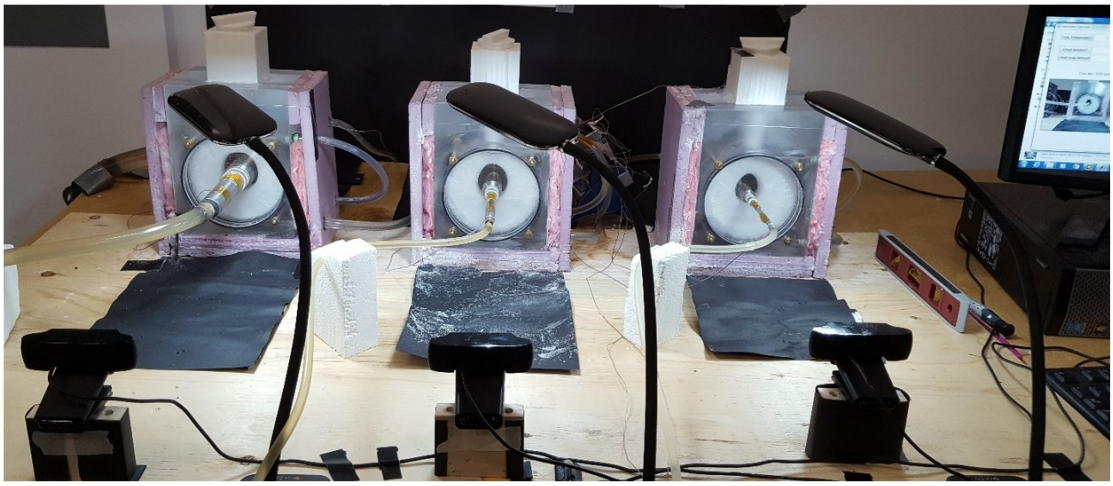

Figure 3.2 A photograph of the experimental setup.

3.1.1 Construction of the enclosures

Each of the PCM enclosures consisted of eight parts, which are shown in Fig. 3.3, made of cast acrylic sheets (except the center-tube, labelled 1 in Fig. 3.3). A PCM cavity of 127 mm diameter was drilled at the center of the lower 152.4 mm × 152.4 mm section of a 152.4 mm × 203.2 mm acrylic sheet of 50.8 mm thickness. The depth of the PCM cavity was 44.4 mm. Two 17.5 mm thick round end plates (plate 3 in Fig. 3.3) were used to close the axial faces of the PCM cavity. Viton Fluoroelastomer chemical resistant O-rings (two black rings, as seen on the circumference of the plate 3 in Fig. 3.3) were used in assembling the cavity and the round end plates to seal any leakage of the PCM from the cavity.

Two other acrylic sheets, 203.2 mm high, 152.4 mm wide, and 25.4 mm thick each were used to create a 127 mm diameter water cavity (plate 4 in Fig. 3.3) at the center of the lower 152.4 mm × 152.4 mm section. Two grooves were cut on the axial faces of these plates. The round endplate was pushed into the groove on the inner side, and the endplate (plate 5

in Fig. 3.3) was pushed into the groove on the outer side. Closure of the large hole in plate 4 from the axial faces created a water cavity of 11 mm depth. Two holes of 6.4 mm diameter (labelled 6 and 7 in Fig. 3.3) were drilled on one side of these plates to facilitate the flow of water into and out of the cavity. Additionally, a hole of 41.3 mm diameter and 57.2 mm height (labelled 2 in Fig. 3.3) was drilled at the top of each of the PCM cavity to allow the accumulation of expanded liquid PCM. At the bottom of this hole, a smaller hole of 12.7 cm diameter was drilled (not visible in the figure). This small hole was created to enable the exchange of liquid PCM between the PCM cavity and reservoir without interfering with the melting dynamics in the cavity.

Finally, the HTF carrying tubes acting as the heat source, inserted through the center of the PCM cavity, were made of stainless steel. The sealing at the contact point of these tubes with other acrylic pieces to stop leakage or mixing of PCM and water was obtained by using Viton Fluoroelastomer chemical resistant O-rings.

Since the experiments required acquiring images at very early stages of the melting process, the tubes with uniform diameter could not be used. If tubes with uniform diameters were used, then the O-rings, used for sealing, and the tubes carrying circulating water would block the views of the melted PCM, as can be seen in Fig. 3.4a). Therefore, three stainless steel cylinders of 44.4 mm length (the same as the depth of the PCM cavity) and 18, 27 and, 36 mm outer diameter were press-fitted on three stainless steel tubes of 6.35 mm, 12.7 mm and 25.4 mm outer diameter, respectively. This made the shooting of images since the beginning of the melting process possible. The visibility of the PCM in contact with the sleeve is depicted in Fig. 3.4b). The schematic of a typical tube (with a diameter of 36 mm) with the sleeve is shown in Fig. 3.5.

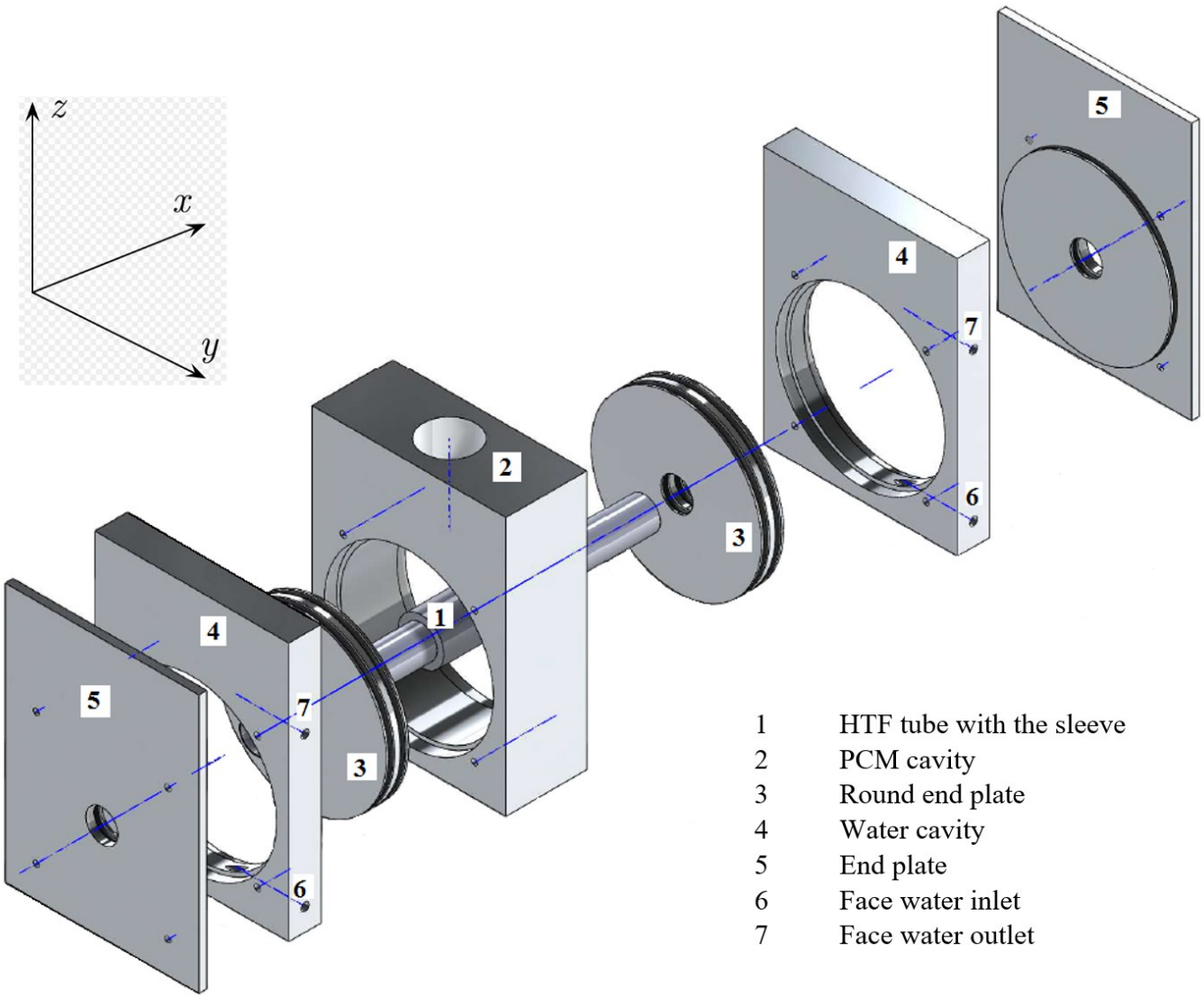

Figure 3.3 Different parts of one of the PCM enclosures.

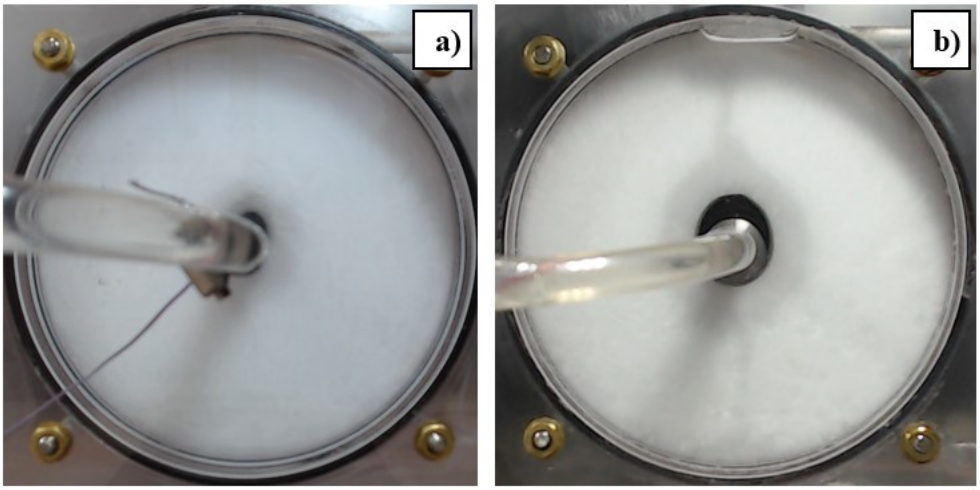

Figure 3.4 Photograph of the PCM enclosures with the center-tube diameter of 18 mm during melting of *n*-octadecane when the center-tube is a) without the sleeve, b) with the sleeve.

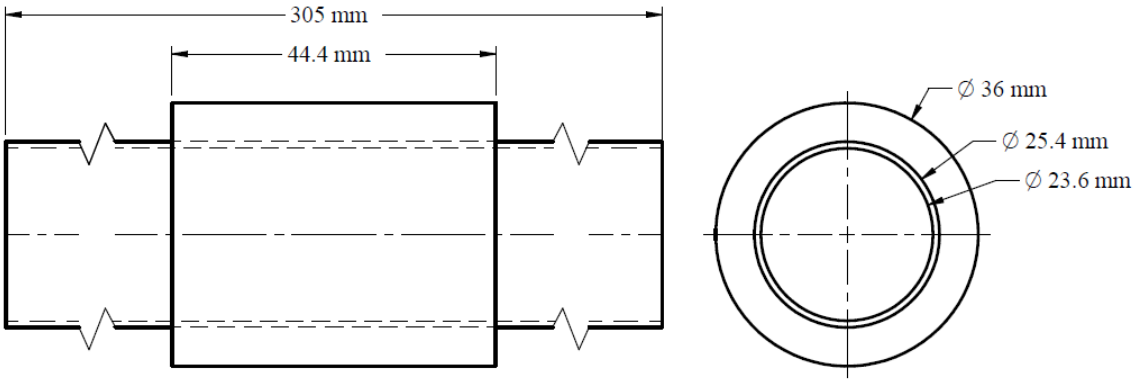

Figure 3.5 Center-tube with a diameter of 36 mm.

The assembly of all parts of the PCM enclosures can be seen in Fig. 3.6, which shows the sectional view of the assembled enclosure. As can be seen from the figure, the PCM cavity (labelled 3 in Fig. 3.6) was in the middle, and two water cavities (5 in Fig. 3.6) were on two axial faces at equidistance from the middle plane, separated from the PCM cavity on each side by a circular disk (labelled 4 in Fig. 3.6). The water cavities on both sides were closed with end plates (6 in Fig. 3.6). Contact points of any two pieces were sealed using O-rings (labelled 9 in Fig. 3.6), which are visible in the figure as black cross-sections. The reservoir for the extra liquid PCM labelled as 7 in Fig. 3.6, was connected to the PCM cavity through an opening labelled 8 in the same figure. This figure shows that the diameter of the stainless-steel sleeves is larger than the diameter of the O-rings used to seal the

contact points of the center-tube and acrylic sheets. The larger diameter of the sleeves facilitated clear visualization of the melting process since the beginning.

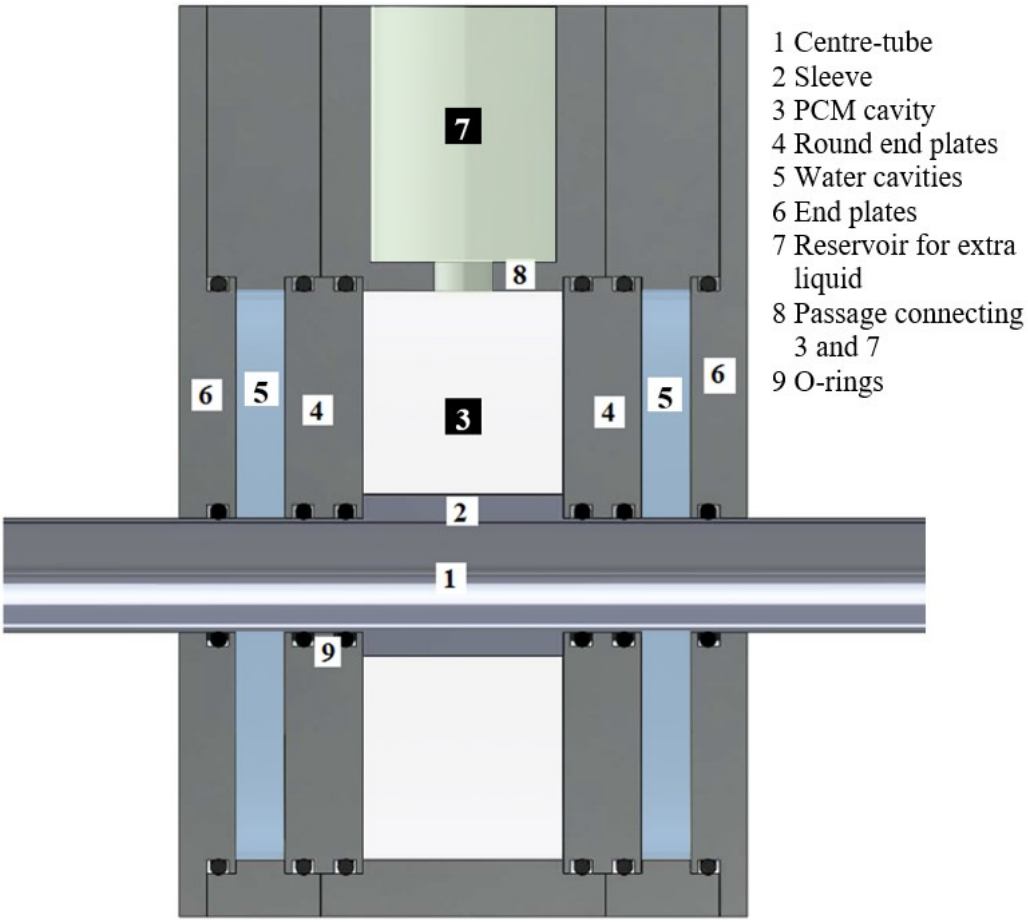

Figure 3.6 Sectional view of the PCM enclosure with the center-tube diameter of 36 mm.

Each enclosure was insulated with a layer of fibreglass first and then a layer of extruded polystyrene (XPS) foam at the bottom and two sides. Thermal conductivities of these materials, in addition to that of cast acrylic sheet, are presented in Table 3.1. A range of thermal conductivity can be derived from the work of Cai *et al.* (2014), who compared the thermal conductivities reported by many groups of researchers. The thermal conductivity of fibreglass varies in the range of 0.030 to 0.055 W/m·K for a mean operating temperature of 10 – 50 °C and that for XPS varies in the range of 0.028 to 0.036 W/m·K for the same mean operating temperatures, as can be seen in Table 3.1. These thermal conductivities are about an order of magnitude smaller than those of the PCMs studied here. The top of the enclosure was open to the atmosphere. However, except for the small reservoir for the extra liquid

PCM, the top of the enclosures was insulated by at least a 76.2 mm thick acrylic layer. Cast acrylic sheets have a thermal conductivity of 0.186 W/m·K (Shah *et al.*, 2015), which is comparable to the thermal conductivities of the PCMs. The photograph of an insulated enclosure with the view of the sleeve is shown in Fig. 3.7.

Table 3.1 Thermal conductivities of the insulating materials.

Material	k (W/m·K)	Temperature range (°C)	Reference
Fibreglass	0.030 – 0.055	10 – 50	Cai *et al.* (2014)
Extruded polystyrene	0.028 – 0.036		
Cast acrylic sheet	0.186	–	Shah *et al.* (2015)

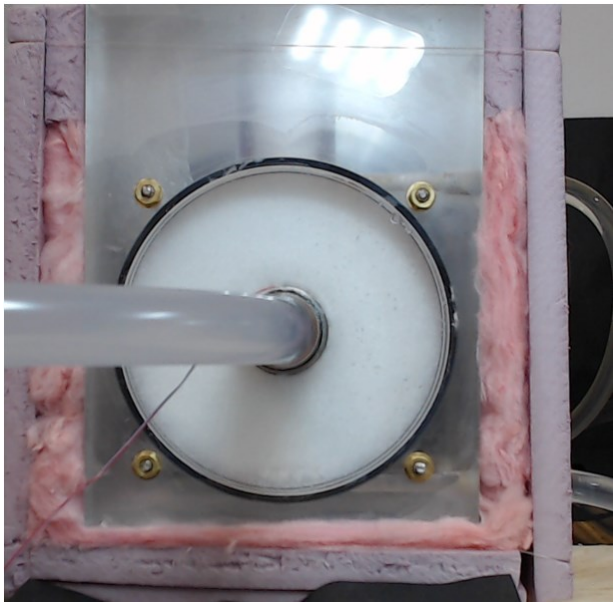

Figure 3.7 Photograph of the enclosures with the center-tube diameter of 36 mm.

3.1.2 Specifications of the equipment

A Thermo Scientific AC200 water bath was used to maintain the face temperature of all the enclosures at the melting point of the PCM. A Thermo Scientific SC150 Arctic bath was used to circulate water through the center-tube of the enclosures with the sleeve diameter of 18 mm and 27 mm. A Polyscience AD bath was used to deliver water through the center-tube of the PCM enclosure with the sleeve diameter of 36 mm. The maximum

working temperature range of these baths is −25°C to 150 °C (depending on the working fluid), and the maximum flow rate is 12 liters per minute.

T-type thermocouples, manufactured by OMEGA, were used to measure the temperatures. These self-adhesive thermocouples were taped on the surface, and thermal paste was used for better contact with the surface. These thermocouples work in the range of −250°C to 350 °C with the manufacturer provided accuracy of ± 1 °C or ± 0.75% above 0 °C, whichever is greater. The accuracy of the thermocouples was checked against the water bath temperatures; the accuracy was within the range given by the manufacturer.

Logitech C920 HD Pro web cameras were used for image acquisition. The resolution of these cameras is 1080p × 720p with a speed of 60 frames per second. The cameras were programmed in MATLAB to acquire images automatically. The data were collected in a Dell computer with 4 GB of RAM and a 2.6 GHz dual-core processor. All three cameras shot images simultaneously. The response time of a web camera is affected not only by the frame rates of the camera but also by the system the camera is run from. The response of the cameras run by the above-mentioned system was closely monitored. The delay between the two images was adjusted in MATLAB such that the delay in the response of the web camera was minimized. Apparently, there was no delay in the response of the web camera at the beginning of the melting process, when the images were shot every 10 s. However, delay propagated with time and reasonable delay in response of the cameras was observed after eight hours of melting experiments. A detailed discussion on delay in image acquisition follows in Chapter 4, where image processing and uncertainties are discussed as well. The delay in the response of the web cameras was accounted for in calculating the uncertainties in Fourier number, which is used to describe the global melt volume results.

3.1.3 Aligning the enclosures and the cameras

The PCM enclosures were placed on a flat horizontal surface. A leveler was used to check the level positioning of the enclosures and the cameras. The process of cancelling the inclination is shown in Fig. 3.8. Levelling the position of the enclosures was important to ensure the symmetry of the solid-liquid interface when the PCM melts. When buoyancy force in the liquid PCM is strong, the melting of the PCM progresses very fast, and the

inclination of the enclosures does not influence the symmetry of the solid-liquid interface significantly. However, when a weak buoyancy force is present, the melting of the PCM progresses at a much slower rate, and the shape of the solid-liquid interface can be affected significantly by gravity. Therefore, any inclination in the PCM enclosure would cause an asymmetric solid-liquid interface. Care was taken to minimize inclination in the orientation of the enclosures as much as possible. However, slight inclination in orientation, especially about the *y*-axis, existed. The results showed that this slight inclination in the orientation of the enclosures did not affect the symmetry of the solid-liquid interface when the wall temperature was high. At low wall temperatures, however, a little asymmetry in the solid-liquid interface was observed. Nonetheless, it is important to note that no asymmetry in the solid-liquid interface was found until the natural convection became pronounced, which leads to the conclusion that the natural convection onset results are free from the errors that could generate from the asymmetry in the solid-liquid interfaces. The orientation of the web cameras was also checked with the leveler to ensure the images acquired by the cameras were not tilted.

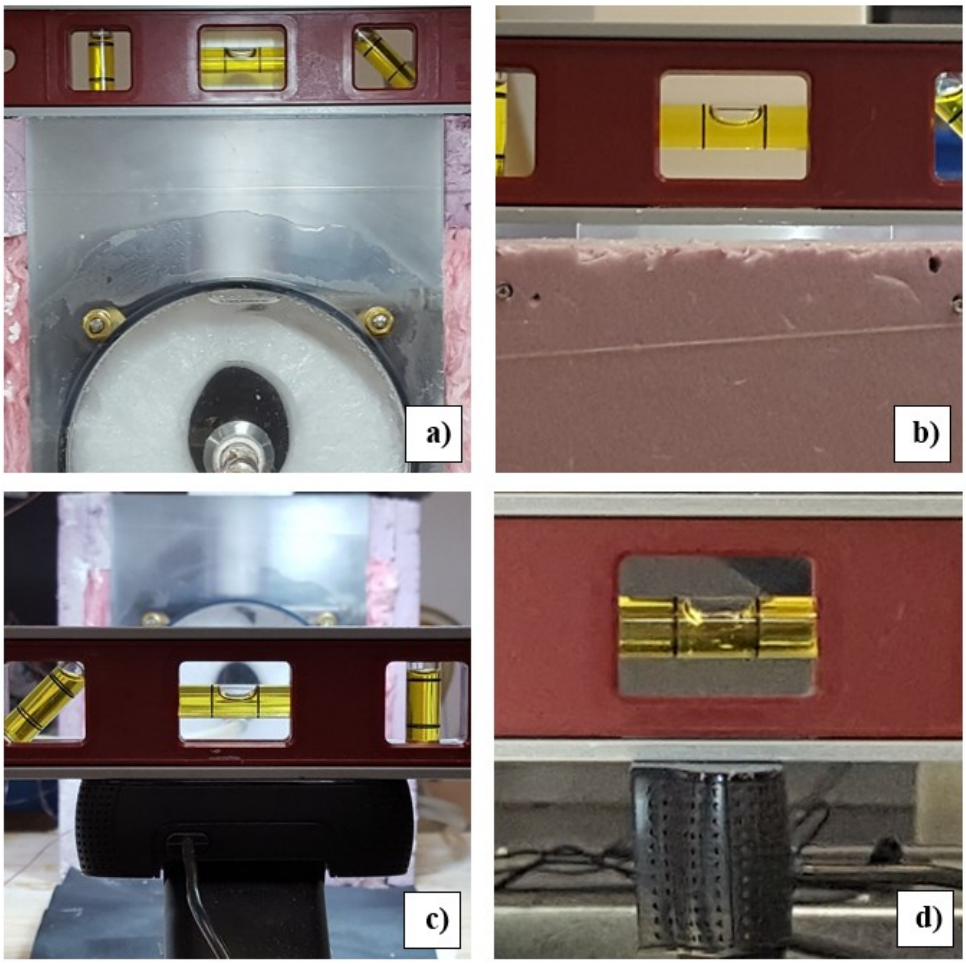

Figure 3.8 Use of a leveler to level the position of the enclosures about the a) *y*-axis and b) *x*-axis and camera about the c) *y*-axis and d) *x*-axis.

Table 3.2 The thermophysical properties of *n*-octadecane (Yaws, 2003) and dodecanoic acid (Desgrosseilliers *et al.*, 2013).

PCM	*n*-octadecane		Dodecanoic acid	
Properties (unit)	Solid (at T_m)	Liquid (at T_m)	Solid (at T_m)	Liquid (at T_m)
k (W/m·K)	0.358	0.145	0.150 ± 0.004	0.148
ρ (kg/m^3)	814	774	930 ± 20	873 ± 20
c_p (J/kg·K)	2150	2240	2400 ± 200	1950 ± 30
μ (Pa·s)	–	0.004	–	0.008
β (K^{-1})	–	0.00073	–	0.00079
L (kJ/kg)	189		180 ± 9	
T_m (°C)	27.5		43 ± 1.5	

3.2 The heat storage materials

One of the objectives of this research work was to investigate the influence of the storage materials on the onset of natural convection. Two organic PCMs were used as heat storage material. The PCMs, from *n*-alkane and fatty acid groups, were *n*-octadecane and dodecanoic acid, respectively. The thermophysical properties of the PCMs, taken from the Handbook of Thermodynamic and Physical Properties of Chemical Compounds by Yaws (2003) and from Desgrosseilliers *et al.* (2013), are listed in Table 3.2. The density decreases by approximately 5% and 7.5% upon melting of *n*-octadecane and dodecanoic acid, respectively. This change in density would cause an increase in the volume of the PCMs once they melt. As will be discussed thoroughly later in the chapter, all the experiments started with the enclosures filled with the solid PCM. Therefore, accommodation was made in the experimental setup, discussed in detail earlier, to hold the extra volume of the PCM upon melting. A significant difference in the properties of these two PCMs can be observed in the melting point, the heat capacity in the solid-state, the density and, more importantly, in the viscosity. The viscosity of dodecanoic acid at the melting temperature is twice as much of *n*-octadecane. The viscosity plays a significant role in the existence and strength of convection current in the molten PCM. It is also noteworthy that the two PCMs have almost the same latent heat of fusion, the difference in the values being approximately 4.8%.

3.3 Experimental conditions

For respective experiments, the PCMs were subcooled by a subcooling temperature differential of 2.5, 7.5, 15, or 22.5 °C before the start of the experiments. This required an initial temperature of 25, 20, 12.5, or 5 °C for *n*-octadecane and 40.5, 35.5, 28, or 20.5 °C for dodecanoic acid. The subcooling temperature differential was defined as given in Eq. (3.1).

$$\Delta T_{\mathrm{s}} = T_{\mathrm{m}} - T_{\mathrm{i}} \tag{3.1}$$

For every subcooled temperature and every center-tube diameter, the PCMs were heated from the center-tube at a melting temperature differential of 8.44, 16.9, 25.3, 33.8 or 42.2 °C for *n*-octadecane and that of 8.44, 25.3 or 42.2 °C for dodecanoic acid.

The melting temperature differential was defined as given in Eq. (3.2).

$$\Delta T_{\mathrm{f}} = T_{\mathrm{w}} - T_{\mathrm{m}} \tag{3.2}$$

The Stefan numbers based on these melting temperature differentials, as defined in Eq. (3.3), were 0.1, 0.2, 0.3, 0.4 and 0.5 for *n*-octadecane and 0.09, 0.27 and 0.46 for dodecanoic acid.

$$\mathrm{Ste} = \frac{c_{\mathrm{l}} \Delta T_{\mathrm{f}}}{L} \tag{3.3}$$

In Eq. (3.3), c_{l} is the specific heat capacity of the PCM and L is the latent heat of fusion of the PCM.

Different center-tube diameters, melting temperature differentials and, initial temperatures led to 60 experiments for *n*-octadecane and 36 experiments for dodecanoic acid. The different conditions of these experiments are summarized in Table 3.3.

Table 3.3 Experimental conditions for melting of PCM in enclosures with center-tube diameters of 18, 27, and 36 mm.

PCM	ΔT_{s} (°C)	2.5	7.5	15	22.5
n-octadecane (T_{m} = 27.5 °C)	T_{i} (°C)	25	20	12.5	5
	ΔT_{f} (°C)	8.44	16.9	25.3	33.8	42.2
	Ste	0.1	0.2	0.3	0.4	0.5
Dodecanoic acid (T_{m} = 43 °C)	T_{i} (°C)	40.5	35.5	28	20.5
	ΔT_{f} (°C)	8.44	25.3	42.2	
	Ste	0.09	0.27	0.46	

3.4 Experimental procedure

3.4.1 Preparing the enclosures and water baths

All three PCM enclosures, including the reservoir for the expanded PCM, were filled with liquid PCM at the beginning of the experiments. The liquid PCM was cooled from the center and the axial faces of the annulus simultaneously at 7 °C. During solidification, the

volume of PCM in the enclosure shrank, and the liquid PCM from the reservoir flowed to the enclosure to keep it full at all times. Once all the PCM was solid, the temperature of the PCM was brought to the initial temperature by heating/cooling it for two days simultaneously from the center and axial faces of the annulus. It was assumed at this point that the PCM had a uniform initial temperature.

At the beginning of every experiment, the water baths were taken offline, and the temperature of the water was raised to the desired values. For example, the temperature of water at the bath that circulated it to the faces of the enclosures was brought to the melting temperature of the PCM, and the temperature of the baths that circulated water through the center-tubes of the enclosures was brought to the different heating temperatures (8.44, 16.9, 25.3, 33.8 and 42.2 °C above the melting temperature for *n*-octadecane and 8.44, 25.3 and 42.2 °C above the melting temperature for dodecanoic acid). Once these temperatures in the baths were achieved, the water baths were connected to the enclosures.

3.4.2 Positioning the cameras

The web-cameras were positioned such that they were colinear with the longitudinal axis of the PCM enclosures. The positioning of the cameras was accomplished by counting the pixels from center in the cross-sectional image to the outer circumference of the enclosure; and, from the center to the outer circumference of the sleeves both in horizontal and vertical directions, as shown in Fig. 3.9. An equal number of pixels in every direction would suggest the cameras were positioned correctly.

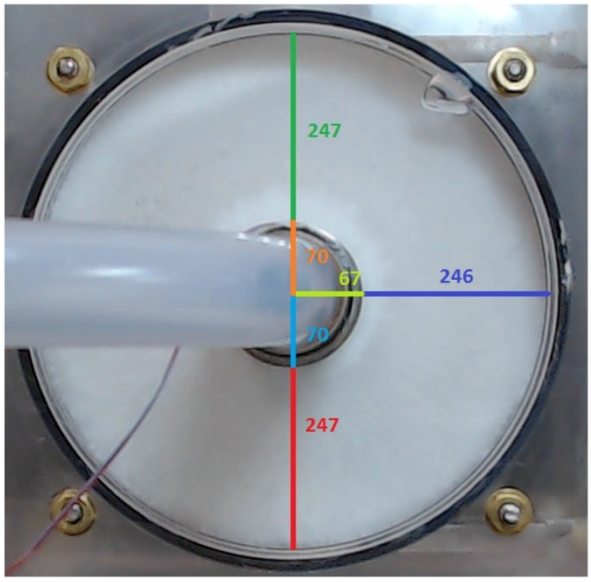

Figure 3.9 Positioning the web camera for the enclosure with the center-tube diameter of 36 mm.

3.4.3 Calibration and observation of the working temperatures

Sleeves of different thicknesses, presented in Table 3.4, were press-fitted on the center-tubes in order to facilitate the visibility of the melt front since the beginning of the melting process. The sleeves added an additional layer of metal on the center-tubes. This additional layer of metal would cause a delay in heating temperature to reach its maximum value on the sleeve surfaces. Calibrations were carried out to identify the time requirement in achieving the steady-state. The calibrations also facilitated an adjustment of the bath temperature so that the desired temperatures at the sleeve surfaces could be achieved. The temperature at the water bath that would cause the desired temperatures on the sleeves, after all the heat losses to the environment, including the losses through the tubing, were determined from these calibrations. For these calibrations, one thermocouple was placed on the surface of the tube at the inlet and another thermocouple was placed on the surface of the sleeve, as shown in Fig. 3.10. It should be noted that the temperature calibration was done before inserting the center-tube into the PCM enclosure.

Table 3.4 Sleeve thicknesses on the center-tubes.

Center-tube diameter (mm)	Sleeve thickness (mm)
18	5.83
27	7.15
36	5.30

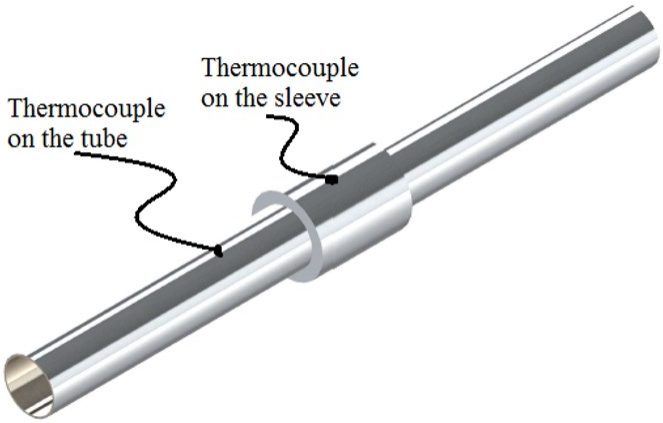

Figure 3.10 Positions of the thermocouples on the tube surface and sleeve surface for temperature calibration.

Consequently, the difference between the calibrations and the experimental conditions was that during calibration, the heat was driven away from the sleeve by air (natural convection), and during the experiment, the sleeves were in direct contact with the PCM. The calibration was conducted for the temperatures of the HTF leading to all the Stefan numbers studied, but the graphs only for two cases are shown in Fig. 3.11, where the temperature of the HTF was 35.9 (leads to the Stefan number of 0.1 for *n*-octadecane) and 85.2 °C (leads to the Stefan number of 0.46 for dodecanoic acid). Figure 3.11 shows that the center-tube with the diameter of 27 mm reaches the steady-state at the slowest rate and the one with 36 mm diameter reaches the steady-state at the fastest rate. One would expect these responses of the temperature on the sleeve surface based on the thicknesses of the sleeves presented in Table 3.4. One of the calibrations presented here was carried out at a temperature of 35.9 °C, which is the lowest heating temperature in the present study. It is seen that at the lowest heating temperature, the time taken by the 27 mm center-tube to reach a steady-state is 180 s and at the highest heating temperature that is 150 s. This time

delay is insignificant compared to the total melting time, which is 8 hours. More importantly, time is not a variable on which the onset of natural convection depends directly, but rather time affects the onset of convection through the transient melting process. Nonetheless, it should be noted that the time required for the onset of convection during melting of *n*-octadecane is 840 s when it is heated at 35.9 °C and 140 s for dodecanoic acid when it is heated at 85.2 °C; in both cases, the PCM was subcooled by 2.5 °C.

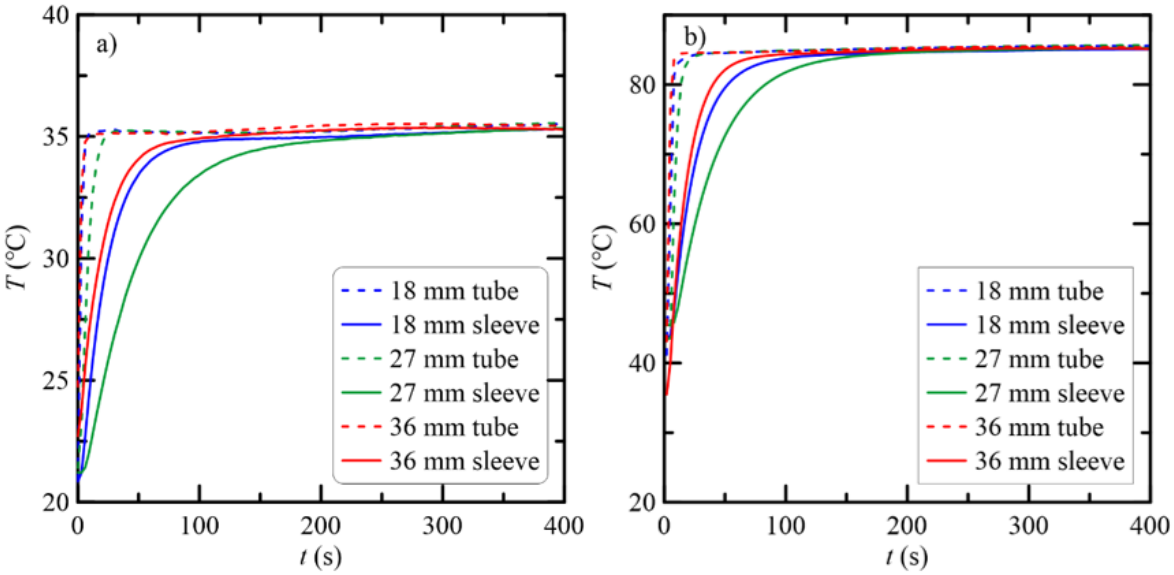

Figure 3.11 Calibration of temperatures at the tube surface and sleeve surface for heating temperatures of a) T = 35.9 °C and b) T = 85.2 °C.

As has been mentioned above, the heat was driven away by air during the calibration process while that would have been driven away by liquid PCMs during the experiments. Temperatures on the sleeve surfaces were measured in the numerical studies that are presented in detail in Chapter 9. The transient temperatures on the sleeve surface during melting of *n*-octadecane at 35.9 °C and dodecanoic acid at 85.2 °C are presented in Fig. 3.12. Both the PCMs in the numerical study were subcooled by 22.5 °C. These temperatures are presented only for the center-tube with the diameter of 27 mm since, as can be seen in Fig. 3.11, the temperature reaches the steady-state at the slowest rate on the sleeve surface of 27 mm in diameter. Figure 3.12 shows that the heat transfer from the sleeve surface to the liquid PCM does not affect the temperature on the sleeve surface when the heating temperature differential is small. However, at high heating temperature

differential, the temperature on the sleeve surface does not reach the desired temperature (Fig. 3.12b). The actual temperature on the sleeve surface is 2.9% below the desired temperature.

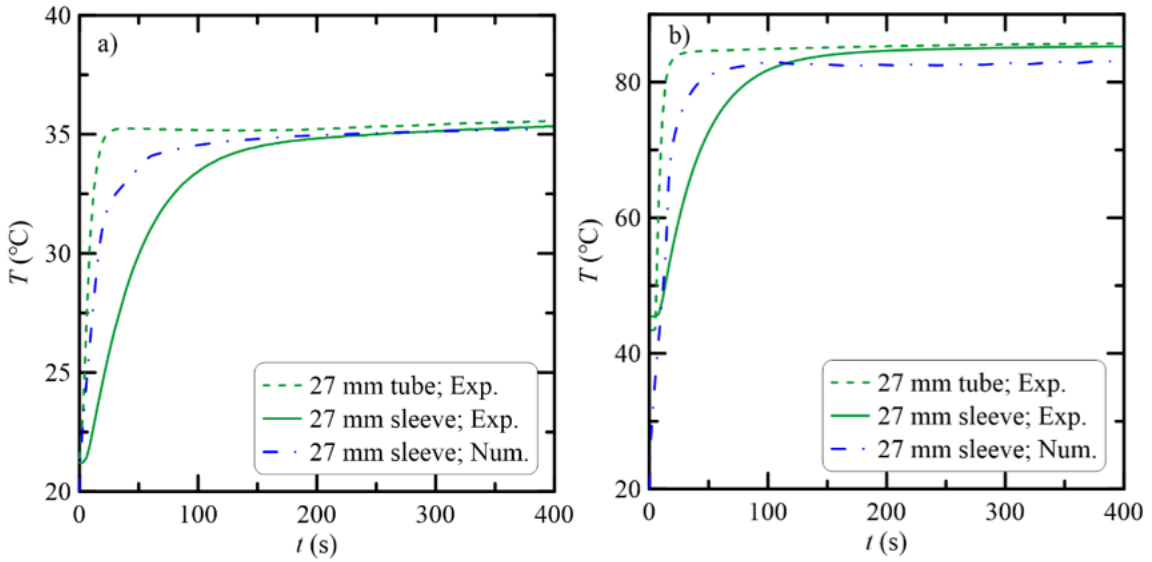

Figure 3.12 Temperatures on the tube and sleeve surfaces derived from calibration and numerical study for heating temperatures of a) T = 35.9 °C and b) T = 85.2 °C.

A theoretical analysis was also done to estimate the actual temperature on the sleeve surface, again for the center-tube with a diameter of 27 mm. Thermal resistance inside the tube was neglected because of the high velocity of the HTF in the tube. Thermal resistances due to conductive heat transfer in the liquid PCM, and the thickness of the sleeve material was calculated.

The thermal resistance of the liquid PCM layer, per unit length of the enclosure, was calculated as given in Eq. (3.4).

$$(R_\theta)_{\text{liquid}} = \frac{\ln\left(d_{\text{liquid}}/d\right)}{2\pi k_{\text{liquid}}} \tag{3.4}$$

In Eq. (3.4), d_{liquid} is the outer diameter of the liquid PCM layer and k_{liquid} is the thermal conductivity of liquid PCM at its melting temperature. The thickness of the liquid PCM layer at the onset of natural convection during melting of dodecanoic acid at 85.2 °C (~ 0.001 m) was used to calculate d_{liquid}.

The thermal resistance due to the sleeve thickness, per unit length of the enclosure, was calculated as given in Eq. (3.5).

$$(R_\theta)_{\text{thick}} = \frac{\ln(d/d_t)}{2\pi k_{\text{steel}}} \tag{3.5}$$

In Eq. (3.9), d_t and k_{steel} are the diameter of the tube without the sleeve and thermal conductivity of stainless steel, which is 14.9 W/m·K.

The total thermal resistance is, therefore, given by Eq. (3.10).

$$R_\theta = (R_\theta)_{\text{liquid}} + (R_\theta)_{\text{thick}} \tag{3.6}$$

The heat transfer rate per unit length of the enclosure is thus:

$$q = \frac{T_w - T_m}{R_\theta} \tag{3.7}$$

In Eq. (3.7), q represents the heat transfer rate per unit length of the enclosure from the center-tube inner wall to the PCM. The temperature of the sleeve surface can thus be calculated as:

$$q = \frac{T_{\text{sur}} - T_m}{(R_\theta)_{\text{liquid}}} \tag{3.8}$$

The surface temperatures calculated using Eq. (3.8) were 35.1 and 81.2 °C, where the desired temperatures were 35.9 and 85.2 °C, respectively. The theoretically calculated results are 2.2% and 4.7% below the desired temperatures.

A comparison of the results from calibration, numerical study, and theoretical analysis suggests that the most pessimistic estimate of the error in the temperature on the surface of the sleeve would be 4.7%.

The temperatures at the inlet and exit of the center-tubes and at the exits of the enclosure faces were recorded for the whole period of the experiments (8 hours) at a frequency of 1/3 Hz. These temperatures are shown in Fig. 3.13 only for two experiments in *n*-octadecane,

at melting temperature differentials of 8.44 and 42.2 °C. The PCM (*n*-octadecane) in these calibrations was subcooled by 22.5 °C. It should be noted from the figures that the inlet and outlet temperatures of the 27 mm center-tube is slightly below the desired temperature for these experiments, the difference in temperature being more pronounced at high temperatures of the center-tubes. This problem could be alleviated by raising the temperature of water at the bath. However, as can be seen in Fig. 3.1, a single bath circulated water through the 27 mm and 18 mm center-tubes. An increase in temperature in the bath for the 27 mm center-tube would increase the temperature at the inlet and outlet of the 18 mm center-tube, and as a result, the 18 mm center-tube would be overheated. This slight deviation of the actual temperature of the center-tubes from the expected temperature was considered in calculating the error in Stefan numbers. It is important to note from Fig. 3.13 that the temperatures remain constant over the entire duration of the experiments in all cases.

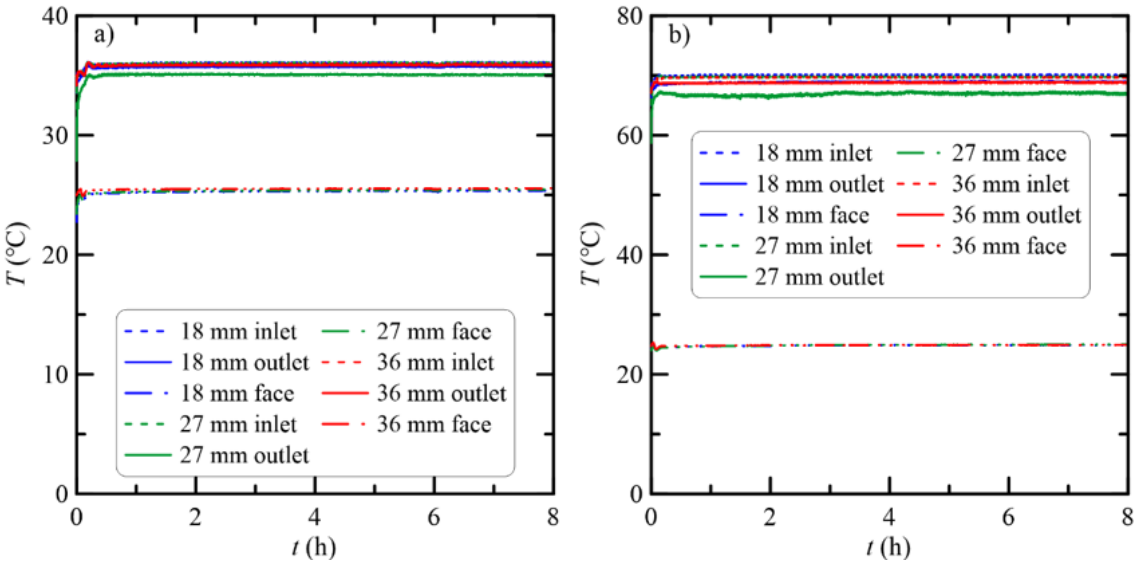

Figure 3.13 Temperatures at the inlet and outlet of the center-tubes and the outlet of the axial faces during melting of *n*-octadecane at heating temperatures of a) ΔT_f = 8.44 °C and b) ΔT_f = 42.2 °C with ΔT_s = 2.5 °C.

3.5 Image acquisition

The shooting of images and recording of temperatures started as soon as the water baths were connected to the PCM enclosures. The web cameras were programmed in MATLAB to acquire images, using the Image Acquisition Toolbox, at certain time intervals. The

codes for the image acquisition program are provided in Appendix A. The images were shot every 10 seconds for the first 30 minutes of melting, during which natural convection would start in any experiment regardless of the initial temperature of the PCM, the heating temperature and the center-tube diameter. Images were acquired so frequently in this stage to ensure that the onset of convection was identified as accurately as possible. After the first 30 minutes of melting, images were shot every 15 minutes for the rest of the 7.5 hours of melting.

3.6 Post-processing of the images

Solid *n*-octadecane and dodecanoic acid are white and become colourless when they melt. The area of the colourless portion on the axial faces represents the melt volume per unit length of the PCM cavity. Melt volumes were calculated only from the right half of the images. All the melt volume results in this study, consequently, represent a double of the volumes calculated from the images. Melt volumes from the images were calculated using MATLAB's Image Processing Toolbox based on the colour codes of the pixels. A detailed discussion on the post-processing of the images follows in Chapter 4.

3.7 Repeatability of the experimental results

The repeatability of the experimental results, both the onset and global melt volumes, was investigated for both *n*-octadecane and dodecanoic acid. The repeatability of the results is discussed in the following two subsections.

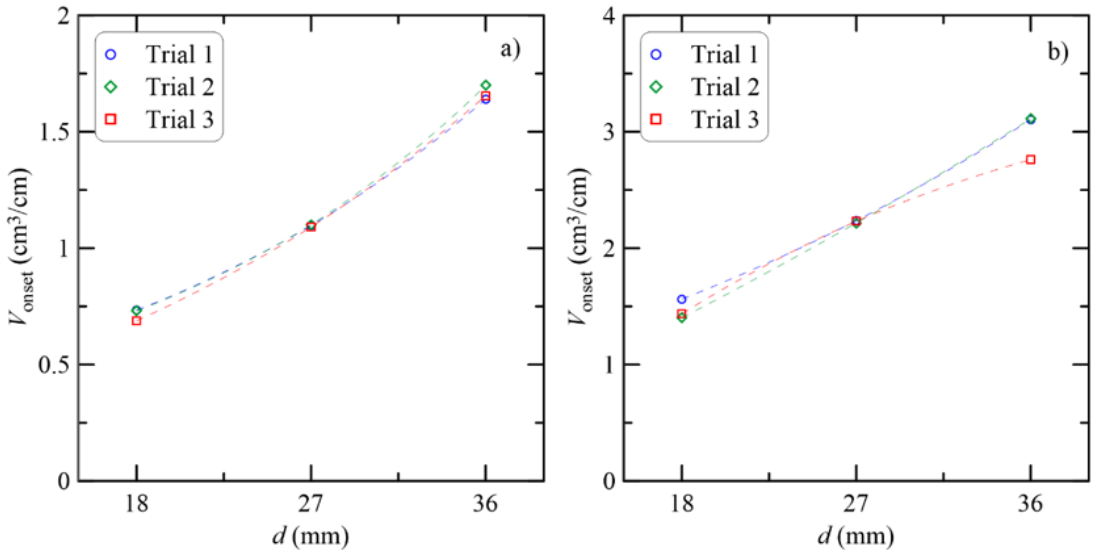

Figure 3.14 Melt volumes at the onset of natural convection for a) *n*-octadecane at ΔT_f = 33.8 °C and b) dodecanoic acid at ΔT_f = 8.44 °C with ΔT_s = 2.5 °C for both the PCMs.

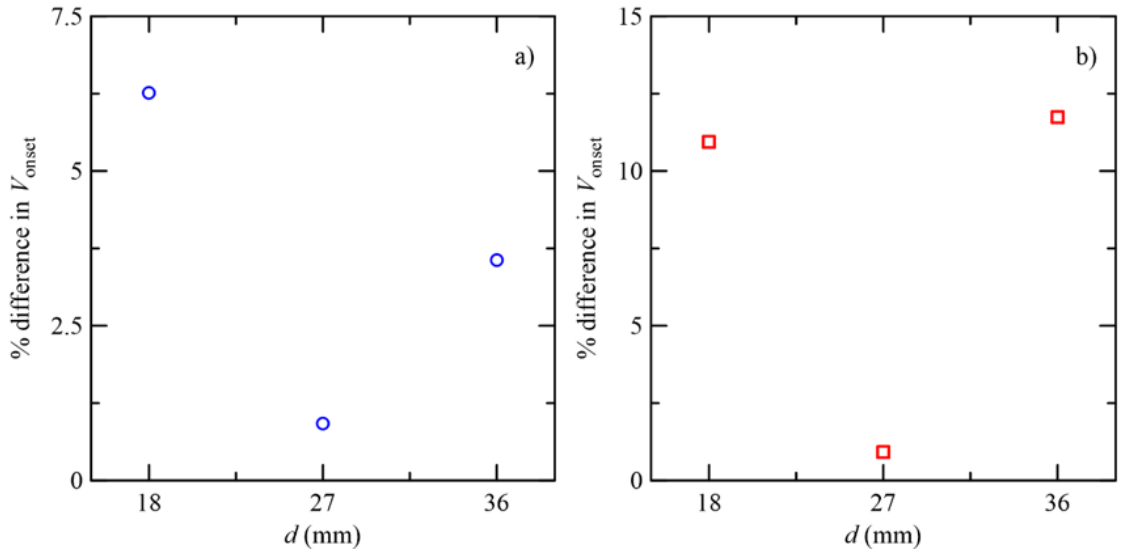

Figure 3.15 Difference in the melt volumes at the onset of natural convection for a) *n*-octadecane at ΔT_f = 33.8 °C and b) dodecanoic acid at ΔT_f = 8.44 °C with ΔT_s = 2.5 °C for both the PCMs.

3.7.1 Repeatability of the melt volumes at the onset of natural convection

The melting experiment of *n*-octadecane at a melting temperature differential of 33.8 °C was repeated three times, with all the experimental conditions the same. Similar experiments were conducted for dodecanoic acid at a melting temperature differential of 8.44 °C. In both cases, the experiments were conducted with the PCMs subcooled by 2.5 °C. Different melting temperature differentials were chosen for *n*-octadecane and

dodecanoic acid to cover this temperature differential both in the upper and lower end. The experiments were conducted over a varied time range with a gap between two experiments being as much as three months and at least one experiment in each PCM being done after reassembling the experimental setups. The melt volumes at the onset of natural convection from the repeated experiments are shown in Fig. 3.14. It is evident that the experiments were highly repeatable. Figure 3.15 shows the greatest percentage difference in the melt volumes of three trials. The maximum difference between melt volumes from two trials was determined by identifying the smallest and largest melt volumes of the three trials. The greatest percentage difference was then calculated with respect to the mean volume of the three trials. The greatest percentage difference in the melt volume of *n*-octadecane at the onset of convection was 6.3%, 1%, and 3.5% for the center-tube diameter of 18, 27, and 36 mm, respectively. Figure 3.15b) shows that the greatest percentage difference in the onset melt volume of dodecanoic acid was 10.9%, 1%, and 11.8% in the same order.

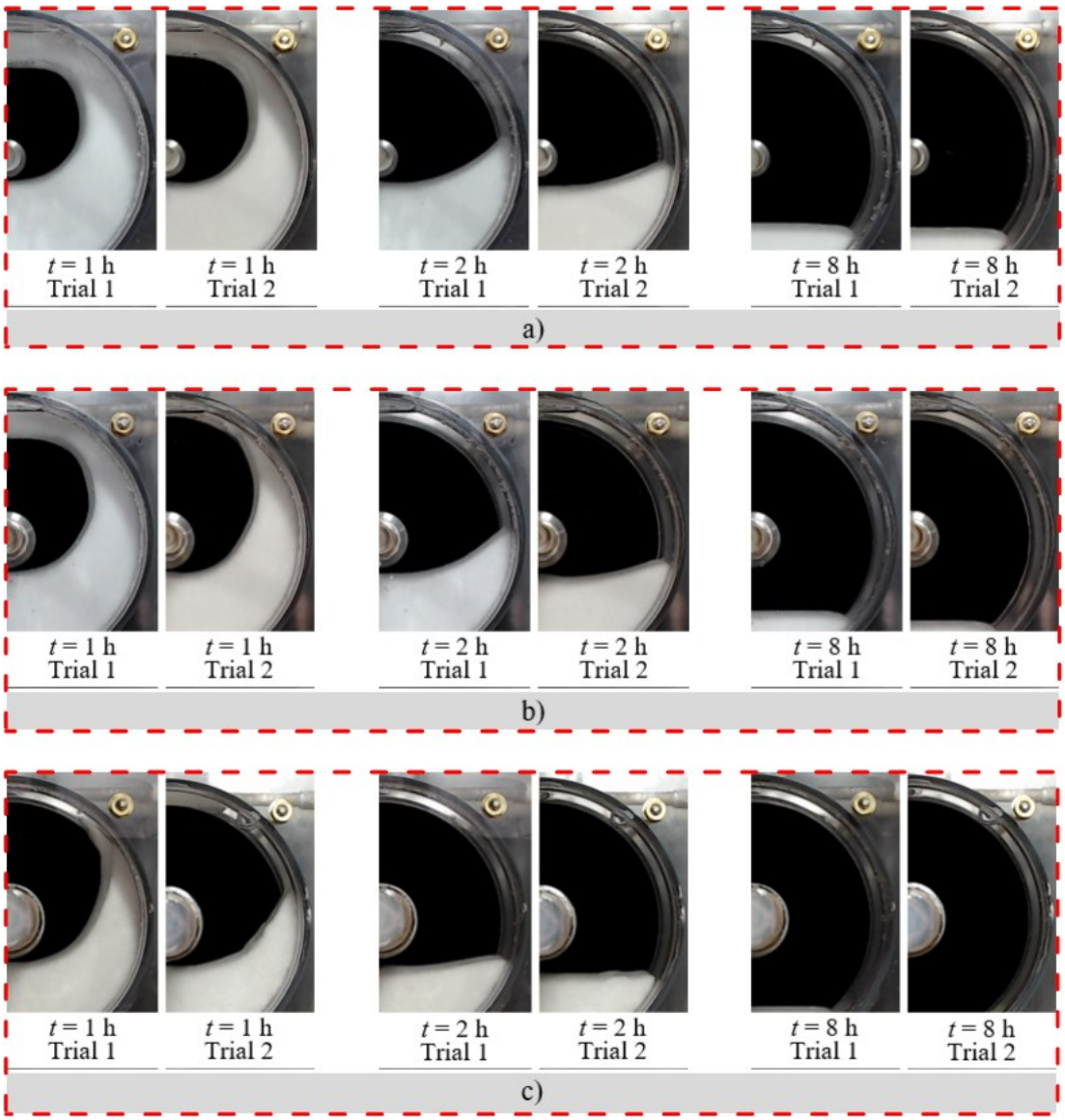

Figure 3.16 Melt profiles for global melting of *n*-octadecane at ΔT_f = 25.3 °C and ΔT_s = 2.5 °C for center-tube diameters of a) 18 mm, b) 27 mm and c) 36 mm.

3.7.2 Repeatability of the global melt profiles and melt volumes

The melt profiles for eight hours of melting are presented in Fig. 3.16 for *n*-octadecane and in Fig. 3.17 for dodecanoic acid. These melt profiles were derived from experiments run twice, with all the experimental conditions the same. For both *n*-octadecane and dodecanoic acid, the experiments were run at ΔT_f = 25.3 °C and ΔT_s = 2.5 °C. The melt profiles at 1, 2, and 8 hours are shown side by side for the two trials of the experiments. The respective melt profiles from the two trials for both the PCMs are similar, which indicates that the melt profiles are repeatable.

Melt volumes were calculated from the images shown in Figs. 3.16 and 3.17, as well as from other images that are not shown. These melt volumes for 8 hours of melting are shown in Fig. 3.18 for both the PCMs. It is evident from the figure that the melt volume results are repeatable with a reasonable difference in the melt volume results between the two trials.

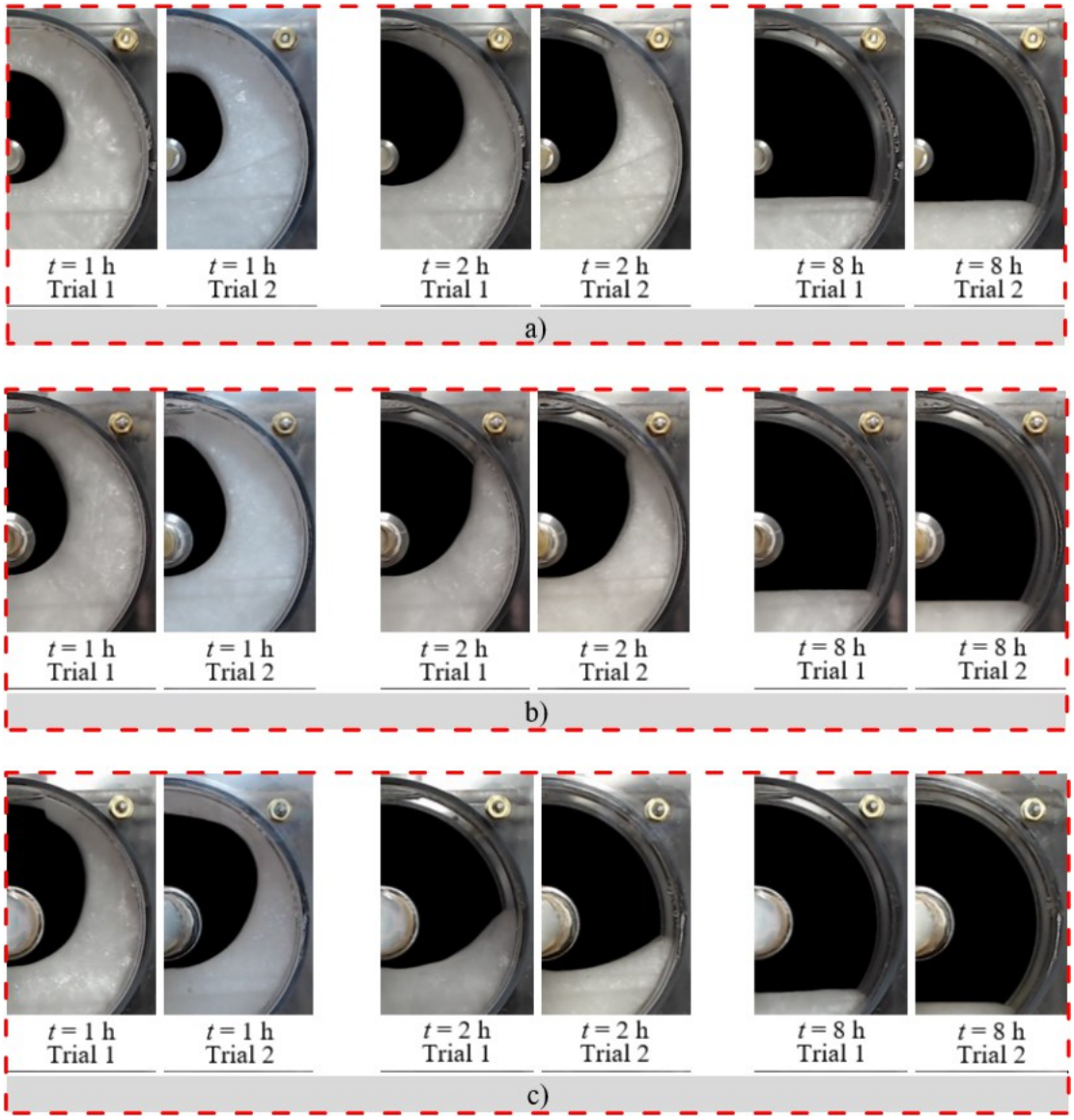

Figure 3.17 Melt profiles for global melting of dodecanoic acid at ΔT_f = 25.3 °C and ΔT_s = 2.5 °C for center-tube diameters of a) 18 mm, b) 27 mm and c) 36 mm.

The difference in the melt volumes from two trials, presented in Fig. 3.18, was calculated for each PCM and each center-tube diameter. The difference and the mean of the melt

volumes from two trials were used to calculate the percentage difference in the melt volumes. The percentage difference in the melt volumes from two trials is presented in Fig. 3.19 for both the PCMs. It can be seen that the difference in melt volume results is arbitrary; however, the difference is more pronounced when the melting is dominated by convective heat transfer. A point to point investigation of the melt volume results reveals that the maximum difference is approximately 14% in the melt volumes of *n*-octadecane regardless of the diameter of the center-tube. This difference is 8.4%, 6.4%, and 14.8% for the melt volumes of dodecanoic acid when the center-tube diameter is 18, 27, and 36 mm, respectively.

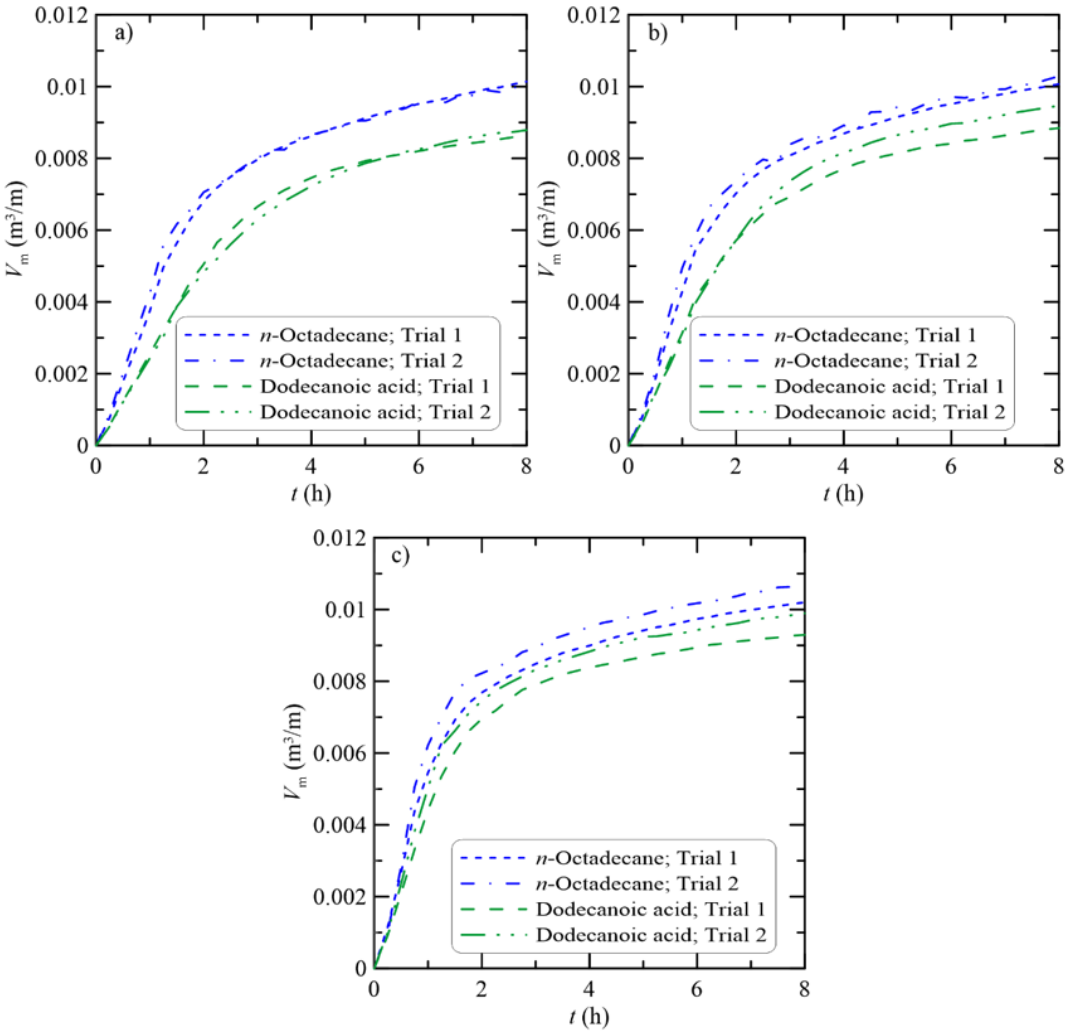

Figure 3.18 Melt volumes for global melting at ΔT_f = 25.3 °C and ΔT_s = 2.5 °C for center-tube diameters of a) 18 mm, b) 27 mm and c) 36 mm.

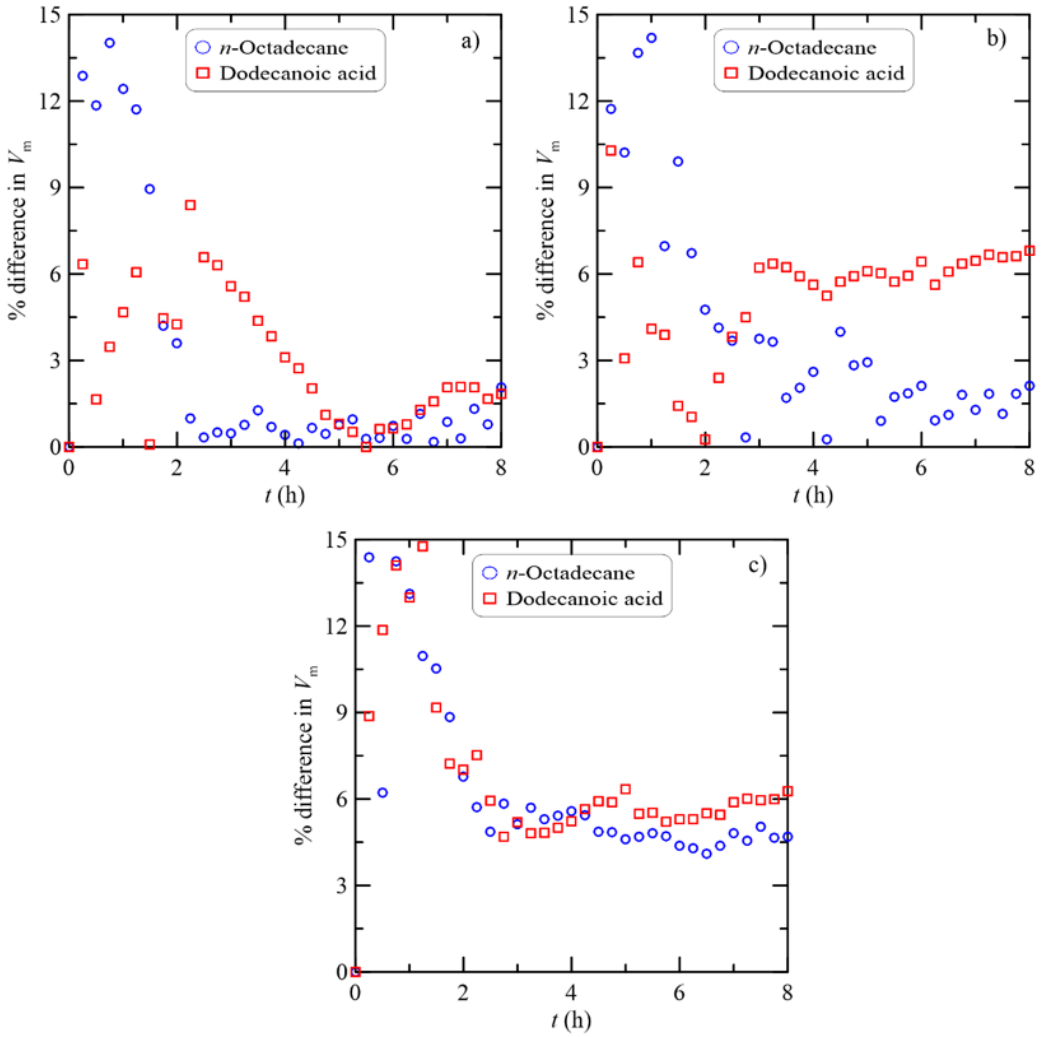

Figure 3.19 Percentage difference between global melt volumes of two trials at ΔT_f = 25.3 °C and ΔT_s = 2.5 °C for center-tube diameters of (a) 18 mm, (b) 27 mm and (c) 36 mm.

3.8 Conclusions

The experimental setup and the experimental methods have been discussed thoroughly in this chapter. Horizontal cylindrical annuli were used as PCM enclosures. Center-tubes with diameters of 18, 27, and 36 mm carried the HTF through the center, and the annular space was filled by the PCMs, *n*-octadecane and dodecanoic acid. The properties of the PCMs and different experimental conditions also have been discussed. Melting of both *n*-octadecane and dodecanoic acid was investigated when they were subcooled by 2.5, 7.5, 15, and 22.5 °C. The melting temperature differentials (the heating temperature above the melting temperature) were 8.44, 16.9, 25.3, 33.8, and 42.2 °C for *n*-octadecane and 8.44,

25.3, and 42.2 °C for dodecanoic acid. The combination of different geometry and experimental conditions resulted in 60 experiments for *n*-octadecane and 36 experiments for dodecanoic acid.

It was shown through the presentation of melt profiles and the melt volume results that the results were reproducible with a reasonable difference between the results from one trial to another. The maximum difference in the melt volume results at the onset of convection from one trial to another was 11.8%, and that for the global melting results was 14.8%.

CHAPTER 4 IMAGE PROCESSING AND UNCERTAINTY ANALYSIS

Image processing techniques are discussed in detail in this chapter. A brief review is first given on image processing techniques adopted by others. It is also discussed why extra precaution is required in the present study. Different sources of uncertainties and their calculation are discussed in this chapter.

4.1 Image processing techniques

Processing of full-color images usually includes the following steps:

- The full-color RGB images are first converted to grayscale images.
- A threshold is applied to convert the grayscale images into binary images.
- The pixel values of the images are calibrated to the physical scale.

The above-described method has been extensively used by researchers to process the images (Kamkari and Groulx, 2018; Fadl and Eames, 2019; Jones *et al.*, 2006). Uncertainties in the processed images originate from three sources: filtering, binarization, and calibration (Duhar and Colin, 2006). In the present study, LED lamps were used to illuminate the area of interest as the melting experiments were ongoing (see Fig. 3.2). Such illumination causes a reflection of different intensity from different regions of the images. Besides, during the span of the experiments, there were multiple sources of lights in the laboratory. The presence of these different shades of light makes the processing of the images more complicated, as has been mentioned by Jones *et al.* (2006). The existence of nonuniform light reflection would cause significant uncertainties due to filtering and binarization.

4.2 Image processing in the present study

The images were first processed semi-automatically using Adobe Photoshop CC, which should have eliminated the uncertainties originating from filtering and binarization, and then an in-house algorithm (given in Appendix A), developed using the MatLab image processing toolbox. Only the right half of the images were analyzed because of the symmetry of the melt profiles about the central vertical axis. The image processing steps adopted in the present study are described in subsections 4.2.1 and 4.2.2.

4.2.1 Pre-processing of the images

Cropped images at two instants of the melting process are shown in Fig. 4.1. The raw images at the onset of convection and well after the onset are shown in Figs. 4.1a) and 4.1b), respectively. The center of the enclosures in these images was known when the cameras were positioned, as shown in Fig. 3.9. The images were cropped (in MatLab) about this center to keep only the area of interest and discard the unnecessary parts. For the onset of convection, a 38 mm × 76 mm section from the center is shown. The radii of the center-tube and the outer shell were also known in pixel values, as shown in Fig. 3.9. Layers were created in Adobe Photoshop CC to mask the center-tube and anything outside the outer shell, which facilitated having the annular space to be modified.

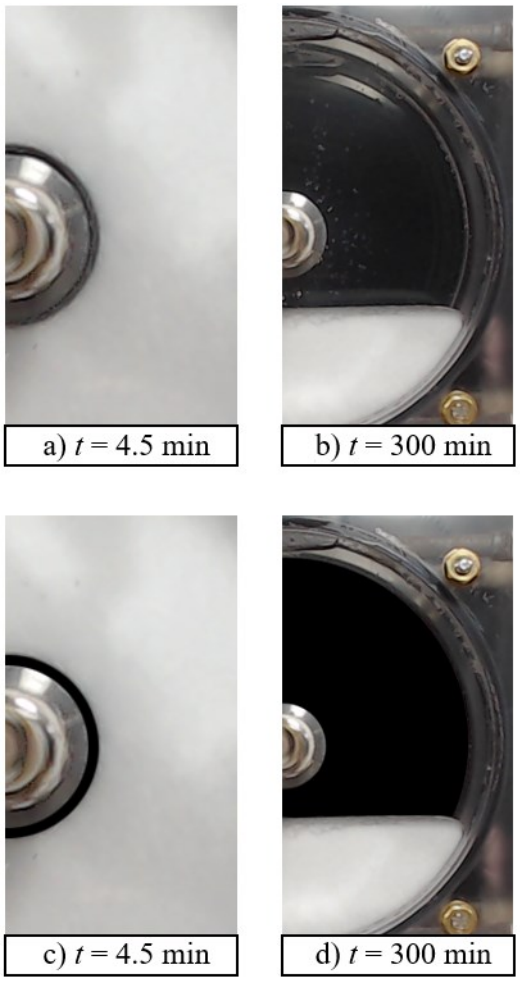

Figure 4.1 Image processing steps. The figure shows liquid and solid *n*-octadecane in the enclosure with the center-tube diameter of 27 mm when ΔT_f = 25.3 °C and ΔT_s = 7.5 °C: a) the cropped raw image at the onset of convection, b) cropped raw image well after the onset of convection, c) after cleaning a), and d) after cleaning b).

As seen in these raw images, the white color represents the solid PCM, and the black color represents the liquid PCM. It should be noted that both *n*-octadecane and dodecanoic acid are white when they are in the solid phase and become colourless when they melt. Black blotting papers were placed behind the enclosures to create a contrast between the solid and liquid PCM and, therefore, the liquid PCM appears black in the images.

As seen in Figs. 4.1a) and 4.1b), there are different shades of light and some shadows in the images. The liquid PCM is not pure black in either of the images. Moreover, the liquid PCM in Fig. 4.1a) appears blurry. Conversion of these raw images to binary images would require a threshold value to be chosen. However, this threshold value should be different for different images because every image is illuminated differently. Therefore, automatic identification of the solid-liquid interface would introduce significant uncertainty in the results, especially in the convection onset results. This uncertainty was eliminated by manually identifying the solid-liquid interface in every single image. All the pixels in the melted area were assigned the background color, pure black with an RGB color code of [0 0 0], as shown in Fig 4.1c) for the onset of convection and Fig. 4.1d) for long after the onset. All pixels outside the melted PCM region had a nonzero RGB color code.

4.2.2 Binarization and calibration of the images

The images processed using Adobe Photoshop CC were fed to the MatLab algorithm. In MatLab, the modified color images were converted to binary images simply based on the RGB value of every pixel. All pixels with zero RGB values were converted to white pixels (with a value of 1) while all with nonzero RGB values were converted to black pixels (with a value of 0). The binary images are shown in Fig. 4.2a) for the onset of convection and in Fig. 4.2b) for well after the onset. In these figures, the pure white portion of the images represents the liquid PCM, and the pure black part denotes the solid PCM or the enclosure.

The calibration for the measurement was done using the radius of the shell as given in Eq. (4.1).

$$\text{pixel length (m)} = \frac{\text{radius of the enclosure (m)}}{\text{radius of the enclosure (pixel)}} \tag{4.1}$$

The volume of liquid PCM per unit length of the enclosure was calculated as given in Eq. (4.2).

$$V_{\mathrm{m}}(\mathrm{m}^3/\mathrm{m}) = \sum_{i}^{n} [\text{pixel length (m)}]_i^2 \qquad (4.2)$$

In Eq. (4.2), n is the total number of white pixels, and i is an iterative variable.

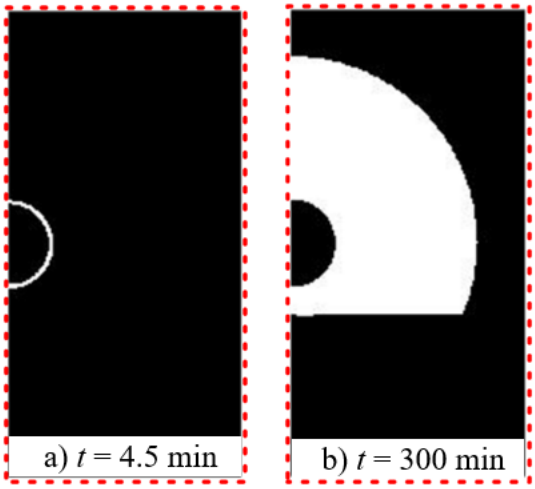

Figure 4.2 Binary images of liquid *n*-octadecane in the enclosure with a center-tube diameter of 27 mm when ΔT_f = 25.3 °C and ΔT_s = 7.5 °C: a) at the onset of convection and b) well after the onset of convection.

4.3 Uncertainties in the results originating from image processing

Uncertainties in the onset of convection results arise from two sources: from the calibration of the images and the choice of onset moment. The global melting results, however, assume uncertainties only from the calibration of the images. The calculation of uncertainties from these two sources is presented in subsections 4.3.1 and 4.3.2.

4.3.1 Calculation of uncertainties from the calibration of the images

The physical measurement of melt thickness at the onset of convection and for global melting of *n*-octadecane in the enclosure with the center-tube diameter of 27 mm is shown in Fig. 4.3. The melting temperature differential was 25.3 °C, and the PCM was subcooled by 7.5 °C. The horizontal and vertical axes in Fig. 4.3 are labelled in mm. It should be noted from Fig. 4.3 that the solid-liquid interface only on the front face of the enclosure is visible at the onset of convection. On the other hand, the solid-liquid interfaces both on

the front and back faces are visible once a lot more PCM has melted. Consequently, the radius of the shell on the front face was used in Eq. (4.1) for calibration at the onset of convection. Of the two solid-liquid interfaces visible in Fig. 4.3b), the one on the back face distinguishes the solid and liquid phases more clearly than does the one on the front face. Therefore, the radius of the shell on the back face was used in Eq. (4.1) for calibration of the images for global melting.

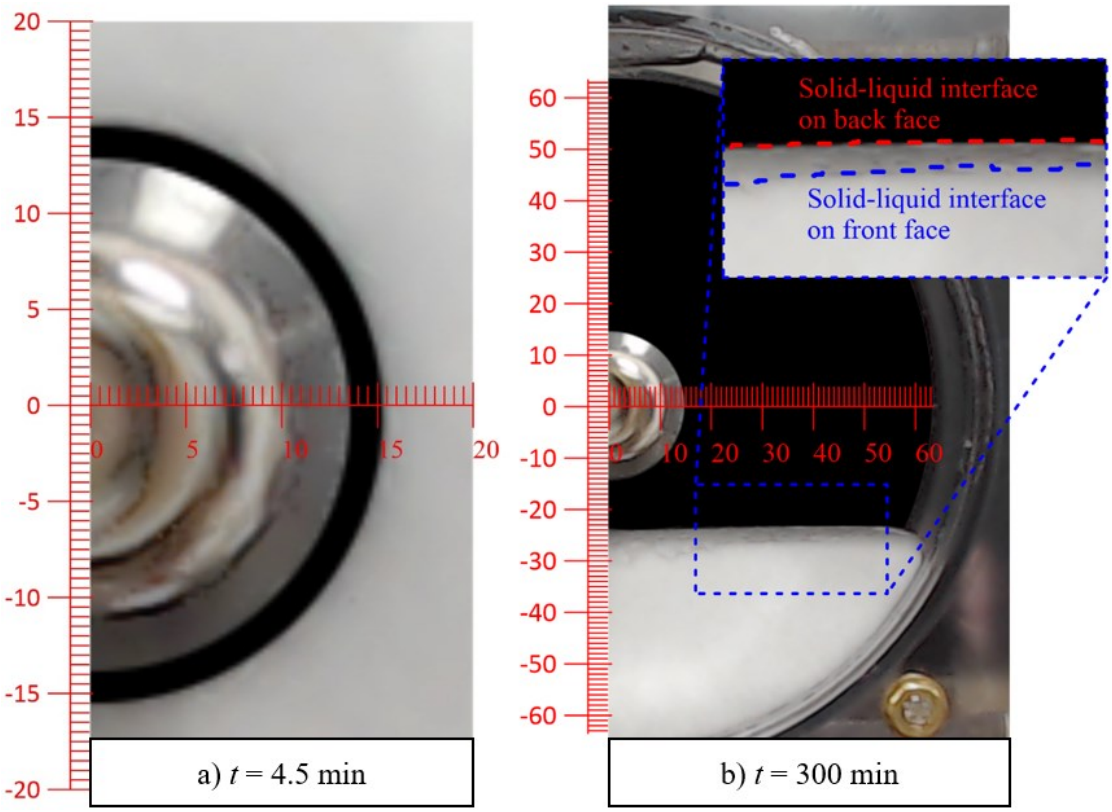

Figure 4.3 Physical measurement of melt thickness for melting of *n*-octadecane in the enclosure with the center-tube diameter of 27 mm for ΔT_f = 25.3 °C and ΔT_s = 7.5 °C: a) at the onset of convection and b) well after the onset of convection.

The melt thicknesses from physical measurement and the algorithm are presented in Table 4.1. Although the melt thicknesses can be measured physically with a ruler, the volume of the liquid PCM cannot be measured directly. For the onset of convection, the solid-liquid interface is circular, and the melt thickness is known from the physical measurement. This melt thickness and the radius of the center-tube were used to calculate the volume of the liquid PCM mathematically. This volume of liquid PCM was compared to that obtained

from the algorithm. It was not possible to determine the volume of liquid PCM, either physically or mathematically, once the convection started but only a fraction of the total PCM volume melted. Therefore, no data is available for the physical measurement of the liquid PCM after the onset of convection. As presented in Table 4.1, the error in the melt thickness varies from ± 1.7% to ± 4.3% for the onset of convection results and from ± 0.6% to ± 2.5% for global melting. The error in the melt volume at the onset of convection is ± 7.3%.

Table 4.1 Comparison of melt thicknesses measured physically and using the algorithm for melting of *n*-octadecane in the enclosure with the center-tube diameter of 27 mm and for ΔT_f = 25.3 °C and ΔT_s = 7.5 °C.

Time		At the onset (t = 4.5 min)			After the onset (t = 300 min)		
Measurement		Physical	Algorithm	Error (%)	Physical	Algorithm	Error (%)
Melt thickness (mm)	Above the center-tube	1.75	1.60	± 4.3	49.5	48.7	± 0.8
	Below the center-tube	1.75	1.69	± 1.7	10.0	9.50	± 2.5
	To the right of the center-tube	1.75	1.69	± 1.7	49.0	48.4	± 0.6
Volume of liquid PCM (cm^3/cm)		0.790	0.674	± 7.3	-	43.1	-

Another experiment was picked to calculate the uncertainties following the method described above. The physical measurement of melt thickness for melting of *n*-octadecane in the enclosure with the center-tube diameter of 18 mm and for ΔT_f = 25.3 °C and ΔT_s = 7.5 °C is presented in Fig. 4.4. The physical measurements and the estimates from the algorithm are shown in Table 4.2. By comparing Tables 4.1 and 4.2, it can be easily concluded that from one experiment to another, the error estimates do not change significantly.

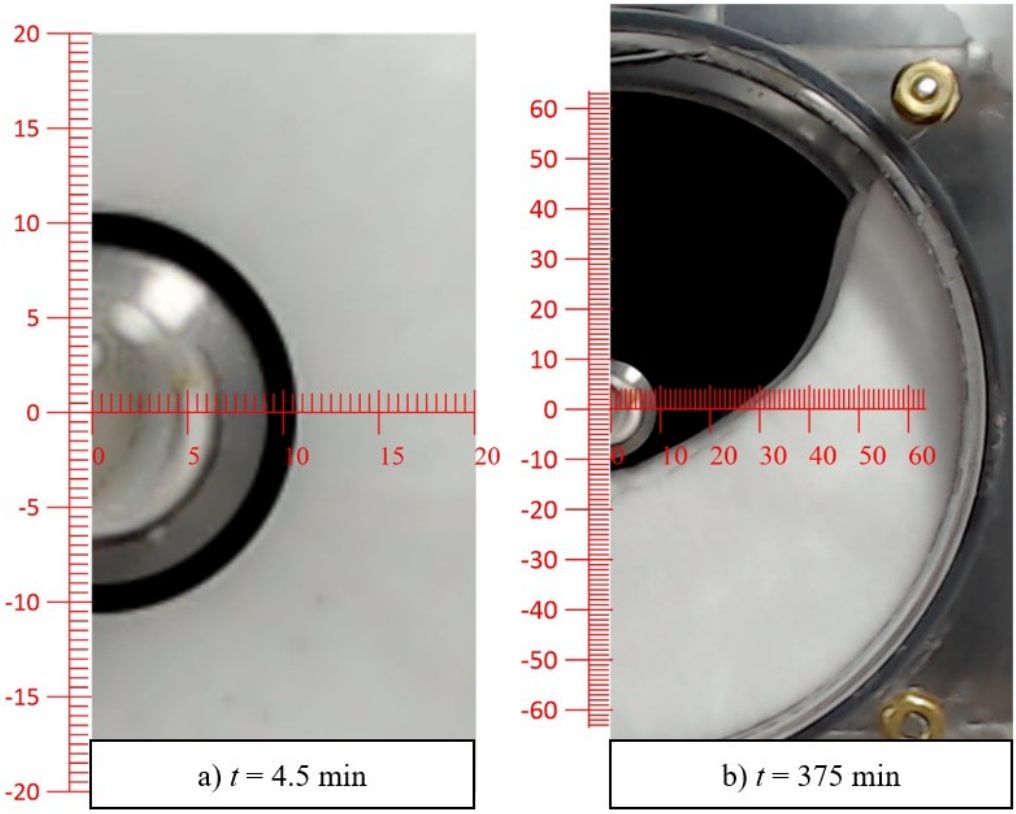

Figure 4.4 Physical measurement of melt thickness for melting of *n*-octadecane in the enclosure with the center-tube diameter of 18 mm for ΔT_f = 25.3 °C and ΔT_s = 7.5 °C: a) at the onset of convection and b) well after the onset of convection.

Table 4.2 Comparison of melt thicknesses measured physically and using the algorithm for melting of *n*-octadecane in the enclosure with the center-tube diameter of 18 mm and for ΔT_f = 25.3 °C and ΔT_s = 7.5 °C.

Time		At the onset (t = 4.5 min)			After the onset (t = 375 min)		
Measurement		Physical	Algorithm	Error (%)	Physical	Algorithm	Error (%)
Melt thickness (mm)	Above the center-tube	1.5	1.54	± 1.3	53.5	52.1	± 1.3
	Below the center-tube	1.5	1.32	± 6	2.5	2.20	± 6.0
	To the right of the center-tube	1.5	1.54	± 1.3	17.0	14.8	± 6.5
Volume of liquid PCM (cm^3/cm)		0.459	0.423	± 3.9	-	23.6	-

As mentioned earlier, to calculate the melt thicknesses and melt volumes for global melting, the radius of the enclosure on the back face was used in Eq. (4.1). It was pointed out that the back face was chosen because it distinguishes the solid-liquid interface more clearly than does the front face. However, an error estimate was carried out using the radius of the enclosure on the front face in Eq. (4.1) to crosscheck the errors. The image shown in Fig. 4.3b) has been modified; the solid-liquid interface on the front face has been identified manually and is presented in Fig. 4.5. The melt thicknesses and melt volume are shown in Table 4.3. A comparison of the values given in Table 4.3 to the respective values presented in Table 4.1 shows that the error estimates are comparable. It is noteworthy that the difference in melt volume in these two cases is ± 1.3%. The melt volume presented in Table 4.1 is more dependable than that shown in Table 4.3 simply because the solid-liquid interface is more accurately distinguishable in the former case. The melt thickness below the center-tube is significantly different in the two cases. The melt thickness presented in Table 4.1 is more dependable for the same reason that differentiates the melt volumes.

Table 4.3 Comparison of melt thicknesses measured physically and using the algorithm for melting of *n*-octadecane in the enclosure with the center-tube diameter of 27 mm and for ΔT_f = 25.3 °C and ΔT_s = 7.5 °C taking front face as the reference.

Time		After the onset (t = 300 min)		
Measurement		Physical	Algorithm	Error (%)
Melt thickness (mm)	Above the center-tube	50.5	50.0	± 0.5
	Below the center-tube	12.0	11.3	± 2.9
	To the right of the center-tube	49.5	49.5	-
Volume of liquid PCM (cm^3/cm)		-	44.2	-

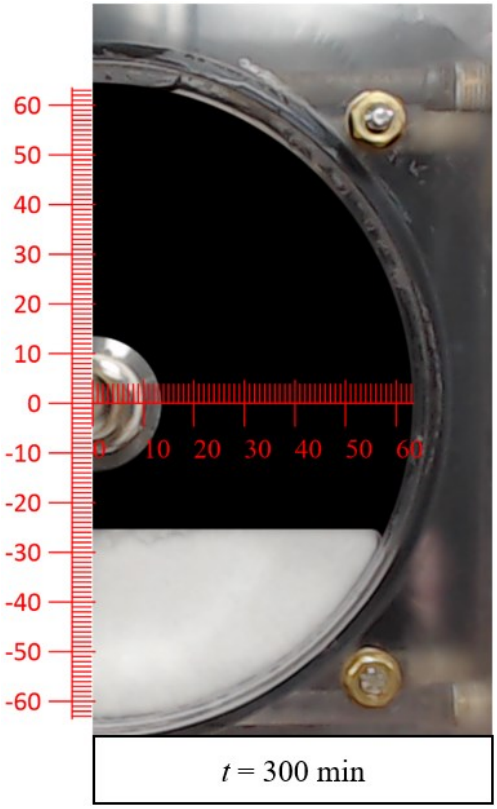

Figure 4.5 Physical measurement of melt thickness for melting of *n*-octadecane in the enclosure with the center-tube diameter of 27 mm for ΔT_f = 25.3 °C and ΔT_s = 7.5 °C using the front face as the reference.

As has been mentioned, it was not possible to validate the algorithm-calculated volume of liquid PCM after the onset of convection when the PCM was not fully in the liquid phase. Therefore, the volume of fully melted PCM was compared to the capacity of the enclosure. This comparison was made for three cases that include enclosures with center-tube diameters of 18, 27, and 36 mm with ΔT_f = 42.2 °C and ΔT_s = 2.5 °C. The calculated volumes, presented in Table 4.4, show that the error can range from ± 1% to ± 2.5%.

Table 4.4 Comparison of melt volume measured physically and using the algorithm.

Center-tube diameter (mm)	Melt volume (cm^3/cm)		Error (%)
	Physical	Algorithm	
18	62.1	60.9	± 1
27	60.5	57.6	± 2.4
36	58.2	55.3	± 2.5

The above discussion about different approaches of error calculation shows that the error in the melt volume results originating from the calibration varies from ± 0.6% to ± 7.3%. The most pessimistic error (± 7.3%) is adopted as the error in melt volume results of the present study that originates from calibration.

4.3.2 Calculation of uncertainties from the choice of onset moment

Images were shot every 10 seconds in the early stage of the melting process, at least until the natural convection started. The onset of convection was assumed to have occurred when the concentric solid-liquid interfaces became nonconcentric, as shown in Fig. 4.6. As Fig. 4.6c) shows, the non-concentricity in the solid-liquid interface becomes very pronounced 60 seconds after the onset of convection. The non-concentricity of the solid-liquid interfaces was more closely determined using Adobe Photoshop CC. The onset of convection was assumed to have occurred before the non-concentricity in the solid-liquid interface became as pronounced as shown in Fig. 4.6c). Three such images are shown in Fig. 4.7: at the onset of convection (Fig. 4.7b), 10 seconds before the onset (Fig. 4.7a), and 10 seconds after (Fig. 4.7c). The difference in these images is very subtle. Any of these three images could represent the onset of convection. The error that would stem from a different choice of onset moment is summarized in Table 4.5. This table shows that the difference between the melt volumes 10 seconds before the onset of convection and 10 seconds after is ± 8.3%. Therefore, the uncertainty from the choice of onset moment is considered ± 8.3%.

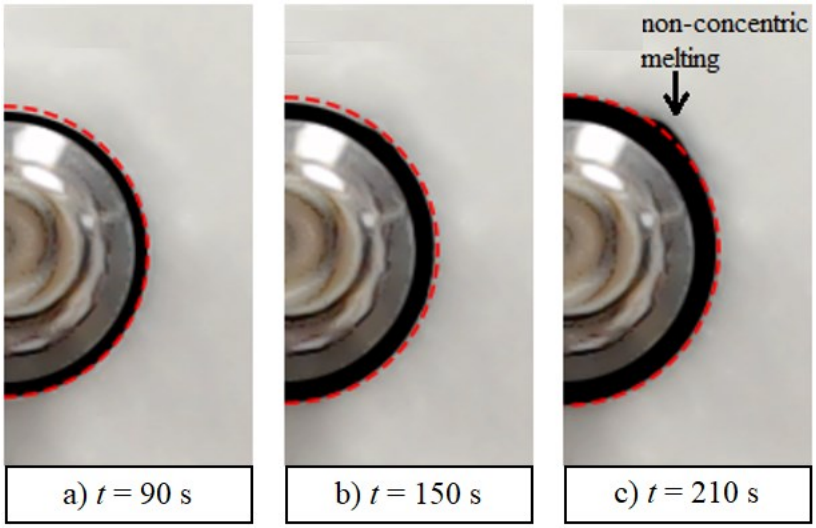

Figure 4.6 Melting of *n*-octadecane in the enclosure with the center-tube diameter of 27 mm when ΔT_f = 25.3 °C and ΔT_s = 2.5 °C.

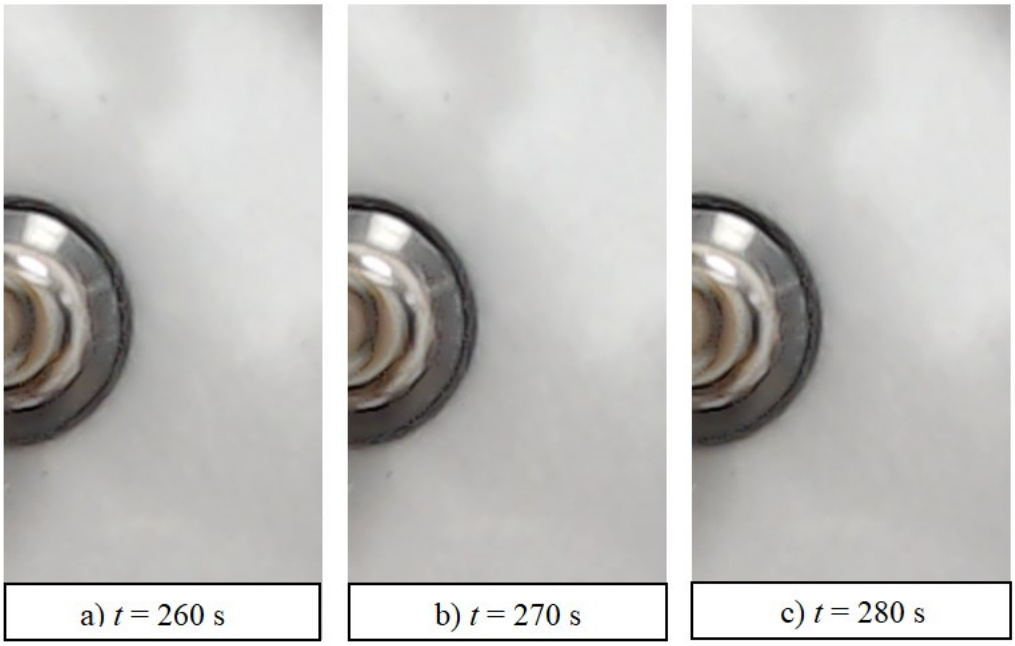

Figure 4.7 Melting of *n*-octadecane in the enclosure with the center-tube diameter of 27 mm when ΔT_f = 25.3 °C and ΔT_s = 7.5 °C.

Table 4.5 Comparison of melt volume measured physically and using the algorithm.

Melt volume (cm^3/cm)			Maximum uncertainty
10 s before the onset of convection	At the onset of convection	10 s after the onset of convection	
0.671	0.674	0.783	± 8.3%

4.3.3 Uncertainties in the melt volume results at the onset of convection

As mentioned, uncertainties in the melt volumes at the onset of convection originate from the calibration and the choice of onset moment. These two sources are, however, unrelated. If a quantity C depends on A and B, where A and B are unrelated, and the standard uncertainties in A and B are u_A and u_B, respectively, then the collective uncertainty in C is given by Eq. (4.3) (Taylor, 1997).

$$u_C = \sqrt{u_A^2 + u_B^2} \tag{4.3}$$

Accounting for uncertainties from calibration, and the choice of onset moment, the combined uncertainty in the melt volume results is calculated as:

$$u_{\text{melt volume}} = \sqrt{u_{\text{calibration}}^2 + u_{\text{choice of onset moment}}^2} \tag{4.4}$$

The uncertainty in the melt volume at the onset of convection, calculated using Eq. (4.4) and the uncertainties originating from calibration (± 7.3%) and the choice of onset moment (± 8.3%) is ± 11.1%.

4.4 Errors in Stefan and Grashof numbers

4.4.1 Bias error in temperature

Errors in Stefan and Grashof numbers are the same as the error in the heating temperature, assuming that the actual values of material properties are known. The error in the heating temperature is a combination of bias error and precision error. The bias error originates from the accuracy of the thermocouples, which in this study is provided by the manufacturer. The T-type thermocouples, used in the present study, has an error of ± 1.0 °C or ± 0.75% above 0 °C, whichever is greater. The temperature of the center-tube wall in this study ranges from 35.9 °C to 85.2 °C. For the wall temperature of 35.9 °C, a ± 1.0 °C error is equivalent to a ± 2.8% error in the temperature data. This error is the largest among all the errors calculated using all the wall temperatures. On the other hand, this error is also greater than the percentage error (± 0.75%) provided by the thermocouple

manufacturer. Therefore, the greater of the two errors (± 2.8%) suggested by the manufacturer is adopted as the bias error.

Table 4.6 Error in temperature measurements.

Center-tube wall temperature (°C)	Error in measured temperature		Precision error (%)	Bias error (%)	Total error (%)
	Standard deviation (°C)	Error (%)			
35.9	± 0.4	± 1.1	± 2.3	± 2.8	± 5.1
52.8	± 1.2	± 2.3			
85.2	± 1.0	± 1.2			

4.4.2 Precision error in temperature

Three sample wall temperatures were considered to calculate the precision error: the lowest (35.9 °C), the highest (85.2 °C), and a medium wall temperature (52.8 °C). At least four experiments were run at each wall temperature with the PCM initially being subcooled by 2.5, 7.5, 15, and 22.5 °C. The temperature of the wall at the inlet and outlet of the center-tubes was measured at 1/3 Hz. These measurements resulted in hundreds of thousands of data for each wall temperature. These data were used to calculate the standard deviation about the respective true wall temperatures, which are shown in Table 4.6. This table shows that the maximum precision error arising from the chosen wall temperatures is ± 2.3%.

The total error in the temperature data is the summation of the bias and precision errors (Aberneth *et al.*, 1985), which is ± 5.1%. The error in the temperature on the sleeve-surface of the center-tube (4.7%), estimated in section 3.4.3 of Chapter 3, is within the error calculated here (± 5.1%).

Both the Stefan and Grashof numbers are defined with the melting temperature differential (T_w - T_m). It is assumed, as mentioned earlier, that there is no uncertainty in the melting temperature and thermophysical properties of the PCM. Therefore, the uncertainty in

Stefan and Grashof numbers is assumed to be that in the center-tube wall temperature, which is ± 5.1%.

4.5 Errors in Fourier number

Fourier number does not directly influence the onset of convection. However, global melting results directly depend on the Fourier number, which in the present study is defined as given in Eq. (4.5), where r and R are the radius of the center-tube and radius of the outer shell, respectively.

$$\mathrm{Fo} = \frac{\alpha_l t}{(R-r)^2} \tag{4.5}$$

Errors in Fourier number would be the error in the time of acquisition of images, ignoring the uncertainties in the thermophysical properties of the PCMs and the geometric dimensions of the enclosures. A delay exists in writing the images on the computer from when the webcam is triggered. This delay propagates as the experiments progress. A sample of propagation of delay over 8 hours (28800 s) of melting experiment is shown in Table 4.7.

Table 4.7 Errors in the time of acquisition of the images.

Intended time of image acquisition (s)	Deviation from expected time (s)	Error (%)
60	2	3.3
180	10	5.6
300	20	6.7
600	44	7.3
1800	64	3.6
7200	78	1.1
28800	87	0.3

The percentage error in the time of image acquisition was calculated as given in Eq. (4.6).

$$\text{error} = \frac{\text{delay in image acquisition}}{\text{intended time of image acquisition}} \times 100\% \qquad (4.6)$$

Table 4.7 shows that the maximum error in the acquisition time of the images is 7.3%.

4.6 Conclusions

Uncertainties arising from different sources were considered thoroughly to calculate the uncertainties in the results presented in this study. The uncertainty in the melt volumes at the onset of convection resulted from two different sources: uncertainty arising from the calibration of the images and uncertainty originating from the choice of onset moment. The uncertainty in the melt volume results at the onset of convection in the present study is ± 11.1%. The uncertainty in the melt volumes for global melting originated only from the calibration of the images, which is ± 7.3%. It was assumed that there are no uncertainties in the thermophysical properties of the PCMs. Based on that, it was assumed that the error in the Grashof and Stefan number would originate only from the center-tube wall temperature and be the same as the uncertainty in the wall temperature. The uncertainty in wall temperature arises from two sources: the bias error from the inaccuracy of the instrument and the precision error from the measurement. Combining these two sources, the error in Grashof and Stefan number in the present study is ± 5.1%. The error in Fourier number arises from the error in the acquisition time of the images, which is 7.3%.

CHAPTER 5 MELTING OF N-OCTADECANE

The results for the onset of natural convection during melting of *n*-octadecane are presented in this chapter. As mentioned in Chapter 3, the melting of *n*-octadecane was studied for the melting temperature differentials of 8.44, 16.9, 25.3, 33.8, and 42.2 °C. These melting temperature differentials correspond to Stefan numbers of 0.1, 0.2, 0.3, 0.4, and 0.5, respectively. The PCM was subcooled by 2.5, 7.5, 15, and 22.5 °C. Melt profiles at the onset of convection, the effects of center-tube diameter, Stefan number, and PCM-subcooling on the onset of natural convection are presented. The melt profiles only for the Stefan numbers of 0.1, 0.3, and 0.5 are presented. Those for the Stefan numbers of 0.2 and 0.4 are not shown because of their similarity to the others.

The melt profiles, effects of diameter and Stefan number on onset melt volumes are presented in two sections. The results for substantially subcooled PCM (ΔT_s = 22.5, 15, and 7.5 °C) are presented in section 5.1 and those for the barely subcooled PCM (ΔT_s = 2.5 °C) are presented in section 5.2. The results on the effects of subcooling on the onset of convection are presented in section 5.3 for all the subcooled cases.

5.1 Substantially subcooled PCM

5.1.1 Melt profiles at the onset of natural convection

The melt profiles at the onset of convection for the PCM initially subcooled by 22.5, 15, and 7.5 °C are presented in Figs. 5.1, 5.2, and 5.3, respectively. The photographs in these figures represent a 30 mm × 60 mm section; 30 mm to the right, 30 mm above, and 30 mm below the center of the enclosure. The reader is reminded that the black color surrounding the center-tube represents the liquid PCM and the white color represents the solid PCM. As mentioned earlier, the onset of convection was identified by the first appearance of a solid-liquid interface that is not concentric to the center-tube.

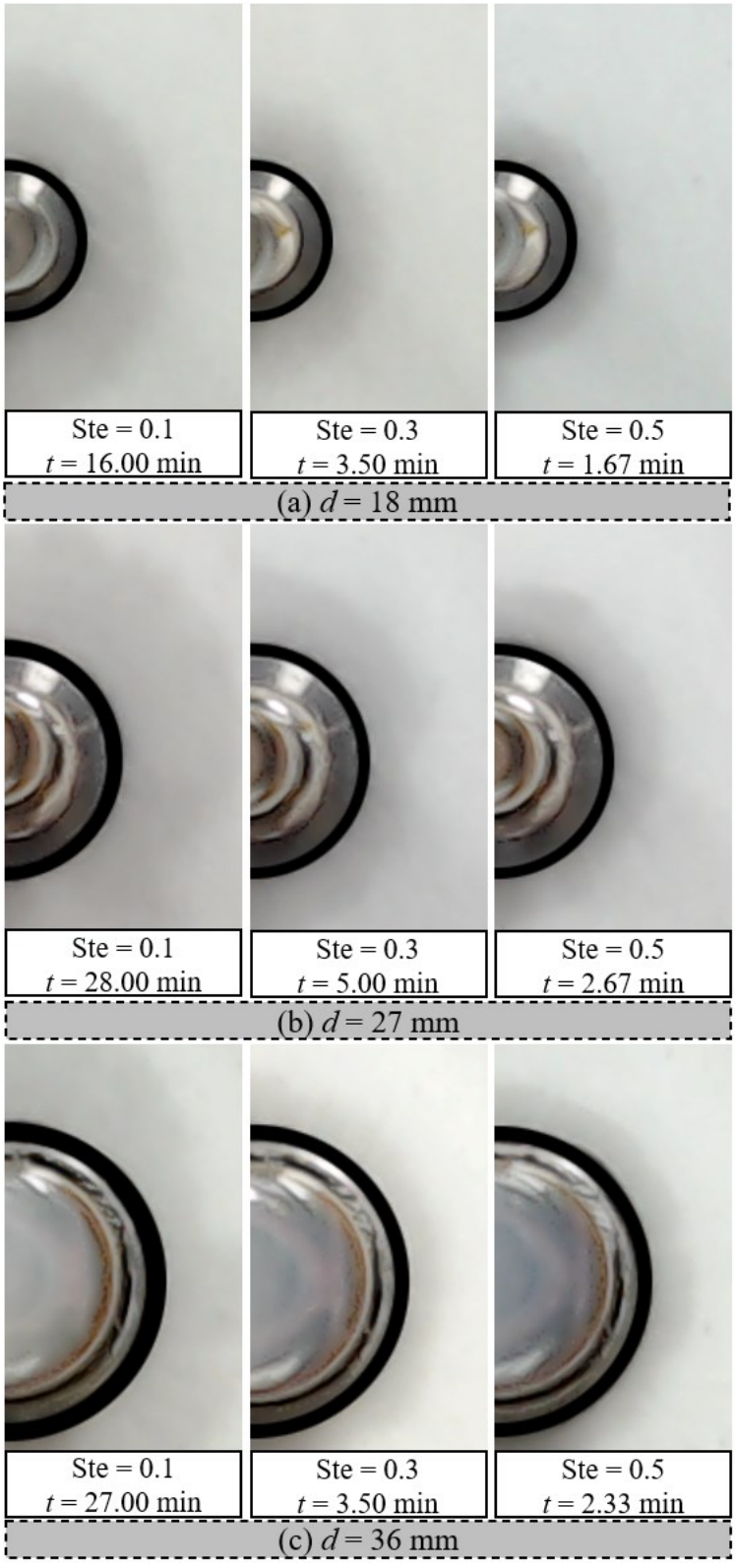

Figure 5.1 Melt profiles at the onset of natural convection for ΔT_s = 22.5 °C.

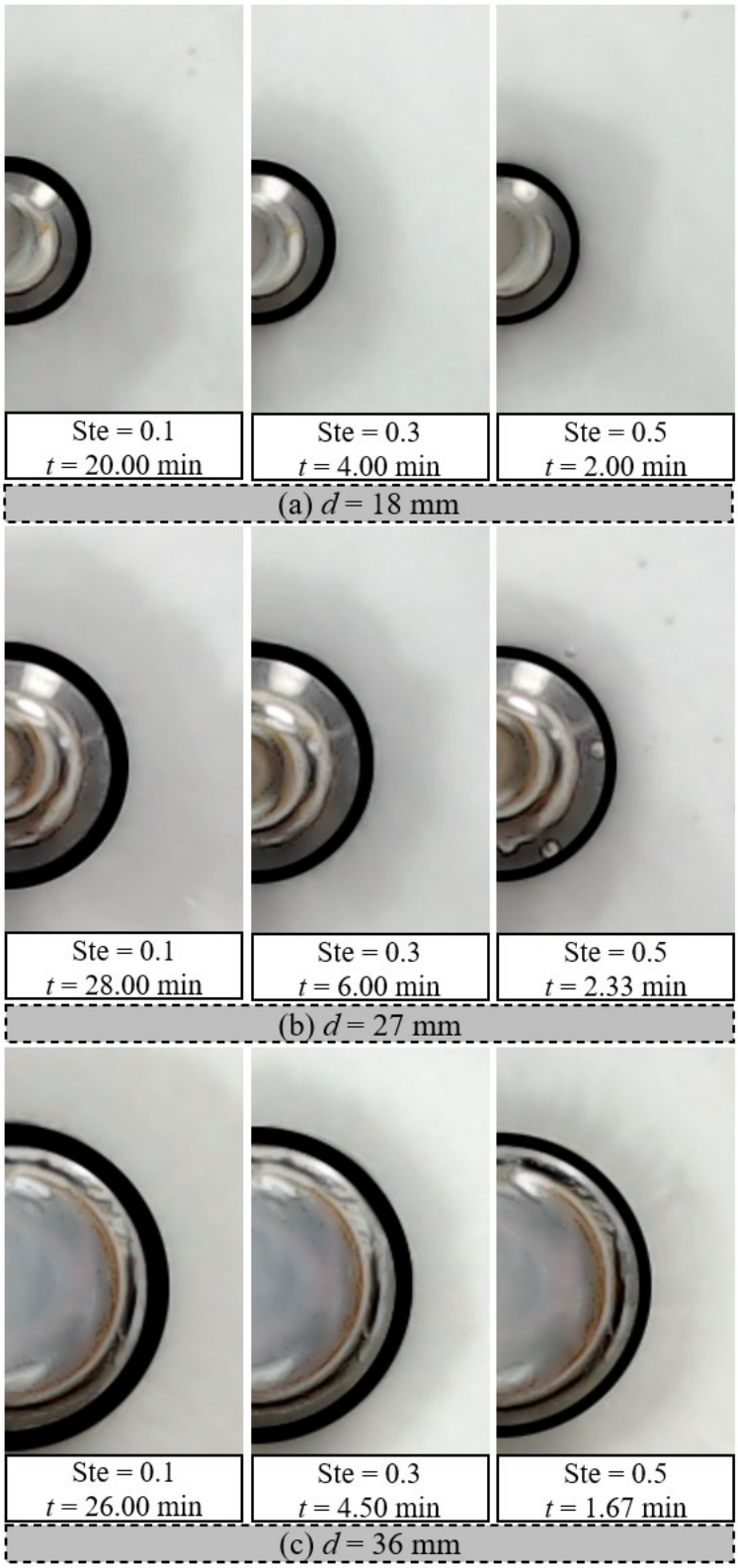

Figure 5.2 Melt profiles at the onset of natural convection for ΔT_s = 15 °C.

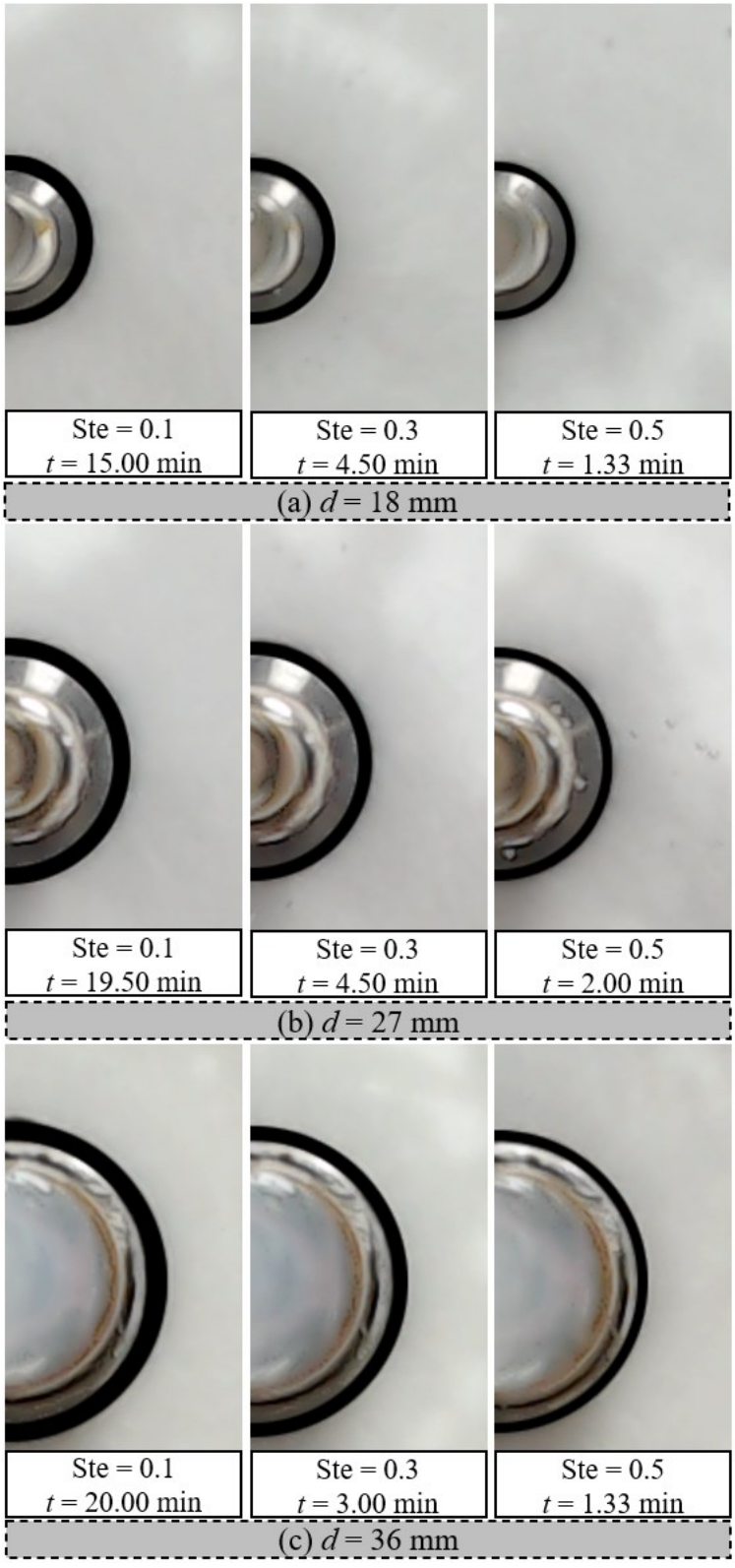

Figure 5.3 Melt profiles at the onset of natural convection for ΔT_s = 7.5 °C.

The photographs clearly show that for every center-tube, more liquid PCM is required for the onset of convection when the PCM is heated at a smaller Stefan number, except when the PCM is subcooled by 22.5 °C. Figure 5.1 shows that the amount of liquid PCM for different Stefan numbers is apparently the same for the center-tube diameter of 18 mm. No significant difference in the onset melt volume is noticeable for the center-tube diameters of 27 and 36 mm for higher Stefan number (≥ 0.2). Regardless of the size of the center-tubes and the subcooling conditions, a comparison of Figs. 5.1 – 5.3 shows that the onset of convection occurs slower at smaller Stefan numbers. This finding is in agreement with the onset results of Wang *et al.* (1999), albeit their experimental geometry and conditions are different. It was found in the study of Wang *et al.* (1999) during melting of polyethylene glycol 900 in a vertical rectangular enclosure that the time required for the onset of convection decreased as the applied heat flux to one of the vertical sides increased. It is noteworthy that although the convection onset occurs slower at smaller Stefan numbers, no such trend is observed with respect to the center-tube diameter or the degree of subcooling.

5.1.2 Effects of center-tube diameter on the onset of natural convection

The melt volumes, per unit length of the enclosure, at the onset of convection for the PCM initially subcooled by 22.5, 15, and 7.5 °C are presented in Figs. 5.4, 5.5, and 5.6, respectively. The volumes of liquid PCM at the onset of convection were calculated for the respective subcooled conditions from the melt profile images shown in Figs. 5.1, 5.2, and 5.3. Results are also incorporated from the experiments performed for Ste = 0.2 and 0.4. Figures 5.4–5.6 show a linear relationship between the onset melt volumes and the size of the center-tubes. A larger amount of liquid PCM is required for the onset of convection as the diameter of the center-tube increases, regardless of the Stefan number and the degree of subcooling.

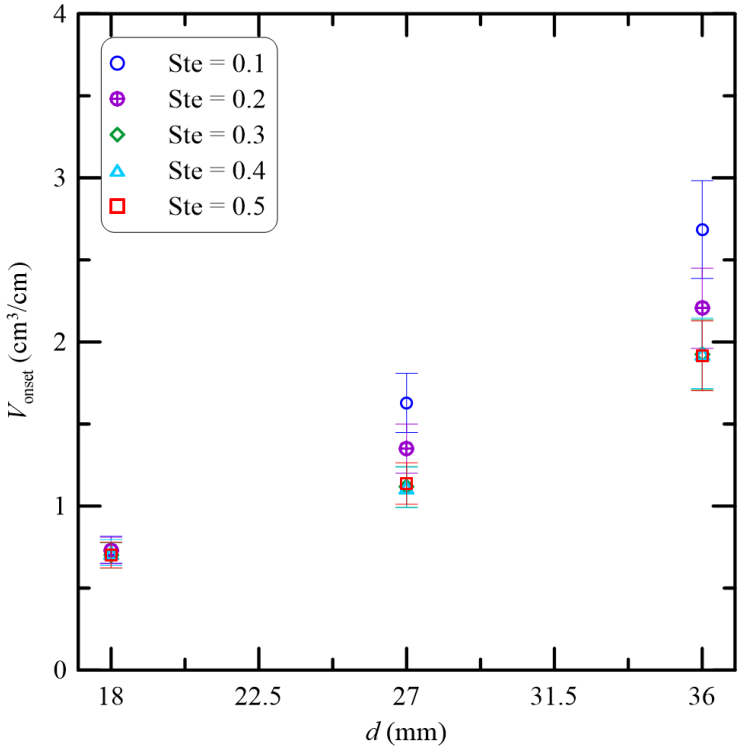

Figure 5.4 Melt volume vs the diameter of the center-tubes at the onset of convection for ΔT_s = 22.5 °C.

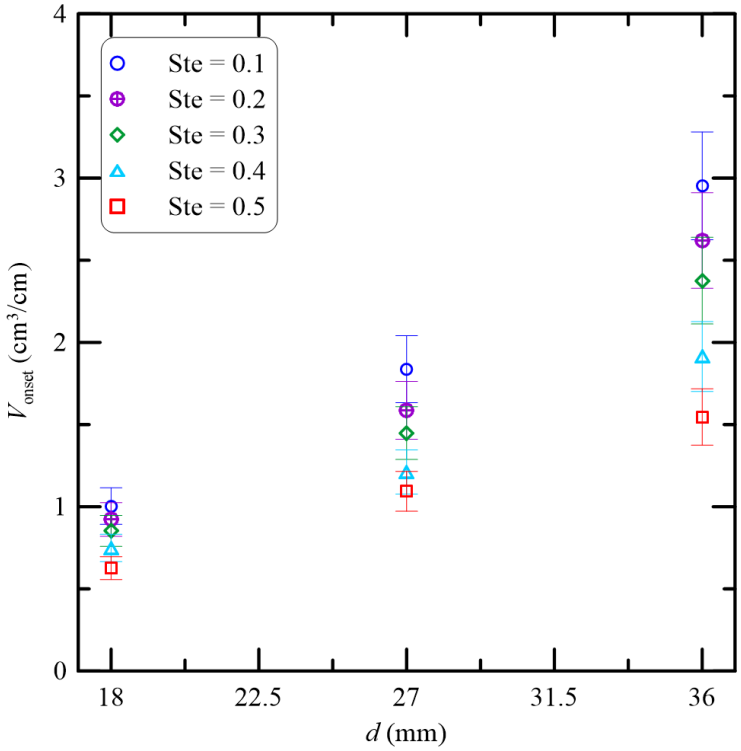

Figure 5.5 Melt volume vs the diameter of the center-tubes at the onset of convection for ΔT_s = 15 °C.

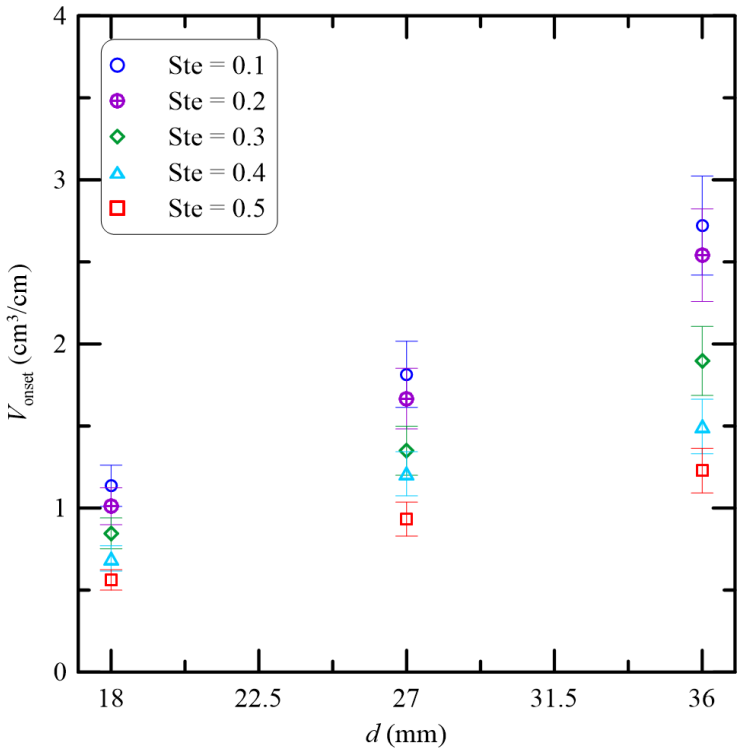

Figure 5.6 Melt volume vs the diameter of the center-tubes at the onset of convection for ΔT_s = 7.5 °C.

Figure 5.4 shows that for the PCM initially subcooled by 22.5 °C and in the enclosure with the center-tube diameter of 18 mm, the melt volume requirement for the onset of convection does not vary with the Stefan number. For the larger center-tube diameters, a difference in the melt volume results is observed only at low Stefan numbers (Ste = 0.1 and 0.2). Figures 5.5 and 5.6 show for the PCM subcooled by 15 and 7.5 °C, respectively, that the values of onset melt volume spread over a narrow range when the diameter is small. The range of these values becomes wider as the diameter of the center-tube gets larger. Also, a comparison of Figs. 5.4, 5.5, and 5.6 show that this range gets wider for any center-tube diameter as the degree of subcooling lessens. These figures show that the center-tubes affect the onset volume differently for different values of the Stefan numbers.

As mentioned earlier, the melt volumes at the onset of natural convection vary linearly with the diameter of the center-tubes. Therefore, the melt volume data presented in Figs. 5.4, 5.5, and 5.6 were fitted to linear correlations. These correlations are shown in Tables 5.1, 5.2, and 5.3, respectively, for the PCM subcooled by 22.5, 15, and 7.5 °C. It is seen that the diameter of the center-tubes greatly influences the required onset volume when the

Stefan number is low. As the Stefan number increases, the influence of the center-tube diameter on the onset of convection diminishes. A comparison of Tables 5.1, 5.2, and 5.3 shows that the influence of the center-tube on the onset volume diminishes as the degree of subcooling decreases, as can be seen by the value of the slopes for these correlations.

Table 5.1 Correlation of melt volume at the onset of convection with the diameter of the center-tubes when the PCM is subcooled by 22.5 °C.

Ste	Correlation	R^2
0.1	$V_{\text{onset}} = 0.108d - 1.24$	0.998
0.2	$V_{\text{onset}} = 0.082d - 0.786$	0.992
0.3	$V_{\text{onset}} = 0.068d - 0.588$	0.968
0.4	$V_{\text{onset}} = 0.068d - 0.568$	0.962
0.5	$V_{\text{onset}} = 0.068d - 0.570$	0.974

Table 5.2 Correlation of melt volume at the onset of convection with the diameter of the center-tubes when the PCM is subcooled by 15 °C.

Ste	Correlation	R^2
0.1	$V_{\text{onset}} = 0.108d - 0.992$	0.993
0.2	$V_{\text{onset}} = 0.094d - 0.836$	0.984
0.3	$V_{\text{onset}} = 0.084d - 0.726$	0.984
0.4	$V_{\text{onset}} = 0.064d - 0.456$	0.986
0.5	$V_{\text{onset}} = 0.052d - 0.290$	0.999

Table 5.3 Correlation of melt volume at the onset of convection with the diameter of the center-tubes when the PCM is subcooled by 7.5 °C.

Ste	Correlation	R^2
0.1	$V_{\text{onset}} = 0.088d - 0.488$	0.993
0.2	$V_{\text{onset}} = 0.086d - 0.556$	0.993
0.3	$V_{\text{onset}} = 0.058d - 0.212$	0.999
0.4	$V_{\text{onset}} = 0.044d - 0.072$	0.973
0.5	$V_{\text{onset}} = 0.036d - 0.092$	0.996

5.1.3 Influence of Stefan number on the onset of natural convection

The melt volumes at the onset of convection are presented against the Stefan numbers in Figs. 5.7, 5.8, and 5.9, respectively, for the PCM initially subcooled by 22.5, 15, and 7.5 °C. The melt volumes do not show the same trend for all the subcooled cases. Whereas the onset melt volumes vary linearly with the Stefan numbers when the PCM is subcooled by 15 and 7.5 °C, it does not vary linearly unconditionally when the PCM is subcooled by 22.5 °C (see Fig. 5.7). Figure 5.7 shows that the onset melt volume is independent of the Stefan number for the center-tube diameter of 18 mm. The onset melt volume varies linearly with the Stefan number for the center-tube diameters of 27 and 36 mm only when the Ste $\leq$ 0.3. For Ste $\geq$ 0.3, the melt volume at the onset of convection becomes independent of the Stefan number. In the cases where the onset melt volume varies linearly with the center-tube diameter, the melt volume data have been fitted to linear correlations.

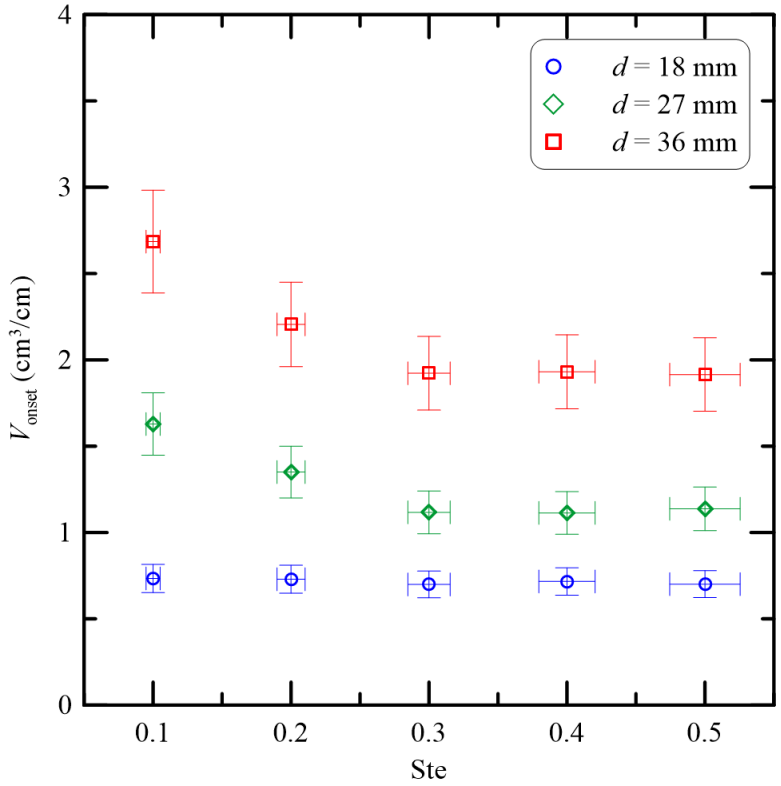

Figure 5.7 Melt volume vs Stefan number at the onset of convection for ΔT_s = 22.5 °C.

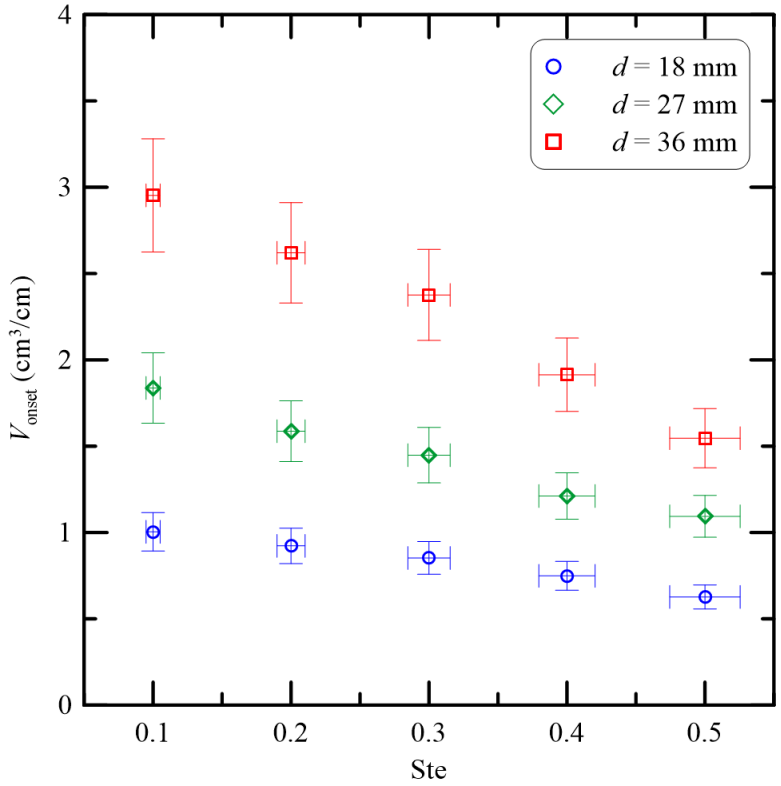

Figure 5.8 Melt volume vs Stefan number at the onset of convection for ΔT_s = 15 °C.

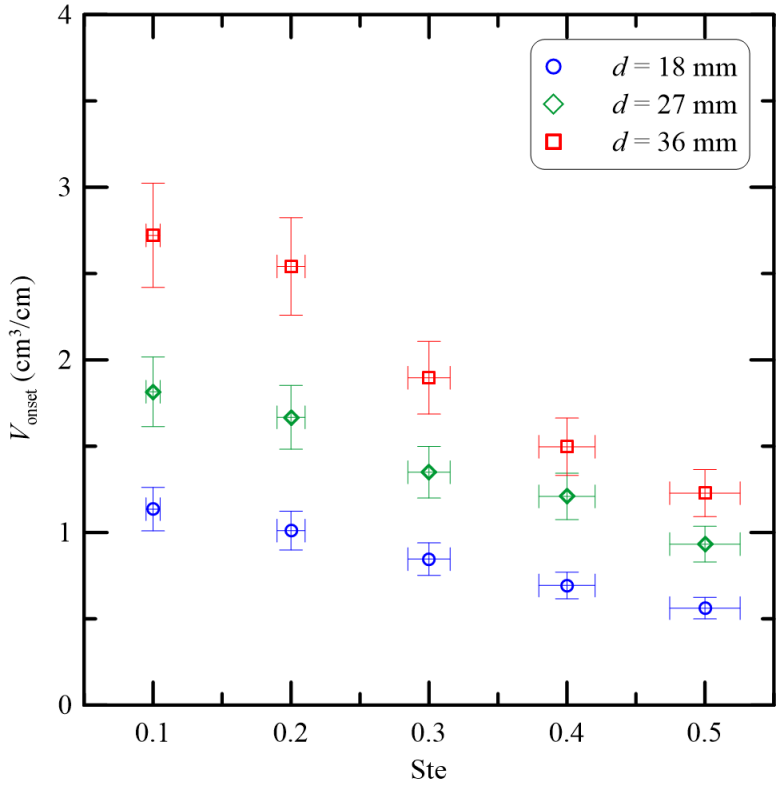

Figure 5.9 Melt volume vs Stefan number at the onset of convection for ΔT_s = 7.5 °C.

These correlations are presented in Tables 5.4 and 5.5, respectively, for the PCM subcooled by 15 and 7.5 °C. These tables show that the dependence of onset melt volumes on Stefan numbers decreases with the diameter of the center-tubes. These tables also show that this dependence decreases as the degree of subcooling increases. The invariance of onset melt volume on the Stefan number with the degree of subcooling is more pronounced when the center-tube diameter is smaller.

As will be presented in the next section, when the PCM is barely subcooled (by 2.5 °C), almost all the heat (a larger amount of heat for a higher Stefan number) is being used to melt the solid PCM and heat the liquid PCM. On the other hand, when the PCM is more subcooled, a portion of the heat is being used to preheat the solid PCM. Therefore, a reduced amount of heat remains available to melt the solid PCM and heat the liquid PCM. This reduction in heat, in turn, causes Stefan number to have a lesser influence on onset volume when the PCM is subcooled to a greater extent. Since heat transfer by conduction takes place slowly when the center tube diameter is small, subcooling will diminish the

influence of Stefan number on the onset melt volume more when the diameter of the center-tube is small.

Nonetheless, whenever the onset melt volume varies with the Stefan number, it is seen that a smaller amount of liquid PCM is required for the onset of convection as the Stefan number increases.

Table 5.4 Correlation of melt volume at the onset of convection with Stefan number when the PCM is subcooled by 15 °C.

d (mm)	Correlation	R^2
18	$V_{\text{onset}} = -0.928\text{Ste} + 1.11$	0.988
27	$V_{\text{onset}} = -1.86\text{Ste} + 1.99$	0.987
36	$V_{\text{onset}} = -3.52\text{Ste} + 3.34$	0.991

Table 5.5 Correlation of melt volume at the onset of convection with Stefan number when the PCM is subcooled by 7.5 °C.

d (mm)	Correlation	R^2
18	$V_{\text{onset}} = -1.46\text{Ste} + 1.29$	0.998
27	$V_{\text{onset}} = -2.22\text{Ste} + 2.06$	0.986
36	$V_{\text{onset}} = -4.04\text{Ste} + 3.18$	0.973

5.2 Barely subcooled PCM

5.2.1 Melt profiles at the onset of natural convection

The melt profiles at the onset of convection for the PCM initially subcooled by 2.5 °C are presented in Fig. 5.10. Similar to other subcooled cases, the photographs in Fig. 5.10 represent a 30 mm × 60 mm section; 30 mm to the right, 30 mm above, and 30 mm below the center of the enclosure. Figure 5.10 shows that the melt profiles are not completely concentric. The PCM melts faster below the center-tube than at the top. Although the solid-liquid interfaces are not fully concentric, a large portion of the interfaces is concentric

to the center-tube (see Fig. 5.10). This concentric portion of the solid-liquid interface was considered in determining the onset of convection.

The presence of non-concentric solid-liquid interfaces in the early stage of the melting process for the PCM subcooled by 2.5 °C, unlike the other subcooled cases, deserves a discussion. It was noticed during the experiments that tiny bubbles formed in the liquid PCM below the center-tube and traveled to the top. Since there was solid PCM above the center-tube, the bubbles could not rise to the top of the enclosure. These bubbles accumulated in the liquid PCM between the center-tube and the solid-liquid interface. As fleets of the bubbles traveled to the top of the center-tube and got trapped between the solid-liquid interface and the center-tube, a thin layer of thermal resistance developed between the center-tube and the solid-liquid interface. This thermal resistance inhibited heat transfer above the center-tube. Therefore, more PCM melted below the center-tube and less above it. Once enough PCM melted, these bubbles were swept away by the circulating liquid PCM.

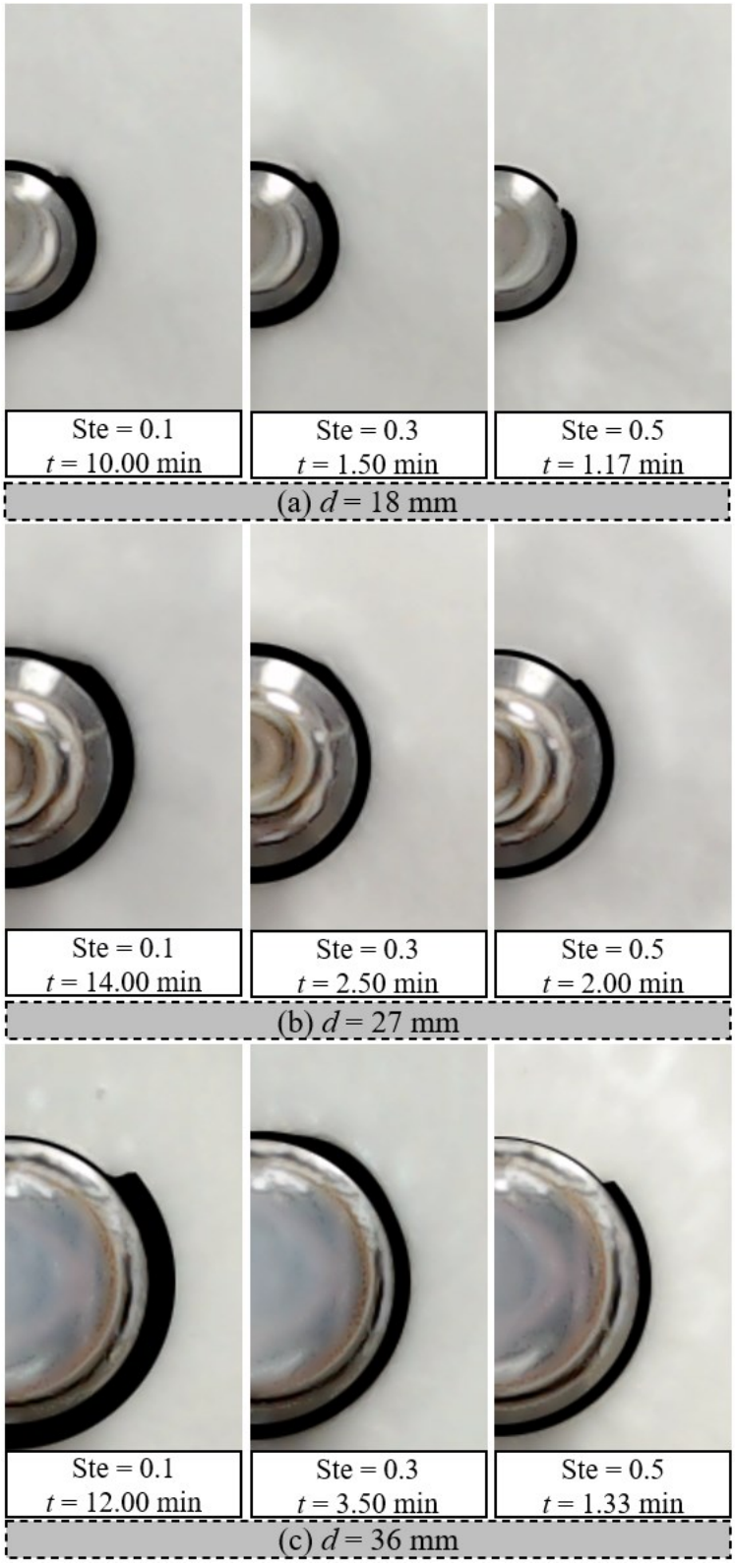

Figure 5.10 Melt profiles at the onset of natural convection for ΔT_s = 2.5 °C.

Bubble formation was observed during melting of dodecanoic acid in a rectangular enclosure by Jevnikar (2018), *n*-eicosane in a vertical cylindrical enclosure by Jones *et al.* (2006), and RT21 in an array of vertical cylindrical enclosures by Rosario (2018). Jevnikar (2018) stated that the dissolved gas in the solid dodecanoic acid came out as bubbles upon melting of the PCM. Jones *et al.* (2006) claimed the presence of bubbles in liquid *n*-eicosane is due to the different solubility of gases in the solid and liquid *n*-eicosane. They asserted that the dissolved gas nucleates at the solid-liquid interface upon melting of the PCM. Rosario (2018) mentioned that bubbles form because of the change in density and pressure of the PCM upon change of its phase. It was mentioned that during solidification of the PCM, the bubble would form from the reduction of PCM volume. It was also asserted that bubbles were more prone to form between the solid PCM and surface of the enclosure because of low adhesive force between them. The bubble formation in the present study deserves an explanation, and a discussion of the solidification process is well warranted in this context.

Before describing the solidification process, it is worthy of mentioning that bubble formation was observed under all operating conditions and for both PCMs in the present study. However, bubbles were not so pronounced during melting of *n*-octadecane under substantial subcooling to create asymmetry in the solid-liquid interface. This can be seen in the melt profiles presented in subsection 5.1.1. Now, a thorough description of the solidification process in the present study may give some insight into why a significant amount of bubbles form only during melting of *n*-octadecane when it is barely subcooled.

Regardless of the PCM and operating and geometric conditions, liquid PCM was solidified at 7 °C. The PCM was solidified from the center-tube and the two axial faces simultaneously. It should be recalled that the center-tubes were made of stainless steel, and the partition walls of the axial faces were made of Plexiglass. The materials used for them essentially means that heat transfer happens much faster in the radial direction than in the axial direction despite the much larger heat transfer area on the axial faces. Therefore, a significant amount of PCM solidified on the center-tubes before the PCM adjacent to the axial walls even reached the solidification temperature. This method of solidification would minimize the chance of air being trapped due to the shrinkage of the

liquid PCM upon solidification, at least in the amount of solid PCM that melts until the onset of convection occurs. Also, the void formation due to the weak adhesive force between the solid PCM and the container does not seem to be the case in the present study. If this was the reason, then significant bubble formation would be observed under all operating conditions. The bubble formation could be due to the presence of dissolved gas in the solid PCM. However, after performing the same experiment over and over, which required multiple solidification and melting cycles, bubble formation was still observed. For this reason, the anticipation that the presence of bubbles could be due to dissolved gas is questionable.

Now, referring back to the results presented in Fig. 5.10, the photographs clearly show that for every center-tube, more liquid PCM is required for the onset of convection when the PCM is heated at a smaller Stefan number. The longer it takes for the onset of convection as the Stefan number gets smaller. However, no such trend is observed with respect to the center-tube diameter.

5.2.2 Effects of center-tube diameter on the onset of natural convection

The volume of liquid PCM at the onset of convection, per unit length of the enclosure, was calculated from the melt profile images shown in Fig. 5.10, and the ones that are not shown (Ste = 0.2 and 0.4). These melt volumes at the onset of convection are presented in Fig. 5.11. This figure reveals a linear relationship between the onset melt volume and the size of the center-tube. A larger amount of liquid PCM is required for the onset of convection as the diameter of the center-tube increases, regardless of the Stefan number. The figure also shows that the requirement of liquid PCM volume for the onset of convection decreases if the PCM is heated at a higher Stefan number. The data presented in Fig. 5.11 were fitted by linear regression, and the relationships are shown in Table 5.6. It is seen that the diameter of the center-tubes greatly influences the onset volume requirements when the Stefan number is low. As the Stefan number increases, the influence of the center-tube diameter of the onset of convection diminishes.

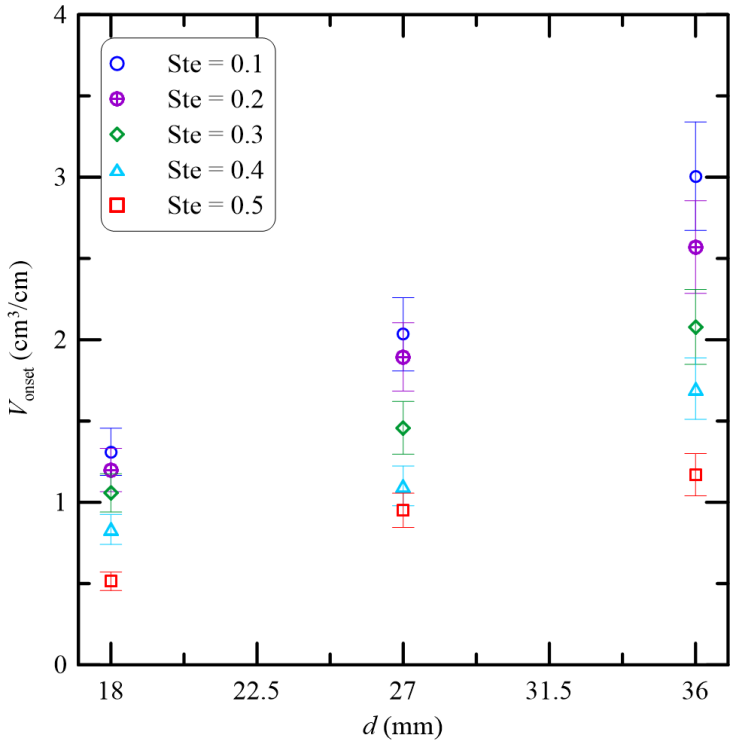

Figure 5.11 Melt volume vs the diameter of the center-tubes at the onset of convection for ΔT_s = 2.5 °C.

Table 5.6 Correlation of melt volume at the onset of convection with the diameter of the center-tubes when the PCM is subcooled by 2.5 °C.

Ste	Correlation	R^2
0.1	$V_{\text{onset}} = 0.094d - 0.428$	0.993
0.2	$V_{\text{onset}} = 0.076d - 0.170$	0.999
0.3	$V_{\text{onset}} = 0.057d$	0.985
0.4	$V_{\text{onset}} = 0.048d - 0.088$	0.954
0.5	$V_{\text{onset}} = 0.036d - 0.106$	0.965

5.2.3 Influence of Stefan number on the onset of natural convection

The melt volume results presented in Fig. 5.11 against the diameter of the center-tubes are illustrated in Fig. 5.12 against the Stefan numbers. This figure shows that the melt volume at the onset of convection varies linearly with the Stefan number. Whereas the melt volume increases with the diameter of the center-tube, high values of Stefan numbers indeed require less amount of liquid PCM for the onset of convection.

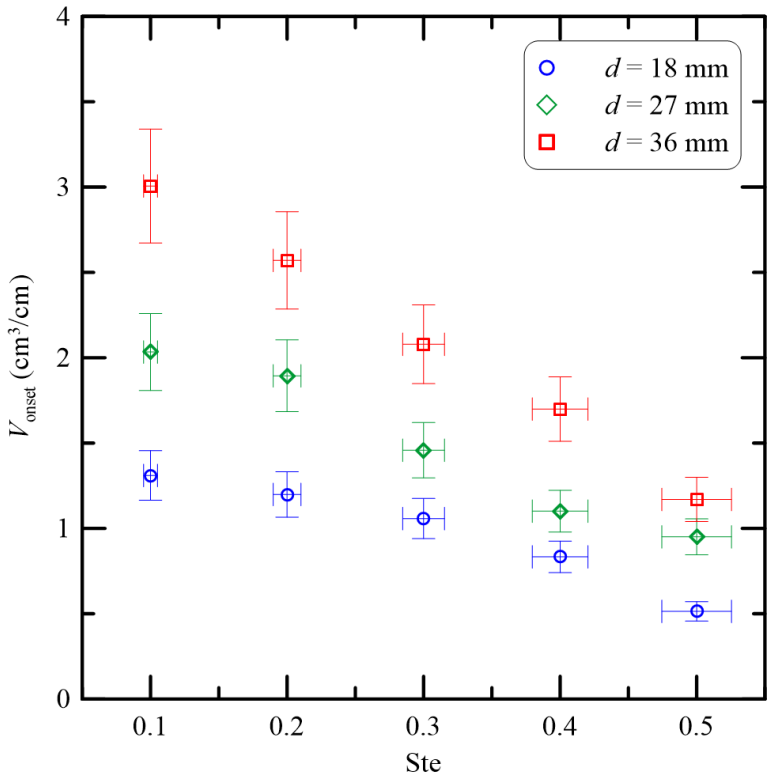

Figure 5.12 Melt volume vs Stefan number at the onset of convection for ΔT_s = 2.5 °C.

This figure also shows that a large amount of liquid PCM is necessary for the onset of convection when a bigger center-tube is used as the heating surface, as was seen in Fig. 5.11. Although it can be seen qualitatively that the influence of Stefan number on the onset of convection weakens when a smaller center-tube is used, the figure does not offer any quantitative measurement. The data were fitted by linear regression to identify the dependence of onset volume on the Stefan number. The fitted equations are presented in Table 5.7. It is seen that Stefan number plays a more significant role in the onset of convection when the center-tube is large. This trend complements the trend discussed in subsection 5.1.2, *i.e.*, the influence of center-tube diameter on the onset of natural convection diminishes as the Stefan number increases. As known, natural convection onset occurs due to the presence of temperature gradient within unstable liquid PCM layers under the action of the gravitational force. While a larger size of the center-tube increases the heat transfer surface area, Stefan number is the primary driving force for melting that results in a larger gradient in the temperature of the PCM. Moreover, the Stefan number plays a superior role to the center-tube diameter of the enclosures in the melting of PCM,

at least at the beginning of the melting process. As seen in Fig. 5.13, for the first 30 minutes of melting, the center-tube diameters play a significant role in the melting of the PCM only at high Stefan numbers.

Table 5.7 Correlation of melt volume at the onset of convection with Stefan number when the PCM is subcooled by 2.5 °C.

d (mm)	Correlation	R^2
18	$V_{onset} = -1.958\text{Ste} + 1.57$	0.954
27	$V_{onset} = -2.96\text{Ste} + 2.38$	0.971
36	$V_{onset} = -4.54\text{Ste} + 3.46$	0.998

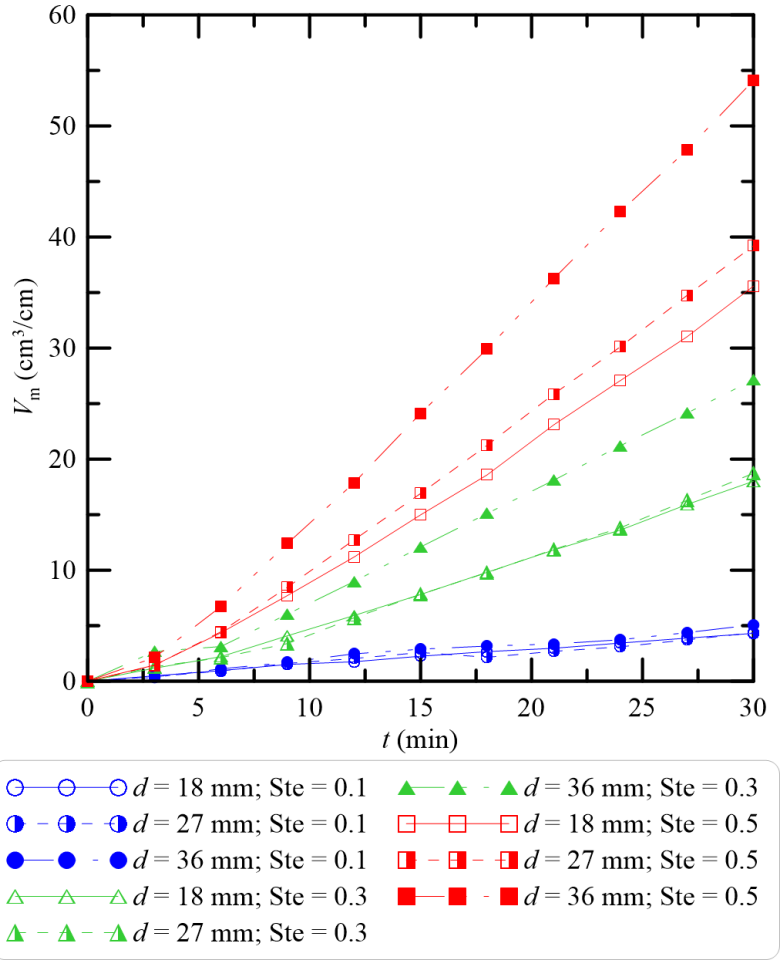

Figure 5.13 Melt volume in the early stage of the melting process for ΔT_s = 2.5 °C.

5.3 Melt thickness at the onset of convection

As seen already, the melt volume at the onset of convection increases with the diameter of the center-tube of the enclosures regardless of the experimental conditions. This is likely due to the increased perimeters of the center-tubes. The melt thicknesses, calculated using Eq. (5.1), are presented against the diameters of the center-tubes in Fig. 5.14.

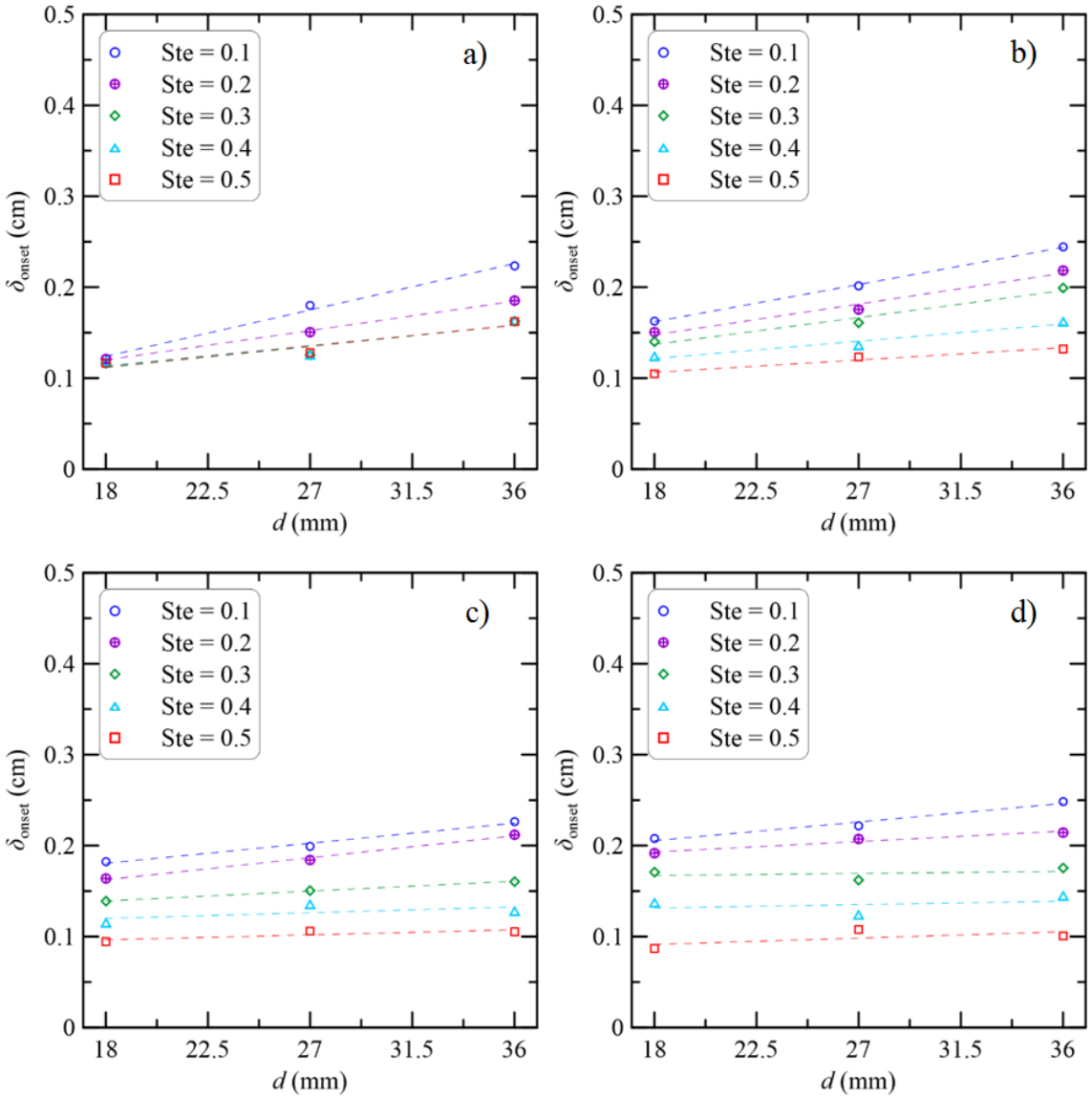

Figure 5.14 Melt thickness at the onset of convection during melting of *n*-octadecane initially subcooled by a) 22.5 °C, b) 15 °C, c) 7.5 °C, and d) 2.5 °C.

$$\delta_{\text{onset}} = \frac{1}{2}\left(\sqrt{d^2 + \frac{4}{\pi}V_{\text{onset}}} - d\right) \tag{5.1}$$

It is seen that the melt thickness remains nearly the same as the diameter of the center-tube increases when the PCM is barely subcooled. As the PCM is subcooled more substantially, the melt thickness starts to increase with the diameter of the center-tube, especially at low Stefan numbers. As has been previously discussed, in the subcooled cases, some of the applied heat transfers to the solid PCM through the solid-liquid interface. In addition, faster conduction through the larger center-tube diameters likely causes more uniform heating of the liquid PCM in the enclosures with large center-tube diameters. The combination of these factors likely causes more PCM to melt before the onset of natural convection in the enclosure with large diameter and substantially subcooled PCM.

5.4 Effects of Grashof number on onset melt volumes

The effects of center-tube diameter and Stefan number on onset melt volume have been discussed in sections 5.1 and 5.2. The Stefan number, defined with the melting temperature differential, and the center-tube diameter are independent of each other. However, both the melting temperature differential and the center-tube diameter appear in the definition of the Grashof number, which is defined as:

$$\text{Gr} = \frac{g\beta\Delta T_{\text{f}} d^3}{\nu^2} \tag{5.2}$$

In Eq. (5.2), g is the gravitational acceleration, ΔT_{f} is the melting temperature differential, d is the center-tube diameter and, β and ν are the thermal expansion coefficient and kinematic viscosity of the PCM.

The variation of onset melt volume with Grashof number is presented in Fig. 5.15 for all 60 experiments on *n*-octadecane. Whereas the onset melt volume was a linear function of Stefan number and center-tube diameter, it is a nonlinear function of Grashof number as given in Eq. (5.3). It is seen that a smaller amount of liquid PCM is required for the onset of convection as the Grashof number increases.

$$\frac{V_{\text{onset}}}{d^2} = \frac{3.853}{\text{Gr}^{0.257}} \tag{5.3}$$

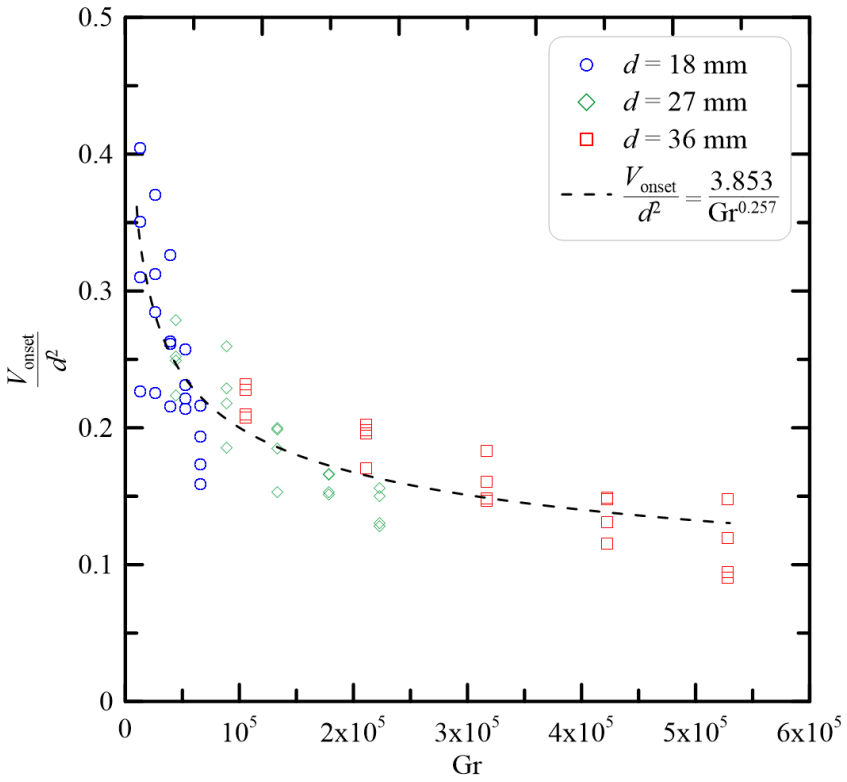

Figure 5.15 Onset melt volume as a function of Grashof number for all the experiments on *n*-octadecane.

5.5 Effects of subcooling on the onset of convection

The melt volumes at the onset of convection are presented against the subcooling temperature differentials in Fig. 5.16 for the center-tube diameter of 18 mm. The same results for the center-tube diameters of 27 and 36 mm are presented in Figs. 5.17 and 5.18, respectively. All these figures show that the onset melt volume decreases as the subcooling temperature differential increases when the Stefan number is low. For high Stefan numbers, the opposite trend is observed. The change in trend occurs gradually as the Stefan number changes from a low to high value. The reasons for these trends in onset melt volumes can be explained as follows.

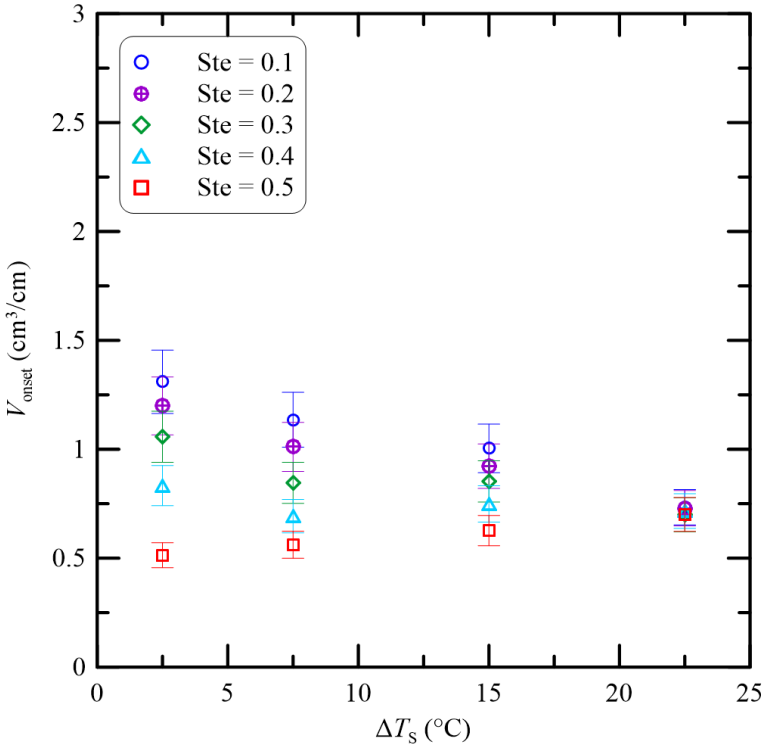

Figure 5.16 Effects of subcooling on melt volume at the onset of natural convection for the center-tube diameter of 18 mm.

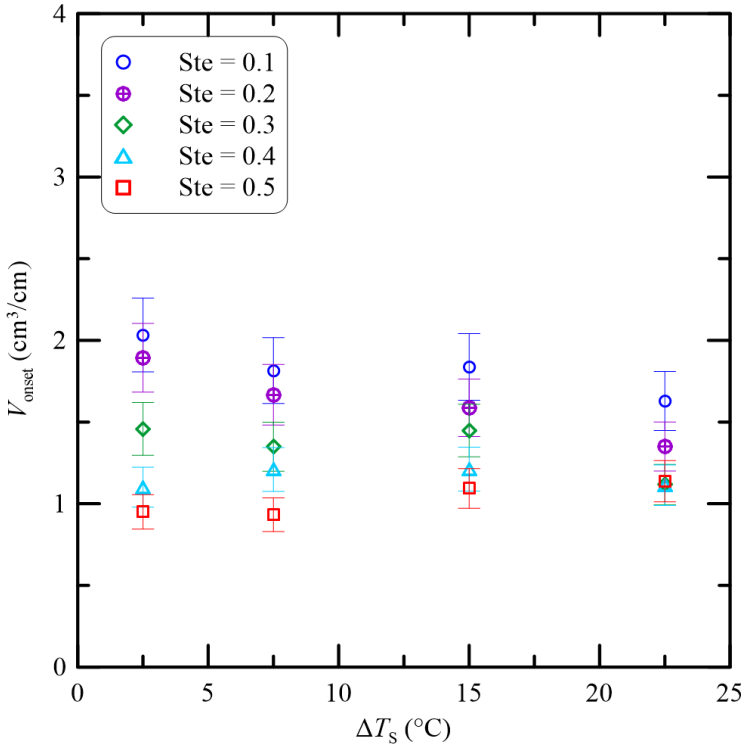

Figure 5.17 Effects of subcooling on melt volume at the onset of natural convection for the center-tube diameter of 27 mm.

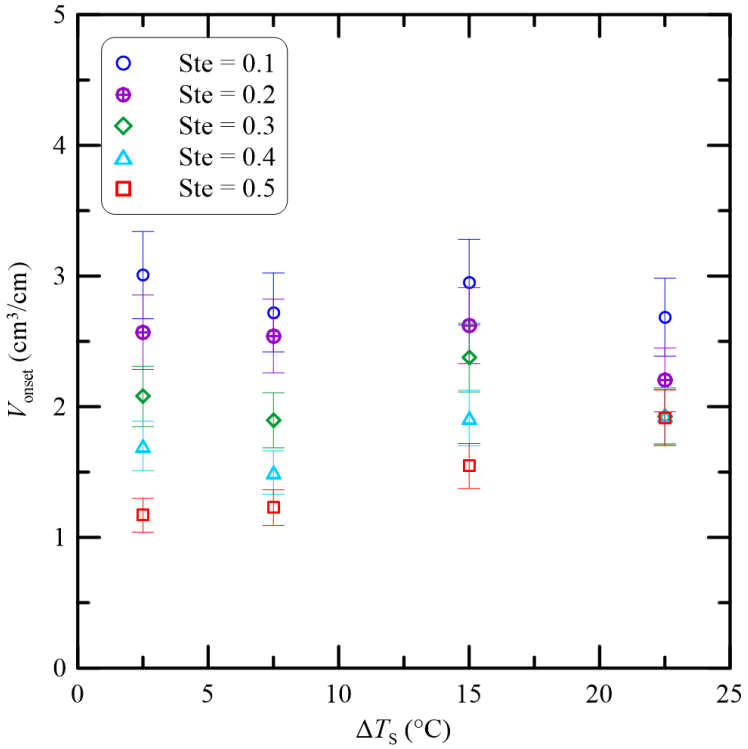

Figure 5.18 Effects of subcooling on melt volume at the onset of natural convection for the center-tube diameter of 36 mm.

It should be remembered here that the onset of convection occurs due to the presence of temperature gradient among the unstable layers of liquid PCM under the presence of gravitational force. When the buoyancy force, due to the difference in densities among unstable layers of liquid PCM, overcomes the viscous force of the liquid PCM, the movement of liquid PCM starts.

When the PCM is barely subcooled, almost no heat is taken away from the liquid PCM by the solid PCM. Further, if the PCM is heated at low temperature, the heat transfer will take place slowly. The slow heat transfer would cause somewhat uniform heating of the liquid PCM. Also, heating at low temperature would not cause a substantial decrease in viscosity of the liquid PCM. All these collectively would mean a higher volume of liquid PCM for the onset of convection. When the PCM is heated at a high temperature, on the other hand, no heat is taken away by the solid PCM from the liquid PCM; moreover, the liquid PCM is heated nonuniformly, and high temperature causes a decrease in viscosity. Ultimately, a small amount of liquid PCM is required for the onset of convection.

When the PCM is substantially subcooled, heating at a low temperature would mean most of the heat is being used to preheat the subcooled PCM, which results in a slow marching of the solid-liquid interface. This, in turn, would mean a small amount of liquid PCM at the onset of convection. On the other hand, heating at high temperature would have more heat to be conducted to the solid PCM, perhaps faster than the heat is being used to warm up the liquid PCM non-uniformly or decreasing the viscosity of liquid PCM significantly. Therefore, at high Stefan numbers, more liquid PCM is required for the onset of convection as the degree of subcooling increases.

Again, referring back to Figs. 5.16, 5.17, and 5.18, it can be seen that the change in onset melt volume with the degree of subcooling occurs at the fastest rate for center-tube diameter of 18 mm, and at the slowest rate for the center-tube diameter of 36 mm. This difference in the rate of change of onset melt volumes can be attributed to the fact that how fast or slow the heat is conducted to the subcooled solid PCM, as has already been discussed above.

5.6 Time of the onset of natural convection

The times for the onset of natural convection are presented in Fig. 5.19 for all 60 experiments on *n*-octadecane in the present study. The figure shows that the onset time is a nonlinear function of Stefan number. The onset of convection occurs faster as the Stefan number increases. Also, it takes longer for the onset of natural convection when the PCM is subcooled to a greater extent, with some exceptions. No such clear trend is observed with respect to the diameter of the center-tube. Benard *et al.* (1985) has provided a correlation for the convection onset time as given in Eq. (2.11) in the literature review section of this study. Their numerical study was on melting of *n*-octadecane, subcooled by 0.4 °C, in a vertical rectangular enclosure. For the Stefan number of 0.09, their study represents a convection onset time of 6 minutes, as calculated from Eq. (2.11). Although they used the same PCM as in the present study, their geometry and the degree of subcooling are different; the least amount of subcooling in the present study was by 2.5 °C. The comparable Stefan number from the present study is 0.1. It can be seen from Fig. 5.10 that in these conditions, the onset time varies from 10 to 14 minutes based on the diameter of the center-tubes. The onset times in the present study are larger than the one from

Benard *et al.* (1985), which is expected given the different geometry and degree of subcooling.

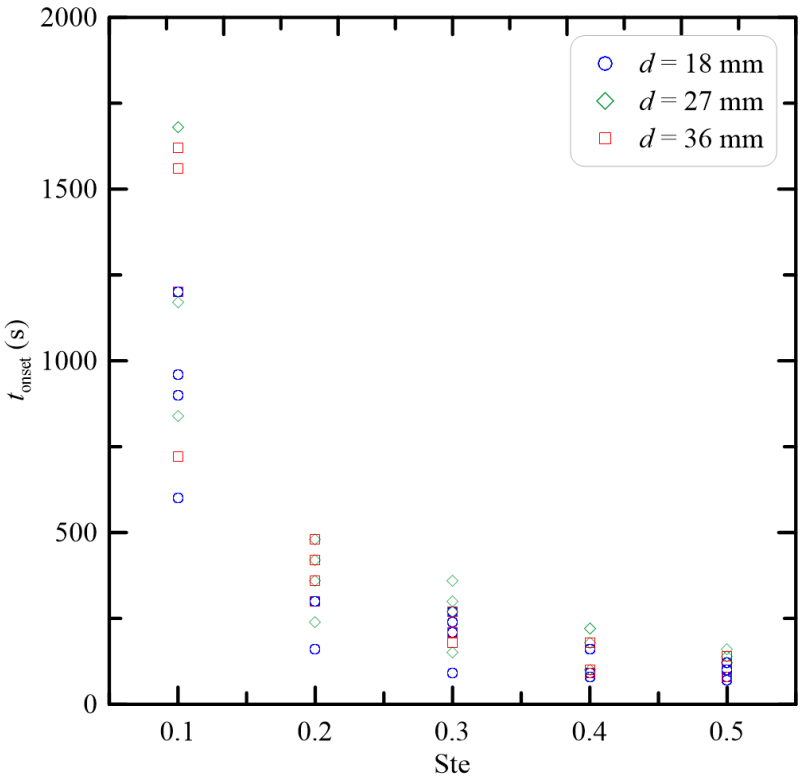

Figure 5.19 Time of the onset of natural convection for all the experiments on *n*-octadecane.

The times of the onset of convection in the enclosure with the center-tube diameter of 27 mm when the PCM is subcooled by 22.5 °C are presented in Fig. 5.20. The times of the onset of convection during melting of polyethylene glycol in a vertical rectangular enclosure under constant heat flux, studied by Wang *et al.* (1999), are also presented in Fig. 5.20 for comparison. Although the boundary conditions, the geometry, and the PCMs are different in the study of Wang *et al.* (1999), the pattern in the onset time of convection in the present study resembles theirs. Despite the similarity in the variation of onset time, it should be noted that the times for the convection onset is much higher in the study of Wang *et al.* (1999) than in the present study. The difference is likely due to the difference in the PCMs and the boundary conditions used in these studies.

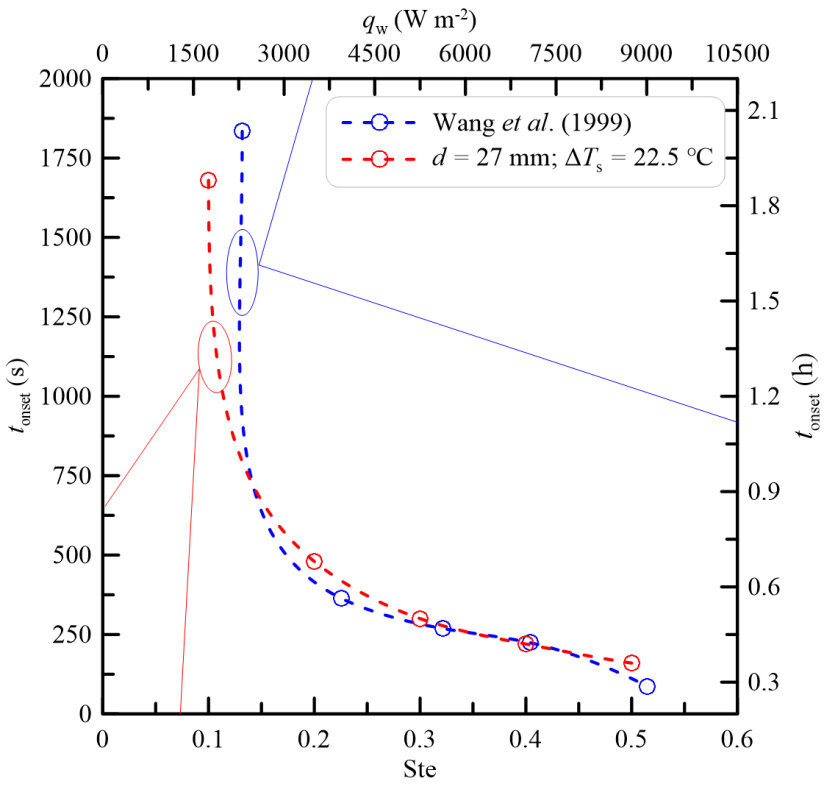

Figure 5.20 Comparison of natural convection onset time.

A more appropriate comparison is shown in Fig. 5.21. The Fourier numbers at the onset of convection in the enclosure with the center-tube diameter of 18 mm are presented. In this experiment, the degree of subcooling, calculated using Eq. (5.4), was 0.0284; and, the Fourier numbers were calculated using Eq. (5.5).

$$\mathrm{Ste}_s = \frac{c_s(T_m - T_i)}{L} \tag{5.4}$$

$$\mathrm{Fo}_{onset} = \frac{\alpha_l t_{onset}}{r^2} \tag{5.5}$$

In Eq. (5.4), c_s is the specific heat of solid PCM, L is the latent heat of fusion, T_i and T_m are the initial and melting temperatures of the PCM, respectively. In Eq. (5.5), α_l is the thermal diffusivity of liquid PCM, r is the radius of the center-tube, and t_{onset} is the elapsed time until the onset of convection.

The Fourier numbers from the study of Bathelt (1979) on melting of *n*-octadecane around a horizontal cylinder of 19 mm diameter are also included in Fig. 5.21. The study of Bathelt

(1979) was done for constant heat flux conditions on the cylinder surface, unlike the constant temperature conditions in the present study. The Fourier numbers from Bathelt (1979), calculated using Eq. (5.6), were not at the onset of convection (as defined by the first appearance of a non-concentric solid-liquid interface) but rather when the first rotating cell formed, which occurs before the onset of convection. The degree of subcooling, defined in Eq. (5.4), was 0.03 in the study of Bathelt (1979), which is comparable to the degree of subcooling of the present experiment (0.0284) shown in Fig. 5.21.

$$\mathrm{Fo_o} = \frac{\alpha_l t_o}{r^2} \tag{5.6}$$

In Eq. (5.6), t_o is the time when the first rotating cell formed in the liquid PCM.

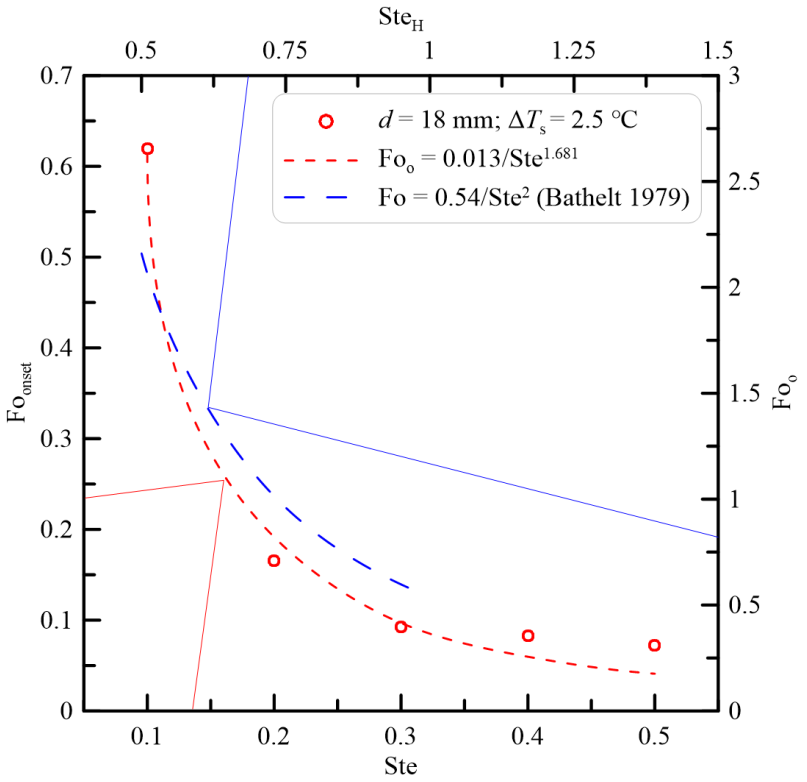

Figure 5.21 Fourier numbers at the onset of natural convection.

Figure 5.21 shows that the Fourier numbers in these studies are the same function of Stefan numbers, albeit with different coefficients and indices. These differences are attributable to the differences in the boundary conditions; also, the fact that Fourier numbers in the study of Bathelt (1979) are at instants slightly before the onset of convection.

Bathelt (1979), in his PhD thesis, also studied melting under constant surface temperature conditions. However, the PCM (*n*-heptadecane), size of the center-tube (25 mm), and degree of subcooling (0.0025) are different from the study with constant heat flux conditions. While this study is for a different PCM, the boundary conditions are the same as in the present study. Moreover, the diameter of the cylinder (25 mm) is comparable to the center-tube diameter of 27 mm in the present study. However, the Fourier numbers from this study of Bathelt (1979) are not available to compare against the ones presented in Fig. 5.21.

For both the studies under constant temperature and constant heat flux boundary conditions, Bathelt (1979) identified the conditions for the onset of natural convection. In his experiments under constant heat flux boundary conditions on *n*-octadecane, he used heat fluxes that led to the Stefan numbers of 0.461, 0.500, 0.608, 0.755, 0.876, and 0.996. The Stefan number was defined as:

$$\mathrm{Ste}_{\mathrm{H}} = \frac{c_{\mathrm{l}} q_{\mathrm{w}} r}{k\, L} \tag{5.7}$$

In Eq. (5.7), k is the thermal conductivity, c_{l} is the specific heat of liquid PCM, L is the latent heat of fusion, r is the radius of the cylinder, and q_{w} is the heat flux.

For each applied heat flux, the temperatures on the cylinder wall were measured, which were used to calculate the Stefan number based on Eq. (5.8). This Stefan number and the Fourier number, calculated using Eq. (5.9), were used to calculate the dimensionless time as given in Eq. (5.10). It was concluded that the dimensionless time for the onset of convection in the case of constant heat flux boundary conditions was 0.132.

$$\mathrm{Ste} = \frac{c_{\mathrm{l}}(T_{\mathrm{w}} - T_{\mathrm{m}})}{L} \tag{5.8}$$

$$\mathrm{Fo}_{\mathrm{onset}} = \frac{\alpha_{\mathrm{l}} t_{\mathrm{onset}}}{r^2} \tag{5.9}$$

$$\tau_{\mathrm{onset}} = \mathrm{Ste}.\,\mathrm{Fo}_{\mathrm{onset}} \tag{5.10}$$

In Eqs. (5.8) and (5.9), T_w is the wall temperature of the cylinder and t_{onset} is the convection onset time.

On the other hand, in the study of melting of *n*-heptadecane surrounding a horizontal cylinder of 25 mm diameter under constant surface temperature boundary conditions, the Stefan numbers calculated using Eq. (5.8) were 0.157 and 0.273. The degree of subcooling, calculated using Eq. (5.4), was 0.0025. He concluded that the solid-liquid interface first departed from the concentric shape when the dimensionless time was 0.0255.

It is seen that the convection onset times are different for the two cases. These two cases are different in their boundary conditions, size of the cylinder, degree of subcooling, and the PCMs being used. The results of the present study should be compared to those of *n*-heptadecane of Bathelt (1979). This is because the boundary conditions in these experiments are similar. Of all the center-tubes used in the present study, the one with the diameter of 27 mm is most comparable to the cylinder of 25 mm diameter in the study of Bathelt (1979). The Fourier numbers against the Stefan number for the center-tube diameter of 27 mm are presented in Fig. 5.22. As seen, the experimental data can be represented by the function:

$$\mathrm{Fo}_{onset} = \frac{0.01}{\mathrm{Ste}^{1.584}} \tag{5.11}$$

Insertion of Stefan numbers of 0.157 and 0.273 from the study of Bathelt (1979) into Eq. (5.11) results in the onset Fourier numbers of 0.1878 and 0.0782. These onset Fourier numbers yield to two dimensionless times of 0.0295 and 0.0213, respectively. These numbers are 15.6% and 16.5% off, respectively, from the onset condition (a dimensionless time of 0.0255) identified by Bathelt (1979). These differences are expected considering the difference in diameters of the center-tubes and PCMs used in these studies. That said, the Stefan number of 0.1 yields to a dimensionless time of 0.0384. This large difference essentially stems from the nonlinear increase in Fourier numbers at a very low Stefan number (see Fig. 5.22). Moreover, Eq. (5.11) does not hold for other center-tube diameters and subcooled cases.

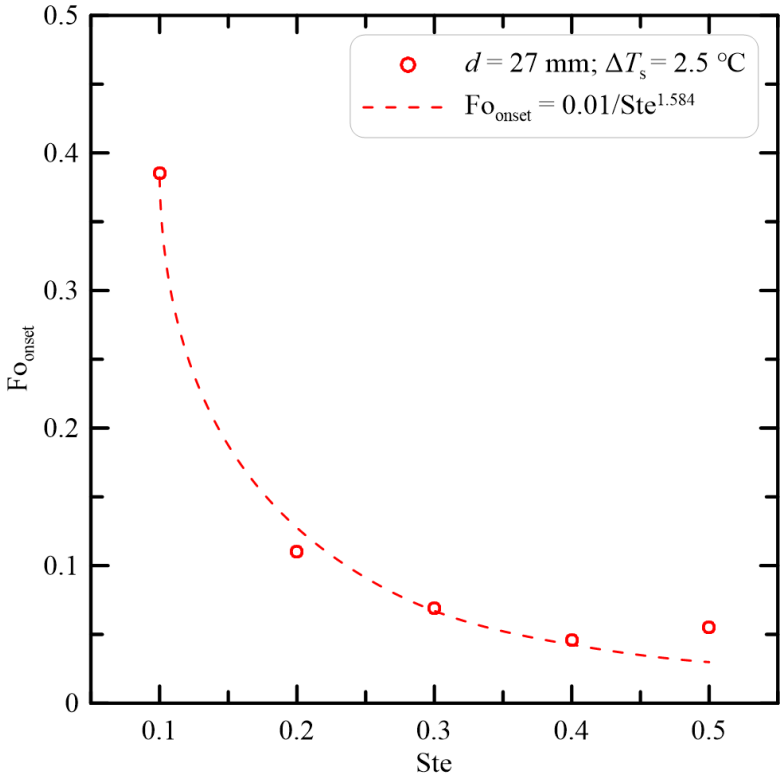

Figure 5.22 Fourier numbers at the onset of convection during melting of *n*-octadecane in the enclosure with the center-tube diameter of 27 mm and subcooled by 2.5 °C.

A generic function that is applicable for all subcooled cases and all center-tube diameters was developed using nonlinear regression. The regression was carried out with dimensionless numbers of $\mathrm{Fo_{onset}}$, Ste, $\mathrm{Ste_s}$, and d/D, and the correlation is shown in Fig. 5.23. The function of the Fourier number at the onset of convection is given by Eq. (5.12).

$$\mathrm{Fo_{onset}} = \frac{\mathrm{Ste_s^{0.2807}} \left(\frac{d}{D}\right)^{0.8551}}{96.68\ \mathrm{Ste^{1.4499}}} - 0.0011648 \qquad (5.12)$$

In Eq. (5.12), $\mathrm{Ste_s}$ is the degree of subcooling as defined in Eq. (5.4), d and D are the diameter of the center-tube and that of the outer shell, respectively. The Fourier number in Eq. (5.12) was defined with the characteristic length of $R - r$, as in Eq. (5.13), instead of r in the other equations. Here, r and R are the radius of the center-tube and that of the outer shell. When the PCM is not subcooled in the beginning, the choice of r as the characteristic length is reasonable because barely any heat will transfer through the solid-liquid interface. However, when the PCM is initially subcooled, heat transfers through the

solid-liquid interface to preheat the subcooled PCM. Therefore, heat transfer takes place through the whole radial depth of the PCM (solid or liquid), and thus, $R - r$ would serve as the more appropriate characteristic length.

$$\mathrm{Fo}_{\mathrm{onset}} = \frac{\alpha_{\mathrm{l}} t_{\mathrm{onset}}}{(R-r)^2} \tag{5.13}$$

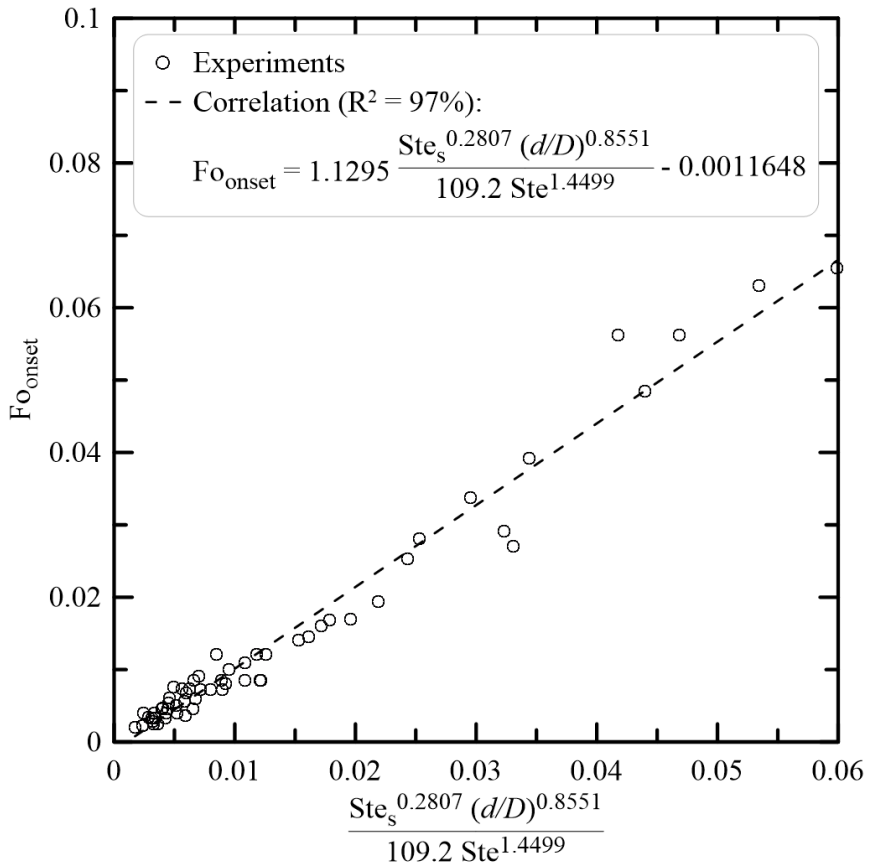

Figure 5.23 Fourier numbers at the onset of natural convection during melting of *n*-octadecane in enclosures with center-tube diameters of 18, 27, and 36 mm and ΔT_{s} = 2.5, 7.5, 15, and 22.5 °C.

5.7 Rayleigh number at the onset of convection

The Rayleigh numbers at the onset of natural convection were calculated using Eq. (5.14).

$$\mathrm{Ra}_{\mathrm{onset}} = \frac{g\beta\Delta T_{\mathrm{f}}\delta_{\mathrm{onset}}^3}{\nu\alpha_{\mathrm{l}}} \tag{5.14}$$

In Eq. (5.14), δ_{onset} is the radial thickness of liquid PCM at the onset of convection, as shown in Fig. 5.24. A mean value of this onset thickness was calculated using Eq. (5.1) rather than measuring it in an isolated location along the x or y-axes. These Rayleigh numbers are presented in Fig. 5.25. It is seen that there is no clear trend in variation of Rayleigh number with Stefan number, although a larger center-tube leads to a larger onset Rayleigh number. However, the onset Rayleigh number varies over a wide range of 251 to 3310. In the study of Bathelt (1979), the onset Rayleigh number calculated using Eq. (5.14) was less than 1700. This upper limit of the onset Rayleigh number is significantly below its highest value in the present study. It should be remembered from section 5.5 that the study of Bathelt (1979) was limited to barely subcooled PCMs, only two sizes of the heat source (one for each PCM), and a narrow range of Stefan numbers. The present study includes significantly subcooled PCMs, three sizes of the heat source, and a wider range of Stefan numbers. Therefore, the wider range of onset Rayleigh number in the present study is expected. Nonetheless, Fig. 5.25 does not provide much useful information regarding Rayleigh number at the onset of convection. It is, therefore, worthwhile to explore an appropriate definition of Rayleigh number in the context of melting of PCMs.

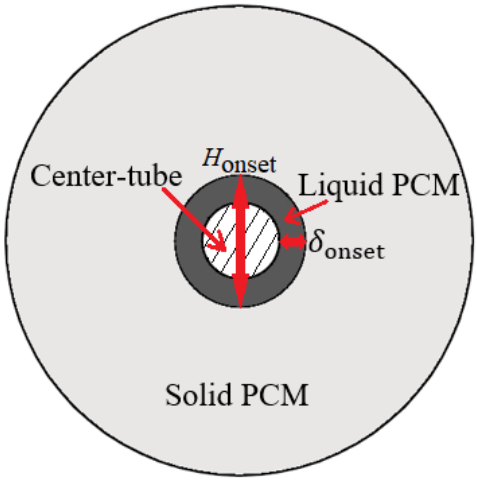

Figure 5.24 Illustration of melt thickness and the projected height of the liquid PCM column at the onset of natural convection.

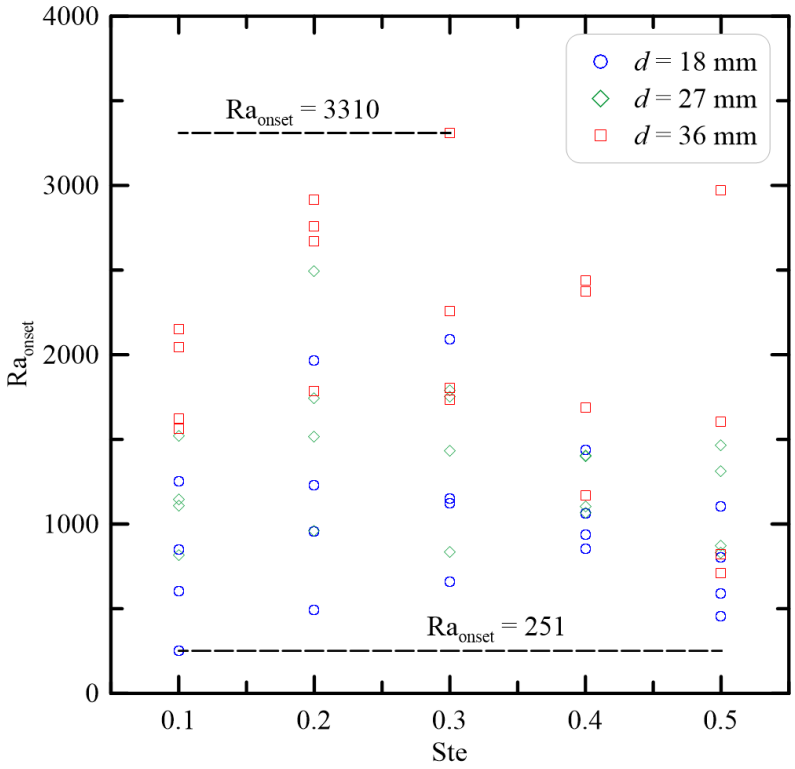

Figure 5.25 Rayleigh numbers at the onset of natural convection for all the experiments on *n*-octadecane.

As known, the Rayleigh number is associated with natural convection in fluids either confined in an enclosure or surrounding a heat source that is submerged in the fluid. In a confined single-phase fluid, the dimension of the fluid layer does not change during the heating process. Therefore, the distance between hot and cold walls is taken as the length scale in the definition of the Rayleigh number. Since natural convection occurs between the hot and cold walls, their temperature difference is taken as the temperature scale (Incropera *et al.*, 2007). When the heat source is submerged in a single-phase fluid, a convection boundary layer forms surrounding the heat source. Therefore, the height of the heat source is taken as the length scale, and the difference between temperatures at the wall of the heat source and the edge of the boundary layer is used as the temperature scale (Incropera *et al.*, 2007).

However, the PCM melting processes experience ever-changing solid-liquid interfaces, and thus, an ever-changing amount of liquid PCM. This poses a challenge in defining the Rayleigh number with a constant length scale. Therefore, the choice of *d* as length scale

in the definition of Rayleigh number is perhaps not appropriate in the context of melting of PCMs in annular enclosures. Alternatively, δ_{onset} does not represent the entire span of the liquid PCM. A length scale that resembles the length scale in single-phase fluid would be a transient one defined as:

$$H_{\text{onset}} = d + 2\delta_{\text{onset}} \tag{5.15}$$

In Eq. (5.15), H_{onset} is the height of the liquid column projected on the vertical central plane, as shown in Fig. 5.24.

Since there is no convection boundary layer surrounding the center-tube until natural convection onset occurs, the difference in the temperature of the center-tube and the melting temperature of the PCM would be an appropriate temperature scale. These length scale and temperature scale were used to define a new onset Rayleigh number as in Eq. (5.16).

$$\text{Ra}_{\text{onset}} = \frac{g\beta\Delta T_{\text{f}} H_{\text{onset}}^3}{\nu\alpha_{\text{l}}} \tag{5.16}$$

This onset Rayleigh number, calculated using Eq. (5.16), is presented against the dimensionless numbers of Ste, Ste_{s}, and *d/D* in Fig. 5.26. This figure shows that the onset Rayleigh number is a nonlinear function of the dimensionless variables on the horizontal axis. The function is given as:

$$\text{Ra}_{\text{onset}} = \frac{10^{9.38}\,\text{Ste}^{0.8919}\left(\frac{d}{D}\right)^{2.7891}}{\text{Ste}_{\text{s}}^{0.0181}} - 15212 \tag{5.17}$$

The intercept in Eq. (5.17) is insignificant compared to the values of the Rayleigh number in Fig. 5.26 and, therefore, neglecting it, the equation for the onset Rayleigh number can be written as given in Eq. (5.18).

$$\text{Ra}_{\text{onset}} = \frac{10^{9.38}\,\text{Ste}^{0.8919}\left(\frac{d}{D}\right)^{2.7891}}{\text{Ste}_{\text{s}}^{0.0181}} \tag{5.18}$$

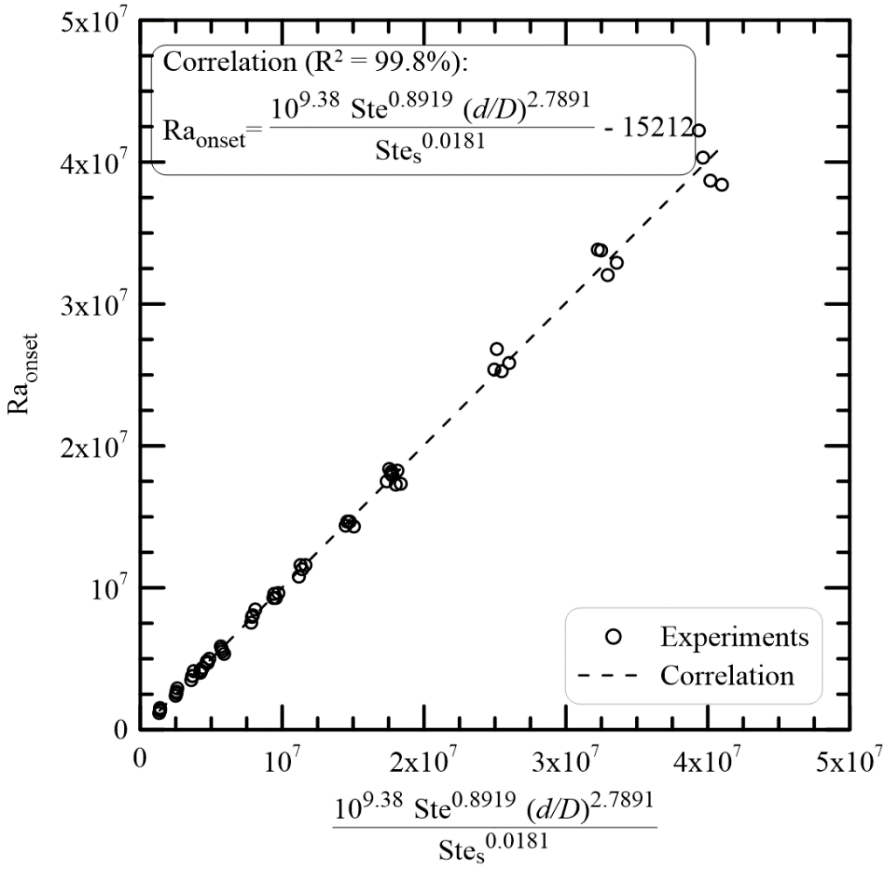

Figure 5.26 Rayleigh numbers at the onset of natural convection during melting of *n*-octadecane under all experimental conditions considered in the present study.

5.8 Conclusions

A few conclusions can be drawn from the results presented in this chapter. In general, more liquid PCM is required for the onset of convection when the PCM is heated at low temperatures. Also, more liquid PCM is required for the onset of convection if the center-tube is large.

It was observed that the onset of convection occurs faster if the PCM is heated at a higher temperature. This observation complements the observation of Wang *et al.* (1999), who observed that the onset of convection occurred faster as the heat flux applied to the vertical side of a rectangular enclosure increased. That said, no clear trend is observed in the present study for the onset time as the diameter of the center-tube, and the subcooling temperature changed. The onset time reduced nonlinearly as the Stefan number increased.

It was also observed that the subcooling of the PCM played a significant role in the onset of convection. When the PCM was barely subcooled, the Stefan number influenced the onset of convection to a greater extent than when the PCM was substantially subcooled.

A correlation was developed for the Fourier number at the onset of convection that could be used to predict the convection onset time for melting of *n*-octadecane in enclosures with different center-tube diameters and the PCM being from barely to substantially subcooled.

Also, a correlation was developed for the onset Rayleigh number that could be used to predict the volume of liquid PCM at the onset of convection, regardless of the size of the center-tube and the degree of subcooling.

CHAPTER 6 MELTING OF DODECANOIC ACID

The results for the onset of natural convection during melting of dodecanoic acid are presented in this chapter. As mentioned in Chapter 3, the melting of dodecanoic acid was studied for the melting temperature differentials of 8.44, 25.3, and 42.2 °C. These melting temperature differentials correspond to Stefan numbers of 0.09, 0.27, and 0.46, respectively. The PCM was subcooled by 2.5, 7.5, 15, and 22.5 °C. Melt profiles at the onset of convection, the effects of center-tube diameter, Stefan number, Grashof number, and PCM-subcooling on the onset of natural convection are presented. Also, the correlations for the Fourier and Rayleigh numbers at the onset of convection during melting of dodecanoic acid are presented.

6.1 Melt profiles at the onset of natural convection

The melt profiles at the onset of natural convection for the PCM initially subcooled by 22.5, 15, 7.5, and 2.5 °C are presented in Figs. 6.1 to 6.4, respectively. The photographs in these figures represent a 30 mm × 60 mm section; 30 mm to the right, 30 mm above, and 30 mm below the center of the enclosure. The reader is again reminded that the black color surrounding the center-tube represents liquid PCM and the white color represents the solid PCM.

The photographs clearly show that for every center-tube and subcooled case, more liquid PCM is required for the onset of convection when the PCM is heated at a smaller Stefan number. Regardless of the size of the center-tubes and the subcooling conditions, a comparison of Figs. 6.1 – 6.4 shows that the onset of convection occurs slower at smaller Stefan numbers. It is noteworthy that although the convection onset occurs slower at smaller Stefan numbers, no such trend is observed with respect to the center-tube diameter or the degree of subcooling. These results are comparable to the ones for *n*-octadecane, except when the PCM is subcooled by 22.5 °C. In this case, the onset melt volume becomes independent of Stefan number during the meting of *n*-octadecane but not dodecanoic acid when the center-tube is small.

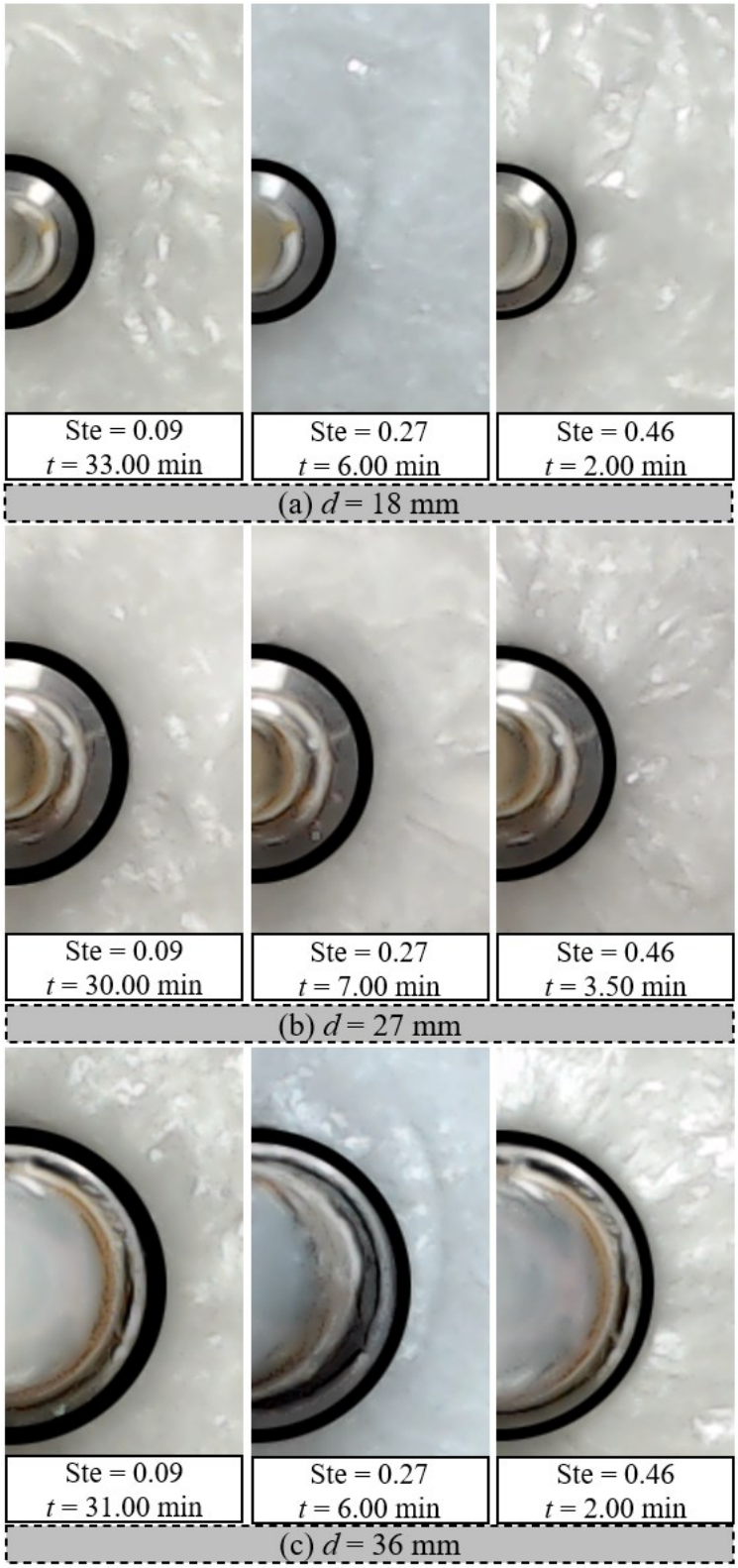

Figure 6.1 Melt profiles at the onset of natural convection for ΔT_s = 22.5 °C.

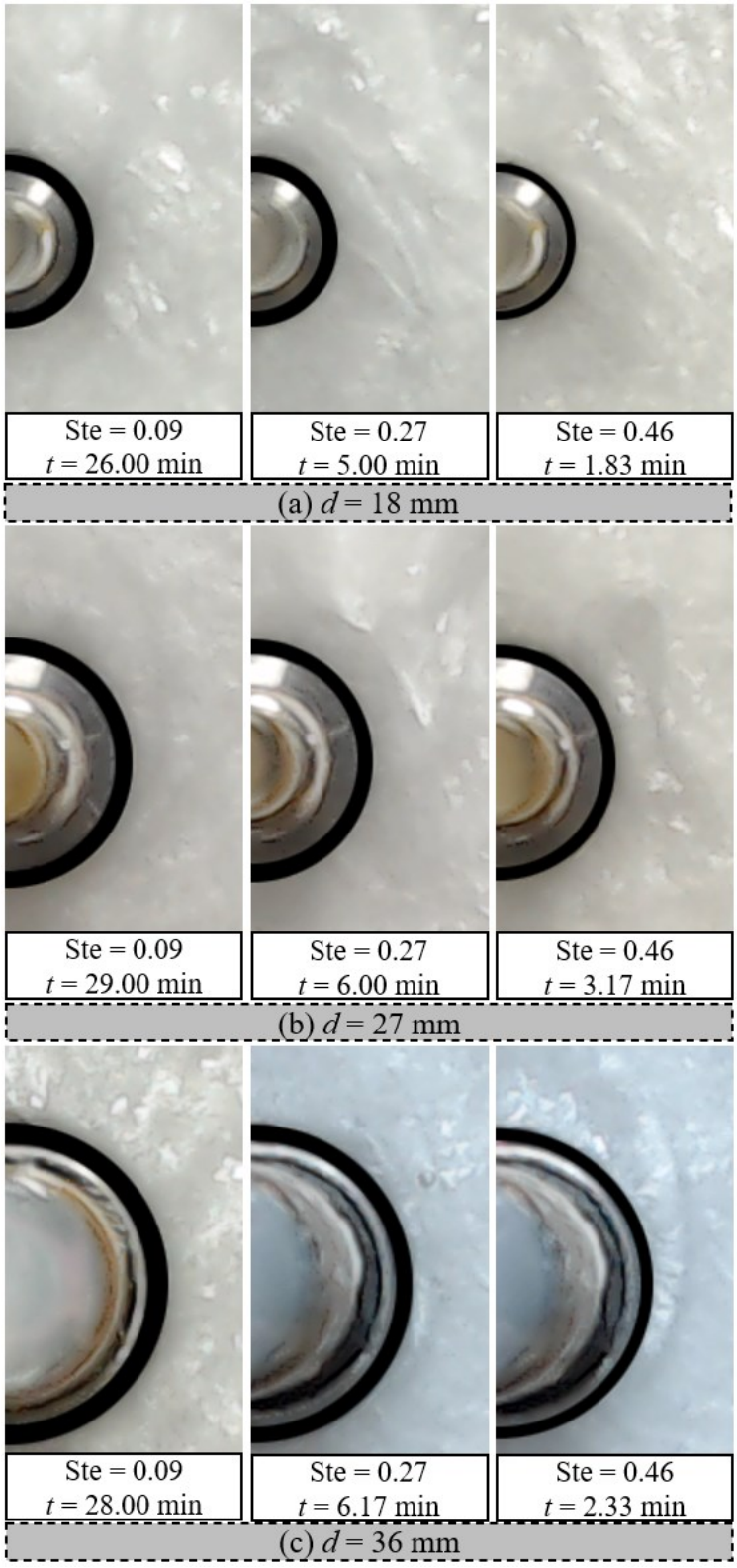

Figure 6.2 Melt profiles at the onset of natural convection for ΔT_s = 15 °C.

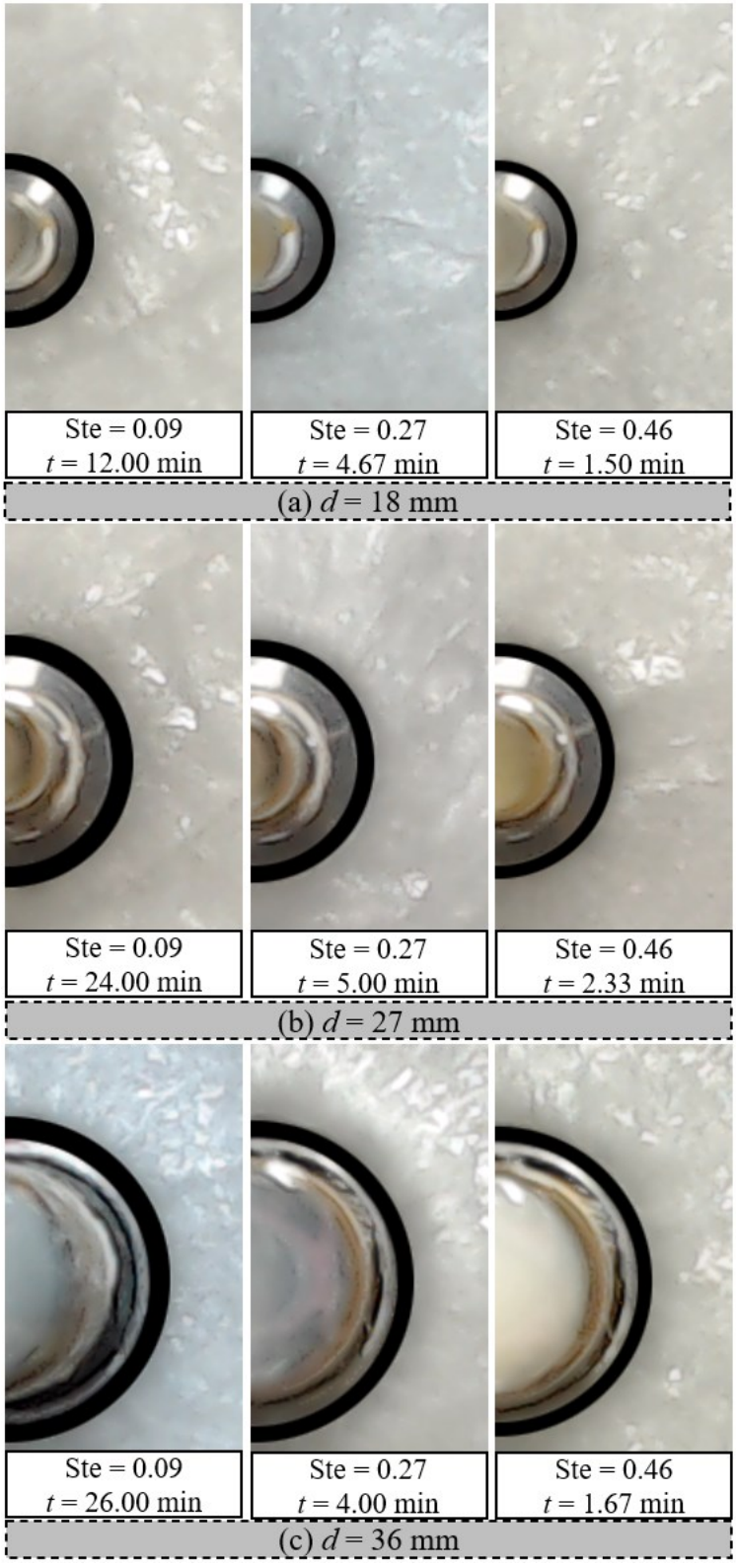

Figure 6.3 Melt profiles at the onset of natural convection for ΔT_s = 7.5 °C.

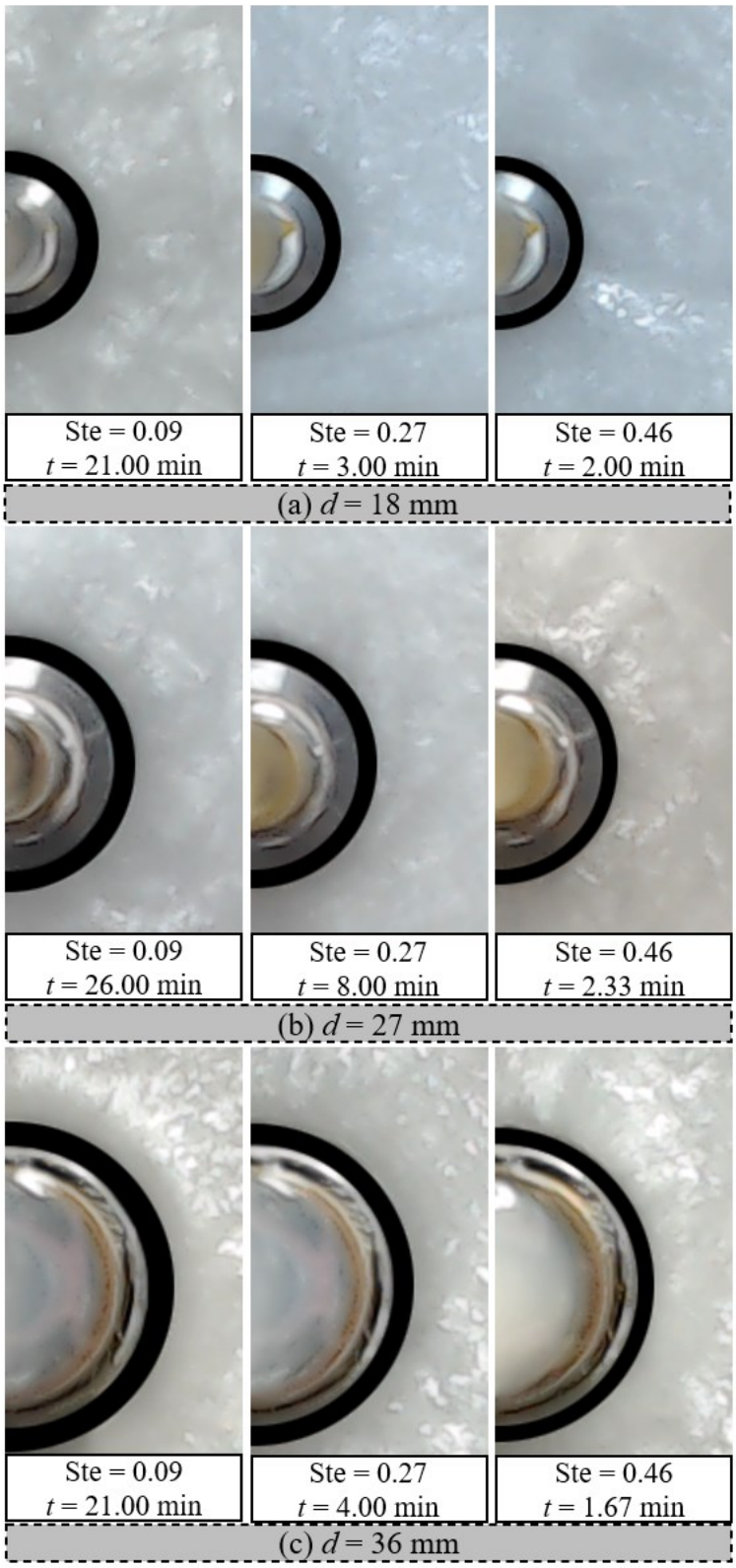

Figure 6.4 Melt profiles at the onset of natural convection for ΔT_s = 2.5 °C.

6.2 Effects of different parameters on the onset of natural convection

The effects of center-tube diameter, Stefan number, and subcooling of the PCM are discussed in this section.

6.2.1 Effects of center-tube diameter on the onset of natural convection

The melt volumes, per unit length of the enclosure, at the onset of convection for the PCM initially subcooled by 22.5, 15, 7.5, and 2.5 °C are presented in Figs. 6.5 to 6.8, respectively. The volumes of liquid PCM at the onset of convection were calculated for the respective subcooled conditions from the melt profile images shown in Figs. 6.1−6.4. Figures 6.5−6.8 show a linear relationship between the onset melt volumes and the size of the center-tubes. A larger amount of liquid PCM is required for the onset of convection as the diameter of the center-tube increases, regardless of the Stefan number and the degree of subcooling. The melt volume data presented in these figures were fitted to linear correlations. These correlations are shown in Tables 6.1 to 6.4, respectively, for the PCM subcooled by 22.5, 15, 7.5, and 2.5 °C. It is seen that the diameter of the center-tubes greatly influences the required onset volume when the Stefan number is low. As the Stefan number increases, the influence of the center-tube diameter on the onset of convection weakens. A comparison of Tables 6.1− 6.4 shows that the influence of the center-tube on the onset volume reduces as the degree of subcooling decreases, as can be seen by the value of the slopes for these correlations.

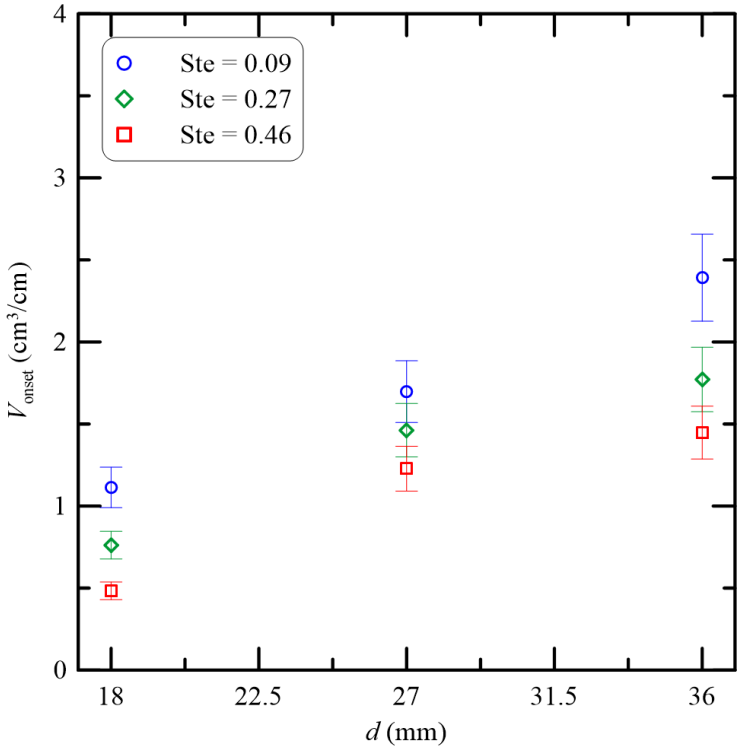

Figure 6.5 Melt volume vs the diameter of the center-tubes at the onset of convection for ΔT_s = 22.5 °C.

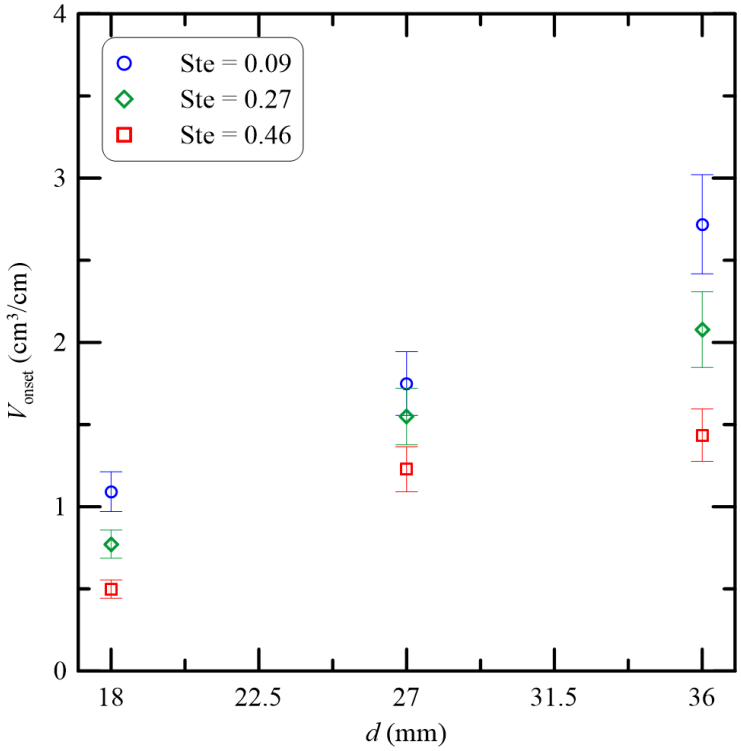

Figure 6.6 Melt volume vs the diameter of the center-tubes at the onset of convection for ΔT_s = 15 °C.

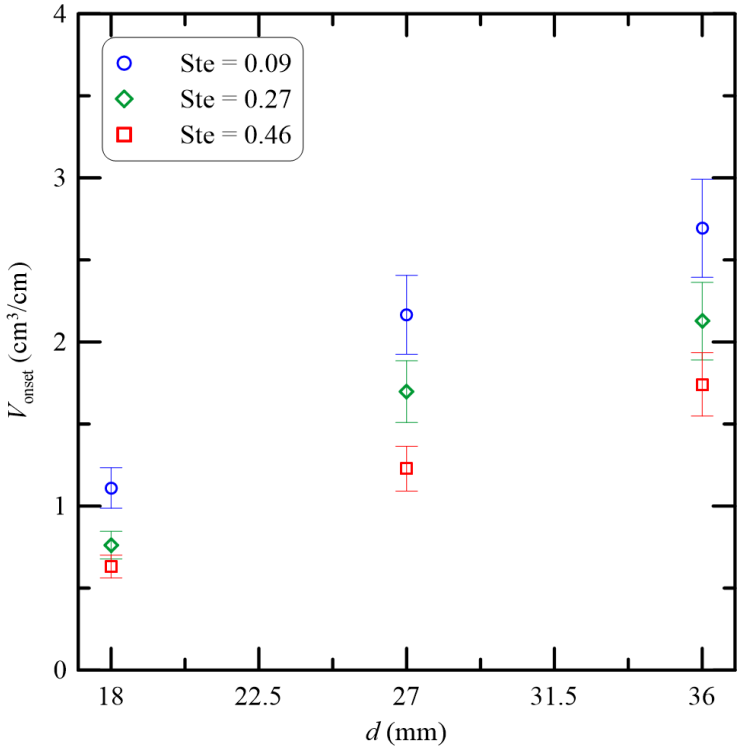

Figure 6.7 Melt volume vs the diameter of the center-tubes at the onset of convection for ΔT_s = 7.5 °C.

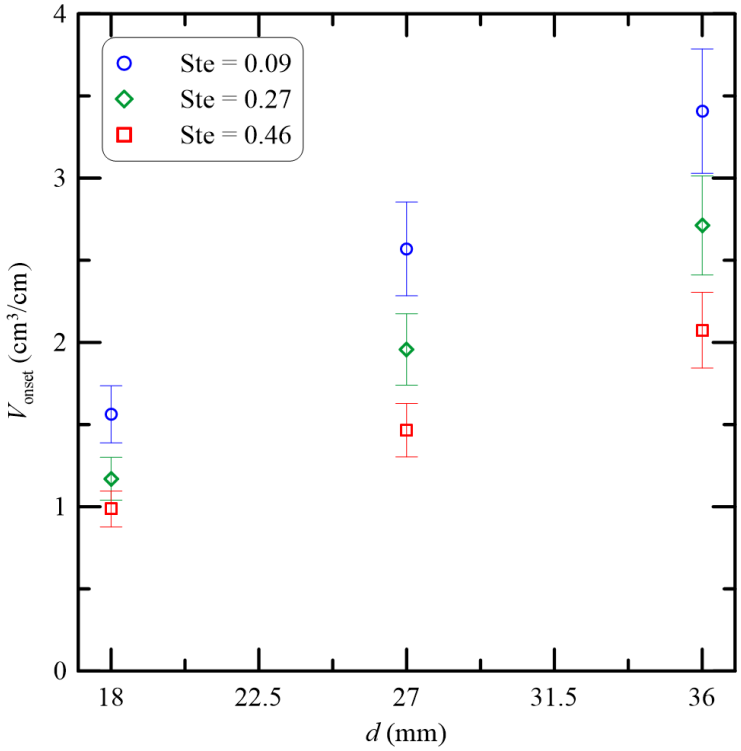

Figure 6.8 Melt volume vs the diameter of the center-tubes at the onset of convection for ΔT_s = 2.5 °C.

Table 6.1 Correlation of melt volume at the onset of convection with diameter of the center-tubes when the PCM is subcooled by 22.5 °C.

Ste	Correlation	R^2
0.1	$V_{\text{onset}} = 0.071d - 0.184$	0.998
0.3	$V_{\text{onset}} = 0.056d - 0.182$	0.952
0.5	$V_{\text{onset}} = 0.054d - 0.393$	0.910

Table 6.2 Correlation of melt volume at the onset of convection with the diameter of the center-tubes when the PCM is subcooled by 15 °C.

Ste	Correlation	R^2
0.1	$V_{\text{onset}} = 0.090d - 0.588$	0.988
0.3	$V_{\text{onset}} = 0.073d - 0.492$	0.988
0.5	$V_{\text{onset}} = 0.052d - 0.351$	0.907

Table 6.3 Correlation of melt volume at the onset of convection with the diameter of the center-tubes when the PCM is subcooled by 7.5 °C.

Ste	Correlation	R^2
0.1	$V_{\text{onset}} = 0.088d - 0.384$	0.964
0.3	$V_{\text{onset}} = 0.076d - 0.519$	0.956
0.5	$V_{\text{onset}} = 0.062d - 0.466$	0.998

Table 6.4 Correlation of melt volume at the onset of convection with the diameter of the center-tubes when the PCM is subcooled by 2.5 °C.

Ste	Correlation	R^2
0.1	$V_{\text{onset}} = 0.103d - 0.255$	0.997
0.3	$V_{\text{onset}} = 0.086d - 0.366$	1.00
0.5	$V_{\text{onset}} = 0.060d - 0.124$	0.995

6.2.2 Influence of Stefan number on the onset of natural convection

The melt volumes at the onset of convection are presented against the Stefan numbers in Figs. 6.9 to 6.12, respectively, for the PCM initially subcooled by 22.5, 15, 7.5, and 2.5 °C. These figures show that a smaller amount of liquid PCM is required for the onset of convection when the Stefan number is high. Also, the melt volumes vary linearly and hence the melt volume data have been fitted to linear correlations. These correlations are presented in Tables 6.5 to 6.8, respectively, for the PCM subcooled by 22.5, 15, 7.5, and 2.5 °C. These tables show that the dependence of onset melt volumes on Stefan numbers diminishes as the diameter of the center-tubes gets smaller. These tables also show that this dependence decreases as the degree of subcooling increases. The invariance of onset melt volume on the Stefan number with the degree of subcooling is more pronounced when the center-tube diameter is smaller.

The effects of Stefan number on onset melt volumes for dodecanoic acid complement the ones for *n*-octadecane presented in Chapter 5, except for the most subcooled case ($\Delta T_s = 22.5$ °C). At the most subcooled case, the onset melt volume for the smallest center-tube diameter does not become independent of the Stefan number during melting of dodecanoic acid. This is likely because the conductive heat transfer to the subcooled solid dodecanoic acid is not as fast as that in subcooled solid *n*-octadecane, the latter having a thermal conductivity in the solid phase that is at least twice that of the former.

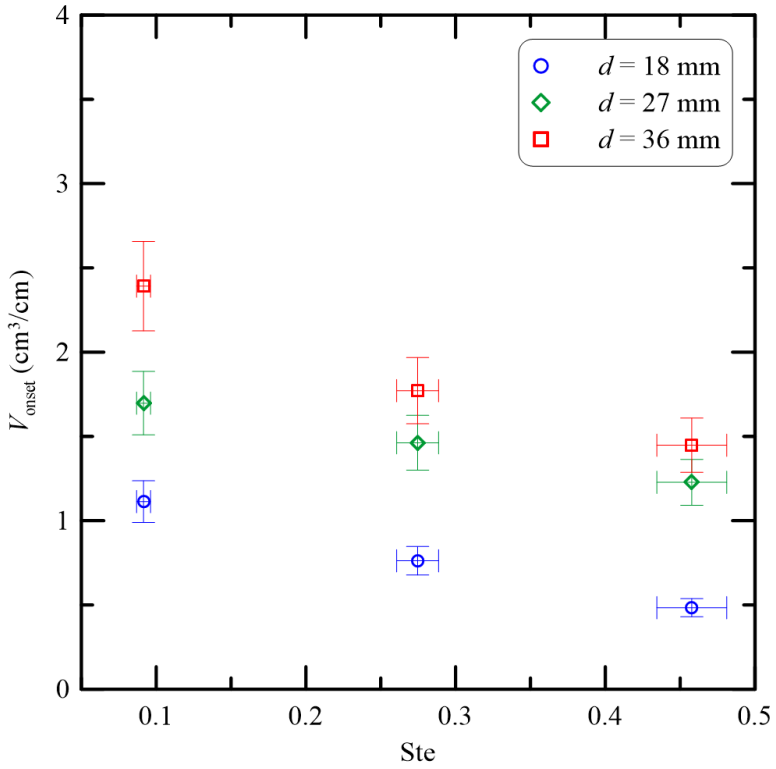

Figure 6.9 Melt volume vs Stefan number at the onset of convection for ΔT_s = 22.5 °C.

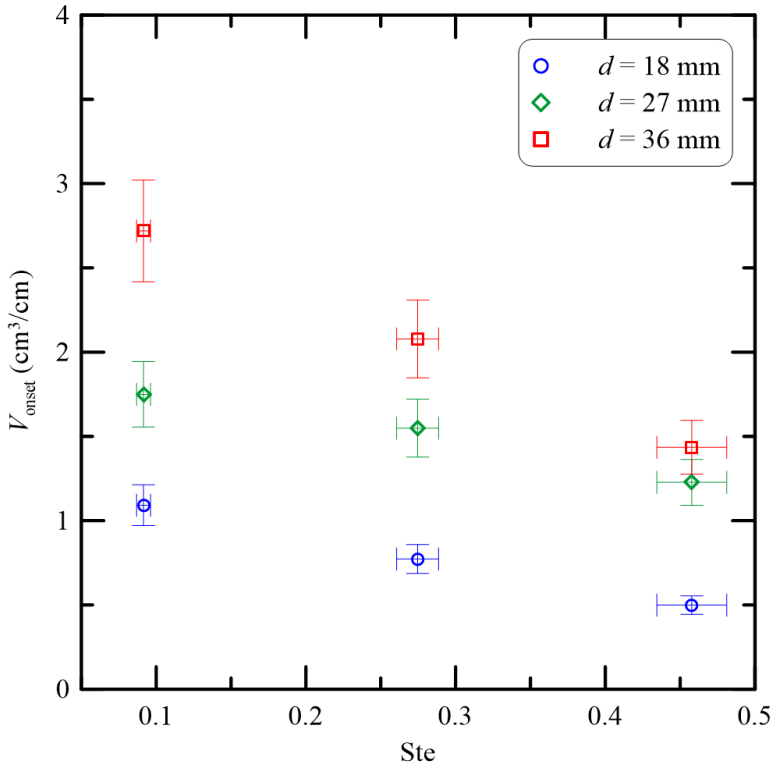

Figure 6.10 Melt volume vs Stefan number at the onset of convection for ΔT_s = 15 °C.

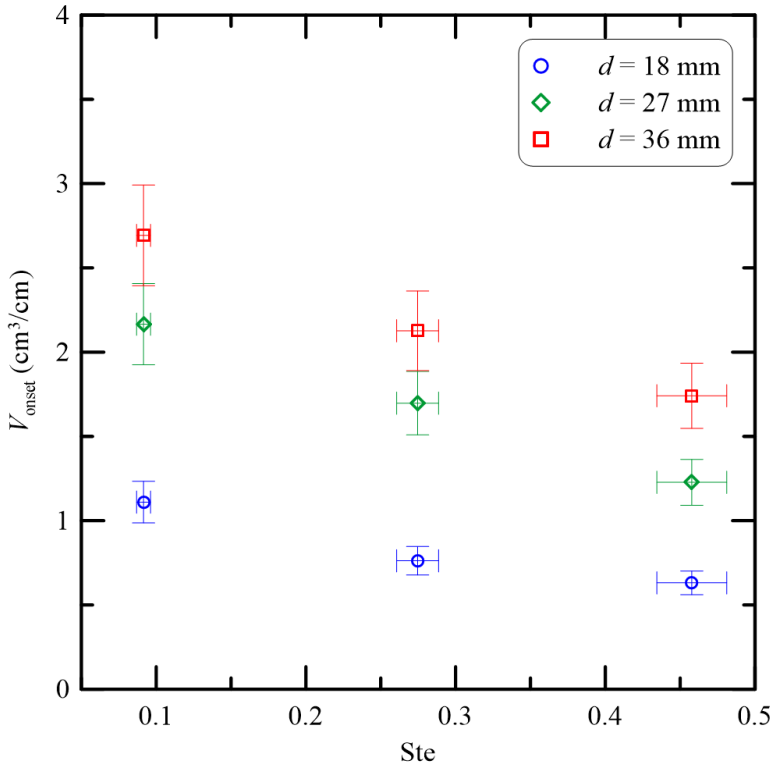

Figure 6.11 Melt volume vs Stefan number at the onset of convection for $\Delta T_s = 7.5$ °C.

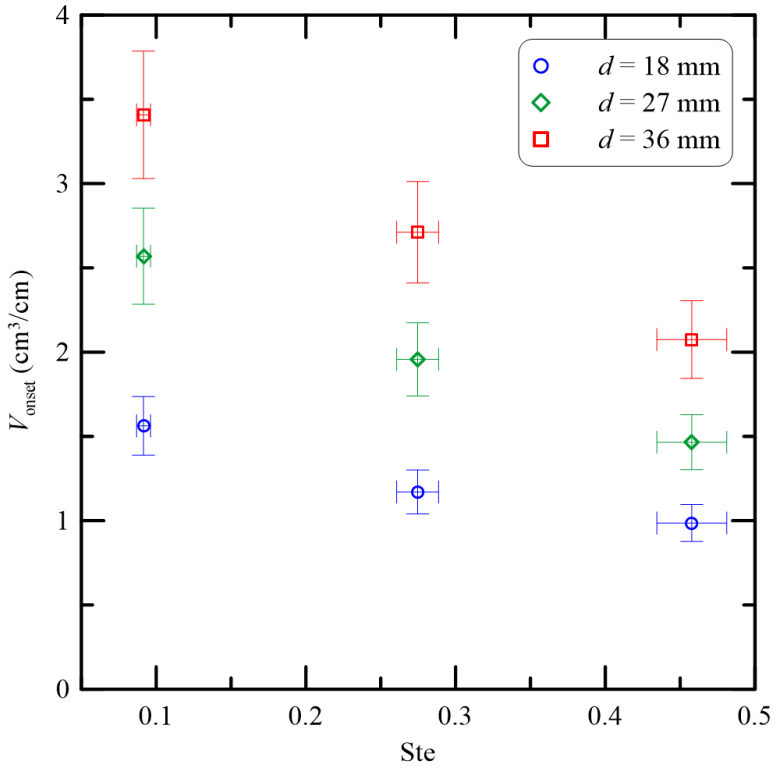

Figure 6.12 Melt volume vs Stefan number at the onset of convection for $\Delta T_s = 2.5$ °C.

Table 6.5 Correlation of melt volume at the onset of convection with Stefan number when the PCM is subcooled by 22.5 °C.

d (mm)	Correlation	R^2
18	$V_{\text{onset}} = -1.72\text{Ste} + 1.26$	0.996
27	$V_{\text{onset}} = -1.28\text{Ste} + 1.81$	1.00
36	$V_{\text{onset}} = -2.58\text{Ste} + 2.58$	0.968

Table 6.6 Correlation of melt volume at the onset of convection with Stefan number when the PCM is subcooled by 15 °C.

d (mm)	Correlation	R^2
18	$V_{\text{onset}} = -1.62\text{Ste} + 1.23$	0.998
27	$V_{\text{onset}} = -1.43\text{Ste} + 1.90$	0.982
36	$V_{\text{onset}} = -3.50\text{Ste} + 3.04$	1.00

Table 6.7 Correlation of melt volume at the onset of convection with Stefan number when the PCM is subcooled by 7.5 °C.

d (mm)	Correlation	R^2
18	$V_{\text{onset}} = -1.31\text{Ste} + 1.19$	0.936
27	$V_{\text{onset}} = -2.56\text{Ste} + 2.40$	1.00
36	$V_{\text{onset}} = -2.60\text{Ste} + 2.90$	0.988

Table 6.8 Correlation of melt volume at the onset of convection with Stefan number when the PCM is subcooled by 2.5 °C.

d (mm)	Correlation	R^2
18	$V_{\text{onset}} = -1.57\text{Ste} + 1.67$	0.958
27	$V_{\text{onset}} = -3.01\text{Ste} + 2.82$	0.996
36	$V_{\text{onset}} = -3.64\text{Ste} + 3.73$	0.999

6.3 Melt thickness at the onset of convection

The melt thicknesses were calculated from the melt profiles shown in Figs. 6.1−6.4 using Eq. (5.1) presented in Chapter 5. The melt thicknesses are shown against the diameters of the center-tubes in Fig. 6.13.

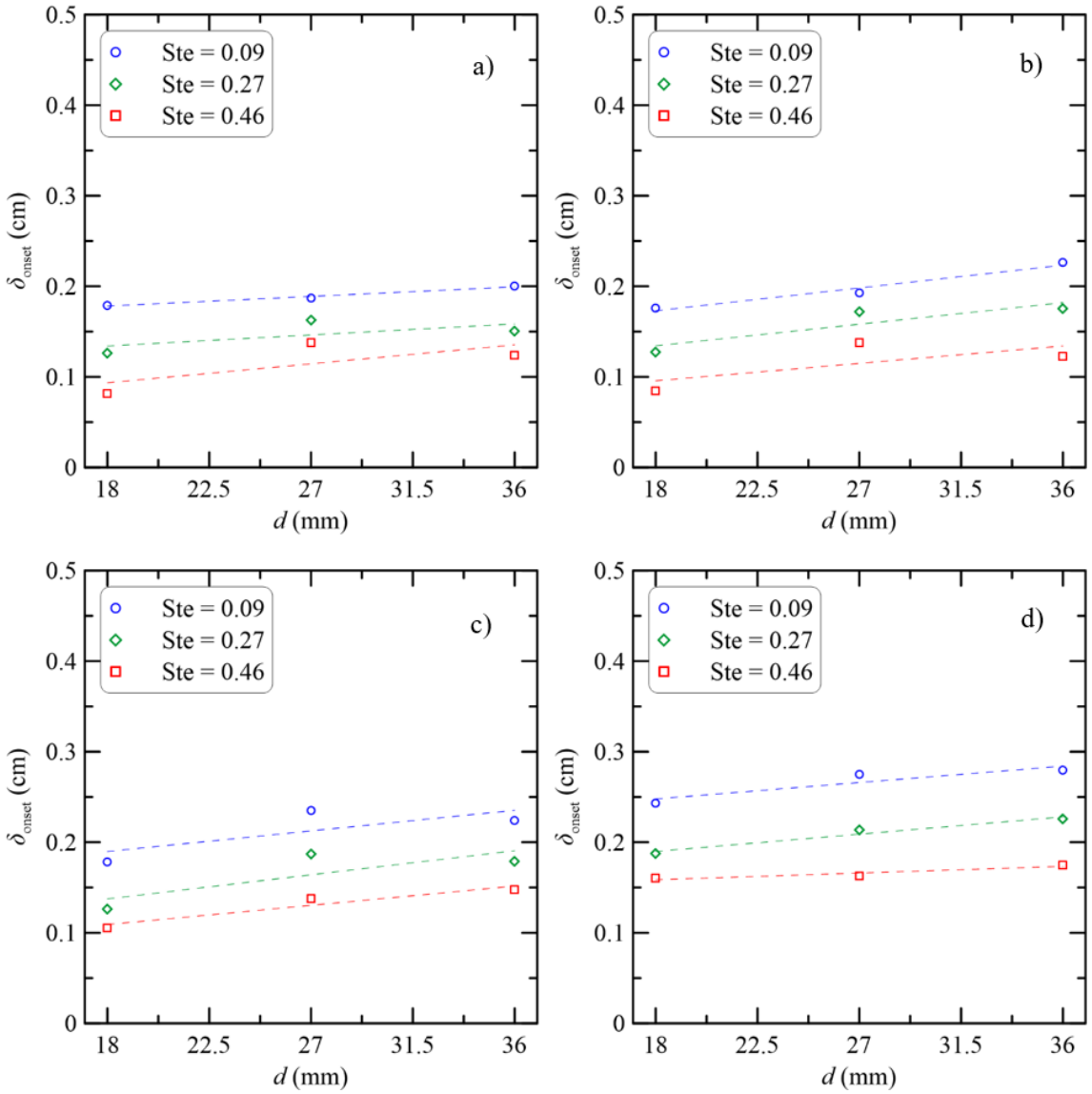

Figure 6.13 Melt thickness at the onset of convection during melting of dodecanoic acid initially subcooled by a) 22.5 °C, b) 15 °C, c) 7.5 °C, and d) 2.5 °C.

It is seen that the melt thickness remains nearly the same as the diameter of the center-tube increases when the PCM is barely subcooled. As the PCM is subcooled more substantially, the melt thickness starts to increase slightly with the diameter of the center-tube. This

increase is much lower compared to the increase for *n*-octadecane, presented in Chapter 5. This difference in the melt thickness variation with subcooling for two PCMs can be recognized to the difference in their thermal conductivities.

6.4 Effects of Grashof number on onset melt volumes

The effects of center-tube diameter and Stefan number on onset melt volume have been discussed in Section 6.2. However, a combined effect of both these parameters can be represented by the Grashof number (defined in Eq. (5.2)). The variation of onset melt volume with Grashof number is presented in Fig. 6.14 for all 36 experiments on dodecanoic acid.

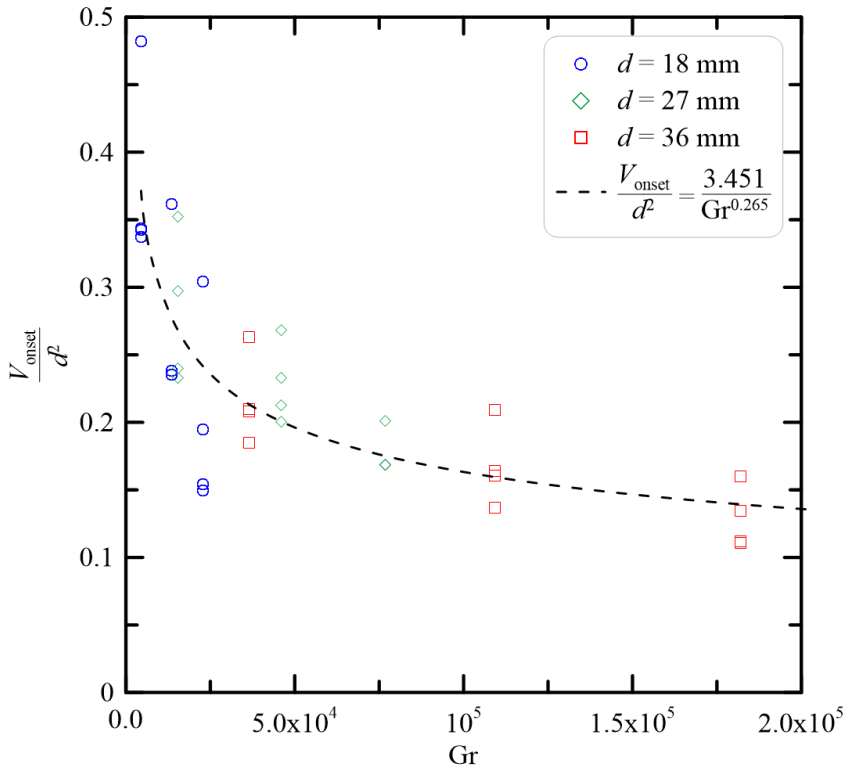

Figure 6.14 Onset melt volume as a function of Grashof number for all the experiments on dodecanoic acid.

Whereas the onset melt volume was a linear function of Stefan number and center-tube diameter, it is a nonlinear function of Grashof number as given in Eq. (6.1). It is seen that a smaller amount of liquid PCM is required for the onset of convection as the Grashof number increases. The index of Grashof number in Eq. (6.1) is 0.265, which is roughly the same as that of *n*-octadecane (0.257), presented in Chapter 5. However, the coefficient

of Grashof number in Eq. (6.1), which is 3.451, is much lower than that for *n*-octadecane (3.853). This indicates that the Grashof number has a greater influence in *n*-octadecane than in dodecanoic acid, which is expected due to the low viscosity of *n*-octadecane.

$$\frac{V_{\text{onset}}}{d^2} = \frac{3.451}{\text{Gr}^{0.265}} \tag{6.1}$$

6.5 Effects of subcooling on the onset of natural convection

The melt volumes at the onset of convection are presented against the subcooling temperature differentials in Fig. 6.15 for the center-tube diameter of 18 mm. The same results for the center-tube diameters of 27 and 36 mm are presented in Figs. 6.16 and 6.17, respectively. All these figures show that the onset melt volume decreases as the subcooling temperature differential increases.

Again, referring back to Figs. 5.16, 5.17, and 5.18, it can be seen that the change in onset melt volume with the degree of subcooling occurs at the fastest rate for center-tube diameter of 18 mm, and at the slowest rate for the center-tube diameter of 36 mm. This difference in the rate of change of onset melt volumes can be attributed to the fact that how fast or slow the heat is conducted to the subcooled solid PCM.

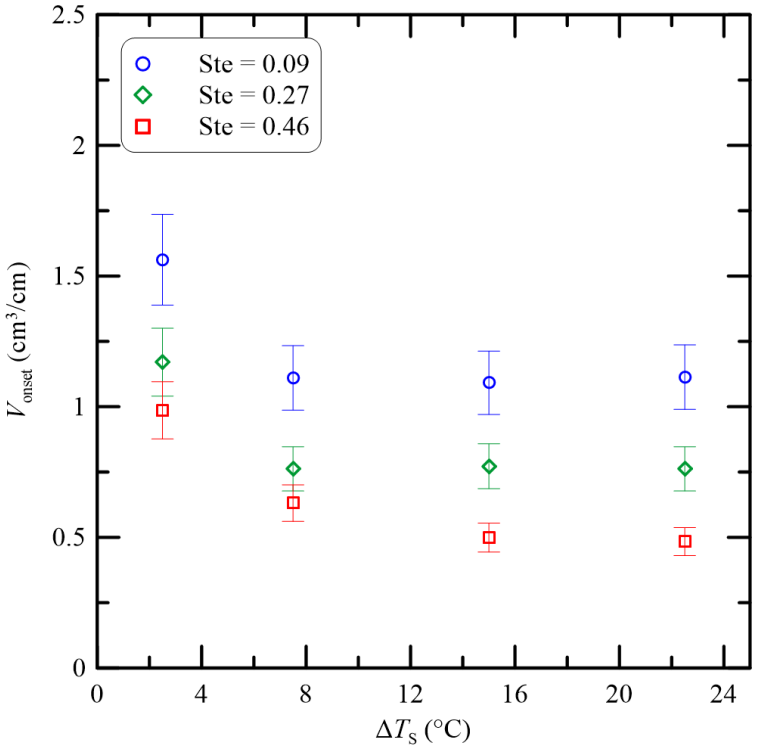

Figure 6.15 Effects of subcooling on melt volume at the onset of natural convection for the center-tube diameter of 18 mm.

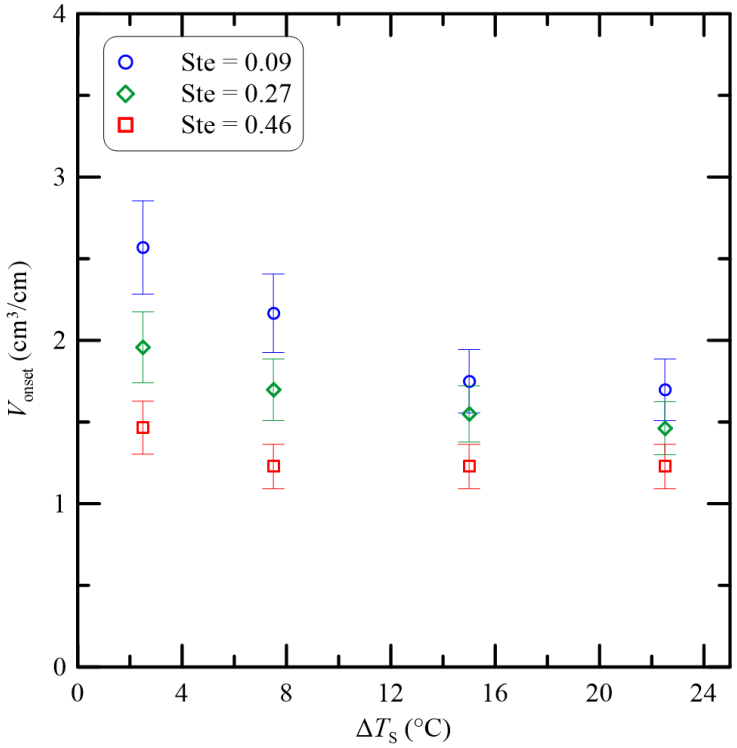

Figure 6.16 Effects of subcooling on melt volume at the onset of natural convection for the center-tube diameter of 27 mm.

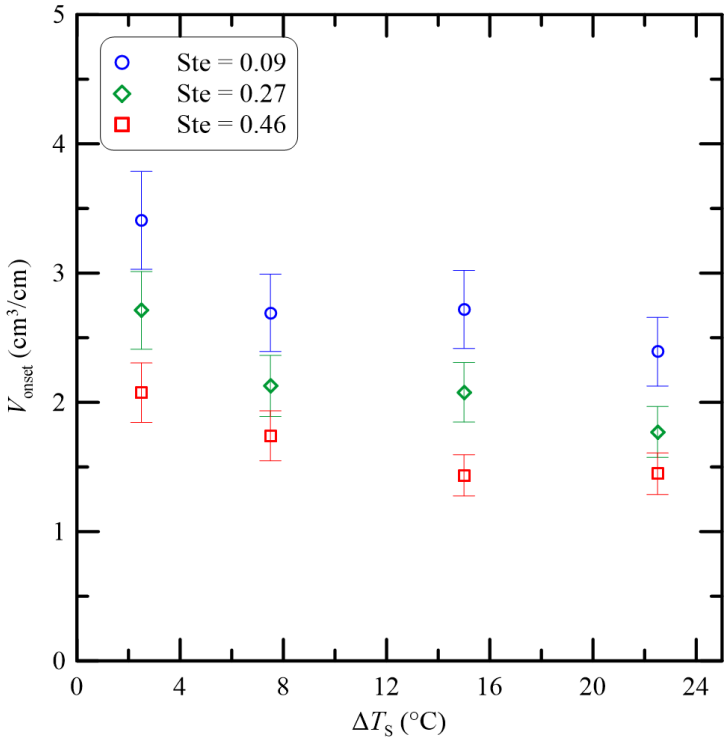

Figure 6.17 Effects of subcooling on melt volume at the onset of natural convection for the center-tube diameter of 36 mm.

6.6 Fourier number at the onset of natural convection

A generic function for Fourier number that is applicable for all subcooled cases and all center-tube diameters was developed using nonlinear regression. The regression was carried out with dimensionless numbers of $\mathrm{Fo}_{\mathrm{onset}}$, Ste, Ste_s, and d/D, and the correlation is shown in Fig. 6.18. All these dimensionless numbers are the same as the ones in Eq. (5.12). The function of the Fourier number at the onset of convection is given by Eq. (6.2).

$$\mathrm{Fo}_{\mathrm{onset}} = \frac{\mathrm{Ste}_s^{0.1371}\left(\frac{d}{D}\right)^{0.7140}}{167.6\,\mathrm{Ste}^{1.5101}} - 0.0004004 \qquad (6.2)$$

The indices of the variables in Eq. (6.2) are comparable to those for *n*-octadecane, as shown in Table 6.9. It is seen that the index of the degree of subcooling for *n*-octadecane is roughly twice that for dodecanoic acid. This is likely due to the higher thermal conductivity of solid *n*-octadecane than that of solid dodecanoic acid (0.358 W/m·K

compared to 0.150 W/m·K), especially when it is considered that Fo_{onset} was defined with the thermal diffusivity of liquid PCM, not the solid PCM.

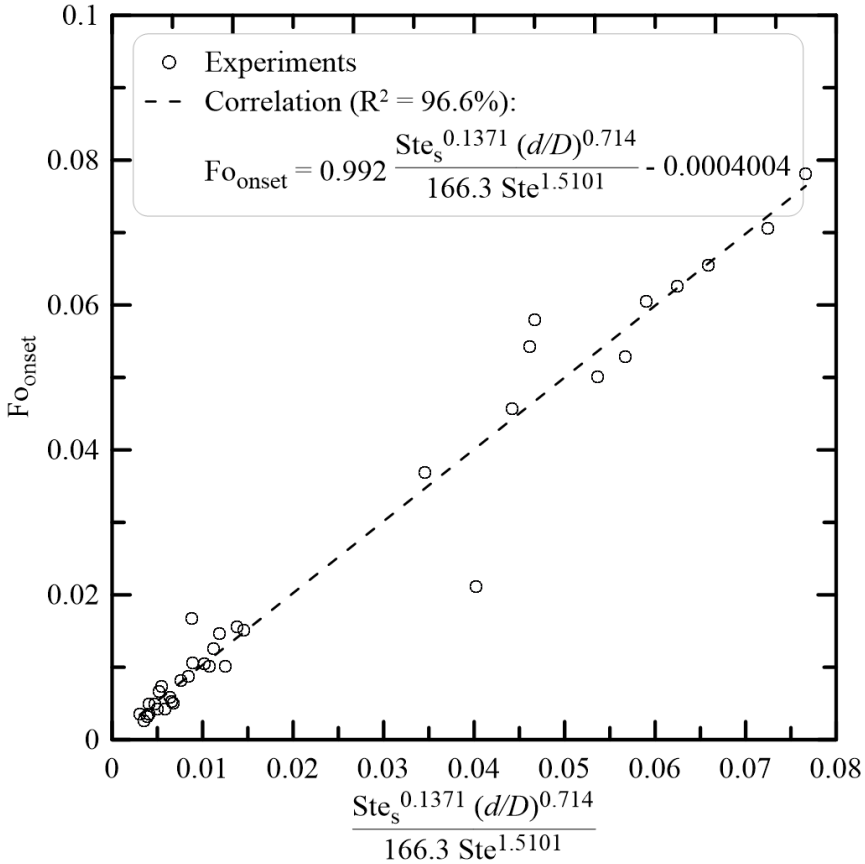

Figure 6.18 Fourier numbers at the onset of natural convection during melting of dodecanoic acid in enclosures with center-tube diameters of 18, 27, and 36 mm and ΔT_s = 2.5, 7.5, 15, and 22.5 °C.

Table 6.9 Comparison of the indices of the variables that the onset Fourier number depends on.

Dimensionless number	Dodecanoic acid	*n*-octadecane
Ste_s	0.1371	0.2807
d/*D*	0.7140	0.8551
Ste	1.5101	1.4499
Constant	166.3	109.2

6.7 Rayleigh number at the onset of convection

The Rayleigh numbers at the onset of natural convection were calculated using Eq. (5.14). These Rayleigh numbers are presented in Fig. 6.19. It is seen that there is no clear trend in the variation of Rayleigh number with Stefan number. However, the onset Rayleigh number varies over a wide range of 225 to 2833. In the study of Bathelt (1979), the onset Rayleigh number calculated using Eq. (5.14) was less than 1700. This upper limit of the onset Rayleigh number is significantly below its highest value in the present study. The wider range of onset Rayleigh number in the present study is expected considering the variation in different experimental parameters.

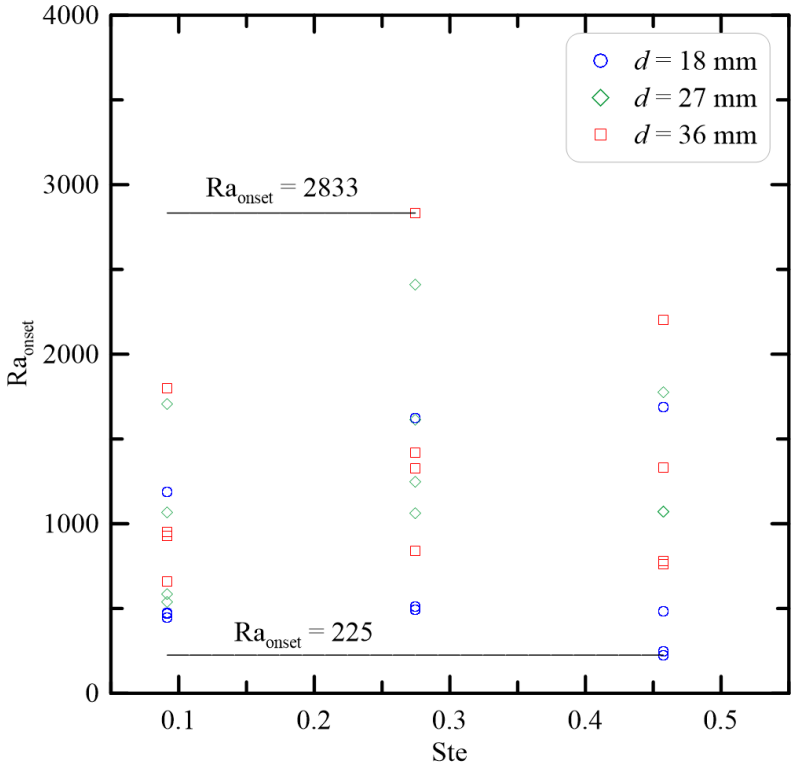

Figure 6.19 Rayleigh numbers at the onset of natural convection for all the experiments on dodecanoic acid.

A new length scale was defined as in Eq. (5.15) to calculate the onset Rayleigh number as defined in Eq. (5.16). These onset Rayleigh numbers are presented against the dimensionless numbers of Ste, Ste_s, and *d/D* in Fig. 6.20. This figure shows that the Rayleigh number at the onset of convection is a nonlinear function of the dimensionless variables on the horizontal axis. The function is given as:

$$\mathrm{Ra_{onset}} = \frac{10^{9.15}\,\mathrm{Ste}^{0.8924}\left(\frac{d}{D}\right)^{2.7729}}{\mathrm{Ste_s}^{0.0614}} - 5196 \qquad (6.3)$$

The intercept in Eq. (6.3) is insignificant compared to the values of the Rayleigh number in Fig. 6.20 and, therefore, neglecting it, the equation for the onset Rayleigh number can be written as given in Eq. (6.4).

$$\mathrm{Ra_{onset}} = \frac{10^{9.15}\,\mathrm{Ste}^{0.8924}\left(\frac{d}{D}\right)^{2.7729}}{\mathrm{Ste_s}^{0.0614}} \qquad (6.4)$$

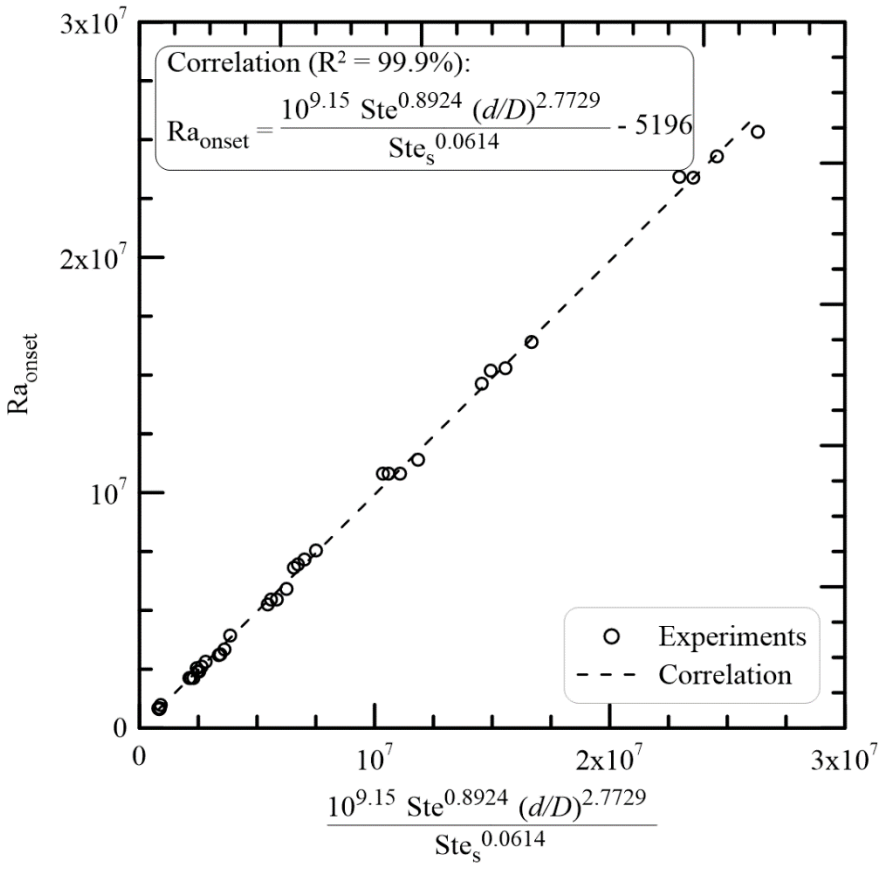

Figure 6.20 Rayleigh numbers at the onset of natural convection during melting of dodecanoic acid under all experimental conditions considered in the present study.

6.8 Conclusions

The results presented in this chapter for dodecanoic acid leads to the same conclusions as those in Chapter 5 for *n*-octadecane. Correlations were developed for Fourier and Rayleigh numbers at the onset of natural convection. These correlations for dodecanoic acid are very similar to those for *n*-octadecane presented in Chapter 5. Additional conclusions are drawn in Chapter 7, where the results for both PCMs are combined and generic correlations are developed.

CHAPTER 7 DIMENSIONAL ANALYSIS

The correlations for the onset of natural convection during melting of *n*-octadecane and dodecanoic acid are presented in this chapter. A dimensional analysis was carried out to identify non-dimensional groups that would influence the onset of natural convection during melting of the PCMs. Nonlinear regression analysis was carried out to develop empirical correlations for natural convection onset. The correlations for the onset of natural convection are first presented for different subcooled conditions, and then a generic correlation is proposed.

7.1 Dimensional analysis

The variables that would influence the melting of PCM in horizontal annular enclosures were identified. These variables are divided into three categories: dependent variables, independent variables, and PCM properties. The properties of the PCMs to be included in the dimensional analysis need to be carefully considered. As can be seen in Table 3.2 in Chapter 3, the values of some properties of the PCMs change as it transitions from solid to liquid phase. In studies of melting of non-subcooled PCMs, the thermophysical properties in the solid phase may be neglected in the dimensional analysis because no heat transfer takes place in the solid portion. However, in studies of subcooled PCMs, it is important to consider the change in values of those properties. This is because it has been shown that a slight subcooling of the PCM can significantly influence the melting process (Bathelt and Viskanta, 1980).

The variables identified in the present study are listed in Table 7.1.

Table 7.1 Variables identified for dimensional analysis.

Variable	Symbol	Unit
Dependent variable		
Melt volume at the onset of natural convection	V_{onset}	m^3
Independent variables		
Diameter of the center-tube	d	m
Diameter of the outer shell	D	m
Gravity	g	$m\ s^{-2}$
Time	t	s
Melting temperature differential	$T_w - T_m$	K
Subcooling temperature differential	$T_m - T_i$	K
Properties of the PCMs		
Coefficient of thermal expansion	β	K^{-1}
Specific heat of liquid PCM	c_l	$J\ kg^{-1}\ K^{-1}$
Specific heat of solid PCM	c_s	$J\ kg^{-1}\ K^{-1}$
Thermal conductivity of liquid PCM	k_l	$W\ m^{-1}\ K^{-1}$
Thermal conductivity of solid PCM	k_s	$W\ m^{-1}\ K^{-1}$
Latent heat of fusion	L	$J\ kg^{-1}$
Dynamic viscosity	μ	$kg\ m^{-1}\ s^{-1}$
Density of liquid PCM	ρ_l	$kg\ m^{-3}$
Density of solid PCM	ρ_s	$kg\ m^{-3}$

There are sixteen variables, of which five are selected as repeating variables. The repeating variables are the melting temperature differential, time, dynamic viscosity, thermal conductivity of solid PCM, and diameter of the center-tube. Choice of these repeaters results in eleven dimensionless groups as:

$$\pi_1 = \beta(T_w - T_m) \tag{7.1}$$

$$\pi_2 = \frac{\mu c_l}{k_s} \tag{7.2}$$

$$\pi_3 = \frac{\mu c_s}{k_s} \tag{7.3}$$

$$\pi_4 = \frac{g t^2}{d} \tag{7.4}$$

$$\pi_5 = \frac{k_\mathrm{l}}{k_\mathrm{s}} \tag{7.5}$$

$$\pi_6 = \frac{\mu L}{k_\mathrm{s}(T_\mathrm{w} - T_\mathrm{m})} \tag{7.6}$$

$$\pi_7 = \frac{d}{D} \tag{7.7}$$

$$\pi_8 = \frac{\rho_\mathrm{l} d^2}{\mu t} \tag{7.8}$$

$$\pi_9 = \frac{\rho_\mathrm{s} d^2}{\mu t} \tag{7.9}$$

$$\pi_{10} = \frac{T_\mathrm{m} - T_\mathrm{i}}{T_\mathrm{w} - T_\mathrm{m}} \tag{7.10}$$

$$\pi_{11} = \frac{V_\mathrm{onset}}{d^3} \tag{7.11}$$

Combining Eqs. (7.1), (7.4), and (7.8) it follows that,

$$\pi_1^* = \frac{g\beta(T_\mathrm{w} - T_\mathrm{m})d^3}{\nu^2} = \mathrm{Gr} \tag{7.12}$$

Combination of Eqs. (7.2), (7.3), (7.5), (7.8), and (7.9) results in,

$$\pi_2^* = \frac{\alpha_\mathrm{l}}{\alpha_\mathrm{s}} \tag{7.13}$$

From Eqs. (7.2) and (7.6),

$$\pi_3^* = \frac{c_\mathrm{l}(T_\mathrm{w} - T_\mathrm{m})}{L} = \mathrm{Ste} \tag{7.14}$$

Combining Eqs. (7.3), (7.6), and (7.10),

$$\pi_4^* = \frac{c_\mathrm{s}(T_\mathrm{m} - T_\mathrm{i})}{L} = \mathrm{Ste_s} \tag{7.15}$$

It should be noted that the Stefan number (Ste) in Eq. (7.14) accounts for sensible heating in liquid PCM and, the Stefan number (Ste_s) in Eq. (7.15) accounts for sensible heating in solid PCM. Hence, the latter also signifies the degree of subcooling of the PCMs.

The eleven dimensionless groups are reduced to six, and the function can be written as:

$$F(\pi_1^*, \pi_2^*, \pi_3^*, \pi_4^*, \pi_7, \pi_{11}) = 0 \tag{7.16}$$

One of the dimensionless groups can be written as a function of the others (Alshqirate *et al.*, 2012), as in Eq. (7.17), and the relation can be written as in Eq. (7.18).

$$\frac{V_{\text{onset}}}{d^3} = F(\pi_1^*, \pi_2^*, \pi_3^*, \pi_4^*, \pi_7) \tag{7.17}$$

$$\frac{V_{\text{onset}}}{d^3} = m\ \text{Gr}^a \left(\frac{\alpha_l}{\alpha_s}\right)^b \text{Ste}^c\ \text{Ste}_s^d \left(\frac{d}{D}\right)^n \tag{7.18}$$

In Eq. (7.18), *a*, *b*, *c*, *d*, *m*, and *n* are constants. It should be noted that although the dependent dimensionless number in this equation is V_{onset}/d^3, in the present study, V_{onset}/d^2 was used for all the correlations. This is because, in the present study, all the volumes represent volume per unit length of the enclosure.

7.2 Empirical correlations

The empirical correlations are presented in Figs. 7.1 to 7.4 for the PCMs subcooled by 22.5, 15, 7.5, and 2.5 °C, respectively. For each subcooled temperature, these figures present the results for experiments with melting temperature differentials of 8.44, 16.9, 25.3, 33.8, and 42.2 for *n*-octadecane and 8.44, 25.3, and 42.2 for dodecanoic acid. It should be noted that although six dimensionless groups were obtained from the dimensional analysis, the nonlinear regression analysis resulted in an exponent of 0 for *d*/*D*. Therefore, *d*/*D* is not included in the figures.

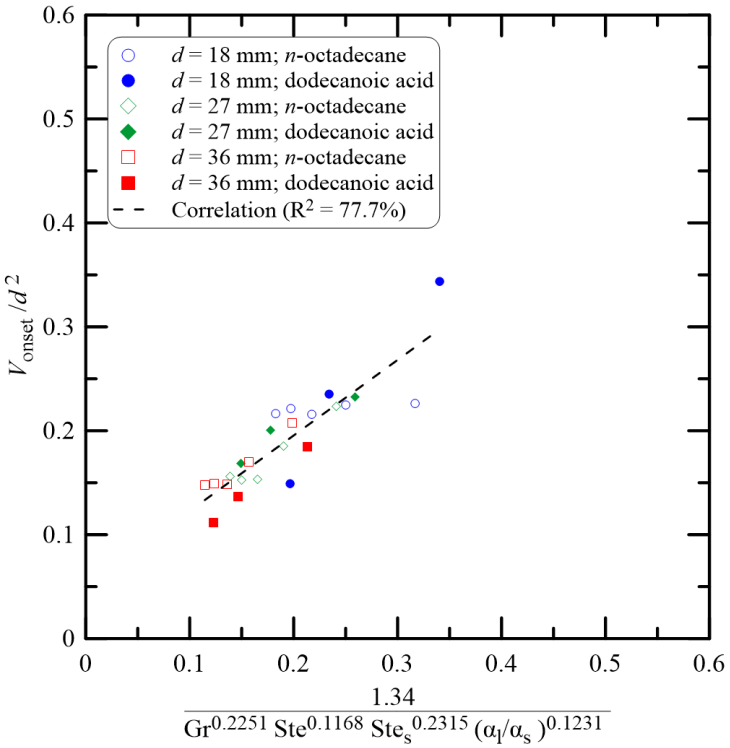

Figure 7.1 Correlation for the onset of natural convection for the PCMs subcooled by 22.5 °C.

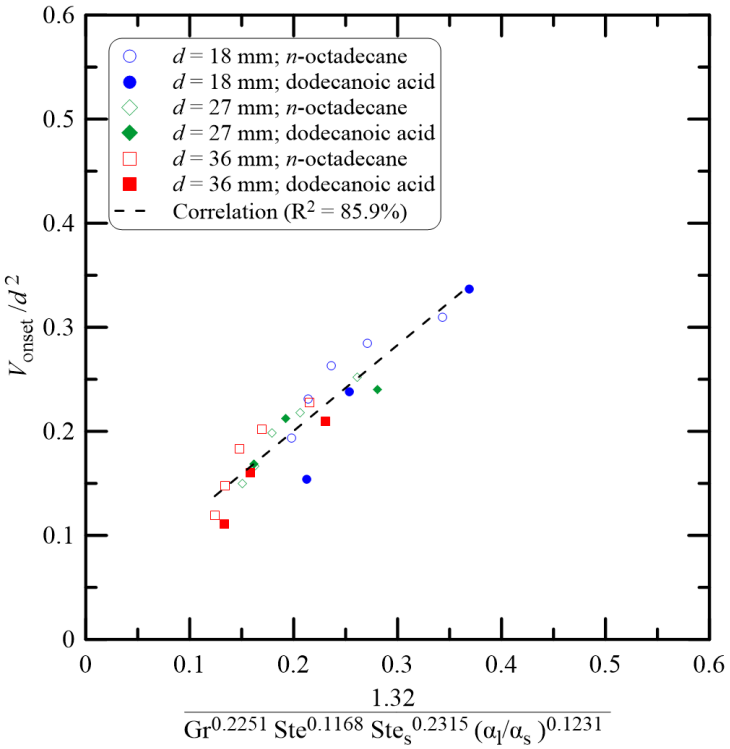

Figure 7.2 Correlation for the onset of natural convection for the PCMs subcooled by 15 °C.

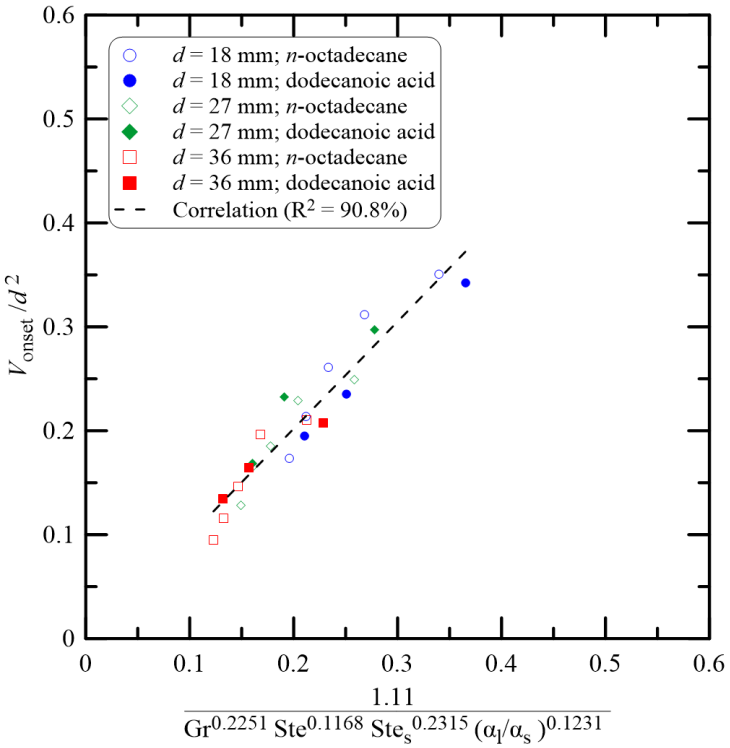

Figure 7.3 Correlation for the onset of natural convection for the PCMs subcooled by 7.5 °C.

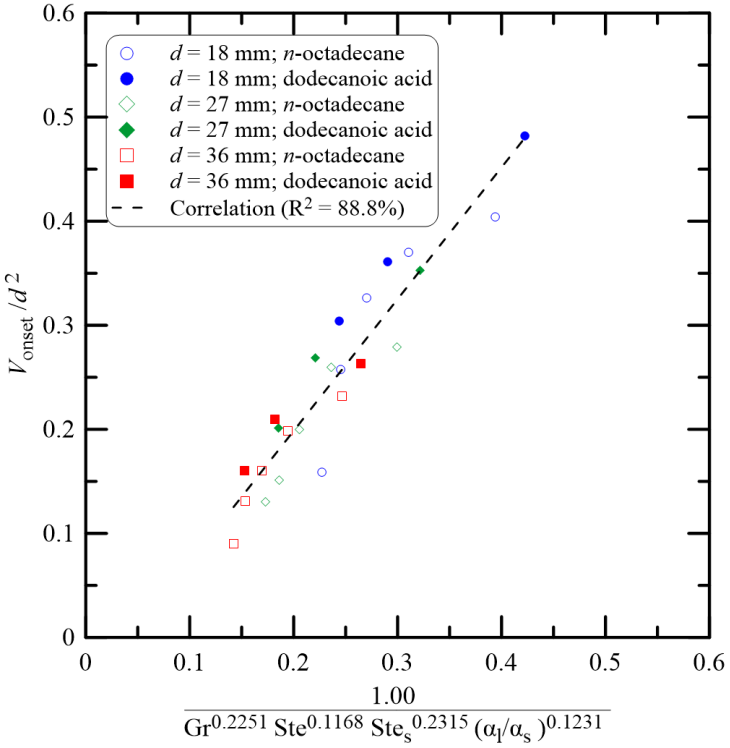

Figure 7.4 Correlation for the onset of natural convection for the PCMs subcooled by 2.5 °C.

The figures show that the correlations estimate the experimental results with reasonable errors. The mean bias error (MBE) and mean absolute error (MAE) in the correlations were calculated following the method in Kato (2016) as:

$$\text{MBE (\%)} = \frac{100}{N}\sum_{1}^{N}\frac{(\frac{V_{\text{onset}}}{d^2})_{\text{exp.}} - (\frac{V_{\text{onset}}}{d^2})_{\text{corr.}}}{(\frac{V_{\text{onset}}}{d^2})_{\text{exp.}}} \tag{7.19}$$

$$\text{MAE (\%)} = \frac{100}{N}\sum_{1}^{N}\left|\frac{(\frac{V_{\text{onset}}}{d^2})_{\text{exp.}} - (\frac{V_{\text{onset}}}{d^2})_{\text{corr.}}}{(\frac{V_{\text{onset}}}{d^2})_{\text{exp.}}}\right| \tag{7.20}$$

In Eqs. (7.19) and (7.20), N is the number of samples. For each subcooled case, the number of samples was 24. The MBE is the average of errors from all experiments, which represents the systematic error by which the correlation can overestimate or underestimate the experimental data. The MAE represents an average of errors in correlated data without referring to whether it is underestimated or overestimated. These errors are summarized in Table 7.2.

Table 7.2 Errors in the empirical correlations for the onset of natural convection.

Error	Subcooling temperature differential (°C)			
	2.5	7.5	15	22.5
MBE (%)	−2.80	−1.46	−1.50	−1.30
MAE (%)	12.56	8.58	8.81	9.33

The equations for the melt volumes at the onset of natural convection under different subcooled conditions are summarized in Table 7.3.

Table 7.3 Correlations for melt volumes at the onset of natural convection.

ΔT_s (°C)	Correlations
2.5	$\frac{V_{onset}}{d^2} = 1.27\,\mathrm{Gr}^{-0.2251}\,\mathrm{Ste}^{-0.1168}\,\mathrm{Ste}_s^{-0.2315}\left(\frac{\alpha_l}{\alpha_s}\right)^{-0.1231} - 5.47\times10^{-2}$
7.5	$\frac{V_{onset}}{d^2} = 1.14\,\mathrm{Gr}^{-0.2251}\,\mathrm{Ste}^{-0.1168}\,\mathrm{Ste}_s^{-0.2315}\left(\frac{\alpha_l}{\alpha_s}\right)^{-0.1231} - 4.14\times10^{-3}$
15	$\frac{V_{onset}}{d^2} = 1.09\,\mathrm{Gr}^{-0.2251}\,\mathrm{Ste}^{-0.1168}\,\mathrm{Ste}_s^{-0.2315}\left(\frac{\alpha_l}{\alpha_s}\right)^{-0.1231} + 3.53\times10^{-2}$
22.5	$\frac{V_{onset}}{d^2} = 0.97\,\mathrm{Gr}^{-0.2251}\,\mathrm{Ste}^{-0.1168}\,\mathrm{Ste}_s^{-0.2315}\left(\frac{\alpha_l}{\alpha_s}\right)^{-0.1231} + 5.01\times10^{-2}$

Table 7.3 shows that the correlations can be written in a generalized form as:

$$\frac{V_{\mathrm{onset}}}{d^2} = M_{\mathrm{onset}}X + I_{\mathrm{onset}} \tag{7.21}$$

The X in Eq. (7.21) is given as:

$$X = \mathrm{Gr}^{-0.2251}\,\mathrm{Ste}^{-0.1168}\,\mathrm{Ste}_s^{-0.2315}\left(\frac{\alpha_l}{\alpha_s}\right)^{-0.1231} \tag{7.22}$$

The M_{onset} and I_{onset}, presented in Fig. 7.5 against the subcooling temperatures are best represented by Eqs. (7.23) and (7.24).

$$M_{\mathrm{onset}} = \frac{1}{0.01137\,\Delta T_s + 0.7679} \tag{7.23}$$

$$I_{\mathrm{onset}} = -0.09984 + 0.04866\log_e \Delta T_s \tag{7.24}$$

For any subcooling temperature, especially within the range used in the present study, Eqs. (7.23) and (7.24) can be utilized to obtain the correlation for the onset of convection.

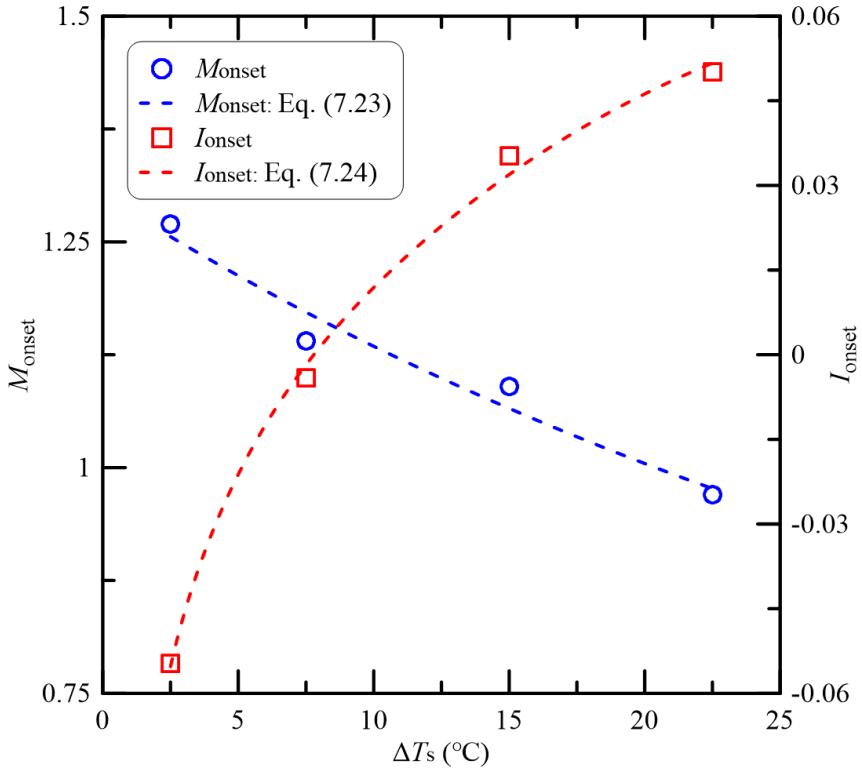

Figure 7.5 Slopes and intercepts of the correlations presented in Table 7.3.

7.3 The generic correlation

The generic empirical correlation was developed, including all experimental results from the present study, a total of 96 experiments. Again, all the dimensionless groups obtained from the dimensional analysis were used in nonlinear regression and d/D had an exponent of 0. The generic correlation, given by Eq. (7.25), is shown in Fig. 7.6. The figure shows that the correlation reasonably represents the experimental results. The mean bias error and mean absolute error calculated using Eqs. (7.19) and (7.20), are −1.95% and 11.19%, respectively.

$$\frac{V_{\text{onset}}}{d^2} = \frac{1.63}{\text{Gr}^{0.2251}\,\text{Ste}^{0.1168}\,\text{Ste}_s{}^{0.0886}\left(\frac{\alpha_l}{\alpha_s}\right)^{0.1428}} - 3.89 \times 10^{-4} \qquad (7.25)$$

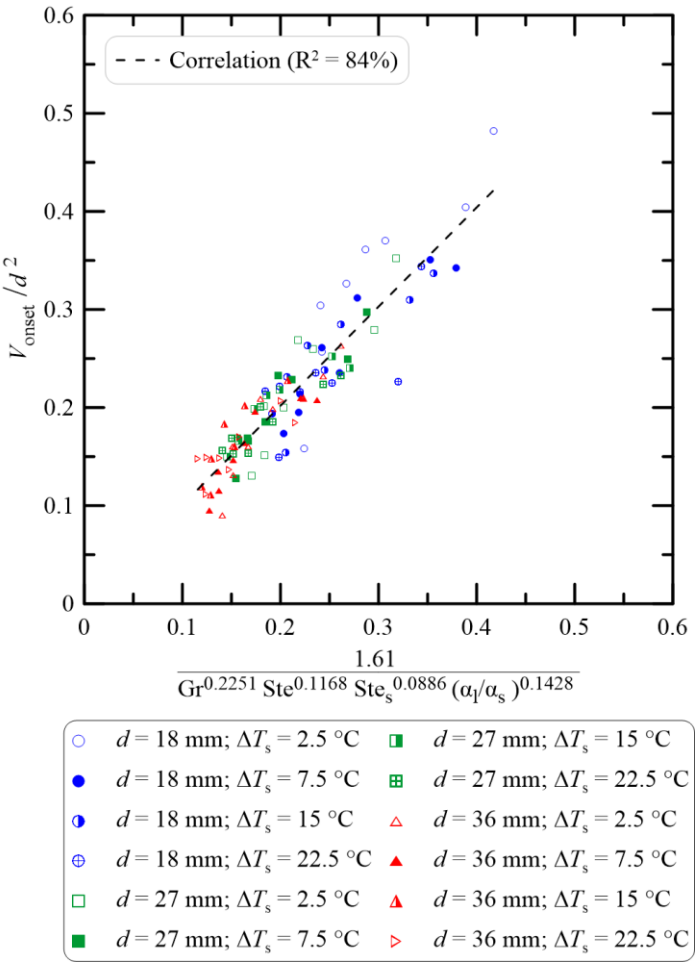

Figure 7.6 Correlation for the onset of natural convection for all experiments.

7.4 The Rayleigh number at the onset of natural convection

In section 7.3, a generic correlation has been provided that can be used to directly estimate the amount of liquid PCM that is required for the convection onset to occur. However, as has been shown in Chapter 5, the Rayleigh number at the onset of convection, often termed as critical Rayleigh number, is well correlated to the experimental results. If the PCM properties and thermal conditions are known, then the melt volume at the onset of convection can be indirectly calculated, as mentioned in detail in Chapter 5. Thus, the correlation for Rayleigh number at the onset of natural convection is presented in Fig. 7.7 for all the experiments. The figure shows that the onset Rayleigh number is very well correlated to the dimensionless numbers such as Stefan number (Ste), degree of subcooling

($\mathrm{Ste_s}$), the ratio of the diameters (d/D), and the ratio of the thermal diffusivities ($\alpha_\mathrm{l}/\alpha_\mathrm{s}$). The correlation for the onset of Rayleigh number is given by:

$$\mathrm{Ra_{onset}} = \frac{10^{9.22}\,\mathrm{Ste}^{0.8921}\left(\frac{d}{D}\right)^{2.7830}}{\mathrm{Ste_s}^{0.0344}\left(\frac{\alpha_\mathrm{l}}{\alpha_\mathrm{s}}\right)^{0.3661}} - 6115 \tag{7.26}$$

The intercept in Eq. (7.26) is negligible compared to the magnitudes of the Rayleigh numbers. Consequently, neglecting the intercept, a simpler correlation for the onset Rayleigh number can be written as:

$$\mathrm{Ra_{onset}} = \frac{10^{9.22}\,\mathrm{Ste}^{0.8921}\left(\frac{d}{D}\right)^{2.7830}}{\mathrm{Ste_s}^{0.0344}\left(\frac{\alpha_\mathrm{l}}{\alpha_\mathrm{s}}\right)^{0.3661}} \tag{7.27}$$

It should be noted that d/D is an important dimensionless number in Eq. (7.27). All three dimensionless groups, namely the degree of subcooling, ratio of thermal diffusivities, and ratio of the diameters, are important only when the PCM is initially subcooled. However, it should also be remembered that the PCM melts only in the vicinity of the center-tube when natural convection onset occurs. Thus, the PCM enclosures can be thought of as a semi-infinite system in the context of onset of convection, and d/D could be considered a negligible variable. In the present study, the temperature of the PCM was not measured, and it is not known how far in the radial direction the solid PCM would be affected by the heat and how much heat would be absorbed by the solid PCM. Therefore, d/D is included in the correlation on the assumption that most of the solid PCM absorbs heat as the natural convection onset occurs.

Now, referring back to the correlation, the Rayleigh numbers at the onset of convection were calculated from experimental data, which is $(\mathrm{Ra_{onset}})_{\mathrm{exp.}}$ and then were calculated from the correlation in Eq. (7.27), which is $(\mathrm{Ra_{onset}})_{\mathrm{corr.}}$. These Rayleigh numbers were used to calculate the mean bias error and mean absolute error from Eqs. (7.28) and (7.29), respectively.

$$\text{MBE}\ (\%) = \frac{100}{N}\sum_{1}^{N}\frac{(\text{Ra}_{\text{onset}})_{\text{exp.}} - (\text{Ra}_{\text{onset}})_{\text{corr.}}}{(\text{Ra}_{\text{onset}})_{\text{exp.}}} \tag{7.28}$$

$$\text{MAE}\ (\%) = \frac{100}{N}\sum_{1}^{N}\left|\frac{(\text{Ra}_{\text{onset}})_{\text{exp.}} - (\text{Ra}_{\text{onset}})_{\text{corr.}}}{(\text{Ra}_{\text{onset}})_{\text{exp.}}}\right| \tag{7.29}$$

In Eqs. (7.28) and (7.29), N is the number of samples, which is 96 in the present study. The mean bias error and mean absolute error were -0.36% and 3.47%, respectively. If the thermophysical properties of the PCM, the dimensions of the geometry and the operating temperatures are known for a specific system, then Eq. (7.27) can be used to calculate the Rayleigh number at the onset of convection. Consequently, the length scale in the Rayleigh number (H_{onset}) can be calculated by using the known properties of the PCM and the operating temperatures. It should be recalled here that the solid-liquid interface remains concentric to the center-tube until the convection onset occurs. Therefore, H_{onset} can be used to calculate the volume of liquid PCM per unit length of the enclosure when the onset of convection occurs.

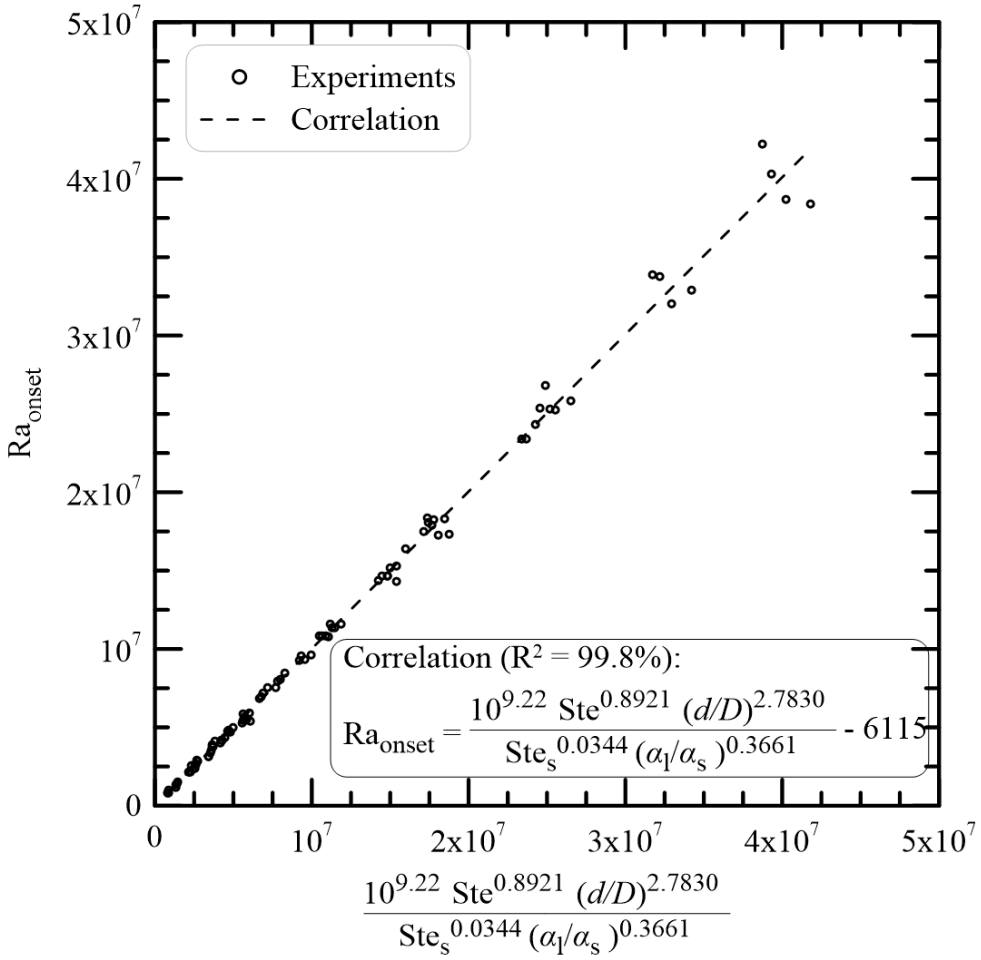

Figure 7.7 The Rayleigh number at the onset of natural convection.

7.5 Conclusions

A dimensional analysis was carried out to develop a correlation for the onset of natural convection. The correlation to directly estimate the required amount of liquid PCM is given by:

$$\frac{V_{\text{onset}}}{d^2} = \frac{1.63}{\text{Gr}^{0.2251}\,\text{Ste}^{0.1168}\,\text{Ste}_s^{\,0.0886}\left(\frac{\alpha_l}{\alpha_s}\right)^{0.1428}} - 3.89\times\,10^{-4}$$

The experimental data were best represented by the Rayleigh number at the onset of natural convection. The height of the liquid column projected on the central vertical plane at the onset of convection was adopted as the length scale in the definition of the Rayleigh number. A correlation for the Rayleigh number was developed using the dimensionless

numbers, which are Stefan number that accounts for sensible heat transfer only in the liquid phase (Ste), degree of subcooling or the Stefan number that accounts for sensible heat transfer only in the solid phase ($\mathrm{Ste_s}$), the ratio of the diameters (d/D), and the ratio of the thermal diffusivities ($\alpha_\mathrm{l}/\alpha_\mathrm{s}$). The correlation is given by:

$$\mathrm{Ra_{onset}} = \frac{10^{9.22}\,\mathrm{Ste}^{0.8921}\left(\frac{d}{D}\right)^{2.7830}}{\mathrm{Ste_s}^{0.0344}\left(\frac{\alpha_\mathrm{l}}{\alpha_\mathrm{s}}\right)^{0.3661}}$$

The mean bias error and mean absolute error were -0.36% and 3.47%, respectively. Since the solid-liquid interface remains concentric until the natural convection onset occurs, the onset Rayleigh number, calculated using the above correlation, can be, in turn, used to calculate the volume per unit length of the liquid PCM at the onset of natural convection.

CHAPTER 8 GLOBAL MELTING

The results on the global melting of both *n*-octadecane and dodecanoic acid are presented in this chapter. As for the onset of convection studies, the experiments for global melting were conducted at melting temperature differentials of 8.44, 16.9, 25.3, 33.8, and 42.2 °C for *n*-octadecane and 8.44, 25.3, and 42.2 °C for dodecanoic acid. These melting temperature differentials correspond to Stefan numbers of 0.1, 0.2, 0.3, 0.4, and 0.5 for *n*-octadecane and 0.09, 0.27, and 0.46 for dodecanoic acid, respectively. The PCMs were subcooled by 2.5, 7.5, 15, and 22.5 °C. The effects of center-tube diameter, Stefan number and PCM-subcooling on the melt volumes of the PCMs are presented.

8.1 Transient melt volume of *n*-octadecane

The transient melt volumes of *n*-octadecane for all the subcooling and melting temperature differentials are presented in Figs. 8.1, 8.2, and 8.3 for center-tube diameters of 18, 27, and 36 mm, respectively. It can be seen that the melt volume increases linearly throughout the eight hours of melting process when the Stefan number is 0.1, except for one case where the center-tube diameter is 36 mm, and the PCM is subcooled by 2.5 °C. In this case, the large diameter of the center-tube and negligible subcooling causes enough heat transfer to have a nonlinear relationship of the melt volume with time. The nonlinear trend of melt volume is observed for all other cases as long as the Stefan number is 0.2 or larger. In these cases, two linear regions can be identified in the melt volume curves. The first region is until at least one half of the solid PCM is melted when strong natural convection is present in the liquid PCM, and the PCM melts faster. In the second region, natural convection weakens, and melting occurs at a much slower rate. These figures also show that the subcooling of the PCM greatly diminishes the melting rate, regardless of the diameter of the center-tubes. However, it is also seen that subcooling does not diminish the melting rate in a linear fashion; a large drop in melt volume is observed when the subcooling increases from 2.5 to 7.5 °C but not when the PCM is subcooled by 15 and 22.5 °C. As expected, the melt volume increases with the Stefan number; however, increasing the Stefan number from 0.1 to 0.2 increases the melt volume significantly but not so when the Stefan number is further increased.

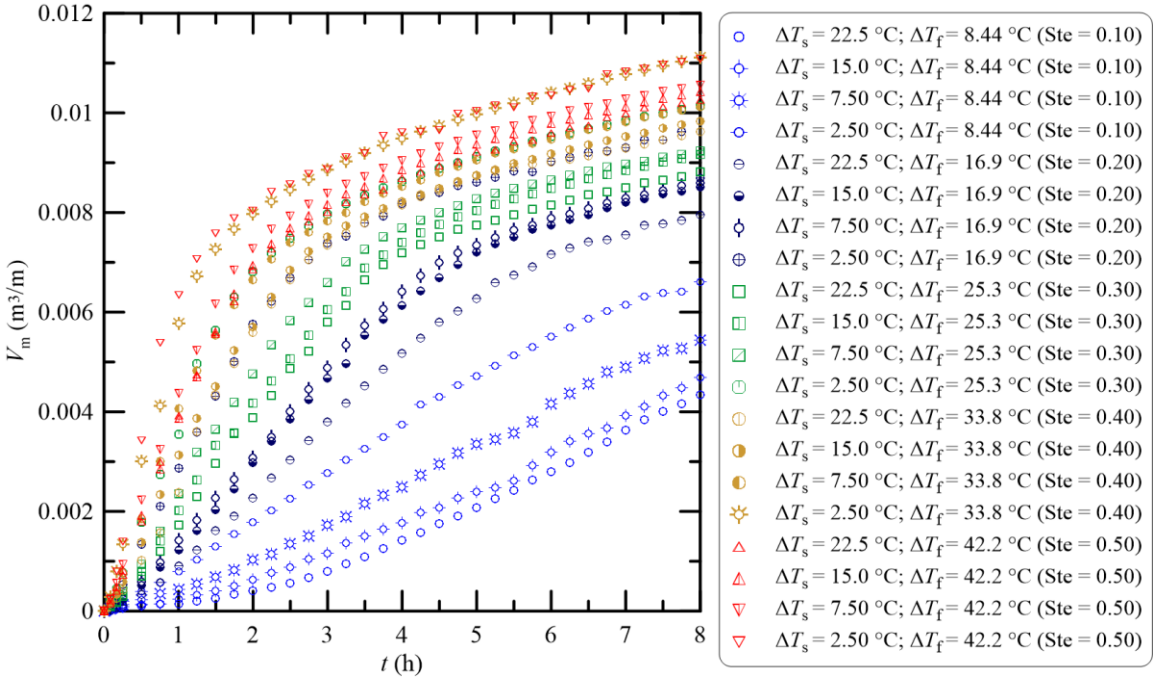

Figure 8.1 Transient melt volume of *n*-octadecane in the enclosure with the center-tube diameter of 18 mm.

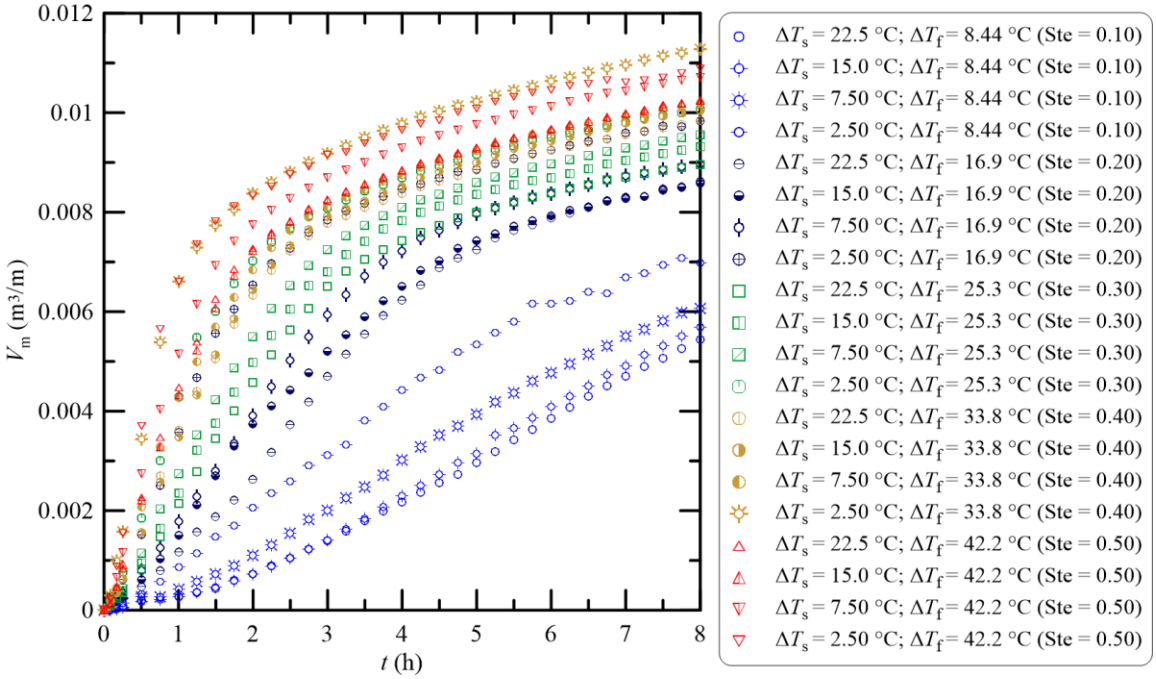

Figure 8.2 Transient melt volume of *n*-octadecane in the enclosure with the center-tube diameter of 27 mm.

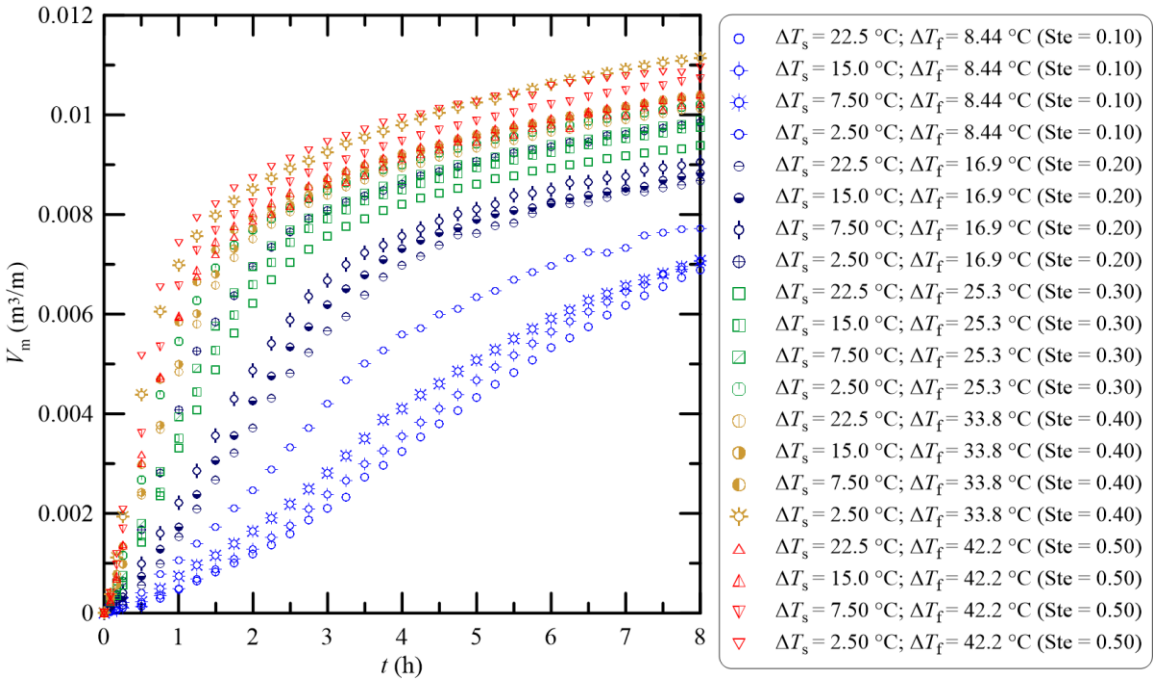

Figure 8.3 Transient melt volume of *n*-octadecane in the enclosure with the center-tube diameter of 36 mm.

8.2 Transient melt volume of dodecanoic acid

The transient melt volume of dodecanoic acid is presented in Figs. 8.4, 8.5, and 8.6 respectively for the center-tube diameters of 18, 27, and 36 mm for all the melting and subcooling temperature differentials. The results are very similar to the ones for *n*-octadecane. It can be seen more clearly in these figures that increasing the Stefan number does not increase the melt volume linearly. One of the main advantages of LHESS is that heat can be stored isothermally. However, due to the low thermal conductivities of the storage materials, an isothermal storage of energy may not be practical. For example, Figs. 8.4 – 8.6 show that the PCM melts very slowly when the Stefan number is 0.1, which would lead to almost isothermal storage of energy. On the other hand, the PCM melts at a much faster rate when the Stefan number is 0.5 but at the expense of a considerable amount of sensible heat storage. A more reasonable Stefan number for thermal storage in the present cases would be 0.3 when the melt volume increases significantly compared to Stefan number 0.1, and a further increase in Stefan number does not increase the melt volume as much. Although the melt volume results of dodecanoic acid are similar to those of *n*-octadecane, the subcooling of the PCM has a much smaller effect on the melt volume

of dodecanoic acid than on *n*-octadecane. The likely reason for this is that the thermal conductivity of solid *n*-octadecane is more than twice that of dodecanoic acid.

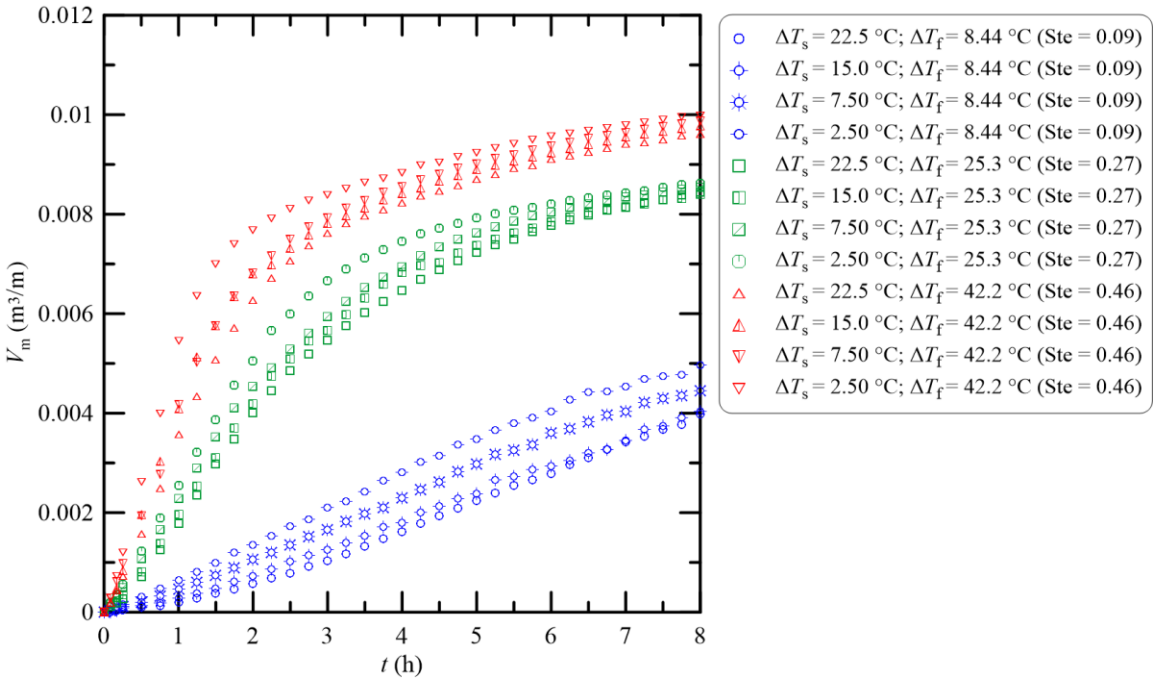

Figure 8.4 Transient melt volume of dodecanoic acid in the enclosure with the center-tube diameter of 18 mm.

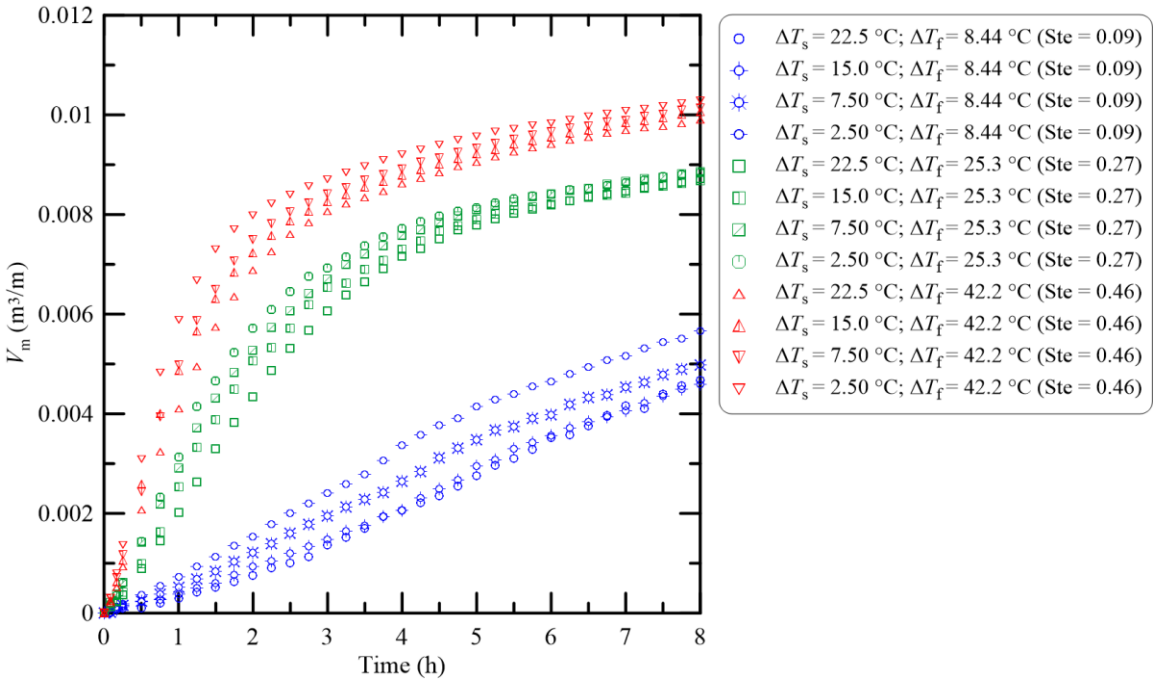

Figure 8.5 Transient melt volume of dodecanoic acid in the enclosure with the center-tube diameter of 27 mm.

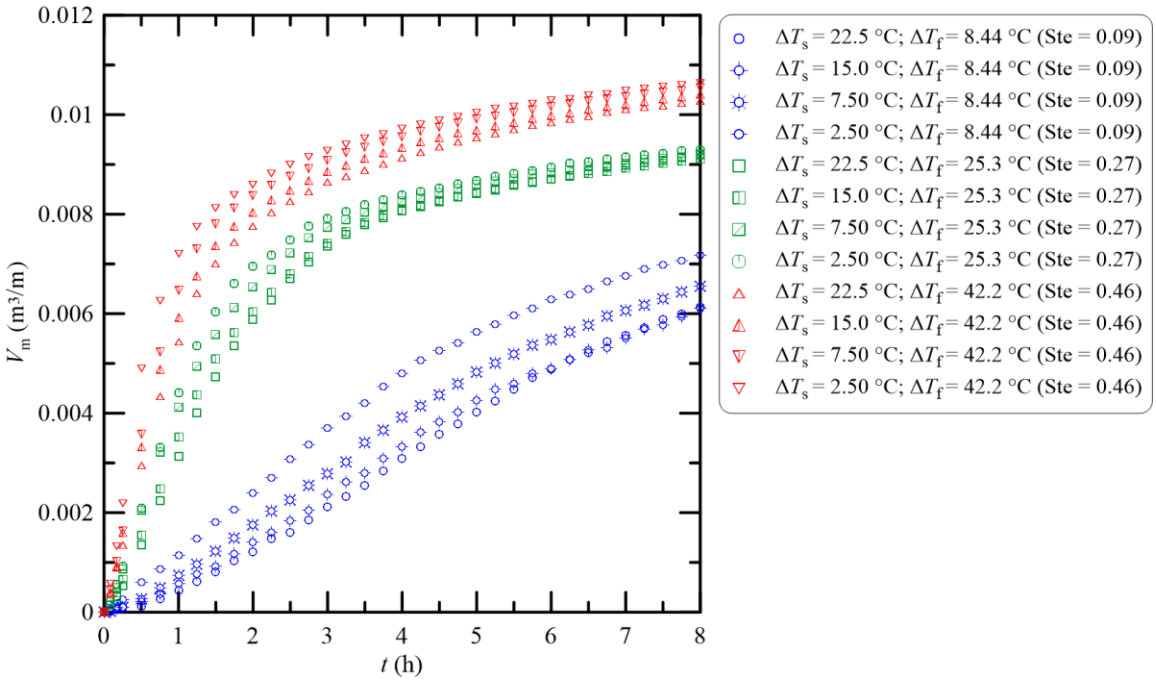

Figure 8.6 Transient melt volume of dodecanoic acid in the enclosure with the center-tube diameter of 36 mm.

8.3 Comparison of transient melt volumes of *n*-octadecane and dodecanoic acid

The transient melt volumes of *n*-octadecane and dodecanoic acid for all center-tube diameters are compared in Figs. 8.7, 8.8, 8.9, and 8.10 for the PCMs initially subcooled by 2.5, 7.5, 15, and 22.5 °C, respectively. It is seen that for any subcooled condition, dodecanoic acid melts slower than *n*-octadecane, although the former has a smaller latent heat of fusion than *n*-octadecane. It is noteworthy that the thermal diffusivity of liquid dodecanoic acid is only 4% higher than that of liquid *n*-octadecane at the melting temperature (8.69×10^{-8} and 8.36×10^{-8} m^2/s, respectively). However, in the solid phase, thermal diffusivity of *n*-octadecane is three times that of dodecanoic acid (2.05×10^{-7} and 6.65×10^{-8} m^2/s, respectively). While the thermal diffusivities in the liquid phase are comparable, higher thermal diffusivity of *n*-octadecane in solid-phase helps preheat the solid *n*-octadecane.

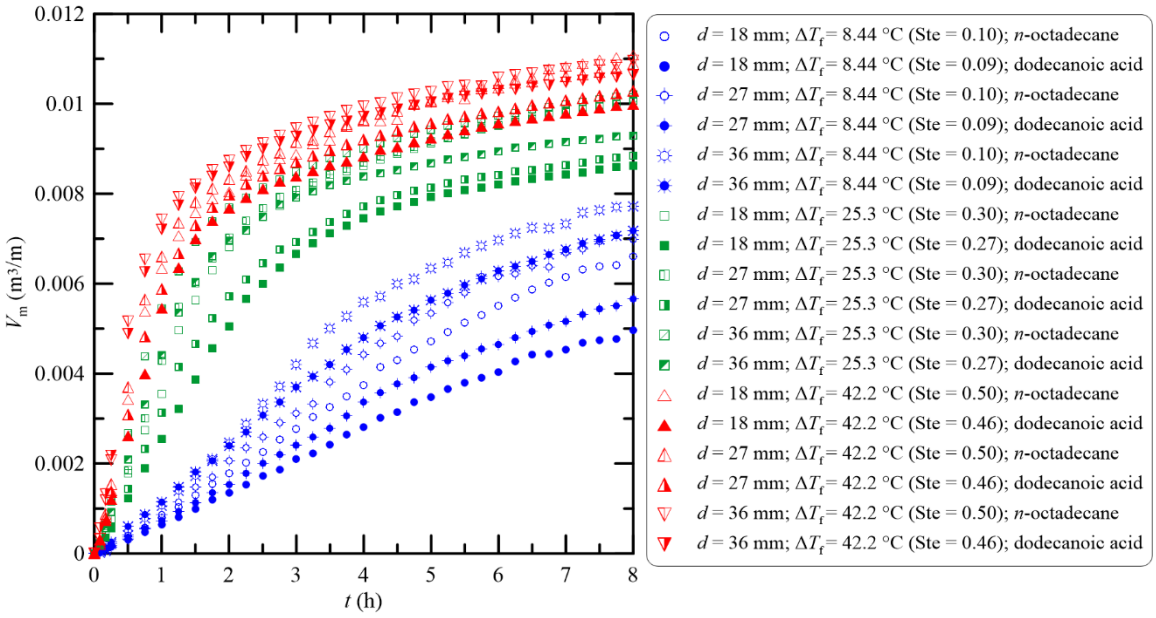

Figure 8.7 Comparison of transient melt volumes for *n*-octadecane and dodecanoic acid when both PCMs are subcooled by 2.5 °C.

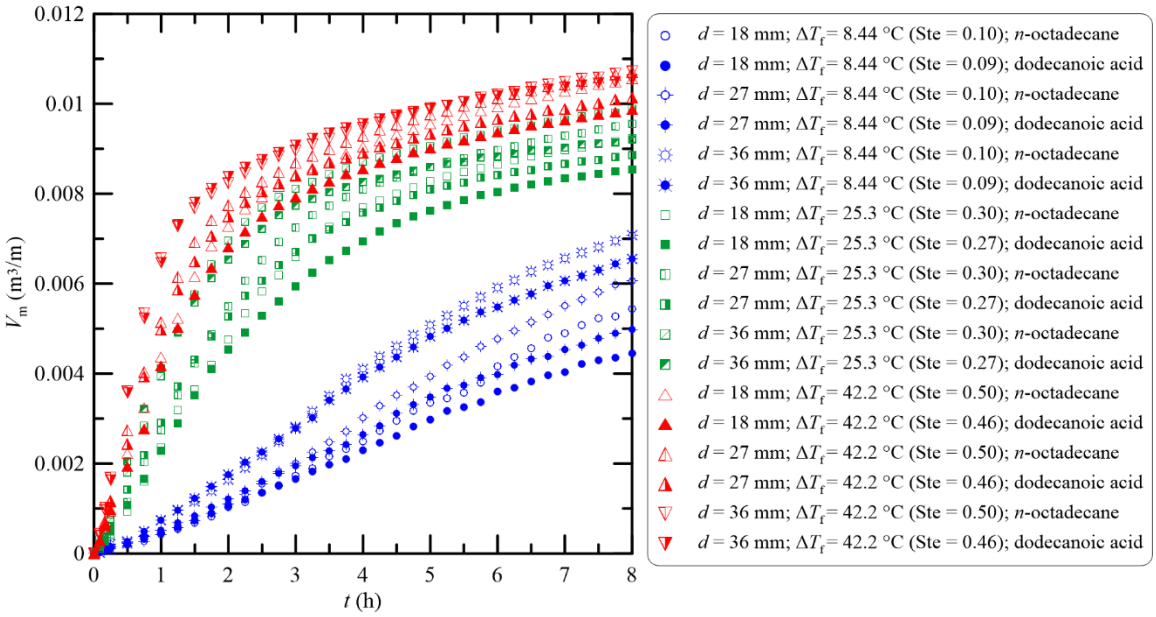

Figure 8.8 Comparison of transient melt volumes for *n*-octadecane and dodecanoic acid when both PCMs are subcooled by 7.5 °C.

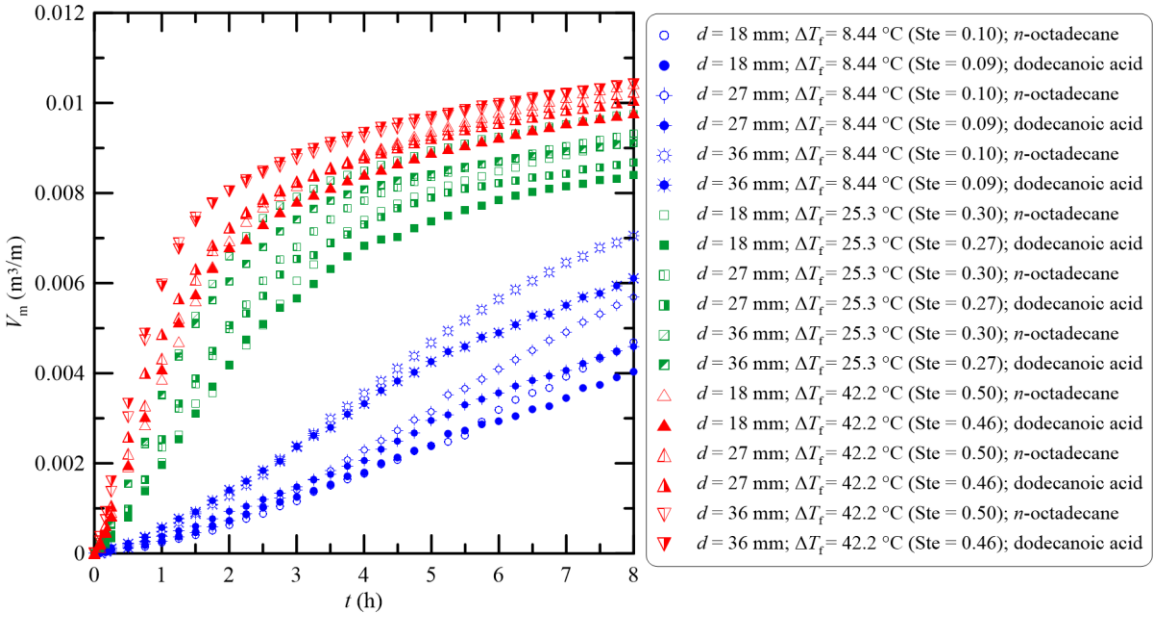

Figure 8.9 Comparison of transient melt volumes for *n*-octadecane and dodecanoic acid when both PCMs are subcooled by 15 °C.

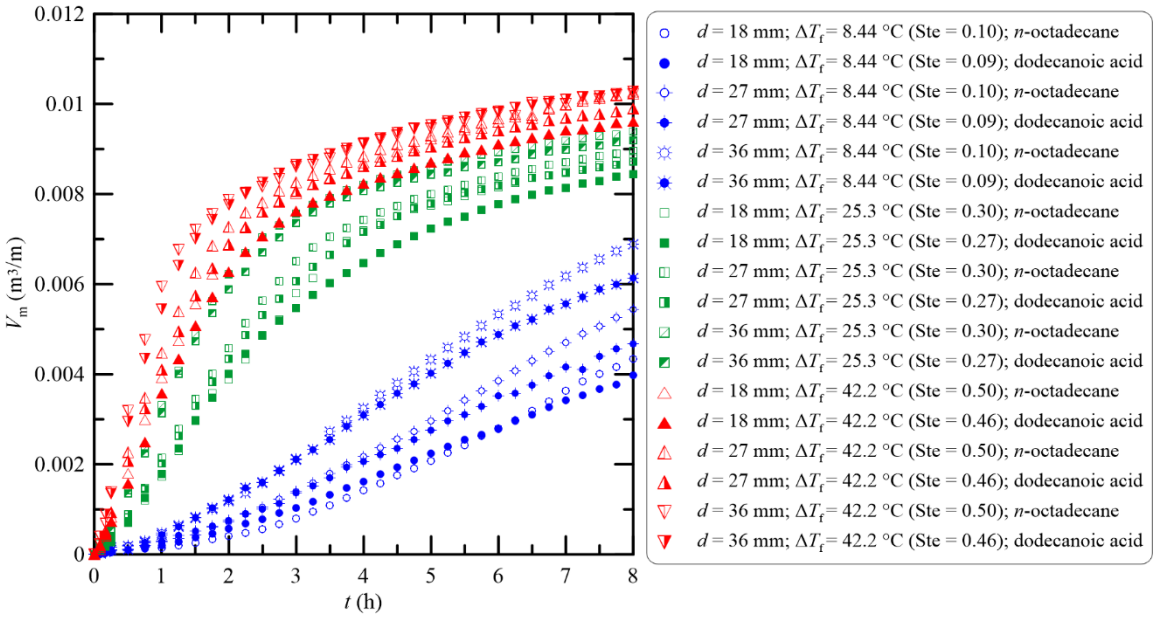

Figure 8.10 Comparison of transient melt volumes for *n*-octadecane and dodecanoic acid when both PCMs are subcooled by 22.5 °C.

Conduction of a large amount of heat to preheat the solid PCM would mean less heat is available to melt the solid PCM. Therefore, all these indicate that *n*-octadecane should have melted slower than dodecanoic acid. It should be remembered that the dynamic viscosity of dodecanoic acid is twice that of *n*-octadecane at melting temperatures of the PCMs. This indicates that the higher dynamic viscosity of dodecanoic acid diminishes the strength of natural convection in liquid dodecanoic acid and thus causes slower melting of it. It has been reported by other researchers as well that an increase in dynamic viscosity suppresses natural convection in liquid PCM (Ho and Gao, 2013).

The difference in the melt volumes is more pronounced when the melting temperature differential is small (8.44 °C). At high melting temperature differentials (25.3 and 42.2 °C), the difference in the melt volumes becomes narrower. At low melting temperature differential (8.44 °C) when the PCMs are significantly subcooled, substantial differences in the melt volumes are observed only at the later stage of the melting process, when conduction is the dominant mode of heat transfer. However, when the PCMs are barely subcooled, and the melting temperature differential is low (8.44 °C), a greater difference in the melt volumes of two PCMs is observed even when convective heat transfer is dominant. The difference in the melt volumes of the PCMs can be explained with the help

of viscosity graphs of the PCMs, which is shown in Fig. 8.11. The viscosity data in Fig. 8.11 have been obtained from Yaws (2003). The figure shows that the difference in viscosity of the PCMs decreases as the melting temperature differential increases. Therefore, when the PCM is barely subcooled and the Stefan number is low (~0.1), a large difference in the viscosity would prevail and affect the strength of natural convection, eventually causing a large difference in the melt volumes. However, when the PCMs are substantially subcooled, dodecanoic acid would conduct heat to the solid PCM at a much slower rate than *n*-octadecane would. The heat that would otherwise be transferred to the solid dodecanoic acid would now heat the liquid dodecanoic acid and increase its temperature. This would cause a smaller difference in the viscosity of the PCMs and thus in the melt volumes.

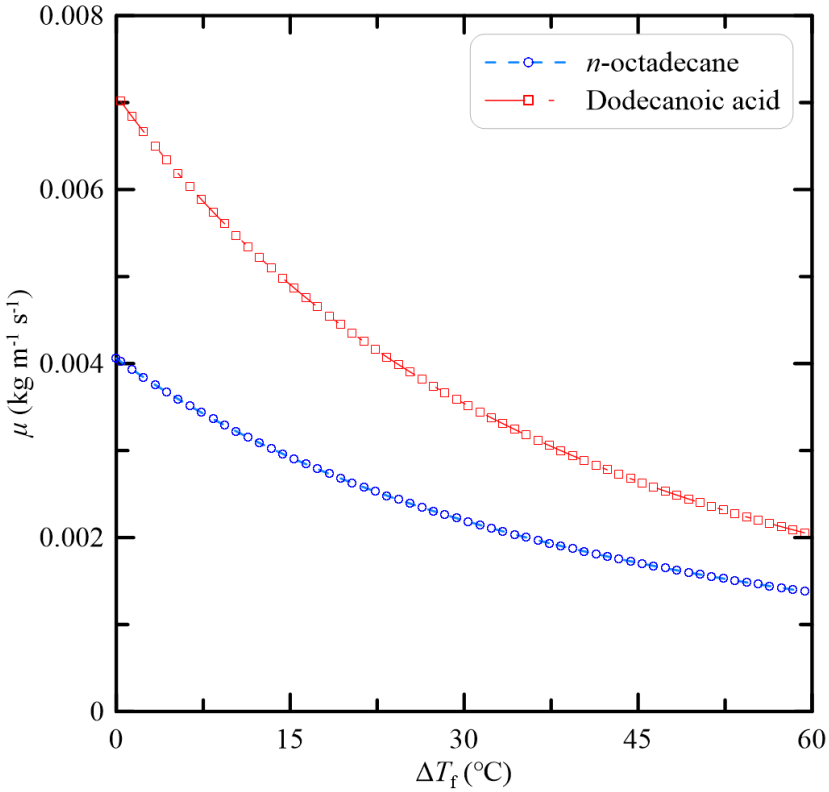

Figure 8.11 Change of dynamic viscosity with the melting temperature differential.

8.4 Correlations for transient melt volumes

The dimensionless groups obtained from the onset of convection results are used to represent the results for transient melting in Fig. 8.12. It should be noted that the diameter of the center-tube was used to define the Grashof number for the onset of convection results. However, the radial thickness of the annular space ($D - d$) was used to define the Grashof number in the context of global melting. Although the Fourier number was not obtained from the dimensional analysis, it is included in the correlation for global melting because global melting clearly depends on the Fourier number. As was seen in sections 8.1 and 8.2, the melt volume increased almost linearly over the entire eight hours of melting when the PCMs were heated at a melting temperature differential of 8.44 °C. For a melting temperature differential above 8.44 °C, the met volume for both the PCMs increased nonlinearly. Therefore, all the transient melt volume results presented in this chapter except when the melting temperature differential was 8.44 °C were used to obtain a correlation for transient melt volumes. The melt volumes were correlated to Eq. (8.1).

$$\frac{V_{\mathrm{m}}}{D^2 - d^2} = \frac{a}{1 + \left(\frac{X_G}{b}\right)^c} \tag{8.1}$$

In Eq. (8.1), a, b, and c are constants and X_{G} is given by Eq. (8.2).

$$X_{\mathrm{G}} = \frac{\mathrm{Fo}^{0.7282}\mathrm{Gr}^{0.0076}\mathrm{Ste}^{0.5279}}{(\alpha_{\mathrm{l}}/\alpha_{\mathrm{s}})^{0.0195}\ \mathrm{Ste}_{\mathrm{s}}^{0.1075}} \tag{8.2}$$

The values of the constants that appear in Eq. (8.1) are listed in Table 8.1.

Table 8.1 Values of the constants appearing in Eq. (8.1).

d (mm)	a	b	c
18	0.7014	0.2622	-1.932
27	0.7115	0.2606	-1.905
36	0.7321	0.2407	-1.832

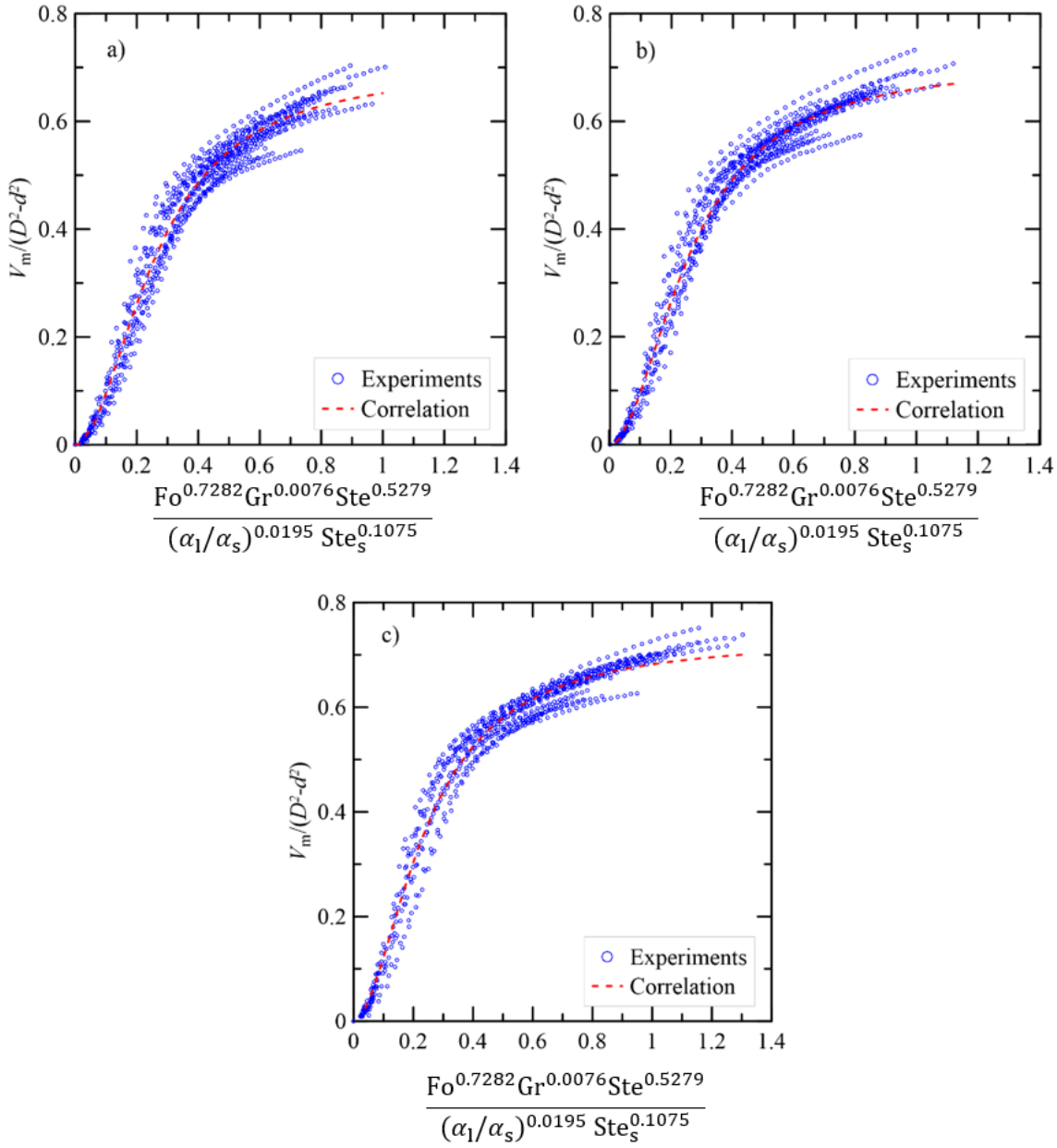

Figure 8.12 Correlations for the transient melt volumes of *n*-octadecane and dodecanoic acid for all the experiments except the melting temperature differential of 8.44 °C for center-tube diameters of a) 18 mm, b) 27 mm, and c) 36 mm.

It is seen that the constants presented in Table 8.1 for different center-tube diameters are comparable, and follow a trend. Therefore, all these melt volume results were combined and another dimensionless number, *d*/*D*, was introduced to develop a generic correlation. The correlated results for all the experiments presented in Fig. 8.12 are shown in Fig. 8.13. The correlation is given by Eq. (8.3).

$$\frac{V_{\mathrm{m}}}{D^2 - d^2} = \frac{0.7294}{1 + \left(\frac{X_G}{0.2628}\right)^{-1.833}} \tag{8.3}$$

In Eq. (8.3), X_{G} is given by Eq. (8.4).

$$X_{\mathrm{G}} = \frac{\mathrm{Fo}^{0.7282}\mathrm{Gr}^{0.0068}\mathrm{Ste}^{0.5285}}{(\alpha_{\mathrm{l}}/\alpha_{\mathrm{s}})^{0.0202}\ \mathrm{Ste}_{\mathrm{s}}^{0.1075}(d/D)^{0.0029}} \tag{8.4}$$

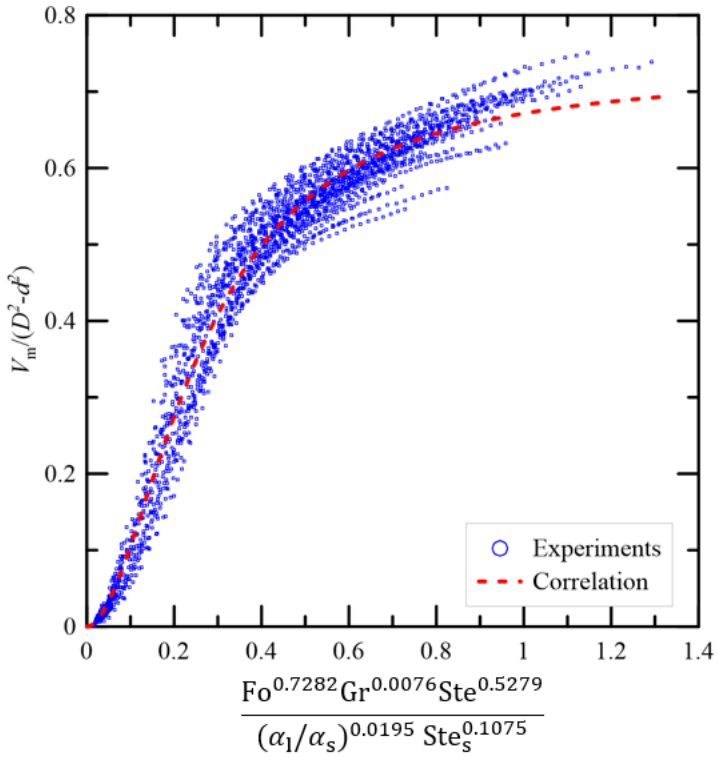

Figure 8.13 Correlations for the transient melt volumes of *n*-octadecane and dodecanoic acid for all the experiments except the melting temperature differential of 8.44 °C.

8.5 Conclusions

From the results presented in this chapter, it can be concluded that the PCMs melt faster at higher Stefan numbers and when the size of the heat source is larger. It can also be concluded that at high melting temperature differentials, dodecanoic acid melts slightly slower than *n*-octadecane although the former has a slightly smaller latent heat of fusion. The difference in melting rate is attributed to the fact that dodecanoic acid has a much higher dynamic viscosity than *n*-octadecane, which suppresses natural convection in liquid

dodecanoic acid to a greater extent than in liquid *n*-octadecane. The difference in melting rates becomes more pronounced when the PCMs are barely subcooled, and the Stefan number is low.

A correlation was developed for the transient melt volumes using several dimensionless groups, which is given as:

$$\frac{V_{\mathrm{m}}}{D^2 - d^2} = \frac{0.7294}{1 + \left(\frac{X_G}{0.2628}\right)^{-1.833}}$$

where

$$X_{\mathrm{G}} = \frac{\mathrm{Fo}^{0.7282}\mathrm{Gr}^{0.0068}\mathrm{Ste}^{0.5285}}{(\alpha_{\mathrm{l}}/\alpha_{\mathrm{s}})^{0.0202}\ \mathrm{Ste}_{\mathrm{s}}^{0.1075}(d/D)^{0.0029}}$$

CHAPTER 9 NUMERICAL STUDY

In this chapter, the results from numerical studies on melting of *n*-octadecane at melting temperature differentials of 8.44, 25.3, and 42.2 K are presented. These melting temperature differentials correspond to the Stefan numbers of 0.1, 0.3, and 0.5. The PCM was subcooled by 2.5, 7.5, 15, and 22.5 K for each Stefan number. All three diameters of the center-tube were used in the simulations. The results from corresponding experiments are also presented for comparison.

9.1 Introduction

The popular enthalpy-porosity method has been employed by many researchers to simulate the melting process of PCMs. In this method, the PCM transitions from solid to liquid phase over a temperature range (ΔT), unlike the physical melting process that occurs at a fixed temperature. The PCM in this temperature band is neither liquid nor solid but rather is considered 'mushy'. In this method, a porous media-like flow is modelled that accounts for natural convection in the PCM. The velocity of the PCM changes from zero at the solid boundary to some appropriate value at the liquid boundary. A source term is added to the conservation of momentum equations that acts as a damping factor. The source term contains a constant, A_{mush}, called the Carman-Kozeny constant or the 'mushy zone' constant. How steep the transition of the velocity in the mushy zone will be depends on the value of A_{mush}. The values of A_{mush}, used by researchers, vary from 10^5 to 10^{10} (Shmueli *et al.*, 2010). Simulations of melting of RT27 in a vertical cylinder of diameter 4 cm and heated from the outer surface at a melting temperature differential of 10 °C show that increasing A_{mush} from 10^5 to 10^8 slows down the melting process and further increase to 10^9 and 10^{10} accelerates the melting process. The melt fractions from the simulations were most comparable to those from the experiment when A_{mush} was 10^8 (Shmueli *et al.*, 2010). However, the opposite trend was observed for a spherical geometry. A value of 10^5 for A_{mush} resulted in melt fractions that are comparable to the experimental ones, and the values 10^6 and 10^7 resulted in low melt fractions during melting of *n*-octadecane in a spherical enclosure heated from the outer surface (Hosseinizadeh *et al.*, 2013). A value of 10^6 for A_{mush} was used for melting of RT50 in horizontal annular enclosures with different wall temperatures (Hosseini *et al.*, 2014). It is clearly seen that different values of A_{mush} are appropriate for different geometries and PCMs.

However, a single value of A_{mush} has also been used for different geometries and different PCMs. For example, a value of 10^5 has been used by Biwole *et al.* (2018) for melting of RT25 in a rectangular enclosure, by Kamkari and Amlashi (2017) for melting of dodecanoic acid in an inclined rectangular enclosure, by Darzi *et al.* (2012) for melting of *n*-eicosane in concentric and eccentric annular enclosures, and by Cao *et al.* (2018) for melting of dodecanoic acid in finned annular enclosures. However, it is not only the mushy zone constant that influences the physics in the mushy zone, the melting temperature range (ΔT) plays a role as well. The appropriate value of A_{mush} is dependent on ΔT, as has been shown by C. Kheirabadi and Groulx (2015). Also, it was shown by C. Kheirabadi *et al.* (2016) that the influence of A_{mush} on melting of dodecanoic acid reduced as the rectangular enclosure was moved from horizontal to 45° to vertical position. As seen, the appropriate value of A_{mush} depends on many parameters such as the geometry and its orientation, the PCM, and the operating temperatures.

There are abundant studies that validated simulation models through the comparison of numerical and experimental melt volumes, ignoring validations at the level of the solid-liquid interfaces. It is of paramount importance to check the validity of a model that can be used to simulate melting in different geometric and operational conditions. In the present numerical study, melting of *n*-octadecane was simulated in annular enclosures with center-tubes of 18, 27, and 36 mm diameter. The PCM was heated at melting temperature differentials of 8.44, 25.3, and 42.2 K and subcooled by 2.5, 7.5, 15, and 22.5 K. Attempts were made to identify appropriate values of A_{mush} and ΔT for the different geometric and operational conditions mentioned above. The melt volumes and melt profiles from the simulations are compared to those from the in-house experiments. In addition, correlations for the onset of natural convection and global melting are developed and compared to those from experiments.

9.2 Numerical model

Following the experiments, the geometric and operational parameters were kept the same in numerical studies. Numerical results were obtained from simulations in two-dimensional domains, in one-half of the horizontal annuli separated by the vertical symmetry line, as shown in Fig. 9.1; this figure shows a typical result of melting simulation in an annulus, where all the PCM has melted, and the system is thermally stratified. Since stainless-steel sleeves

were press-fitted on the center-tubes of the annuli in the experimental setup, a circular domain was created in numerical simulations, which represented the stainless-steel sleeves of the experimental setup. The properties of this domain, provided in Table 9.1, were set to that of the stainless-steel.

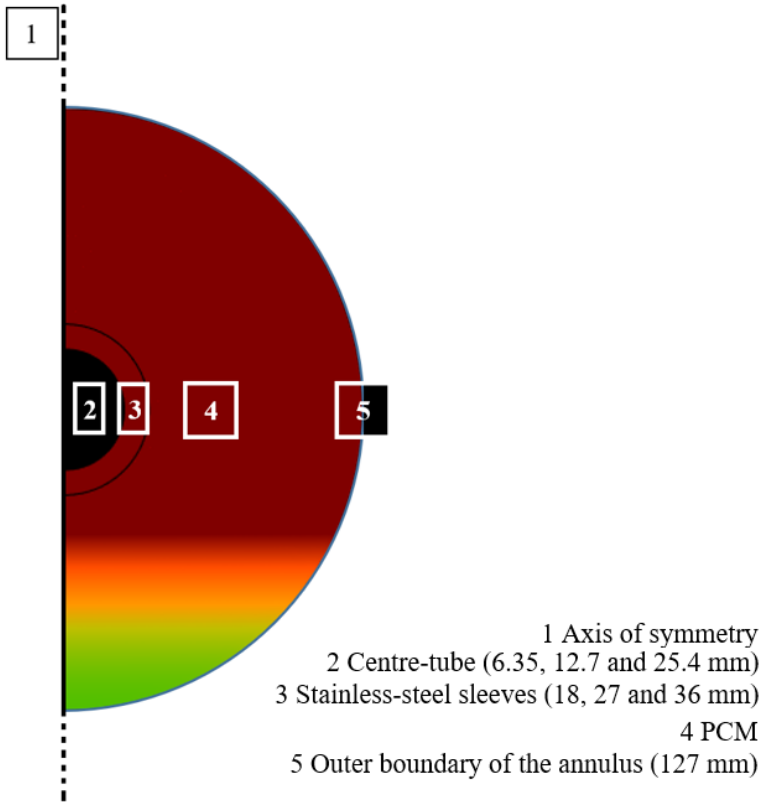

Figure 9.1 The computational domain.

Table 9.1 Thermophysical properties of stainless steel.

Properties	Solid
k	14.90 W/m·K
ρ	7900 kg/m^3
c_s	477 J/kg·K

Constant temperatures were applied at the inner surface of the center-tube, and the outer circumferential surface was insulated. The laminar flow physics and heat transfer in liquid physics in COMSOL Multiphysics 5.3 were used in the PCM domain; the heat transfer in solids physics in COMSOL was used in the stainless-steel domain.

The modified heat capacity-porosity method, the details of which can be found in C. Kheirabadi and Groulx (2015), was used to simulate the melting process. In this method, the heat capacity of the PCM is modified using the latent heat of fusion and the melt fraction of the PCM. The modified heat capacity is accomplished using a Gaussian function, given in Eq. (9.1), which has non-zero values over a temperature range ΔT (the mushy zone temperature interval) from $T_\mathrm{m} - \Delta T/2$ to $T_\mathrm{m} + \Delta T/2$ and integrates to 1, ensuring energy conservation.

$$D(T) = e^{-\frac{(T-T_\mathrm{m})^2}{(\Delta T/4)^2}} \Big/ \sqrt{\pi(\Delta T/4)^2} \tag{9.1}$$

The state of the PCM at a temperature below T_m - $\Delta T/2$ is modelled as a solid and at a temperature above $T_\mathrm{m} + \Delta T/2$ as a liquid. The PCM at a temperature between T_m - $\Delta T/2$ and $T_\mathrm{m} + \Delta T/2$ is modelled as 'mushy.' The liquid fraction of the PCM is calculated using Eq. (9.2) and the heat capacity of the PCM is modified using the liquid fraction and the latent heat of fusion as given in Eq. (9.3).

$$\varphi(T) = \begin{cases} 0, & T < T_\mathrm{m} - \frac{\Delta T}{2} \\ \frac{T-(T_\mathrm{m}-\Delta T/2)}{\Delta T}, & T_\mathrm{m} - \frac{\Delta T}{2} < T < T_\mathrm{m} + \frac{\Delta T}{2} \\ 1, & T > T_\mathrm{m} + \frac{\Delta T}{2} \end{cases} \tag{9.2}$$

$$c_\mathrm{p}(T) = c_\mathrm{ps} + \left(c_\mathrm{pl} - c_\mathrm{ps}\right)\varphi(T) + L \cdot D(T) \tag{9.3}$$

The thermal conductivity of the PCM was also modified similarly, excluding the latent heat term that appears in Eq. (9.3). The Boussinesq approximation was used to simulate the buoyancy induced natural convection in the PCM using Eq. (9.4).

$$\overrightarrow{F_\mathrm{b}} = \rho_\mathrm{l}\vec{g}\beta(T - T_\mathrm{m}) \tag{9.4}$$

The porous-media-like flow through the mushy zone (*i.e.*, the porosity method) was facilitated through the use of a source term, defined in Eq. (9.5), coupled with the velocity vector, which is added to the inertial force term of the Navier-Stokes equation (C. Kheirabadi and Groulx, 2015).

$$S(T) = A_{\text{mush}} \frac{\left(1-\varphi(T)\right)^2}{\left(\varphi(T)\right)^3 + \epsilon} \tag{9.5}$$

The source term acts as a damping factor, taking a very high value when melt fraction approaches zero and a very low value when melt fraction approaches 1; ϵ is used (with a value of 10^{-3}) to avoid division by zero when the melt fraction is zero. The constant, A_{mush}, is the Carman-Kozeny constant or the 'mushy zone' constant.

Beyond the additional source term in the governing equations, the solid phase of the PCM is also ensured by using large values of viscosity (in the magnitude of 10^{10}), through Eq. (9.6), when the temperature of the PCM is below $T_{\text{m}} - \Delta T/2$. From Eq. (9.6), the viscosity reduces to the actual liquid PCM value for temperatures above $T_{\text{m}} + \Delta T/2$, with a transition over the mushy zone temperature range.

$$\mu(T) = \mu_l(1 + S(T)) \tag{9.6}$$

The temperature-dependent viscosity of liquid PCM was provided through Eq. (9.7).

$$\mu_l(T) = 10^{\left(A+\frac{B}{T}+CT+ET^2\right)} \times 10^{-3}\ [\text{Pa} \cdot \text{s}] \tag{9.7}$$

The parameters in Eq. (9.7) adopted from Yaws (2003) are given in Table 9.2.

Table 9.2 Parameters in the viscosity equation, Eq. (9.7).

A	-8.551
B	1670 K
C	0.0157 K^{-1}
E	-1.234×10^{-5} K^{-2}

9.3 Mesh convergence

Quadrilateral elements were used to mesh both the PCM and stainless-steel domains, as shown in Fig. 9.2. In addition to the mesh elements in the domains, 12 boundary layers were used on the boundaries.

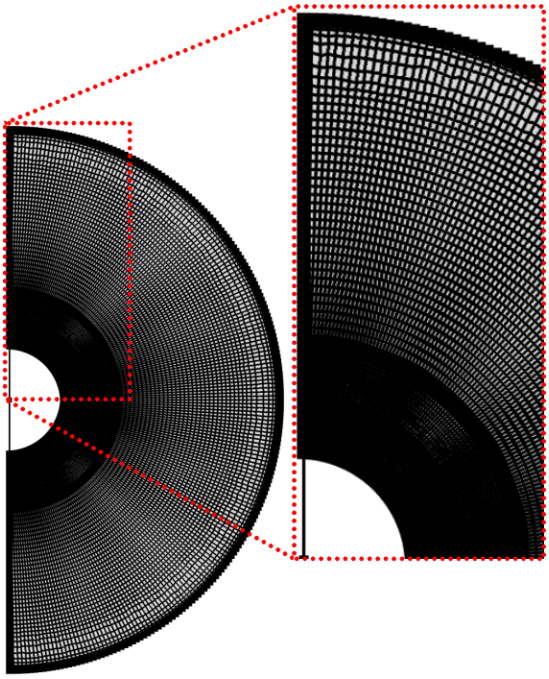

Figure 9.2 Mesh used in the simulation.

The domain for the stainless-steel tube used elements with a size of 0.5 mm. In the PCM, an area with a radius of 25.4 mm from the center of the annuli had a higher mesh density than the rest of the PCM domain. This area was given a higher mesh density because it was seen from the experimental results that the radial thickness of the PCM melt at the onset of convection, in any case, is well within this area; and, it was observed that the melt fraction might become mesh independent at low mesh density while the shape of the solid-liquid interface is not. The shape of the solid-liquid interface in this region of the domain is more important than anywhere else because the onset of convection was identified based on the non-concentricity of the solid-liquid interfaces, as was done in the experiments. Accordingly, a fixed smaller size of the mesh element was chosen in this area, which was 0.5 mm. In the PCM domain far from the center-tube, the size of the mesh elements varied from 0.5 mm to 1 mm, yielding 20,400 (hereafter referred to as 20,000) mesh elements in the simulation domain of the enclosure with the center-tube diameter of 36 mm. The number of mesh elements changed with the size of the center-tube; the enclosure with the 27 mm center-tube had 22,600 mesh elements, and the one with 18 mm center-tube had 24,000 mesh elements.

Mesh independence was checked through simulations with 20000, 50000, 180000, and 690000 elements in the simulated domain, keeping the value of A_{mush} and ΔT unchanged with

values of 10^6 and 1 K respectively. The melt volumes corresponding to these simulations are shown in Fig. 9.3. It is seen that there is hardly any difference in the melt volume when the number of elements is 20000 and 50000. However, a significant increase in mesh density (690000 elements) causes a difference in the melt volume. The choice of 20000 elements underestimates the melt volume by 4.8% compared to the highest mesh-density simulation.

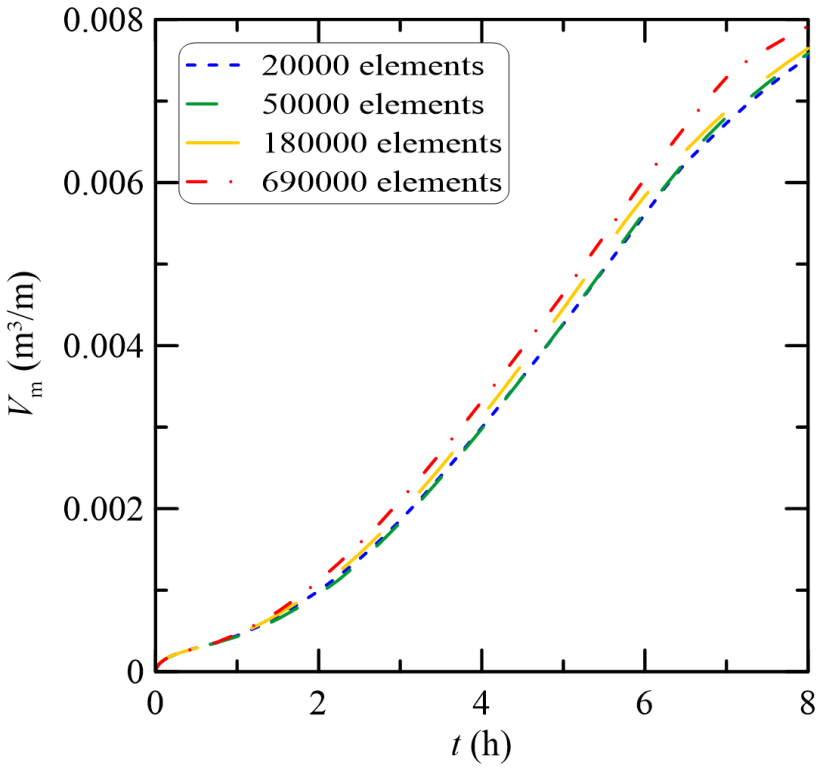

Figure 9.3 Melt volume over time for different number of elements during melting of *n*-octadecane at ΔT_m= 8.4 K, ΔT_s = 22.5 K, ΔT = 1 K and A_{mush} = 10^6 in the annulus with *d* = 36 mm.

Care was taken in selecting the mesh elements not only in terms of the melt volume but also in terms of the shape of the solid-liquid interface far from the center-tube. The solid-liquid interfaces over 6 hours of melting from simulations with 20000, 50000, 180000, and 690000 elements and from the experiment are shown in Fig. 9.4. The figure shows that at higher mesh densities, the progression of the melting interface grows in a way that does not reflect the experimental results. Therefore, 20,000 mesh elements were used, which satisfies the convergence of the simulation results in terms of the melt volume to an acceptable level and the shape of the solid-liquid interface, while achieving the fastest simulation progress. It should, however, be noted that the number of mesh elements, A_{mush}, and ΔT have a combined

impact on the melting dynamics in a simulation, which is clearly a limitation of the porosity method to model natural convection melting in a mushy zone.

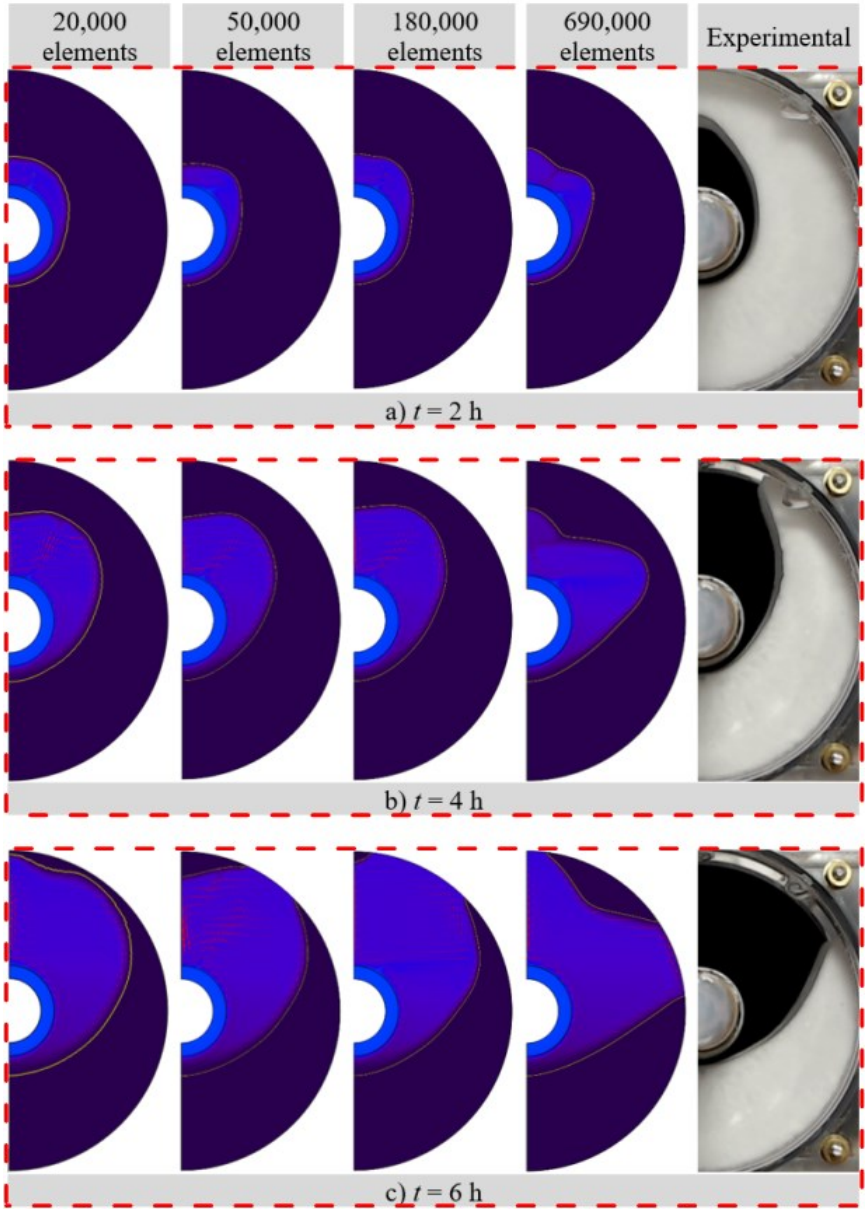

Figure 9.4 Comparison of solid-liquid interfaces for different mesh size during the melting of *n*-octadecane at ΔT_m= 8.4 K, ΔT_s = 22.5 K, ΔT = 1 K and A_{mush} = 10^6 in the annulus with d = 36 mm.

9.3 Numerical study

Three center-tube diameters of 18, 27, and 36 mm were used in this study. For each center-tube diameter, 12 simulations were conducted for three Stefan numbers (0.1, 0.3 and 0.5),

each of them being in four different initial temperatures (ΔT_s = 2.5, 7.5, 15 and, 22.5 K). The simulations were performed on an Intel Xeon quad-core processor at 3.07 GHz with 12 GB RAM. For the selected mesh size, the simulations took up to 15 times longer to run than the simulated time (8 hours), with the simulation times increasing at higher Stefan numbers and larger center-tube diameters.

9.5 Numerical behaviour

The porous-media-like flow through the mushy zone in these simulations is facilitated through the use of the 'mushy zone' constant, A_{mush}. The effects of A_{mush} and ΔT on melt volume is shown in Fig. 9.5 where the melt volume of *n*-octadecane with ΔT_s = 22.5 K and ΔT_f = 8.44 K is presented for 8 hours of melting. Insight can be gained on the impact ΔT by comparing two pairs of data. The first pair being ΔT = 2 K and 3 K and $A_{mush} = 10^4$ and the second pair being ΔT = 1 K and 2 K and $A_{mush} = 10^8$. For a particular value of A_{mush}, a smaller ΔT results in a higher melt volume. Besides, a comparison of another pair, with the values of ΔT = 2 K and $A_{mush} = 10^4$ and 10^8, shows that for a specific value of ΔT, a larger A_{mush} causes a slower melting of the PCM. These conclusions complement the ones reported on the melting of dodecanoic acid in a rectangular enclosure by C. Kheirabadi and Groulx (2015).

Nonetheless, it can also be seen that different combinations of ΔT and A_{mush} may result in similar melt volumes. For example, the pair of simulations where ΔT = 2 K, $A_{mush} = 10^4$ and ΔT = 1 K, $A_{mush} = 10^8$ has similar melt volumes. The same is true for another pair, ΔT = 3 K, $A_{mush} = 10^4$ and ΔT = 2 K, $A_{mush} = 10^8$.

Therefore, there is no clear indication as to what the appropriate values of ΔT and A_{mush} should be for a particular operating condition based solely on the melt volume (or melted fraction by extension). However, in the present study, an attempt was made to use a small ΔT to simulate the experimental condition as accurately as possible. A combination of ΔT = 0.5 K and $A_{mush} = 10^{10}$ results in melt volume that is comparable to those obtained from the experiment.

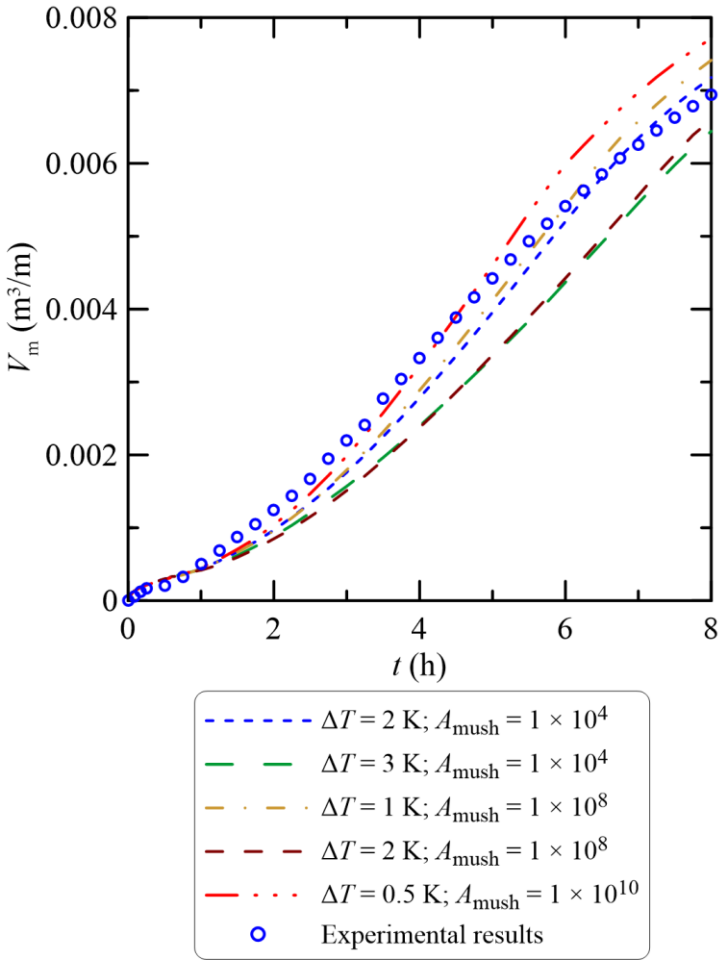

Figure 9.5 Effect of melting temperature range and mushy zone constant on melting of PCM.

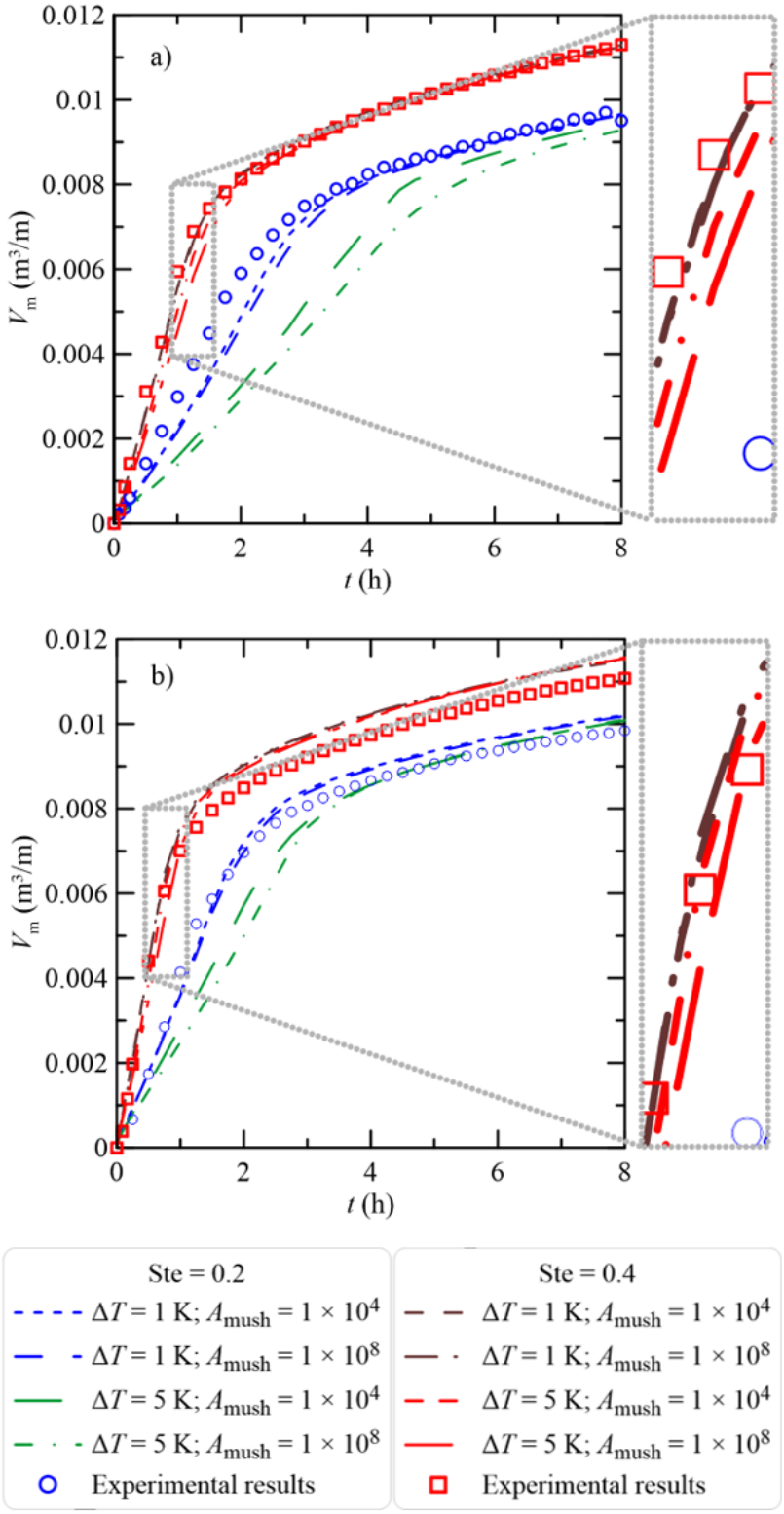

Figure 9.6 Comparison of numerical results from simulations with different A_{mush} and ΔT_m at Stefan numbers of 0.2 and 0.4 to those from experiments: a) d = 18 mm and b) d = 36 mm.

The above discussion pertains to a single operating and geometric condition; however, the present study includes multiple geometric and operating conditions. There is no work in the literature that suggests what these values should be for different operating or geometric conditions, such as for different initial temperatures of the PCMs, diameters of the center-tubes, and heating temperatures. The effects of ΔT and A_{mush} on melting of *n*-octadecane at Stefan numbers of 0.2 and 0.4, and at $\Delta T_s = 2.5$ K in the annuli with center-tube diameters of 18 and 36 mm have been investigated in an unrelated study in the authors' lab. Two values of ΔT (1 K and 5 K) and two different A_{mush} (10^4 and 10^8) were used in this study. These values led to four possible combinations of ΔT and A_{mush} for each center-tube diameter and Stefan number. The melt volumes from this study are presented in Fig. 9.6. This figure shows that ΔT has a greater impact on the melt volume than the A_{mush} does. These impacts are more significant when the Stefan number and the center-tube diameter is small. Also, at high Stefan number, although ΔT has some effect on the melt volume, A_{mush} leaves an impact only at large ΔT. These observations lead to the choice of ΔT and A_{mush} in the present study for melting at higher Stefan numbers. Since ΔT affects the melting to a greater extent than does A_{mush} at higher Stefan numbers, the value of ΔT was increased while keeping A_{mush} unchanged for melting at higher Stefan numbers. The value of ΔT was 0.5, 3, and 5 K for Stefan numbers of 0.1, 0.3, and 0.5 respectively, regardless of the geometry of the annuli and initial temperature of the PCM; still the value of A_{mush} used was 10^{10} for all the simulations.

9.6 Results and discussion

All the results from numerical studies are presented in two groups. The results related to the onset of natural convection are presented in subsection 9.6.1, and those related to global melting are presented in subsection 9.6.2.

9.6.1 Onset of natural convection

The melt profiles and melt volumes at the onset of natural convection are presented in this subsection. The correlations developed for the Fourier number and Rayleigh number at the onset of natural convection are also presented in this subsection.

9.6.1.1 Melt profiles at the onset of natural convection

The melt profiles obtained from numerical studies at the start of natural convection when PCM was subcooled by 22.5 and 2.5 K are presented in Figs. 9.7 and 9.8, respectively. The same results when the PCM was subcooled by 7.5 and 15 K are not shown because they are qualitatively the same as the ones presented here. A 31.75 mm × 63.5 mm section from the center, *i.e.*, 31.75 mm to the right, up and below the center is shown in the figures. The yellow lines in the figures for the simulated results represent the solid-liquid interface; the black semi-circles represent the boundary of the stainless-steel sleeves and the black semi-circular area at the center represents the pipes on which the sleeves are press-fitted. The purple area represents the solid PCM and the PCM bounded by the black semi-circles and the yellow lines is liquid.

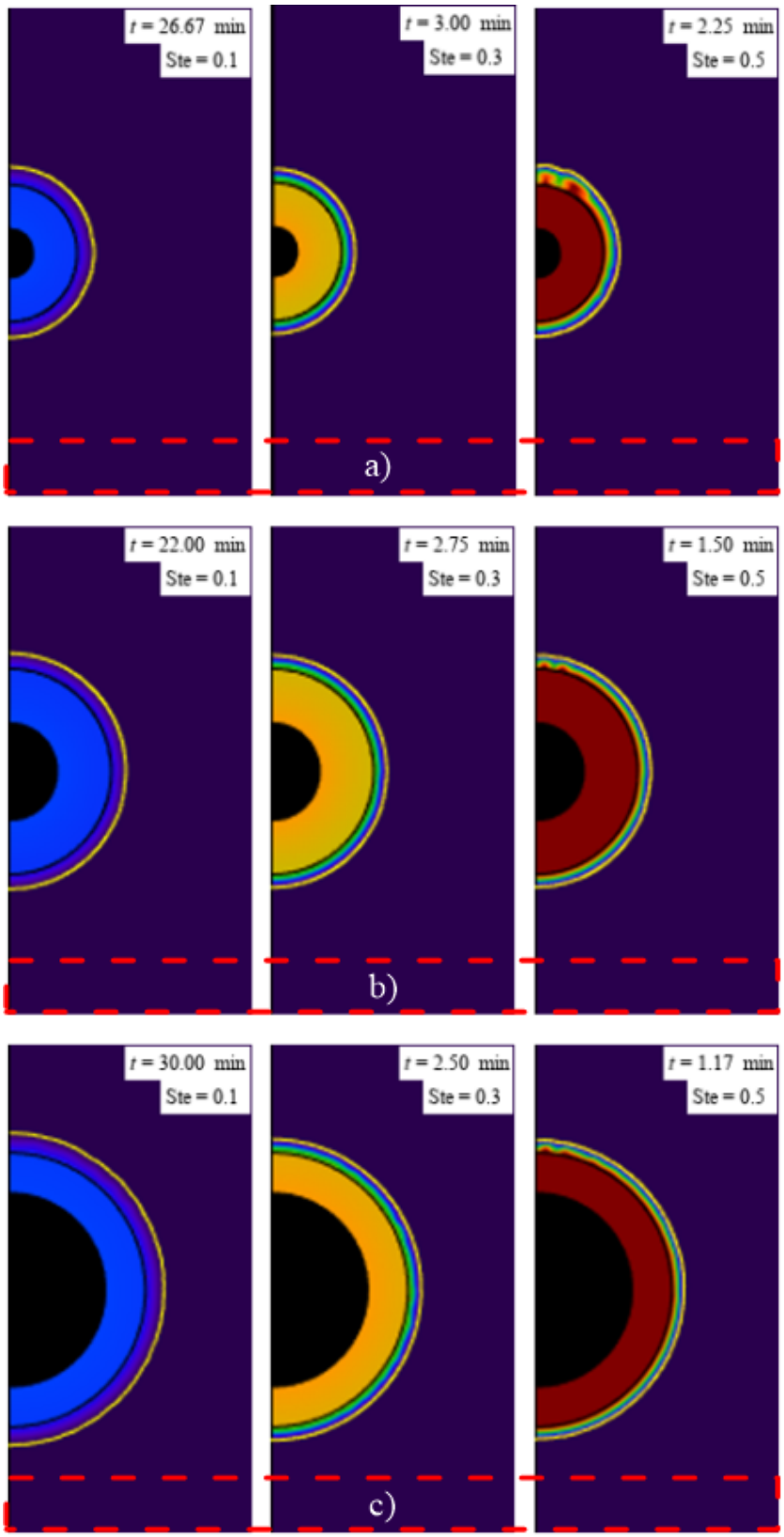

Figure 9.7 Solid-liquid interface locations from numerical studies at ΔT_s = 22.5 K for the center-tube diameter of a) 18 mm, b) 27 mm, and c) 36 mm.

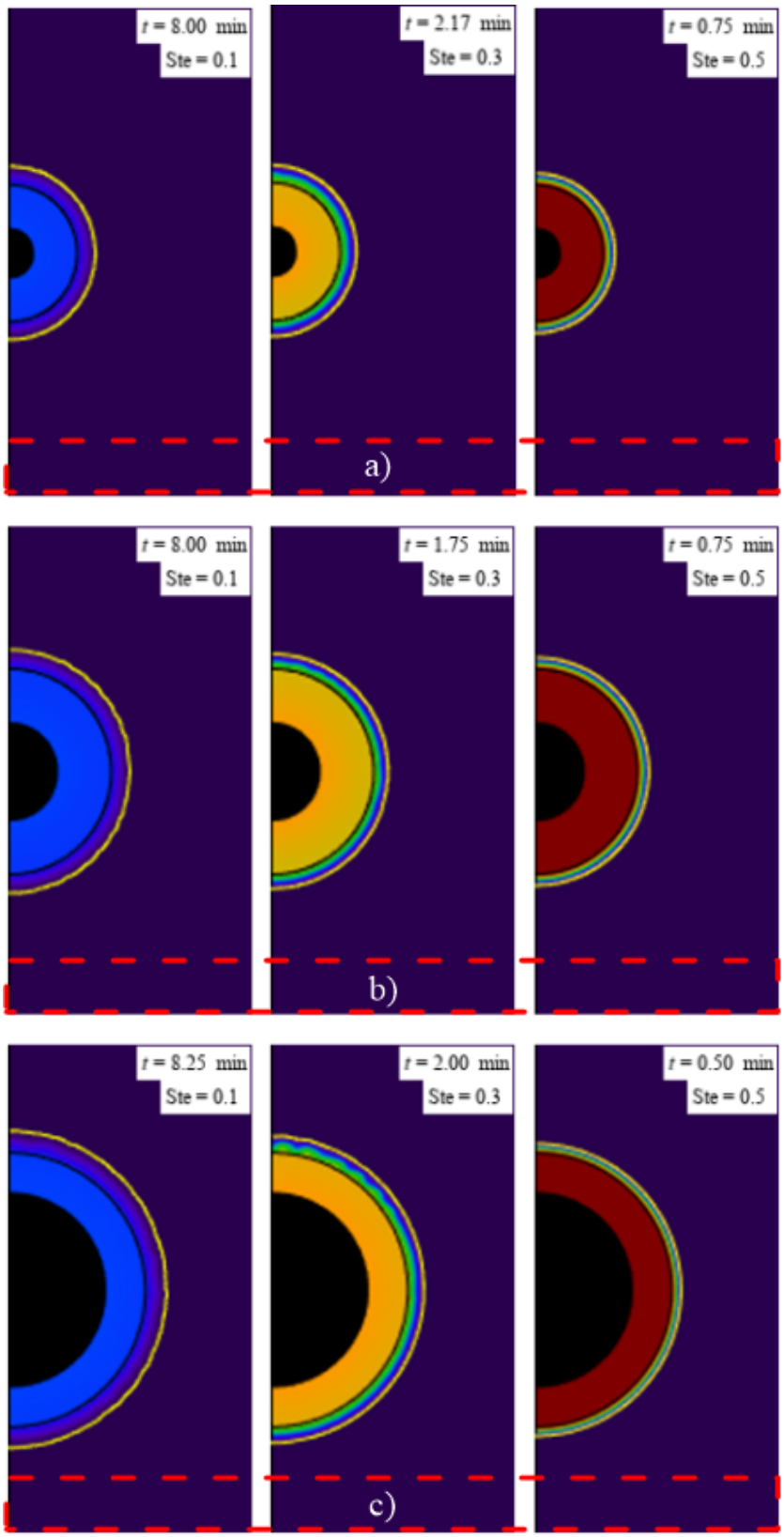

Figure 9.8 Solid-liquid interface locations from numerical studies at ΔT_s = 2.5 K for the center-tube diameter of a) 18 mm, b) 27 mm, and c) 36 mm.

As was done for experimental results, the appearance of the non-concentric shape of the melt front was taken as the criterion to identify the onset of natural convection. It can be seen from Figs. 9.7 and 9.8 that, as was in experimental results, the onset of convection occurs faster at high Stefan numbers. Also, it can be clearly seen that the radial thickness of the liquid PCM is larger at a low Stefan number than that at a high Stefan number. The difference in the radial thickness is not as appreciable with respect to the diameter of the center-tubes. All these results complement the ones from the experiments, presented in Chapter 5.

9.6.1.2 Melt volume at the onset of natural convection

The melt volumes, which in this study is the volume per unit length of the annuli, were calculated at the onset of natural convection using the built-in surface integrator in COMSOL. The melt volumes from the experimental profiles, presented in Chapter 5, are compared to those from numerical studies. The onset melt volumes from all the simulations and the corresponding ones from the experiments are presented in Fig. 9.9 against the diameter of the center-tube, and in Fig. 9.10 against the Stefan number. Qualitatively, the melt volumes from the simulations exhibit the same trend as those from the experiments.

The amount of melt volumes required for the emergence of convection in the simulation is larger compared to those in the experiments. It should be noted that a 'mushy zone' exists in the simulation domain in the proximity of the solid-liquid interface, which is not present in the experimental domain. This essentially means that all the properties of the PCM abruptly transforms from that of solid to liquid in the experiment. On the other hand, the properties such as thermal conductivity and viscosity of the PCM transition from that of solid to liquid over a temperature range (ΔT), the mushy zone thickness in the simulation domain. In this mushy zone, the viscosity of the PCM is much larger than the viscosity of the liquid PCM in the experimental domain. This high viscosity in the mushy zone would lead to an increased volume requirement for the onset of natural convection. This would mean a slower onset of convection in the simulation. However, most of the data indicate that the onset occurs faster in the simulation. It should be remembered here that the heat transfer is purely by conduction in this early stage and that the thermal conductivity of the PCM in the solid phase is more than twice of that in the liquid phase. Also, the thermal conductivity of the solid PCM transitions to that of the liquid PCM over the temperature range ΔT. This results in a higher thermal

conductivity in the mushy zone than in the liquid, which in turn results in more liquid PCM having higher thermal conductivity in the simulation domain than in the experimental domain. The thermal resistance to the conductive heat flow, *i.e.*, the resistance of the liquid layer between the heat source and the solid-liquid interface is smaller in the simulation domain than in the experimental domain. This difference between the simulation and experiment thus leads to a faster melting in simulation than in the experiment and, in turn, faster onset of natural convection.

Overall, more liquid PCM is required for the onset of convection as the center-tube diameter gets larger, and the change occurs linearly. Figure 9.10 shows that the onset volume of liquid PCM changes linearly with the Stefan number and less amount of liquid PCM is required as the Stefan number gets larger.

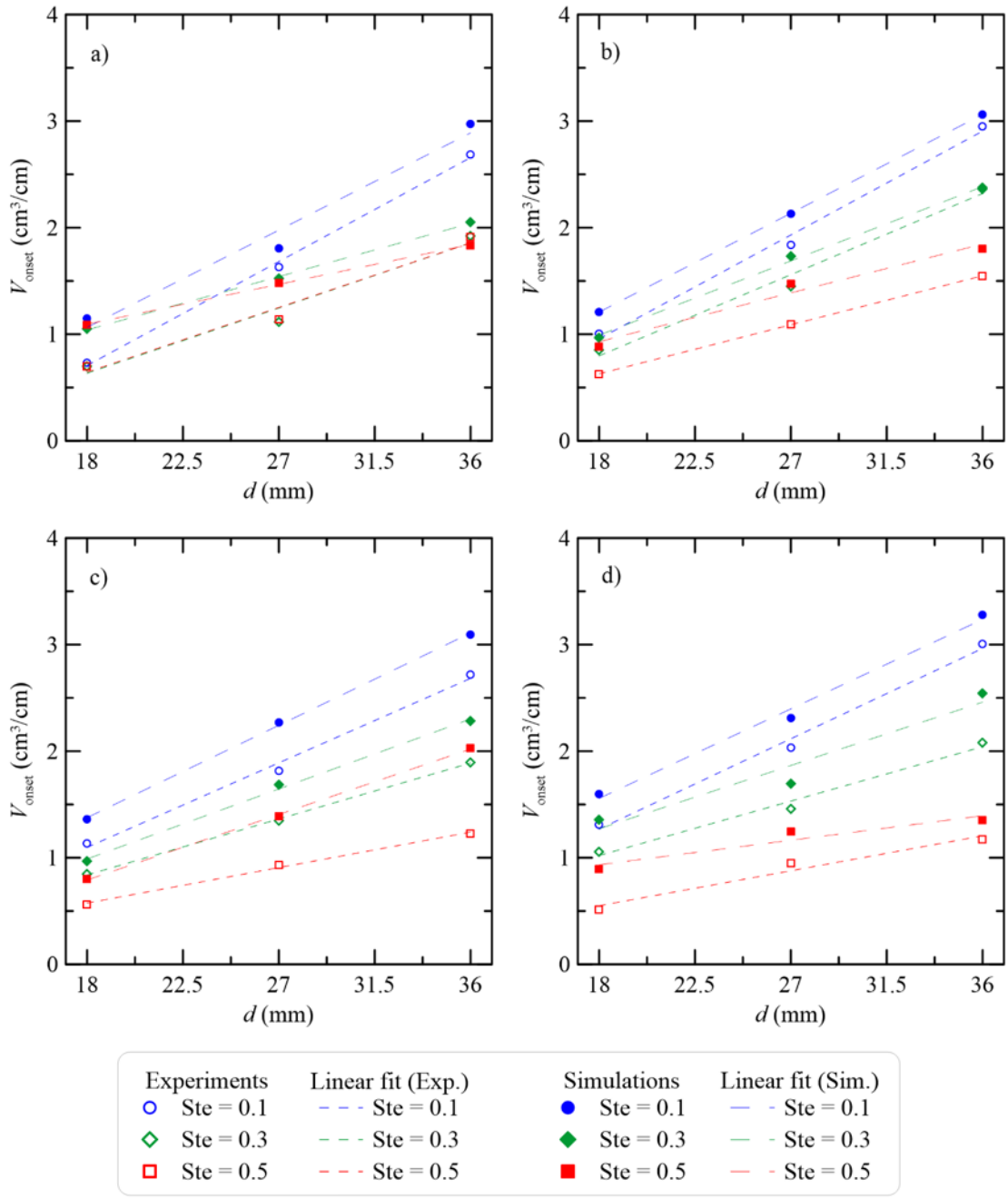

Figure 9.9 Comparison of experimental and numerical melt volume vs center-tube diameter at the onset of natural convection for: (a) ΔT_s = 22.5 K, (b) ΔT_s = 15 K, (c) ΔT_s = 7.5 K, and (d) ΔT_s = 2.5 K.

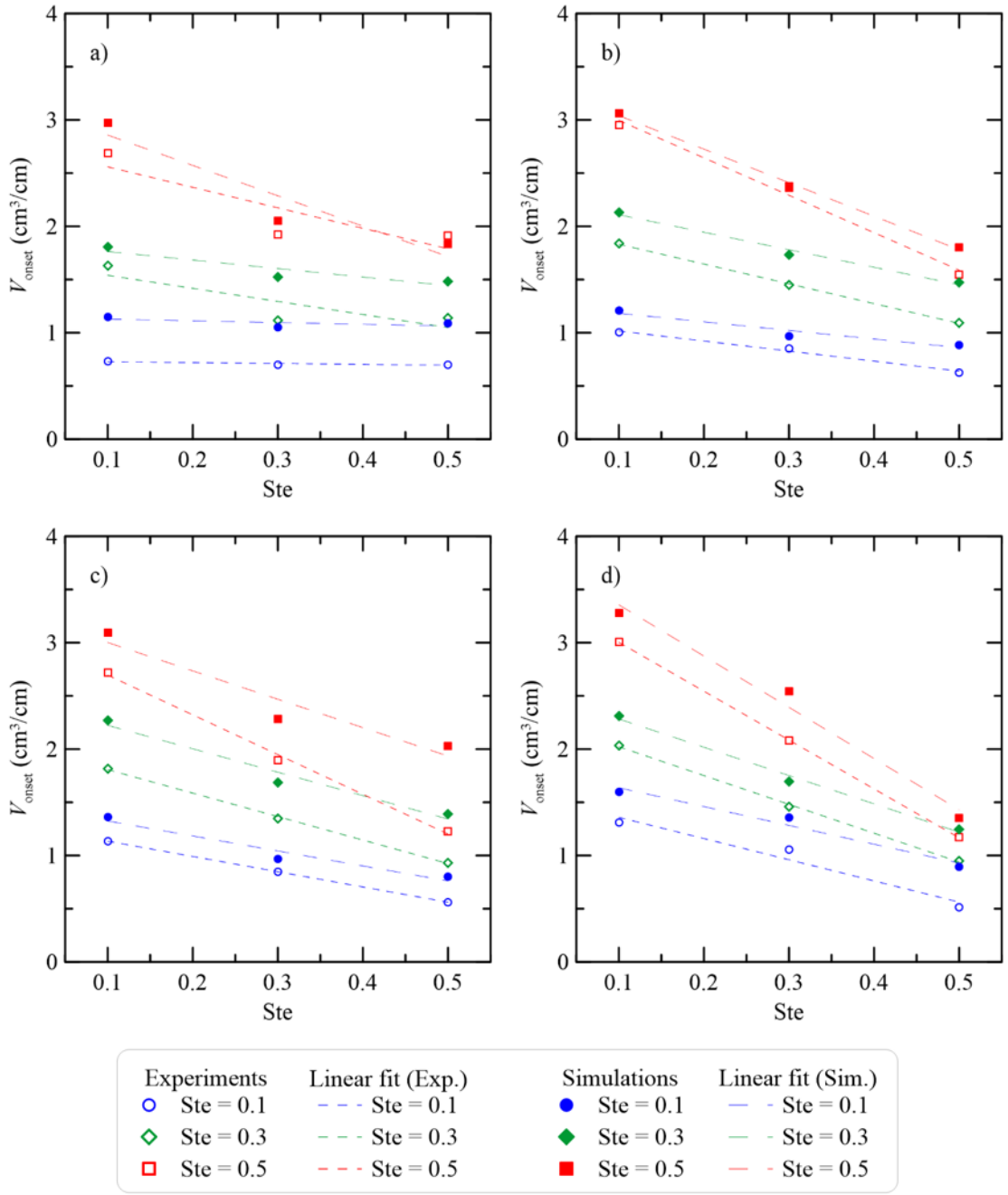

Figure 9.10 Comparison of experimental and numerical melt volume vs. Stefan number at the onset of natural convection for: (a) ΔT_s = 22.5 K, (b) ΔT_s = 15 K, (c) ΔT_s = 7.5 K, and (d) ΔT_s = 2.5 K.

9.6.1.3 Fourier number at the onset of natural convection

A correlation for the Fourier number at the onset of natural convection was developed using the same non-dimensional groups, as discussed in section 5.6 of Chapter 5. The onset Fourier

number obtained from the numerical study is presented in Fig. 9.11. The correlation is given as:

$$\mathrm{Fo_{onset}} = \frac{\mathrm{Ste_s^{0.3443}} \left(\frac{d}{D}\right)^{0.529}}{262.1\ \mathrm{Ste^{1.6495}}} - 0.0014839 \tag{9.8}$$

The indices for the different dimensionless groups in Eq. (9.8) are compared to those in Eq. (5.12), which is the experimental correlation, in Table 9.3. The table shows that the indices are comparable; the difference in the indices is attributable to the fact that the PCM melts faster in simulations than in experiments, which has already been discussed in subsection 9.6.1.2. The numerical results are not as well represented by the correlation as the experimental results are (see section 5.6 of Chapter 5).

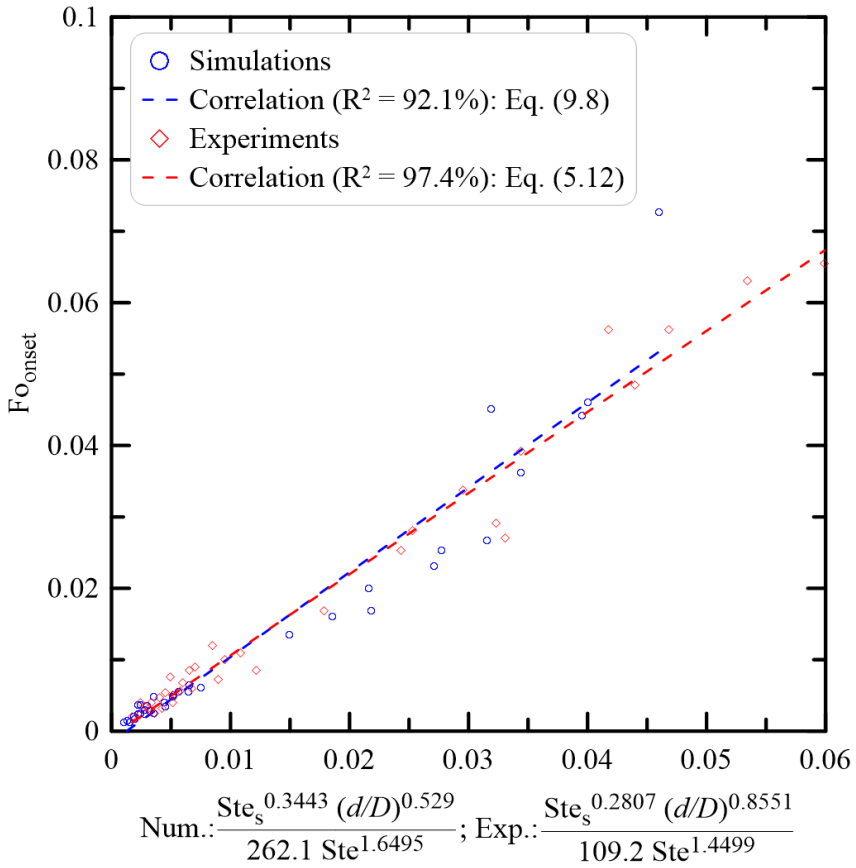

Figure 9.11 Correlation for the Fourier number at the onset of natural convection obtained from the numerical study on the melting of *n*-octadecane.

Table 9.3 Comparison of the indices of the variables in the numerical and experimental correlations for the onset Fourier number.

Dimensionless number	Simulation	Experiment
$\mathrm{Ste_s}$	0.3443	0.2807
d/*D*	0.529	0.8551
Ste	1.6495	1.4499
Constant	262.1	96.68

9.6.1.4 Rayleigh number at the onset of natural convection

A correlation for the Rayleigh number at the onset of natural convection was developed using the same non-dimensional groups, as discussed in section 5.6 of Chapter 5. The onset Rayleigh number obtained from the numerical study is presented in Fig. 9.12. The correlation is given as:

$$\mathrm{Ra_{onset}} = \frac{10^{9.34}\,\mathrm{Ste}^{0.9035}\left(\frac{d}{D}\right)^{2.6719}}{\mathrm{Ste_s}^{0.0163}} - 5308 \qquad (9.9)$$

The intercept (5308) in Eq. (9.9) is negligible compared to the Rayleigh number at the onset of natural convection. Neglecting the intercept, a simpler correlation for the onset Rayleigh number can be written as:

$$\mathrm{Ra_{onset}} = \frac{10^{9.34}\,\mathrm{Ste}^{0.9035}\left(\frac{d}{D}\right)^{2.6719}}{\mathrm{Ste_s}^{0.0163}} \qquad (9.10)$$

The indices for the different dimensionless groups in Eq. (9.10) are compared to those in Eq. (5.18), which is the experimental correlation, in Table 9.4. The table shows that the indices are very comparable between the experimental and numerical correlations.

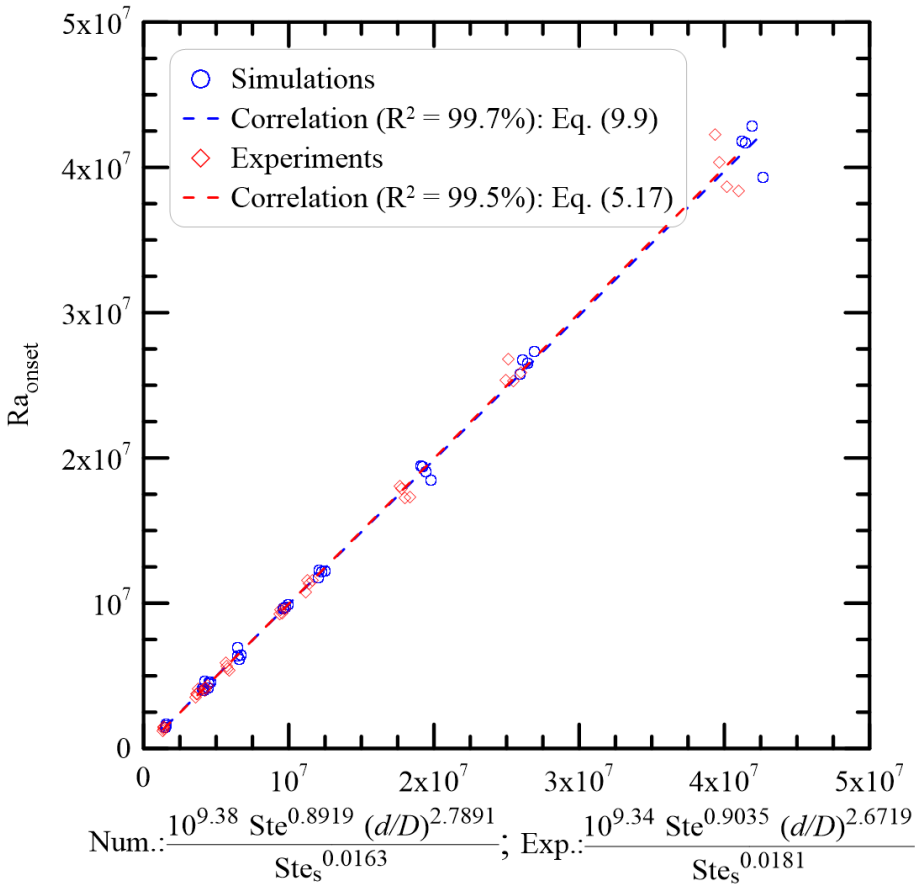

Figure 9.12 Correlation for the Rayleigh number at the onset of natural convection obtained from the numerical study on the melting of *n*-octadecane.

Table 9.4 Comparison of the indices of the variables in the numerical and experimental correlations for the onset Rayleigh number.

Dimensionless number	Simulation	Experiment
Ste_s	0.0163	0.0181
d/D	2.6719	2.7891
Ste	0.9035	0.8919
Constant	$10^{9.34}$	$10^{9.38}$

9.6.1.5 Maximum velocity of liquid PCM at the onset of natural convection

The maximum velocities of liquid PCM on the axial face at the onset of natural convection were obtained from COMSOL. These velocities are presented against Stefan numbers in Fig. 9.13. It can be seen from Fig. 9.13 that the maximum velocities span over a large range at every Stefan number and no clear trend is present in the data. These velocities were correlated to dimensionless variables, namely, Gr, Ste, and $\mathrm{Ste_s}$ as defined in Eqs. (7.12), (7.14), and (7.15), respectively. It should be noted that the outlying data points encircled with dashed lines in Fig. 9.13 were excluded from the correlation. The correlation is shown in Fig. 9.14. The maximum velocity at the onset of natural convection is given as in Eq. (9.11).

$$v_{\max} = 1.669 \times 10^{-4} \frac{\mathrm{Ste}^{0.5136}\,\mathrm{Gr}^{0.1589}}{\mathrm{Ste_s}^{0.0647}} + 5.062 \times 10^{-6} \tag{9.11}$$

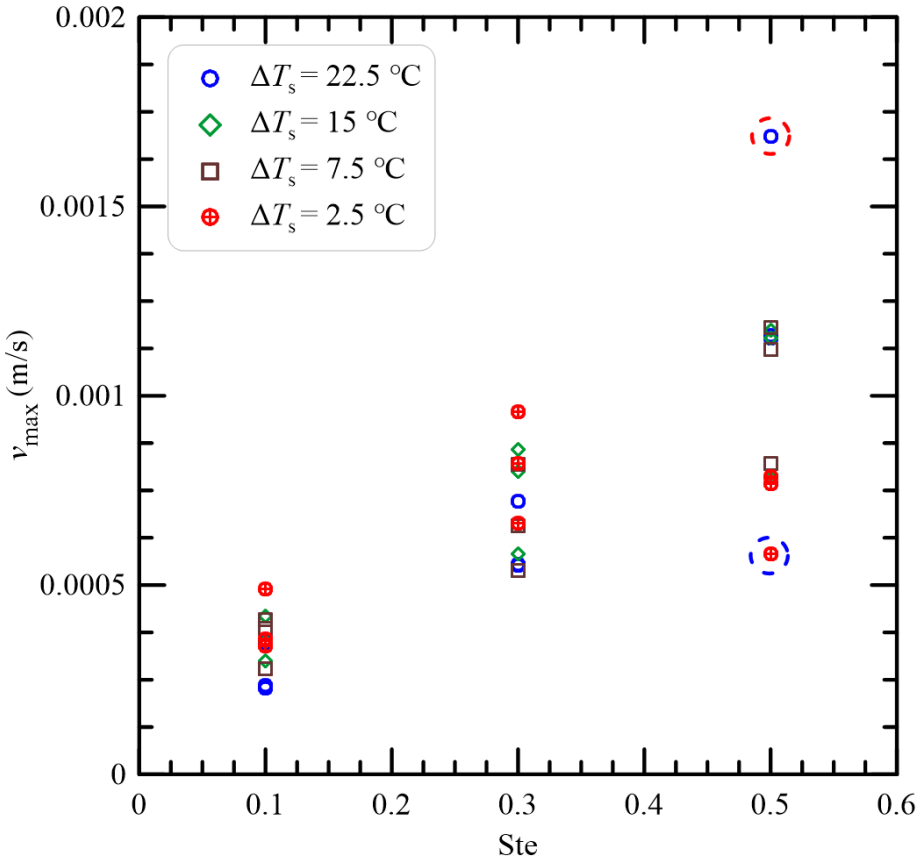

Figure 9.13 Maximum velocity of liquid PCM at the onset of natural convection.

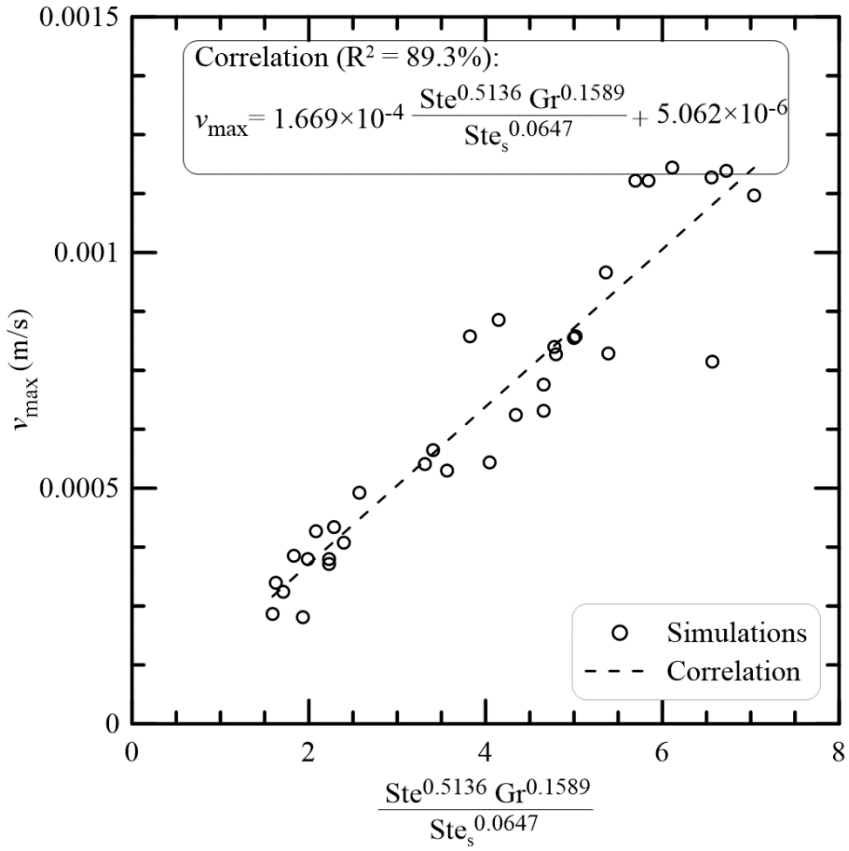

Figure 9.14 Correlation for the maximum velocity of liquid PCM at the onset of natural convection.

9.6.2 Global melting of n-octadecane

The transient melt volumes, the correlations for transient melt volumes, and the transient solid-liquid interfaces are presented in this section.

9.6.2.1 Transient melt volumes

The volumes of liquid PCM over eight hours of melting are presented in Fig. 9.15 for different subcooled conditions. The figure shows that the melt volumes from the numerical simulations are comparable to those obtained from the experiments for every case of geometric and thermal conditions. This shows that numerical models can predict the experimental results. The overall melt volume curves follow the same trend regardless of the degree of subcooling. Also, after an eight-hour melting period, the subcooling of the PCM does not show a significant impact on the melt volumes. Nevertheless, the melt volume curves show a similar pattern for the Stefan numbers of 0.3 and 0.5, and this pattern is entirely different from that when the Stefan number is 0.1. The results from other

experiments (Ste = 0.2 and 0.4 in addition to the ones shown here), presented in Chapter 8, indicate that the similarity in the melt volume curve is achieved when the Stefan number is 0.2 or above.

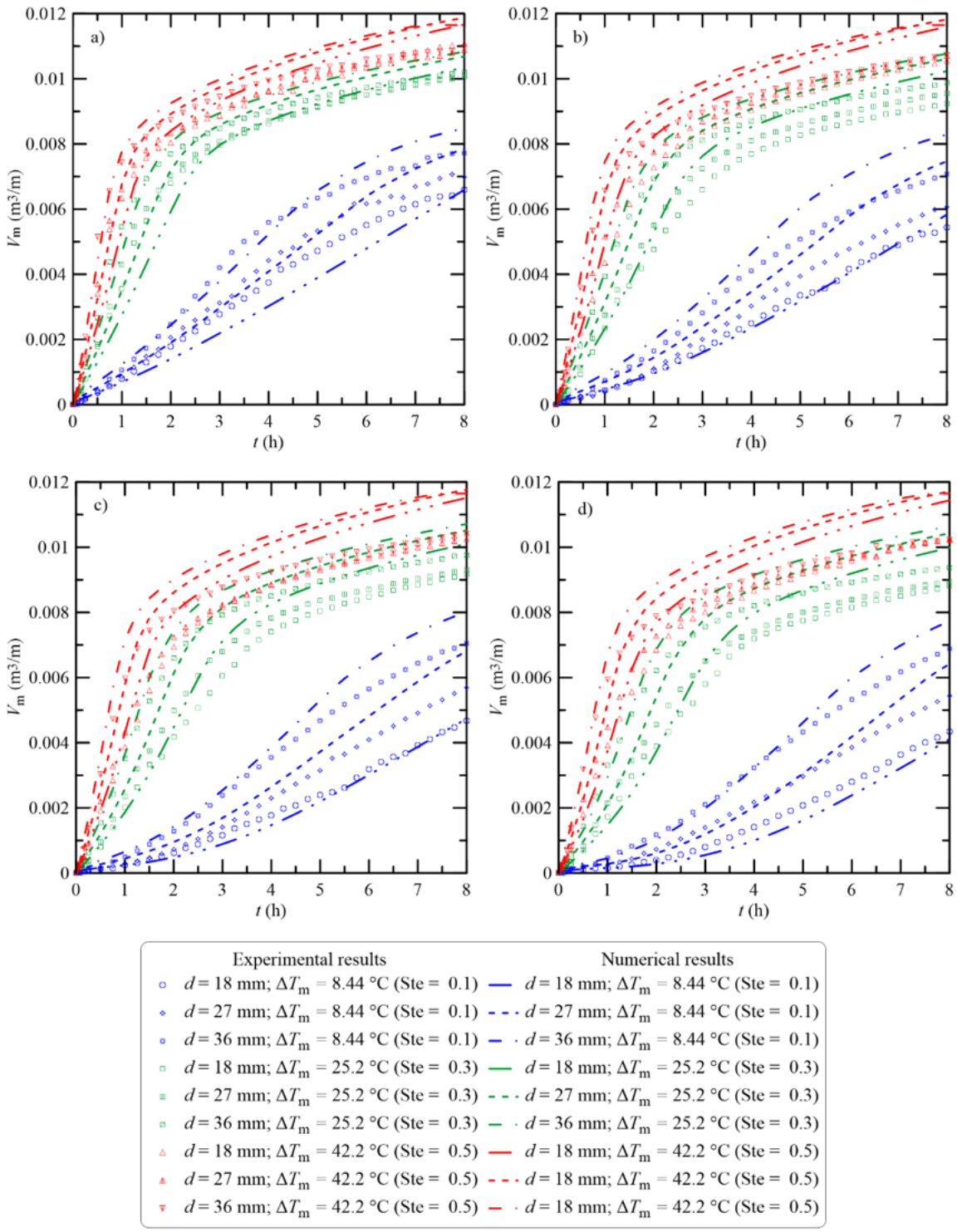

Figure 9.15 Comparison of melting of *n*-octadecane from experimental and numerical studies when it is subcooled by: a) ΔT_s = 2.5 °C, b) ΔT_s = 7.5 °C, c) ΔT_s = 15 °C, and d) ΔT_s = 22.5 °C.

9.6.2.2 Correlations for the transient melt volumes

As mentioned in subsection 9.6.2.1, the melt volumes exhibit the same trend when the Stefan number is 0.2 or larger. Consequently, the correlations developed for the experimental results presented in Chapter 8, are used for the results obtained from the numerical study for Stefan numbers of 0.3 and 0.5. The results from the dimensional analysis are presented in Fig. 9.16.

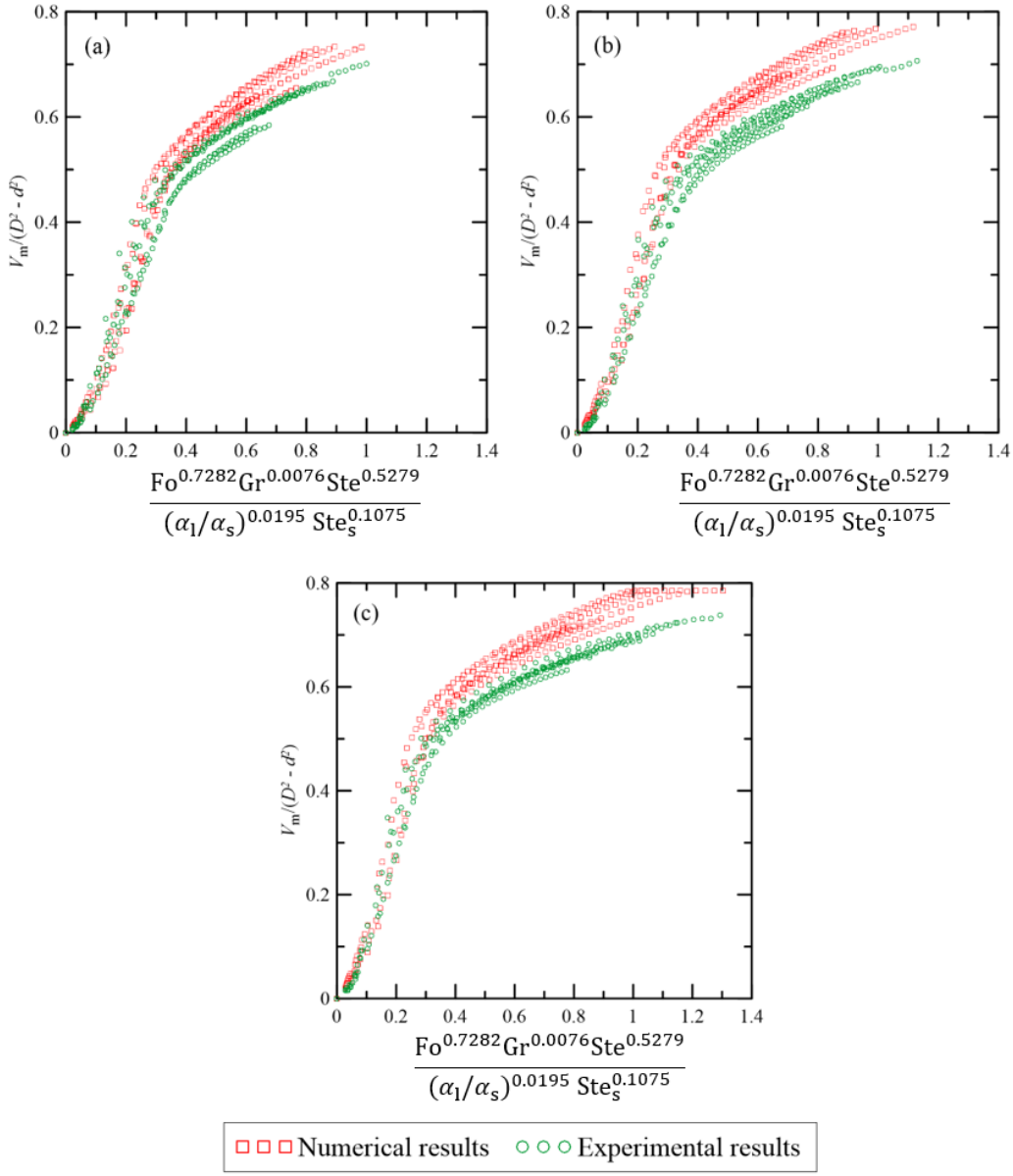

Figure 9.16 Correlations for the numerical study of melting of *n*-octadecane for the center-tube diameter of the enclosures: (a) 18 mm, (b) 27 mm, and (c) 36 mm.

In Fig. 9.16, the green symbols represent the experimental melt volumes under different thermal conditions, and the red symbols represent the melt volumes from the numerical simulations under the corresponding thermal conditions. The melt volumes from the numerical simulations are slightly larger than those obtained from the experiments, especially during the last stage of the melting process, *i.e.*, during the phase when conduction dominates the melting process below the center-tubes.

The likely reason for this discrepancy is the difference between the simulated domain and the experimental setup. In the experiment, water at the melting temperature of the PCM was circulated through the axial faces of the annulus so that the melt interface would be visible by the camera. While the liquid PCM inside the annulus would be in a higher than melting temperature, heat from the liquid PCM would be transferred to the circulating water. Since at the beginning of the melting process, natural convection is very dominant, and the liquid volume is small, the heat loss to the water faces is not significant. As the melting process goes on, the liquid volume increases and natural convection starts to become less significant, the heat loss through the faces increases and causes slower melting in the experiment. On the contrary, there is no heat loss through the faces in the simulation, and thus slightly more melting in the simulations. Nonetheless, the figure shows that the melt volumes from numerical studies can be represented by the same correlations that are obtained from the experimental results. The non-dimensional melt volumes in the different geometries can be predicted by the same equation presented in Chapter 8, Eq. (8.1).

9.6.2.3 Transient melt profiles

In order to design efficient latent heat energy storage systems, it is crucial to be able to predict the shape of the solid-liquid interfaces under different geometric and thermal conditions. It is, therefore, critical for any numerical model to be able to predict the solid-liquid interface correctly. The predictability of the current model was tested in the present study; the melt profiles from simulations and experiments are presented in Fig. 9.17 for the PCM that was subcooled by 22.5 K and in Fig. 9.18 for the PCM that was subcooled by 2.5 K. In those figures, points represent experimental results and lines represent numerical ones. The figures show that the models can reasonably predict the shape of the solid-liquid interfaces.

The models have better predictability of the solid-liquid interfaces in the early stages of the melting process compared to the later stages, especially once the melting is dominated by conduction heat transfer. This is because, as has already been mentioned, in experiments, water at the melting temperature of the PCM was circulated through the axial faces of the annulus that would take away heat from the experimental domain. There was no such circulation of water in the simulations and, therefore, no drawing of heat from the simulation domain, eventually leading to more melting in the simulation than in the experiment. It can be anticipated that in an applied heat storage system, where there would be no need to circulate water through the axial faces, the shape of the solid-liquid interface would be more predictable.

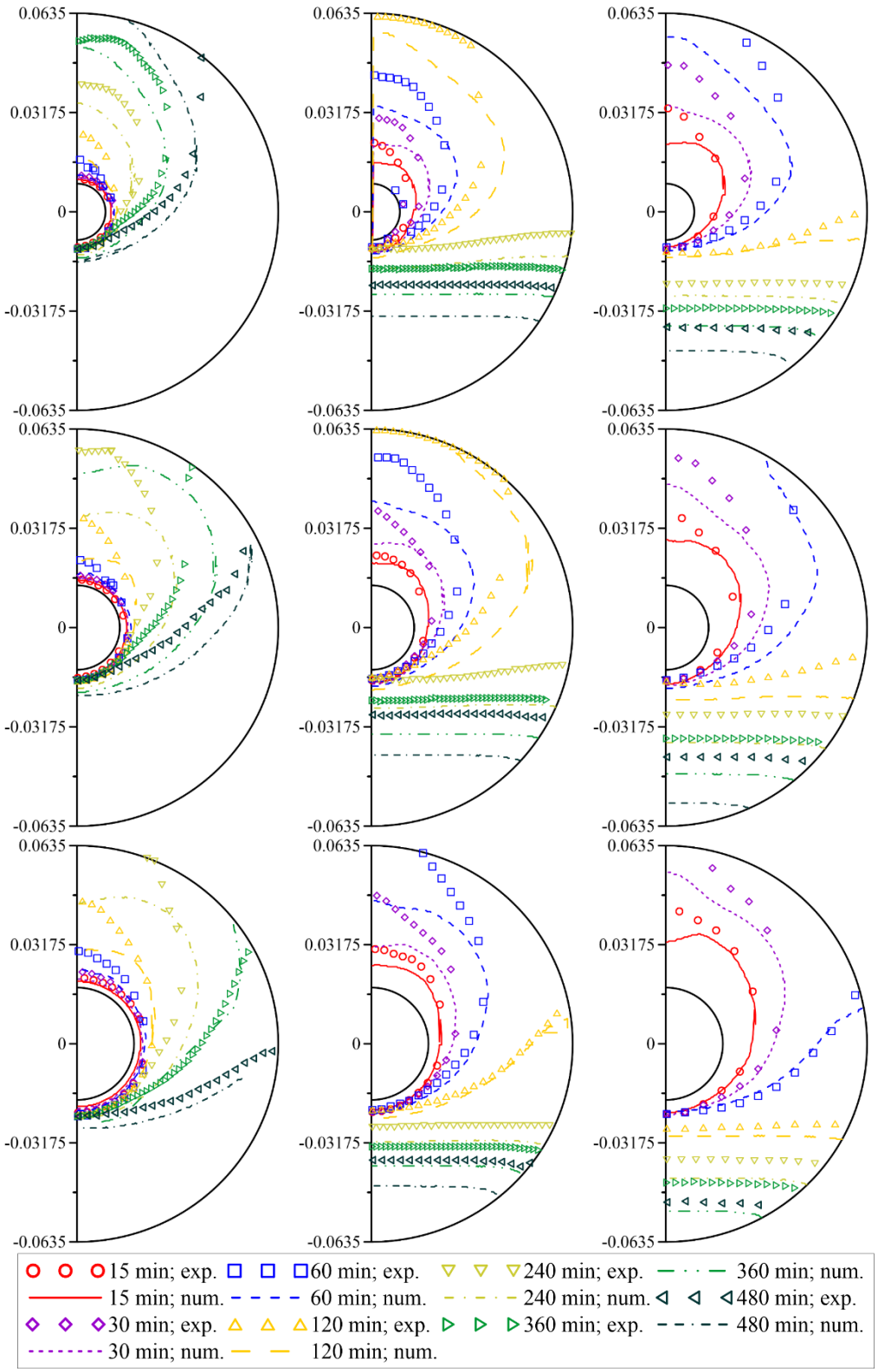

Figure 9.17 Comparison of solid-liquid interface position from experimental and numerical studies at ΔT_s = 22.5 K for the center-tube diameter of 18 mm, 27 mm, and 36 mm (from top to bottom row) and Stefan number of 0.1, 0.2 and 0.3 (from left to right column). The dimensions on the vertical axis are in m.

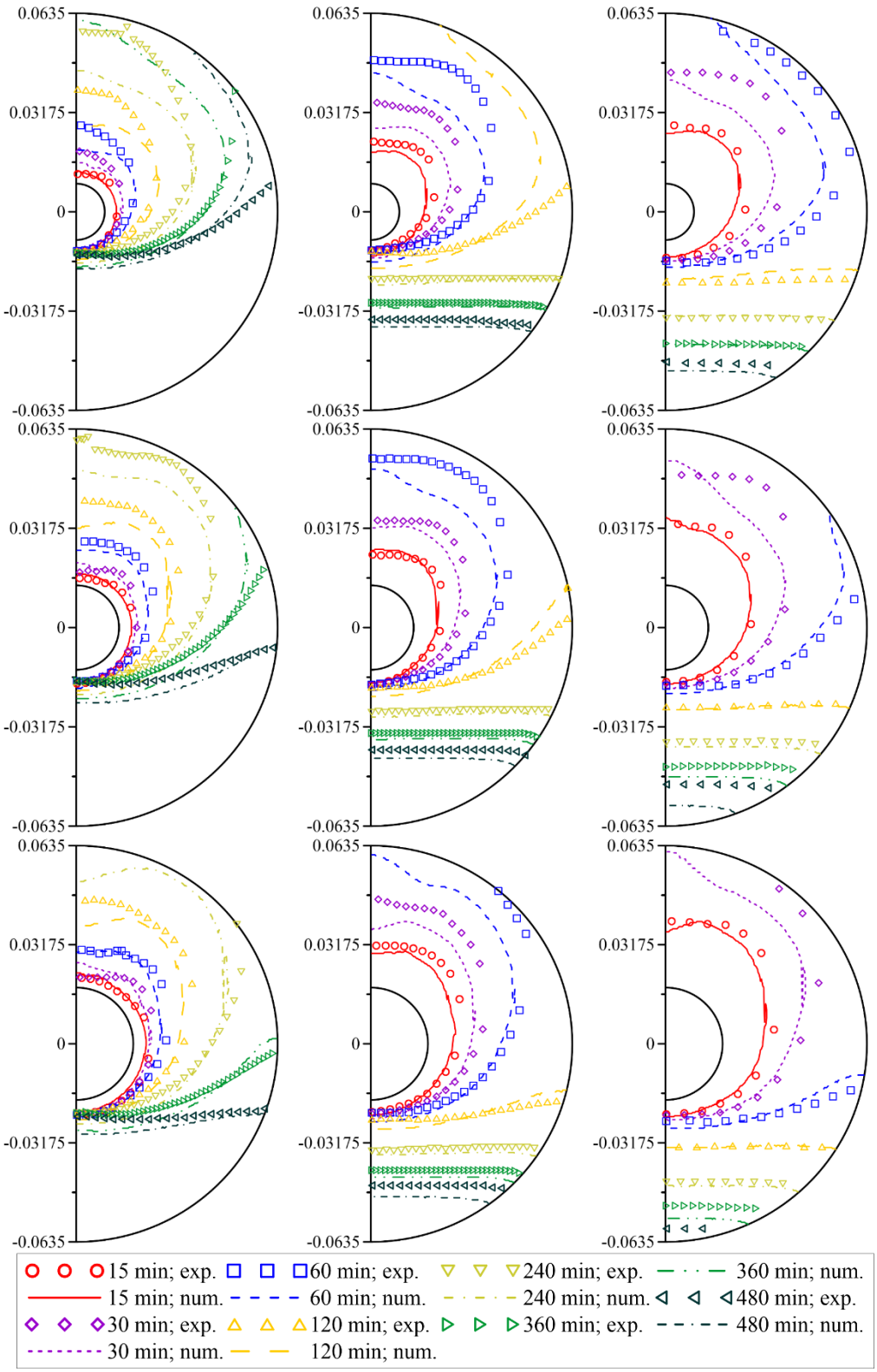

Figure 9.18 Comparison of solid-liquid interface position from experimental and numerical studies at ΔT_s = 2.5 K for the center-tube diameter of 18 mm, 27 mm, and 36 mm (from top to bottom row) and Stefan number of 0.1, 0.2 and 0.3 (from left to right column). The dimensions on the vertical axis are in m.

9.7 Conclusions

The 'mushy zone' constant (A_{mush}) and 'mushy zone' temperature range (ΔT) affect the melting dynamics differently based on the heating temperature differential and the size of the heating surface. In general, the melting rate slows down at higher values of A_{mush} and ΔT, although the latter has a greater impact at high heating temperature differentials. In the case of a larger heating surface, ΔT has a less significant impact on melting compared to the case where the heating surface is smaller.

It was found that the value of A_{mush} could have a single value (10^{10}) regardless of the geometry and thermal condition. However, different values of ΔT is required for different thermal conditions to mimic the experimental results. These values of ΔT were 0.5, 3, and 5 K for the Stefan numbers of 0.1, 0.3, and 0.5, respectively.

Correlations for the onset of natural convection and global melt volumes were developed. The correlation for the onset Rayleigh number, derived from the numerical studies, are in-line with those obtained from experiments. Also, the correlation for the onset Fourier number obtained from the numerical study is comparable to that obtained from experiments. Besides, the relationships of global melt volume with the different geometric and operational parameters derived numerically commensurate the ones obtained experimentally. However, the PCM melts slightly faster at the last stage of the melting process (conduction dominated) in the simulations.

The velocity of liquid PCM at the onset of natural convection can be represented by the equation:

$$v_{\max} = 1.669 \times 10^{-4} \frac{\mathrm{Ste}^{0.5136}\ \mathrm{Gr}^{0.1589}}{\mathrm{Ste}_s^{0.0647}} + 5.062 \times 10^{-6}\ \mathrm{m/s}$$

CHAPTER 10 CONCLUSIONS AND RECOMMENDATIONS

The objective of this study was to gain insights on how different geometric and thermal parameters influence the onset of natural convection during melting of PCMs. The conclusions of the results are first presented in section 10.1 for the onset of natural convection and then in section 10.2 for global melting. Then the conclusions from numerical studies are presented for both in section 10.3. The recommendations for future work follow in section 10.4.

10.1 The onset of natural convection

10.1.1 Melting of n-octadecane

During melting of *n*-octadecane, more liquid PCM is required for the onset of convection when the PCM is heated at low temperatures. Also, more liquid PCM is required for the onset of convection when the center-tube is large.

It was observed that the onset of convection occurs faster when the PCM is heated at a higher temperature. Overall, it takes longer for the onset of natural convection when the PCM is subcooled to a greater extent; however, some exceptions exist. Additionally, no clear trend is observed in the present study for the onset time as the diameter of the center-tube changes. The onset time reduced nonlinearly as the Stefan number increased.

It was observed that the subcooling of the PCM played a significant role in the onset of convection. When the PCM was barely subcooled, the Stefan number influenced the onset of convection to a greater extent than when the PCM was substantially subcooled.

A correlation was developed for the Fourier number at the onset of convection that can be used to predict the convection onset time for melting of *n*-octadecane in enclosures with different center-tube diameters, heated at different temperatures and the PCM being from barely to substantially subcooled. The correlation is given as:

$$\mathrm{Fo}_{\mathrm{onset}} = \frac{\mathrm{Ste}_s^{0.2807}\left(\frac{d}{D}\right)^{0.8551}}{96.68\ \mathrm{Ste}^{1.4499}} - 0.0011648$$

Also, a correlation was developed for the onset Rayleigh number that can be used to predict the volume of liquid PCM at the onset of convection, regardless of the size of the center-tube, the heating temperature, and the degree of subcooling. The correlation is given as:

$$\mathrm{Ra}_{\mathrm{onset}} = \frac{10^{9.38}\ \mathrm{Ste}^{0.8919}\ \left(\frac{d}{D}\right)^{2.7891}}{\mathrm{Ste}_{\mathrm{s}}^{0.0181}}$$

10.1.2 Melting of dodecanoic acid

The results from the melting of dodecanoic acid lead to the same conclusions as those for *n*-octadecane. The correlation for onset Fourier number during melting of dodecanoic acid is given as:

$$\mathrm{Fo}_{\mathrm{onset}} = \frac{\mathrm{Ste}_{\mathrm{s}}^{0.1371}\left(\frac{d}{D}\right)^{0.7140}}{167.6\ \mathrm{Ste}^{1.5101}} - 0.0004004$$

The correlation for the Rayleigh numbers at the onset of natural convection is given as:

$$\mathrm{Ra}_{\mathrm{onset}} = \frac{10^{9.15}\ \mathrm{Ste}^{0.8924}\ \left(\frac{d}{D}\right)^{2.7729}}{\mathrm{Ste}_{\mathrm{s}}^{0.0614}}$$

10.1.3 General conclusions

All the conclusions drawn for *n*-octadecane also apply for the combined results of the two PCMs. A general correlation, for non-dimensional melt volumes at the onset of convection, was developed using dimensionless groups such as Ste, $\mathrm{Ste_s}$, Gr, and (α_l/α_s). The correlation is given as:

$$\frac{V_{\mathrm{onset}}}{d^2} = \frac{1.63}{\mathrm{Gr}^{0.2251}\ \mathrm{Ste}^{0.1168}\ \mathrm{Ste_s}^{0.0886}\ \left(\frac{\alpha_l}{\alpha_s}\right)^{0.1428}} - 3.89 \times\ 10^{-4}$$

The experimental data are best represented by the Rayleigh number at the onset of natural convection. The height of the liquid column projected on the central vertical plane at the onset of convection was adopted as the length scale in the definition of the onset Rayleigh number. The correlation for the onset Rayleigh number was developed using the

dimensionless numbers, which are Stefan number that accounts for sensible heat transfer only in the liquid phase (Ste), Degree of Subcooling or the Stefan number that accounts for sensible heat transfer only in the solid phase ($\mathrm{Ste_s}$), the ratio of the diameters (d/D), and the ratio of the thermal diffusivities ($\alpha_\mathrm{l}/\alpha_\mathrm{s}$). The correlation is given by:

$$\mathrm{Ra_{onset}} = \frac{10^{9.22}\ \mathrm{Ste}^{0.8921}\ \left(\frac{d}{D}\right)^{2.7830}}{\mathrm{Ste_s}^{0.0344}\ \left(\frac{\alpha_\mathrm{l}}{\alpha_\mathrm{s}}\right)^{0.3661}}$$

If the melting temperature differentials, subcooling temperature differentials, geometric dimensions, and the properties of the PCMs are known, then the Rayleigh number at the onset of convection can be calculated from the above equation. This onset Rayleigh number can be used to calculate the projected height of the liquid PCM surrounding the center-tubes. Since the solid-liquid interfaces remain concentric until the natural convection onset occurs, the volume at the onset of natural convection can be calculated.

10.2 Global melting of the PCMs

For the global melting of the PCMs, it can be concluded that the PCMs melt faster at higher Stefan numbers and when the size of the heat source is large. It can also be concluded that at high melting temperature differentials, dodecanoic acid melts slightly slower than *n*-octadecane although the former has a slightly smaller latent heat of fusion. The difference in melting rates becomes more pronounced when the PCMs are barely subcooled, and the Stefan number is low.

A correlation was developed for the transient melt volumes using several dimensionless groups, which is given as:

$$\frac{V_\mathrm{m}}{D^2 - d^2} = \frac{0.7294}{1 + \left(\frac{X_G}{0.2628}\right)^{-1.833}}$$

where

$$X_{\mathrm{G}} = \frac{\mathrm{Fo}^{0.7282}\mathrm{Gr}^{0.0068}\mathrm{Ste}^{0.5285}}{(\alpha_{\mathrm{l}}/\alpha_{\mathrm{s}})^{0.0202}\ \mathrm{Ste}_{\mathrm{s}}^{0.1075}(d/D)^{0.0029}}$$

10.3 Conclusions of the numerical study

The 'mushy zone' constant (A_{mush}) and 'mushy zone' temperature range (ΔT) affect the melting dynamics differently based on the heating temperature differential. In general, the melting rate slows down at higher values of A_{mush} and ΔT, although the latter has a greater impact at high heating temperature differentials. In the case of a larger heating surface, ΔT has a less significant impact on melting compared to the case where the heating surface is smaller.

It was found that the value of A_{mush} could have a single value (10^{10}) regardless of the geometry and thermal condition. However, different values of ΔT is required for different thermal conditions to mimic the experimental results. These values of ΔT were 0.5, 3, and 5 K for the Stefan numbers of 0.1, 0.3, and 0.5, respectively.

Correlations for the onset of natural convection and global melt volumes were developed. The correlation for the onset Rayleigh number, derived from the numerical studies, are in-line with those obtained from experiments. Also, the correlation for the onset Fourier number obtained from the numerical study is comparable to that obtained from experiments. In addition, the relationships of global melt volume with the different geometric and operational parameters derived numerically commensurate the ones obtained experimentally. However, the PCM melts slightly faster at the last stage of the melting process (conduction dominated) in the simulations.

The velocity of liquid PCM at the onset of natural convection can be represented by the equation:

$$v_{\max} = 1.669 \times 10^{-4}\,\frac{\mathrm{Ste}^{0.5136}\ \mathrm{Gr}^{0.1589}}{\mathrm{Ste}_{\mathrm{s}}^{0.0647}} + 5.062 \times 10^{-6}\ \mathrm{m/s}$$

10.4 Recommendations for future work

Improvement of this study can be made both on the experimental setup and the experimental study. The recommendations to improve the experimental setup are provided in subsection 10.4.1, and those to improve experimental results are provided in subsection 10.4.2.

10.4.1 Recommendations on the experimental setup

In the present study, three enclosures with center-tube diameters of 18, 27, and 36 mm were used. Parallel experiments were run in all three enclosures. Water baths were used to circulate hot water through the center-tubes. One bath was dedicated to circulating water through the 36 mm center-tube. Another bath was used to circulate water through the 18 and 27 mm center-tubes. The flow rate of the bath was not high enough to precisely control the tube temperature. If the temperature of one tube was to be controlled precisely, then sacrifice had to be made on the other tube. It is recommended that one bath should be dedicated to circulating water through each center-tube or more powerful baths to be used.

Web cameras were used in the present study to record images of the melt fronts. The distance of the cameras from the PCM enclosures was not the same from experiment to experiment. Therefore, it was very important to calibrate the cameras before each experiment was run. It is recommended that a single metal frame will be fabricated that will hold the PCM enclosures and the web cameras rigidly. This will remove the risk of displacement of the cameras from experiment to experiment.

10.4.2 Recommendations for future study

The experimental results show that only a small amount of PCM melts surrounding the center-tubes when the onset of convection occurs. Therefore, the diameter of the center-tube is the most important geometric parameter. However, ideally, no heat would be conducted to the solid PCM when it is not subcooled; but the heat would be conducted to the solid portion when it is substantially subcooled. In the latter case, the diameter of the outer shell also plays an important role in the onset of natural convection. In the present study, the ratio of d/D was varied by varying the diameter of the center-tube and leaving the diameter of the outer shell unchanged. It is recommended that the ratio of d/D be varied

by changing the diameter of the outer shell and keeping the diameter of the center-tube unchanged; also, by varying both the diameters. The results should be compared to the current ones to verify if the proposed correlations still hold.

Only thermal analysis was done in the present study, and no study on fluid dynamics was done. In the extant literature, it has been reported that during the melting process, cells of rotating fluid form in the liquid portion of the PCM, which have been reviewed in Chapter 2 of this thesis. It has been reported that the number of cells and their interaction, and whether the flow is laminar or turbulent depend on the geometric and thermal operating conditions. However, all those studies were done numerically. A fluid dynamic study for the liquid portion will reveal if any rotating cells form in the liquid portion of the PCM and how it affects the onset of natural convection. The present study proposes correlations based on the geometric and thermal parameters. A fluid dynamic analysis may lead to correlation with parameters such as the experimentally obtained velocities of the liquid PCM at the onset of natural convection. Therefore, a fluid dynamic analysis will add another dimension to the present study.

REFERENCES

Abdulateef, A. M., Abdulateef, J., Sopian, K., Mat, S., and Ibrahim, A. (2019). Optimal fin parameters used for enhancing the melting and solidification of phase-change material in a heat exchanger unite. *Case Studies in Thermal Engineering,* 14**,** 12p.

Abedin, A. H., and Rosen, M. A. (2011). A Critical Review of Thermochemical Energy Storage Systems. *The Open Renewable Energy Journal,* 4**,** 42-46.

Aberneth, R. B., Benedict, R. P., and Dowdell, R. B. (1985). ASME Measurement Uncertainty. *Journal of Fluids Engineering,* 107**,** 161-164.

Abhat, A. (1983). Low temperature latent heat thermal energy storage: heat storage materials. *Solar Energy,* 30**,** 313-332.

Adine, H. A., and El Qarnia, H. (2009). Numerical analysis of the thermal behaviour of a shell-and-tube heat storage unit using phase change materials. *Applied Mathematical Modelling,* 33**,** 2132-2144.

Adref, K. T., and Eames, I. W. (2002). Experiments on charging and discharging of spherical thermal (ice) storage elements. *International Journal of Energy Research,* 26**,** 949-964.

Agrawal, A., and Sarviya, R. M. (2015). Numerical investigation of the effects of natural convection on the melting process of phase change material in cylindrical annulus. *International Journal for Research in Applied Science & Engineering Technology (IJRASET),* 3**,** 853-861.

Agyenim, F., Eames, P., and Smyth, M. (2009). A comparison of heat transfer enhancement in a medium temperature thermal energy storage heat exchanger using fins. *Solar Energy,* 83**,** 1509-1520.

Agyenim, F., Hewitt, N., Eames, P., and Smyth, M. (2010). A review of materials, heat transfer and phase change problem formulation for latent heat thermal energy storage systems (LHTESS). *Renewable and Sustainable Energy Reviews,* 14**,** 615-628.

Akhilesh, R., Narasimhan, A., and Balaji, C. (2005). Method to improve geometry for heat transfer enhancement in PCM composite heat sinks. *International Journal of Heat and Mass Transfer,* 48**,** 2759-2770.

Allen, M. J., Bergman, T. L., Faghri, A., and Sharifi, N. (2015). Robust Heat Transfer Enhancement During Melting and Solidification of a Phase Change Material Using a Combined Heat Pipe-Metal Foam or Foil Configuration. *Journal of Heat Transfer,* 137**,** 102301-1 - 102301-12.

Alshqirate, A. a. S., Tarawneh, M., and Hammad, M. (2012). Dimensional Analysis and Empirical Correlations for Heat Transfer and Pressure Drop in Condensation and

Evaporation Processes of Flow Inside Micropipes: Case Study with Carbon Dioxide (CO2). *J. of the Braz. Soc. of Mech. Sci. & Eng.,* XXXIV**,** 89-96.

Aneke, M., and Wang, M. (2016). Energy storage technologies and real life applications – A state of the art review. *Applied Energy,* 179**,** 350-377.

Archibold, A. R., Gonzalez-Aguilar, J., Rahman, M. M., Yogi Goswami, D., Romero, M., and Stefanakos, E. K. (2014). The melting process of storage materials with relatively high phase change temperatures in partially filled spherical shells. *Applied Energy,* 116**,** 243-252.

Assis, E., Katsman, L., Ziskind, G., and Letan, R. (2007). Numerical and experimental study of melting in a spherical shell. *International Journal of Heat and Mass Transfer,* 50**,** 1790-1804.

Avci, M., and Yazici, M. Y. (2013). Experimental study of thermal energy storage characteristics of a paraffin in a horizontal tube-in-shell storage unit. *Energy Conversion and Management,* 73**,** 271-277.

Azad, M., Groulx, D., and Donaldson, A. (2017). A Study of the Onset of Natural Convection during Melting of PCMs in a Cylindrical Enclosure. *Proceedings of CHT-17 ICHMT International Symposium on Advances in Computational Heat Transfer*, Napoli, Italy, 1133-1155.

Azad, M., Groulx, D., and Donaldson, A. (2016). Melting of Phase Change Materials in a Cylindrical Enclosure: Parameters Influencing Natural Convection Onset. *4th International Forum on Heat Transfer*, Sendai, Japan, 6p.

Baetens, R., Jelle, B. P., and Gustavsen, A. (2010). Phase change materials for building applications: A state-of-the-art review. *Energy and Buildings,* 42**,** 1361-1368.

Bathelt, A. G. (1979). *Experimental study of heat transfer during solid liquid phase change around a horizontal heat source/sink.* PhD, Purdue University. 214p.

Bathelt, A. G., and Viskanta, R. (1980). Heat transfer at the solid-liquid interface during melting from a horizontal cylinder. *International Journal of Heat and Mass Transfer,* 23**,** 1493-1503.

Benard, C., Gobin, D., and Martinez, F. (1985). Melting in Rectangular Enclosures: Experiments and Numerical Simulations. *Journal of Heat Transfer,* 107**,** 794-803.

Biwole, P. H., Groulx, D., Souayfane, F., and Chiu, T. (2018). Influence of fin size and distribution on solid-liquid phase change in a rectangular enclosure. *International Journal of Thermal Sciences,* 124**,** 433-446.

C. Kheirabadi, A., and Groulx, D. (2015). The Effect of the Mushy-Zone Constant on Simulated Phase Change Heat Transfer. *CHT-15 ICHMT International Symposium on Advances in Computational Heat Transfer*, Piscataway, USA, 22 p.

C. Kheirabadi, A., Kabbara, M., and Groulx, D. (2016). Geometrical impacts on phase change heat transfer modeling. *Proceedings of the First Pacific Rim Thermal Engineering Conference, PRTEC*, Hawaii's Big Island, USA, 5p.

Cai, S., Cremaschi, L., and Ghajar, A. J. (2014). Pipe insulation thermal conductivity under dry and wet condensing conditions with moisture ingress: A critical review. *HVAC&R Research,* 20**,** 458-479.

Cao, X., Yuan, Y., Xiang, B., Sun, L., and Xingxing, Z. (2018). Numerical investigation on optimal number of longitudinal fins in horizontal annular phase change unit at different wall temperatures. *Energy and Buildings,* 158**,** 384-392.

Carrillo, A. J., Moya, J., Bayón, A., Jana, P., De La Peña O'shea, V. A., Romero, M., Gonzalez-Aguilar, J., Serrano, D. P., Pizarro, P., and Coronado, J. M. (2014). Thermochemical energy storage at high temperature via redox cycles of Mn and Co oxides: Pure oxides versus mixed ones. *Solar Energy Materials and Solar Cells,* 123**,** 47-57.

Chen, Q., Zhang, Y., and Yang, M. (2011). An Interfacial Tracking Model for Convection-Controlled Melting Problems. *Numerical Heat Transfer, Part B: Fundamentals,* 59**,** 209-225.

Cheng, W.-L., Zhang, R.-M., Xie, K., Liu, N., and Wang, J. (2010). Heat conduction enhanced shape-stabilized paraffin/HDPE composite PCMs by graphite addition: Preparation and thermal properties. *Solar Energy Materials and Solar Cells,* 94**,** 1636-1642.

Chung, J. D., Lee, J. S., and Yoo, H. (1997). Thermal instability during the melting process in an isothermally heated horizontal cylinder. *Int. J. Heat Mass Transfer,* 40**,** 3899-3907.

D'orazio, M. C., Cianfrini, C., and Corcione, M. (2004). Rayleigh–Bénard convection in tall rectangular enclosures. *International Journal of Thermal Sciences,* 43**,** 135-144.

Darzi, A. R., Farhadi, M., and Sedighi, K. (2012). Numerical study of melting inside concentric and eccentric horizontal annulus. *Applied Mathematical Modelling,* 36**,** 4080-4086.

Desgrosseilliers, L., Whitman, C. A., Groulx, D., and White, M. A. (2013). Dodecanoic acid as a promising phase-change material for thermal energy storage. *Applied Thermal Engineering,* 53**,** 37-41.

Duhar, G., and Colin, C. (2006). Dynamics of bubble growth and detachment in a viscous shear flow. *Physics of Fluids,* 18**,** 077101-1 - 077101-13.

Eames, I. W., and Adref, K. T. (2002). Freezing and melting of water in spherical enclosures of the type used in thermal (ice) storage systems. *Applied Thermal Engineering,* 22**,** 733-745.

Esapour, M., Hamzehnezhad, A., Rabienataj Darzi, A. A., and Jourabian, M. (2018). Melting and solidification of PCM embedded in porous metal foam in horizontal multi-tube heat storage system. *Energy Conversion and Management,* 171**,** 398-410.

Esen, M., and Ayhan, T. (1996). Development of a model compatible with solar assisted cylindrical energy storage tank and variation of stored energy with time for different phase change materials. *Energy Convers. Mgmt,* 37**,** 1775-1785.

Ettouney, H., El-Dessouky, H., and Al-Kandari, E. (2004). Heat transfer characteristics during melting and solidification of phase change energy storage process. *Ind. Eng. Chem. Res,* 43**,** 5350-5357.

Fadl, M., and Eames, P. C. (2019). An experimental investigations of the melting of RT44HC inside a horizontal rectangular test cell subject to uniform wall heat flux. *International Journal of Heat and Mass Transfer,* 140**,** 731-742.

Fallahi, A., Guldentops, G., Tao, M., Granados-Focil, S., and Van Dessel, S. (2017). Review on solid-solid phase change materials for thermal energy storage: Molecular structure and thermal properties. *Applied Thermal Engineering,* 127**,** 1427-1441.

Fan, Z., Infante Ferreira, C. A., and Mosaffa, A. H. (2014). Numerical modelling of high temperature latent heat thermal storage for solar application combining with double-effect H 2 O/LiBr absorption refrigeration system. *Solar Energy,* 110**,** 398-409.

Farid, M., Kim, Y., Honda, T., and Kanzawa, A. (2007). The Role of Natural Convection during Melting and Solidification of Pcm in a Vertical Cylinder. *Chemical Engineering Communications,* 84**,** 43-60.

Farid, M. M., Hamad, F. A., and Abu-Arabi, M. (1998). Melting and solidification in multi-dimensional geometry and presence of more than one interface. *Energy Convers. Mgmt,* 39**,** 809–818.

Farid, M. M., Khudhair, A. M., Razack, S. a. K., and Al-Hallaj, S. (2004). A review on phase change energy storage: materials and applications. *Energy Conversion and Management,* 45**,** 1597-1615.

Fernandez, A. I., Martínez, M., Segarra, M., Martorell, I., and Cabeza, L. F. (2010). Selection of materials with potential in sensible thermal energy storage. *Solar Energy Materials and Solar Cells,* 94**,** 1723-1729.

Gong, Z., and Mujumdar, A. S. (1998). Flow and heat transfer in convection-dominated melting in a rectangular cavity heated from below. *Int. J. Heat Mass Transfer,* 41**,** 2573-2580.

Groulx, D. (2015). Numerical Study of Nano-Enhanced PCMs: Are they worth it? *1st Thermal and Fluid Engineering Summer Conference, TFESC*, New York City, USA, 14p.

Groulx, D., C. Kheirabadi, A., Desgrosseilliers, L., Kabbara, M., Azad, M., Donaldson, A., Joseph, A., and White, M. A. (2016). Working towards solving the Rate Problem: Geometric vs NanoEnhanced PCM Solutions. *INNOSTORAGE Conference*, Be'er Sheva, Israel, 4p.

Groulx, D., and Lacroix, M. (2007). Study of the effect of convection on close contact melting of high Prandtl number substances. *International Journal of Thermal Sciences,* 46**,** 213-220.

Hamdan, M. A., and Al-Hinti, I. (2004). Analysis of heat transfer during the melting of a phase-change material. *Applied Thermal Engineering,* 24**,** 1935-1944.

Hlimi, M., Hamdaoui, S., Mahdaoui, M., Kousksou, T., Ait Msaad, A., Jamil, A., and El Bouardi, A. (2016). Melting inside a horizontal cylindrical capsule. *Case Studies in Thermal Engineering,* 8**,** 359-369.

Ho, C. J., and Gao, J. Y. (2013). An experimental study on melting heat transfer of paraffin dispersed with Al2O3 nanoparticles in a vertical enclosure. *International Journal of Heat and Mass Transfer,* 62**,** 2-8.

Ho, C. J., and Viskanta, R. (1984). Heat transfer during inward melting in a horizontal tube. *International Journal of Heat and Mass Transfer,* 27**,** 705-716.

Hollands, K. G. T., and Konicek, L. (1973). Experimental Study of the Stability of Differentially Heated Inclined Air Layers. *International Journal of Heat and Mass Transfer,* 16**,** 1467-1476.

Hollands, K. G. T., Unny, T. E., Raithby, G. D., and Konicek, L. (1976). Free Convective Heat Transfer Across Inclined Air Layers. *Journal of Heat Transfer,* May**,** 189-193.

Hosseini, M. J., Rahimi, M., and Bahrampoury, R. (2014). Experimental and computational evolution of a shell and tube heat exchanger as a PCM thermal storage system. *International Communications in Heat and Mass Transfer,* 50**,** 128-136.

Hosseinizadeh, S. F., Rabienataj Darzi, A. A., Tan, F. L., and Khodadadi, J. M. (2013). Unconstrained melting inside a sphere. *International Journal of Thermal Sciences,* 63**,** 55-64.

Huang, M. J., Eames, P. C., Norton, B., and Hewitt, N. J. (2011). Natural convection in an internally finned phase change material heat sink for the thermal management of photovoltaics. *Solar Energy Materials and Solar Cells,* 95**,** 1598-1603.

Incropera, F. P., Dewitt, D. P., Bergman, T. L., and Lavine, A. S. (2007). *Fundamentals of Heat and Mass Transfer (6th ed.)*, John Wiley & Sons Inc. 1070p.

Ismail, K. a. R., Alves, C. L. F., and Modesto, M. S. (2001). Numerical and experimental study on the solidi®cation of PCM around a vertical axially finned isothermal cylinder. *Applied Thermal Engineering,* 21**,** 53-77.

Jany, P., and Bejan, A. (1988). Scaling theory of melting with natural convection in an enclosure. *Int. J. Heat Mass Transfer,* 31**,** 1221-1235.

Jaworski, M. (2012). Thermal performance of heat spreader for electronics cooling with incorporated phase change material. *Applied Thermal Engineering,* 35**,** 212-219.

Jevnikar, S. (2018). *Experimental Investigation of the Heat Source Orientation on the Transient Flow and Thermal Behaviour of Phase Change Material During Phase Transition.* Master's Electronic, The University of Western Ontario. 110p.

Ji, C., Qin, Z., Dubey, S., Choo, F. H., and Duan, F. (2018). Simulation on PCM melting enhancement with double-fin length arrangements in a rectangular enclosure induced by natural convection. *International Journal of Heat and Mass Transfer,* 127**,** 255-265.

Jones, B. J., Sun, D., Krishnan, S., and Garimella, S. V. (2006). Experimental and numerical study of melting in a cylinder. *International Journal of Heat and Mass Transfer,* 49**,** 2724-2738.

Kamkari, B., and Amlashi, H. J. (2017). Numerical simulation and experimental verification of constrained melting of phase change material in inclined rectangular enclosures. *International Communications in Heat and Mass Transfer,* 88**,** 211-219.

Kamkari, B., and Groulx, D. (2018). Experimental investigation of melting behaviour of phase change material in finned rectangular enclosures under different inclination angles. *Experimental Thermal and Fluid Science,* 97**,** 94-108.

Kamkari, B., and Shokouhmand, H. (2014). Experimental investigation of phase change material melting in rectangular enclosures with horizontal partial fins. *International Journal of Heat and Mass Transfer,* 78**,** 839-851.

Kamkari, B., Shokouhmand, H., and Bruno, F. (2014). Experimental investigation of the effect of inclination angle on convection-driven melting of phase change material in a rectangular enclosure. *International Journal of Heat and Mass Transfer,* 72**,** 186-200.

Kato, T. (2016). Prediction of photovoltaic power generation output and network operation. *Integration of Distributed Energy Resources in Power Systems.* Elsevier Inc.**,** 77-108.

Kenisarin, M. M. (2014). Thermophysical properties of some organic phase change materials for latent heat storage. A review. *Solar Energy,* 107**,** 553-575.

Khillarkar, D. B., Gong, Z. X., and Mujumdar, A. S. (2000). Melting of a phase change material in concentric horizontal annuli of arbitrary cross-section. *Applied Thermal Engineering,* 20**,** 893-912.

Khodadadi, J. M., and Zhang, Y. (2001). Effects of buoyancy-driven convection on melting within spherical containers. *International Journal of Heat and Mass Transfer,* 44**,** 1605-1618.

Kim, M. C., and Kim, S. (2001). The Onset of Natural Convection and Heat Transfer Correlation in Horizontal Fluid Layer Heated Uniformly from Below. *KSME International Journal,* 15**,** 1451-1460.

Kousksou, T., Bruel, P., Jamil, A., El Rhafiki, T., and Zeraouli, Y. (2014). Energy storage: Applications and challenges. *Solar Energy Materials and Solar Cells,* 120**,** 59-80.

Kozak, Y., Rozenfeld, T., and Ziskind, G. (2014). Close-contact melting in vertical annular enclosures with a non-isothermal base: Theoretical modeling and application to thermal storage. *International Journal of Heat and Mass Transfer,* 72**,** 114-127.

Lacroix, M. (2001). Contact melting of a phase change material inside a heated parallelepedic capsule. *Energy Conversion and Management,* 42**,** 35-47.

Li, W. Q., Qu, Z. G., He, Y. L., and Tao, W. Q. (2012). Experimental and numerical studies on melting phase change heat transfer in open-cell metallic foams filled with paraffin. *Applied Thermal Engineering,* 37**,** 1-9.

Li, Y. Q., He, Y. L., Song, H. J., Xu, C., and Wang, W. W. (2013). Numerical analysis and parameters optimization of shell-and-tube heat storage unit using three phase change materials. *Renewable Energy,* 59**,** 92-99.

Liu, C., and Groulx, D. (2014). Experimental study of the phase change heat transfer inside a horizontal cylindrical latent heat energy storage system. *International Journal of Thermal Sciences,* 82**,** 100-110.

Liu, C., Murray, R. E., and Groulx, D. (2012). Experimental Study of Cylindrical Latent Heat Energy Storage Systems Using Lauric Acid as the Phase Change Material. *ASME 2012 Summer Heat Transfer Conference*, Puerto Rico, USA, 10 p.

Liu, Z., and Ma, C. (2002). Numerical analysis of melting with constant heat flux heating in a thermal energy storage system. *Energy Conversion and Management,* 43**,** 2521-2538.

Longeon, M., Soupart, A., Fourmigué, J.-F., Bruch, A., and Marty, P. (2013). Experimental and numerical study of annular PCM storage in the presence of natural convection. *Applied Energy,* 112**,** 175-184.

Mahdi, J. M., and Nsofor, E. C. (2017). Melting enhancement in triplex-tube latent thermal energy storage system using nanoparticles-fins combination. *International Journal of Heat and Mass Transfer,* 109**,** 417-427.

Mahlia, T. M. I., Saktisahdan, T. J., Jannifar, A., Hasan, M. H., and Matseelar, H. S. C. (2014). A review of available methods and development on energy storage; technology update. *Renewable and Sustainable Energy Reviews,* 33**,** 532-545.

Medrano, M., Yilmaz, M. O., Nogués, M., Martorell, I., Roca, J., and Cabeza, L. F. (2009). Experimental evaluation of commercial heat exchangers for use as PCM thermal storage systems. *Applied Energy,* 86**,** 2047-2055.

Mehling, H., and Cabeza, L. F. (2008). *Basic thermodynamics of thermal energy storage In: Heat and cold storage with PCM.* Heat and Mass Transfer. Springer, Berlin, Heidelberg. 1-10.

Mettawee, E.-B. S., and Assassa, G. M. R. (2007). Thermal conductivity enhancement in a latent heat storage system. *Solar Energy,* 81**,** 839-845.

Motahar, S., Alemrajabi, A. A., and Khodabandeh, R. (2017). Experimental investigation on heat transfer characteristics during melting of a phase change material with dispersed TiO2 nanoparticles in a rectangular enclosure. *International Journal of Heat and Mass Transfer,* 109**,** 134-146.

Murray, R. E., Desgrosseilliers, L., Stewart, J., Osbourne, N., Marin, G., Safatli, A., Groulx, D., and White, M. A. (2011). Design of a Latent Heat Energy Storage System Coupled with a Domestic Hot Water Solar Thermal System. *World Renewable Energy Congress 2011*, Linköping, Sweden, 8 p.

Murray, R. E., and Groulx, D. (2014). Experimental study of the phase change and energy characteristics inside a cylindrical latent heat energy storage system: Part 1 consecutive charging and discharging. *Renewable Energy,* 62**,** 571-581.

Ng, K. W., Gong, Z. X., and Mujumdar, A. S. (1998). Heat transfer in free convection-dominated melting of a phase change material in a horizontal annulus. *Int. Comm. Heat Mass Transfer,* 25**,** 631-640.

Niedermeier, K., Flesch, J., Marocco, L., and Wetzel, T. (2016). Assessment of thermal energy storage options in a sodium-based CSP plant. *Applied Thermal Engineering,* 107**,** 386-397.

Ogoh, W., and Groulx, D. (2012a). Effects of the heat transfer fluid velocity on the storage characteristics of a cylindrical latent heat energy storage system: a numerical study. *Heat and Mass Transfer,* 48**,** 439-449.

Ogoh, W., and Groulx, D. (2012b). Effects of the number and distribution of fins on the storage characteristics of a cylindrical latent heat energy storage system: a numerical study. *Heat and Mass Transfer,* 48**,** 1825-1835.

Pahamli, Y., Hosseini, M. J., Ranjbar, A. A., and Bahrampoury, R. (2016). Analysis of the effect of eccentricity and operational parameters in PCM-filled single-pass shell and tube heat exchangers. *Renewable Energy,* 97**,** 344-357.

Pal, D., and Joshi, Y. K. (2001). Melting in a side heated tall enclosure by a uniformly dissipating heat source. *International Journal of Heat and Mass Transfer,* 44**,** 375-387.

Pirasaci, T., and Goswami, D. Y. (2016). Influence of design on performance of a latent heat storage system for a direct steam generation power plant. *Applied Energy,* 162**,** 644-652.

Pointner, H., De Gracia, A., Vogel, J., Tay, N. H. S., Liu, M., Johnson, M., and Cabeza, L. F. (2016). Computational efficiency in numerical modeling of high temperature latent heat storage: Comparison of selected software tools based on experimental data. *Applied Energy,* 161**,** 337-348.

Prieto, C., Cooper, P., Fernández, A. I., and Cabeza, L. F. (2016). Review of technology: Thermochemical energy storage for concentrated solar power plants. *Renewable and Sustainable Energy Reviews,* 60**,** 909-929.

Rathod, M. K., and Banerjee, J. (2013). Thermal stability of phase change materials used in latent heat energy storage systems: A review. *Renewable and Sustainable Energy Reviews,* 18**,** 246-258.

Regin, A. F., Solanki, S. C., and Saini, J. S. (2006). Latent heat thermal energy storage using cylindrical capsule: Numerical and experimental investigations. *Renewable Energy,* 31**,** 2025-2041.

Rieger, H., Projahn, U., Bareiss, M., and Beer, H. (1983). Heat Transfer During Melting Inside a Horizontal Tube. *Journal of Heat Transfer,* 105**,** 226-234.

Rizan, M. Z. M., Tan, F. L., and Tso, C. P. (2012). An experimental study of *n*-octadecane melting inside a sphere subjected to constant heat rate at surface. *International Communications in Heat and Mass Transfer,* 39**,** 1624-1630.

Rosario, M. a. O. (2018). *Customizable latent heat thermal energy storage and transfer system for air-cooling in buildings : design and thermal analysis.* PhD, Université de Bordeaux. 255p.

Rozenfeld, T., Kozak, Y., Hayat, R., and Ziskind, G. (2015). Close-contact melting in a horizontal cylindrical enclosure with longitudinal plate fins: Demonstration, modeling and application to thermal storage. *International Journal of Heat and Mass Transfer,* 86**,** 465-477.

Şahan, N., Fois, M., and Paksoy, H. (2015). Improving thermal conductivity phase change materials—A study of paraffin nanomagnetite composites. *Solar Energy Materials and Solar Cells,* 137**,** 61-67.

Sarı, A., Alkan, C., and Biçer, A. (2012). Synthesis and thermal properties of polystyrene-graft-PEG copolymers as new kinds of solid–solid phase change materials for thermal energy storage. *Materials Chemistry and Physics,* 133**,** 87-94.

Sattari, H., Mohebbi, A., Afsahi, M. M., and Azimi Yancheshme, A. (2017). CFD simulation of melting process of phase change materials (PCMs) in a spherical capsule. *International Journal of Refrigeration,* 73**,** 209-218.

Seddegh, S., Wang, X., and Henderson, A. D. (2016). A comparative study of thermal behaviour of a horizontal and vertical shell-and-tube energy storage using phase change materials. *Applied Thermal Engineering,* 93**,** 348-358.

Seeniraj, R. V., and Narasimhan, N. L. (2008). Performance enhancement of a solar dynamic LHTS module having both fins and multiple PCMs. *Solar Energy,* 82**,** 535-542.

Shah, D. U., Bock, M. C. D., Mulligan, H., and Ramage, M. H. (2015). Thermal conductivity of engineered bamboo composites. *Journal of Materials Science,* 51**,** 2991-3002.

Sharifi, N., Robak, C. W., Bergman, T. L., and Faghri, A. (2013). Three-dimensional PCM melting in a vertical cylindrical enclosure including the effects of tilting. *International Journal of Heat and Mass Transfer,* 65**,** 798-806.

Sharma, A., Tyagi, V. V., Chen, C. R., and Buddhi, D. (2009). Review on thermal energy storage with phase change materials and applications. *Renewable and Sustainable Energy Reviews,* 13**,** 318-345.

Sharma, R. K., Ganesan, P., Tyagi, V. V., Metselaar, H. S. C., and Sandaran, S. C. (2016). Thermal properties and heat storage analysis of palmitic acid-TiO 2 composite as nano-enhanced organic phase change material (NEOPCM). *Applied Thermal Engineering,* 99**,** 1254-1262.

Shatikian, V., Ziskind, G., and Letan, R. (2005). Numerical investigation of a PCM-based heat sink with internal fins. *International Journal of Heat and Mass Transfer,* 48**,** 3689-3706.

Shatikian, V., Ziskind, G., and Letan, R. (2008). Numerical investigation of a PCM-based heat sink with internal fins: Constant heat flux. *International Journal of Heat and Mass Transfer,* 51**,** 1488-1493.

Shmueli, H., Ziskind, G., and Letan, R. (2010). Melting in a vertical cylindrical tube: Numerical investigation and comparison with experiments. *International Journal of Heat and Mass Transfer,* 53**,** 4082-4091.

Shokouhmand, H., and Kamkari, B. (2013). Experimental investigation on melting heat transfer characteristics of lauric acid in a rectangular thermal storage unit. *Experimental Thermal and Fluid Science,* 50**,** 201-212.

Stritih, U. (2004). An experimental study of enhanced heat transfer in rectangular PCM thermal storage. *International Journal of Heat and Mass Transfer,* 47**,** 2841-2847.

Su, W., Darkwa, J., and Kokogiannakis, G. (2015). Review of solid–liquid phase change materials and their encapsulation technologies. *Renewable and Sustainable Energy Reviews,* 48**,** 373-391.

Sun, X., Zhang, Q., Medina, M. A., and Lee, K. O. (2016). Experimental observations on the heat transfer enhancement caused by natural convection during melting of solid–liquid phase change materials (PCMs). *Applied Energy,* 162**,** 1453-1461.

Tan, F. L. (2008). Constrained and unconstrained melting inside a sphere. *International Communications in Heat and Mass Transfer,* 35**,** 466-475.

Tan, F. L., Hosseinizadeh, S. F., Khodadadi, J. M., and Fan, L. (2009). Experimental and computational study of constrained melting of phase change materials (PCM) inside a spherical capsule. *International Journal of Heat and Mass Transfer,* 52**,** 3464-3472.

Tao, Y. B., and Carey, V. P. (2016). Effects of PCM thermophysical properties on thermal storage performance of a shell-and-tube latent heat storage unit. *Applied Energy,* 179**,** 203-210.

Tao, Y. B., and He, Y. L. (2011). Numerical study on thermal energy storage performance of phase change material under non-steady-state inlet boundary. *Applied Energy,* 88**,** 4172-4179.

Tao, Y. B., and He, Y. L. (2015). Effects of natural convection on latent heat storage performance of salt in a horizontal concentric tube. *Applied Energy,* 143**,** 38-46.

Tay, N. H. S., Belusko, M., and Bruno, F. (2012). An effectiveness-NTU technique for characterising tube-in-tank phase change thermal energy storage systems. *Applied Energy,* 91**,** 309-319.

Taylor, J. R. (1997). *An introduction to error analysis: the study of unertainties in physical measurements (2nd ed.)*, University Science Books. 349p.

Tehrani, S. S. M., Diarce, G., and Taylor, R. A. (2018). The error of neglecting natural convection in high temperature vertical shell-and-tube latent heat thermal energy storage systems. *Solar Energy,* 174**,** 489-501.

Vogel, J., Felbinger, J., and Johnson, M. (2016). Natural convection in high temperature flat plate latent heat thermal energy storage systems. *Applied Energy,* 184**,** 184-196.

Wang, Y., Amiri, A., and Vafai, K. (1999). An experimental investigation of the melting process in a rectangular enclosure. *International Journal of Heat and Mass Transfer,* 42**,** 3659-3672.

Wu, S., Zhou, C., Doroodchi, E., Nellore, R., and Moghtaderi, B. (2018). A review on high-temperature thermochemical energy storage based on metal oxides redox cycle. *Energy Conversion and Management,* 168**,** 421-453.

Yaws, C. L. (2003). Yaws' Handbook of thermodynamic and Physical Properties of Chemical Compounds. *Knovel*.

Yazıcı, M. Y., Avcı, M., Aydın, O., and Akgun, M. (2014). Effect of eccentricity on melting behavior of paraffin in a horizontal tube-in-shell storage unit: An experimental study. *Solar Energy,* 101**,** 291-298.

Zhou, D., and Zhao, C. Y. (2011). Experimental investigations on heat transfer in phase change materials (PCMs) embedded in porous materials. *Applied Thermal Engineering,* 31**,** 970-977.

Zivkovic, B., and Fujii, I. (2001). An analysis of isothermal phase change of phase change material within rectangular and cylindrical containers. *Solar Energy,* 70**,** 51–61.

APPENDIX A MATLAB SCRIPT FOR IMAGE ACQUISITION

```
%Prompt for input
T = input('What is the heating temperature in degree celcius? ');

Onset_Duration = input('How many minutes is the onset duration? ');
Onset_Duration = Onset_Duration*60;

Onset_Delay = input('How many seconds is the delay in onset acquisition?
');

Intermediate_Duration = input('How many minutes is the intermediate
duration? ');
Intermediate_Duration = Intermediate_Duration*60;

Intermediate_Delay = input('How many minutes is the delay in intermediate
acquisition? ');
Intermediate_Delay = Intermediate_Delay*60;

Final_Duration = input('How many hours is the final duration? ');
Final_Duration = Final_Duration*3600;

Final_Delay = input('How many minutes is the final delay? ');
Final_Delay = Final_Delay*60;

PCM = input('Enter 1 for n-octadecane or 2 for dodecanoic acid');

%Creates directories
TempUnit = ' deg.C\';
SDiameter = 'Core Diameter = 18 mm';
MDiameter = 'Core Diameter = 27 mm';
LDiameter = 'Core Diameter = 36 mm';

%PCM properties
if(PCM == 1)
   L=189000;
   Cp=2240;
   Tm=27.5;
elseif(PCM == 2)
   L=180000;
   Cp=1950;
   Tm=43;
end

%Calculates Stefan number
Ste=(Cp*(T-Tm)/L);

destinationFolder1 = ['C:\',PCM,'Ste = ',Ste, ' - Core Temperature =
',T,TempUnit,SDiameter];
if ~exist(destinationFolder1, 'dir')
  mkdir(destinationFolder1);
end

destinationFolder2 = ['C:\',PCM,'Ste = ',Ste, ' - Core Temperature =
',T,TempUnit,MDiameter];
if ~exist(destinationFolder2, 'dir')
```

```
  mkdir(destinationFolder2);
end

destinationFolder3 = ['C:\',PCM,'Ste = ',Ste, ' - Core Temperature =
',T,TempUnit,LDiameter];
if ~exist(destinationFolder3, 'dir')
  mkdir(destinationFolder3);
end

%Creates camera list
camList = webcamlist;
cam1 = webcam(1);
cam2 = webcam(2);
cam3 = webcam(3);

%Sets the camera resolutions
cam1.Resolution = '2304x1536';
cam2.Resolution = '2304x1536';
cam3.Resolution = '2304x1536';

%Calculates the number of frames
Onset_Frames = Onset_Duration/Onset_Delay+1;
Intermediate_Frames = Intermediate_Duration/Intermediate_Delay;
Final_Frames = Final_Duration/Final_Delay;

count=0;

%Image acquisition
tic

%Image acquisition for the convection onset period
for i = 1:Onset_Frames

        img1 = snapshot(cam1);
        axes(handles.SDia)
        imshow(img1);
        imwrite(img1,       fullfile(destinationFolder1,sprintf('d=18mm-
Ste=0.2-n_octadecane_%d sec.png',count)));

        img2 = snapshot(cam2);
        axes(handles.MDia)
        imshow(img2);
        imwrite(img2,       fullfile(destinationFolder2,sprintf('d=27mm-
Ste=0.2-n_octadecane_%d sec.png',count)));

        img3 = snapshot(cam3);
        axes(handles.LDia)
        imshow(img3);
        imwrite(img3,       fullfile(destinationFolder3,sprintf('d=36mm-
Ste=0.2-n_octadecane_%d sec.png',count)));

        pause(Onset_Delay);
        count = count+Onset_Delay;
end

%Delay after the image acquisition for the onset period
pause(Intermediate_Delay-Onset_Delay);
```

```
count = count+Intermediate_Delay-Onset_Delay;

%Image acquisition for at a slower rate than for onset frames
for i = 1:Intermediate_Frames

        img1 = snapshot(cam1);
        axes(handles.SDia)
        imshow(img1);
        imwrite(img1,       fullfile(destinationFolder1,sprintf('d=18mm-
Ste=0.2-n_octadecane_%d sec.png',count)));

        img2 = snapshot(cam2);
        axes(handles.MDia)
        imshow(img2);
        imwrite(img2,       fullfile(destinationFolder2,sprintf('d=27mm-
Ste=0.2-n_octadecane_%d sec.png',count)));

        img3 = snapshot(cam3);
        axes(handles.LDia)
        imshow(img3);
        imwrite(img3,       fullfile(destinationFolder3,sprintf('d=36mm-
Ste=0.2-n_octadecane_%d sec.png',count)));

        pause(Intermediate_Delay);
        count = count+Intermediate_Delay;
end

%Delay before the images acquisition in the final phase
pause(Final_Delay-Intermediate_Delay);
count = count+Final_Delay-Intermediate_Delay;

%Image acquisition in the final phase of the melting process
for i = 1:Final_Frames

        img1 = snapshot(cam1);
        axes(handles.SDia)
        imshow(img1);
        imwrite(img1,       fullfile(destinationFolder1,sprintf('d=18mm-
Ste=0.2-n_octadecane_%d sec.png',count)));

        img2 = snapshot(cam2);
        axes(handles.MDia)
        imshow(img2);
        imwrite(img2,       fullfile(destinationFolder2,sprintf('d=27mm-
Ste=0.2-n_octadecane_%d sec.png',count)));

        img3 = snapshot(cam3);
        axes(handles.LDia)
        imshow(img3);
        imwrite(img3,       fullfile(destinationFolder3,sprintf('d=36mm-
Ste=0.2-n_octadecane_%d sec.png',count)));

        pause(Final_Delay);
        count = count+Final_Delay;
end

clear cam1;
```

```
clear cam2;
clear cam3;
end
```

APPENDIX B MATLAB SCRIPT FOR IMAGE PROCESSING

```
% the folder in which the images exists
srcFiles = dir('C:\Processing\*.png');

% destination folder to store right half of the cleaned images
destinationFolder1 = ['C:\Processing\Cleaned Images Right Half'];
if ~exist(destinationFolder1, 'dir')
  mkdir(destinationFolder1);
end


% prompts to get the variables to define the geometry
prompt = 'What is the X coordinate of the origin? ';
x = input(prompt);

prompt = 'What is the Y coordinate of the origin? ';
y = input(prompt);

prompt = 'What is the diameter of the enclosure in pixel? ';
enclosure_radius_in_pixels = input(prompt)/2;

prompt = 'What is the tube diameter in pixel? ';
tube_radius_in_pixels = input(prompt)/2;

% loop to process batch data
for k = 1 : length(srcFiles)

    % extraction of file name and different operating conditions
    filename = strcat('C:\Processing\',srcFiles(k).name);
    im = imread(filename);

    ix1 = strfind(filename,'-');
    ix2 = strfind(filename,'sec');
    ix3 = strfind(filename,'=');
    ix4 = strfind(filename,'mm');
    ix5 = strfind(filename,'_');
    ix6 = strfind(filename,'degC');

    t= filename(ix5(2)+1:ix2(1)-2);
    t = str2double(t);
    diameter = filename(ix3(1)+1:ix4(1)-1);
    diameter = str2double(diameter);
    Ste = filename(ix3(2)+1:ix1(3)-1);
    Ste = str2double(Ste);
    Ti = filename(ix3(3)+1:ix6(1)-1);
    Ti = str2double(Ti);

width = 1.25*enclosure_radius_in_pixels;
height  = width*2;
enclosure_radius_in_meter = 2.5*0.0254;

%Pixel to meter conversion
length_factor = enclosure_radius_in_pixels/enclosure_radius_in_meter;
area_factor = length_factor*length_factor;
```

```
%Assign the RGB values
R_Value = 0;
G_Value = 0;
B_Value = 0;

% legend set up
text_str = cell(2,1);
legend = [Ste t/60];
text_str{1} = ['Ste = ' num2str(legend(1),'%0.1f') ';'];
text_str{2} = ['t = ' num2str(legend(2),'%0.2f') ' min'];
box_color = {'white','white'};
font = 'Times New Roman';

%Crop the image
enclosure_image = imcrop(im,[x y-width width height]);
position_enclosure = [0 height;120 height];
enclosure_image_legend =
insertText(enclosure_image,position_enclosure,text_str,'FontSize',28,'F
ont', font,'BoxColor',box_color,'BoxOpacity',0.95,'TextColor','black');
imwrite(enclosure_image_legend,
fullfile(destinationFolder1,sprintf('n_octadecane_D=%d
mm_Ste=%.2f_Ti=%.2fdegC-%d sec.png',diameter, Ste, Ti, t)));


%Make the extra area, outside the PCM cavity and the tube, red
 for x1=1:height
           for y1=1:width
               if ((x1-width)^2 + (y1-0)^2) >
enclosure_radius_in_pixels^2
               enclosure_image(x1,y1,:)=[255 0 0];
               end

               if ((x1-width)^2 + (y1-0)^2) < tube_radius_in_pixels^2
               enclosure_image(x1,y1,:)=[255 0 0];
               end
           end
 end

%Select the color values below the thresholds
Red = enclosure_image(:,:,1)<=R_Value;
Green = enclosure_image(:,:,2)<=G_Value;
Blue = enclosure_image(:,:,3)<=B_Value;

%Combine the colors to form binary image
modified_enclosure_image = Red & Green & Blue;

%Count the nonzero pixels
pixelCount_enclosure_image = sum(modified_enclosure_image(:));

%Phase change area in square meter
liquid_area = pixelCount_enclosure_image/area_factor;

%Repeat the above to calculate interface length along x axis
image_along_x = imcrop(enclosure_image,[0 width width 0]);
Red = image_along_x(:,:,1)<=R_Value;
Green = image_along_x(:,:,2)<=G_Value;
Blue = image_along_x(:,:,3)<=B_Value;
```

```
modified_image_along_x = Red & Green & Blue;
pixelCount_image_along_x = sum(modified_image_along_x(:));
x_length = pixelCount_image_along_x/length_factor;

%Repeat the above to calculate interface length along positive y axis
image_along_positive_y = imcrop(enclosure_image,[0 0 1 width]);
Red = image_along_positive_y(:,:,1)<=R_Value;
Green = image_along_positive_y(:,:,2)<=G_Value;
Blue = image_along_positive_y(:,:,3)<=B_Value;
modified_image_along_positive_y = Red & Green & Blue;
subplot(1,4,3),imshow(modified_image_along_positive_y);
pixelCount_image_along_positive_y =
sum(modified_image_along_positive_y(:));
positive_y_length = pixelCount_image_along_positive_y/length_factor;

%Repeat the above to calculate interface length along positive y axis
image_along_negative_y = imcrop(enclosure_image,[0 width 1 width]);
Red = image_along_negative_y(:,:,1)<=R_Value;
Green = image_along_negative_y(:,:,2)<=G_Value;
Blue = image_along_negative_y(:,:,3)<=B_Value;
modified_image_along_negative_y = Red & Green & Blue;
subplot(1,4,2),imshow(modified_image_along_negative_y);
pixelCount_image_along_negative_y =
sum(modified_image_along_negative_y(:));
negative_y_length = pixelCount_image_along_negative_y/length_factor;

results(k,:,:,:,:)=[diameter Ti Ste t liquid_area x_length
positive_y_length negative_y_length];
sorted_results = sortrows(results,4);
end
```

ELSEVIER LICENSE
TERMS AND CONDITIONS

Jul 02, 2020

This Agreement between Mohammad Azad ("You") and Elsevier ("Elsevier") consists of your license details and the terms and conditions provided by Elsevier and Copyright Clearance Center.

License Number	4860990440784
License date	Jul 02, 2020
Licensed Content Publisher	Elsevier
Licensed Content Publication	Experimental Thermal and Fluid Science
Licensed Content Title	Experimental investigation on melting heat transfer characteristics of lauric acid in a rectangular thermal storage unit
Licensed Content Author	Hossein Shokouhmand,Babak Kamkari
Licensed Content	Date Oct 1, 2013
Licensed Content Volume	50
Licensed Content Issue	n/a
Licensed Content Pages	12
Start Page	201
End Page	212
Type of Use	reuse in a thesis/dissertation
Portion	figures/tables/illustrations
Number of figures/tables/illustrations	4
Format	both print and electronic
Are you the author of this Elsevier article?	No
Will you be translating?	No
Title	A STUDY OF NATURAL CONVECTION ONSET AND MELTING PROCESS OF PHASE CHANGE MATERIALS IN HORIZONTAL CYLINDRICAL ENCLOSURES
Institution name	Dalhousie University
Expected presentation date	Aug 2020
Order reference number	4842960315382
Portions	Fig. 4
Requestor Location	Mohammad Azad B-30 West St Antigonish, NS B2G1R8 Canada Attn: Mohammad Azad
Publisher Tax ID	GB 494 6272 12
Total	0.00 CAD

ELSEVIER LICENSE
TERMS AND CONDITIONS

Jul 02, 2020

This Agreement between Mohammad Azad ("You") and Elsevier ("Elsevier") consists of your license details and the terms and conditions provided by Elsevier and Copyright Clearance Center.

License Number	4860990909346
License date	Jul 02, 2020
Licensed Content Publisher	Elsevier
Licensed Content Publication	International Journal of Heat and Mass Transfer
Licensed Content Title	Experimental and computational study of constrained melting of phase change materials (PCM) inside a spherical capsule
Licensed Content Author	F.L. Tan,S.F. Hosseinizadeh,J.M. Khodadadi,Liwu Fan
Licensed Content Date	Jul 1, 2009
Licensed Content Volume	52
Licensed Content Issue	15-16
Licensed Content Pages	9
Start Page	3464
End Page	3472
Type of Use	reuse in a thesis/dissertation
Portion	figures/tables/illustrations
Number of figures/tables/illustrations	2
Format	both print and electronic
Are you the author of this Elsevier article?	No
Will you be translating?	No
Title	A STUDY OF NATURAL CONVECTION ONSET AND MELTING PROCESS OF PHASE CHANGE MATERIALS IN HORIZONTAL CYLINDRICAL ENCLOSURES
Institution name	Dalhousie University
Expected presentation date	Aug 2020
Order reference number	4842960133210
Portions	Fig. 2
Requestor Location	Mohammad Azad B-30 West St Antigonish, NS B2G1R8 Canada Attn: Mohammad Azad
Publisher Tax ID	GB 494 6272 12
Total	0.00 CAD

ELSEVIER LICENSE
TERMS AND CONDITIONS

Jul 02, 2020

This Agreement between Mohammad Azad ("You") and Elsevier ("Elsevier") consists of your license details and the terms and conditions provided by Elsevier and Copyright Clearance Center.

License Number	4860981491499
License date	Jul 02, 2020
Licensed Content Publisher	Elsevier
Licensed Content Publication	International Journal of Heat and Mass Transfer
Licensed Content Title	Melting in a vertical cylindrical tube: Numerical investigation and comparison with experiments
Licensed Content Author	H. Shmueli,G. Ziskind,R. Letan
Licensed Content Date	Sep 1, 2010
Licensed Content Volume	53
Licensed Content Issue	19-20
Licensed Content Pages	10
Start Page	4082
End Page	4091
Type of Use	reuse in a thesis/dissertation
Portion	figures/tables/illustrations
Number of figures/tables/illustrations	5
Format	both print and electronic
Are you the author of this Elsevier article?	No
Will you be translating?	No
Title	A STUDY OF NATURAL CONVECTION ONSET AND MELTING PROCESS OF PHASE CHANGE MATERIALS IN HORIZONTAL CYLINDRICAL ENCLOSURES
Institution name	Dalhousie University
Expected presentation date	Aug 2020
Order reference number	4842960589737
Portions	Fig. 5
Requestor Location	Mohammad Azad B-30 West St Antigonish, NS B2G1R8 Canada Attn: Mohammad Azad
Publisher Tax ID	GB 494 6272 12
Total	0.00 CAD